Erasmus MC
Universitair Medisch Centrum Rotterdam

Erasmus MC
THORAXCENTRUM

The 26th European Symposium on Ultrasound Contrast Imaging

- An ICUS Conference -

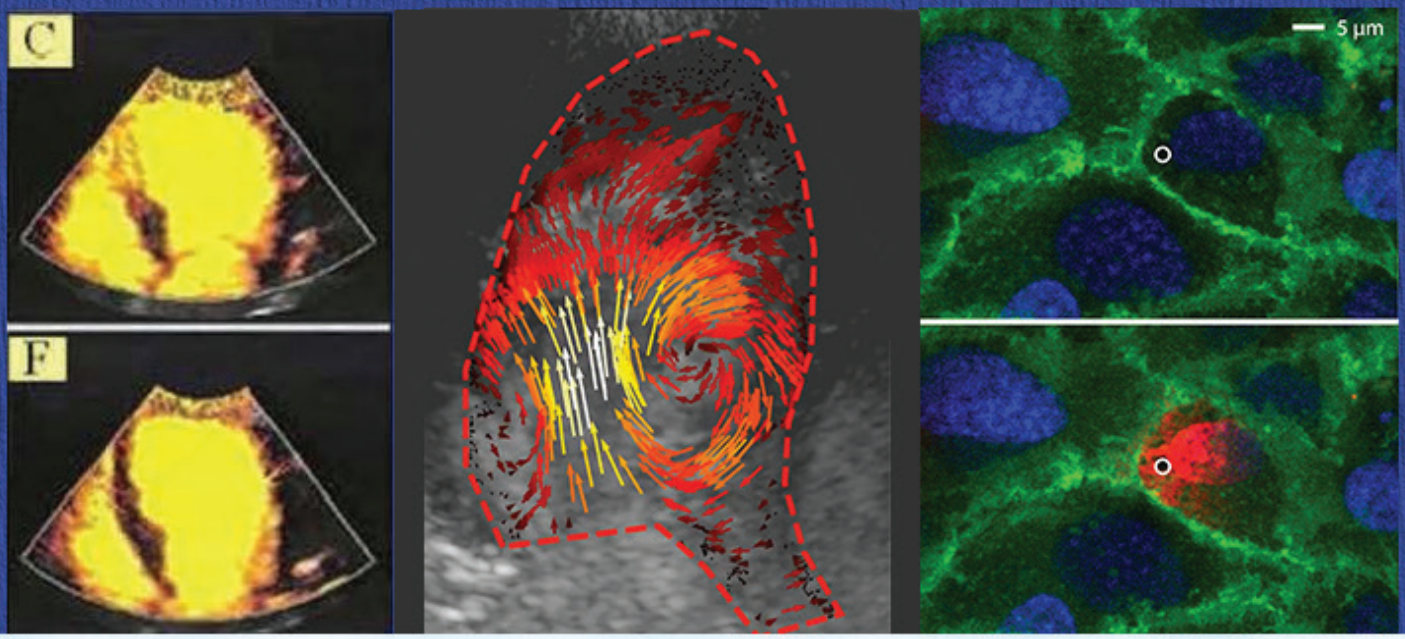

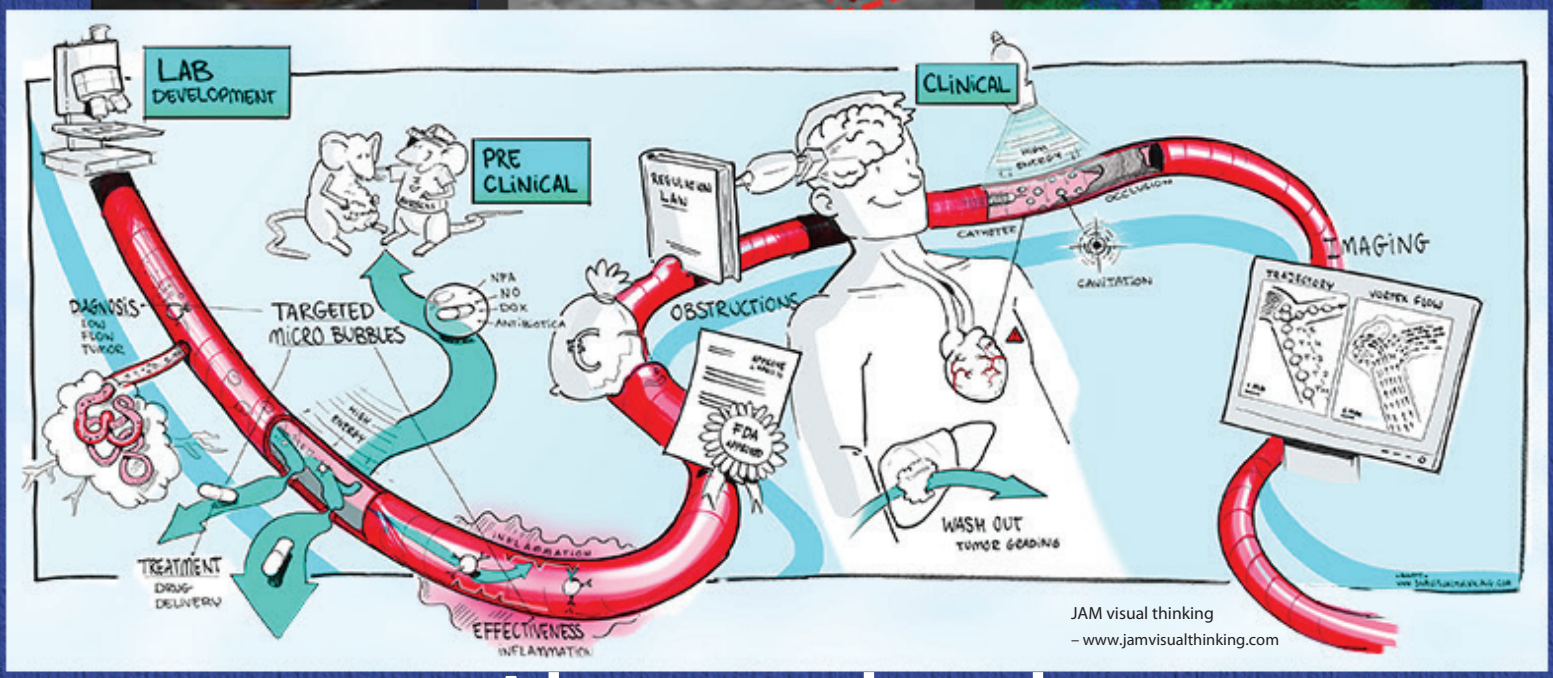

Abstract book

14-15 January 2021, Online

Organised by Nico de Jong, Folkert ten Cate, Rik Vos, Klazina Kooiman, Annemien van den Bosch, and Arend Schinkel

Erasmus MC Rotterdam

26th EUROPEAN SYMPOSIUM ON ULTRASOUND CONTRAST IMAGING
14-15 JANUARY 2021, online

THURSDAY, 14 January 2021

13.00 CET	Webportal will be open	
14.00 – 14.10 CET	Welcome by the chairs	
14.10 – 15.30 CET	CLINICAL IMAGING & THERAPY ..... Chair: Annemien van den Bosch	
14.10 Tom Porter	Immediate Improvement in Systolic Function Following Sonothrombolysis Applied After Emergent Percutaneous Coronary Intervention in Anterior ST Segment Elevation Myocardial Infarction	1
14.35 Pavel Taimr	Performance of CEUS versus MRI and value of point shear wave elastography for diagnosis hepatocellular adenoma and focal nodular hyperplasia.	2
15.00 Stefan Engelhard	Ultrasound velocimetry in the diseased aorto-iliac tract: a clinical feasibility study	4
15.15 Zhiyang Jin	Genetically Encoded Acoustic Biosensors for Ultrasonic Imaging of Intracellular Enzyme	6
15.30 – 15.50 CET	DISCUSSION PANEL ..... ……..Chair: Olivier Couture	
15.50 – 16.15 CET	Break	
16.15 – 17.30 CET	PARALLEL ORAL SESSIONS A (Technology imaging) and B (Technology other) *The best presentation in each session will be awarded with the ESUCI Research Award supported by Bracco*	
17.30 – 17.45 CET	Break	
17.45 – 18.55 CET	THERAPY: Towards clinical use ..... Chair: Klazina Kooiman	
17.45 Hong Chen	Microbubbles-enabled sonobiopsy for noninvasive diagnosis of brain tumors	8
18.10 Paul M. Johnson	Non-invasive receptor-specific millimeter-precision manipulation of brain circuits	10
18.25 Joop Kouijzer	Vancomycin-targeted microbubbles for the treatment of *Staphylococcus aureus* biofilms under flow	15
18.40 Alexandre Helbert	Ultrasound molecular imaging for the guidance of ultrasound triggered release of liposomal doxorubicin and its treatment monitoring in an orthotopic prostatic tumor model in rat	18
18.55 – 19.00 CET	Adjourn	
19:00 – 20.15 CET	Online pubquiz –Zoom link will be provided	

Organised by: Rik Vos, Klazina Kooiman, Annemien van den Bosch, Arend Schinkel, Folkert ten Cate, Nico de Jong.

Scientific board: Mike Averkiou, Mark Borden, Paolo Colonna, Olivier Couture, Beat Kaufmann, Eleanor Stride.

26th EUROPEAN SYMPOSIUM ON ULTRASOUND CONTRAST IMAGING
14-15 JANUARY 2021, online

FRIDAY, 15 January 2021

13.00 CET	Webportal will be open	
14.00 – 14.05 CET	Welcome by the chairs	
14.05 – 15.15 CET	BUBBLE TECHNOLOGY ..... Chair: Klazina Kooiman	
14.05 Eleanor Stride	Which came first, the bubble or the droplet? (and other vaporisation questions)	20
14.30 Gonzalo C. Lara	Super-localization of superheated nanodroplet vaporization during proton irradiation using high frame-rate differential imaging	25
14.45 Benjamin van Elburg	Dilatational surface tension curves of monodisperse microbubbles with a tuned shell stiffness	28
15.00 Simone Langeveld	Lipid handling and phase distribution affect the acoustic behavior of DSPC-based microbubbles	31
15.15 – 15.35 CET	BREAK-OUT ROOMS	
15.35 – 15.50 CET	Break	
15.50 – 16.35 CET	COMPETITION: ARTIFICIAL INTELLIGENCE ..... Chair: Nico de Jong	
15.50 Jihwan Youn	Task-Adaptive Beamforming for Microbubble Localization using Deep Learning	34
16.05 Ben Luijten	Microbubble Localization in High-Clutter Environments using Fullwave Simulations and Model-Based Deep Learning.....	37
16.20 Nathan Blanken	Contrast-enhanced single-RF-line simulations and super-resolution microbubble detection using deep learning	39
16.35 – 16.40 CET	Break	
16.40 – 18.05 CET	PARALLEL ORAL SESSIONS C (Biology/Clinical) and D (Bubble technology) *The best presentation in each session will be awarded with the ESUCI Research Award supported by Bracco*	
18.05 – 18.15 CET	Break	
18.15 – 18.55 CET	ADVANCED CONTRAST IMAGING ..... Chair: Rik Vos	
18.15 Pengfei Song	Challenges and Opportunities in Microbubble Localization for Super-Resolution Microvascular Imaging.....	42
18.40 Arthur Chavignon	3D Transcranial Ultrasound Localization Microscopy in rat with a multiplexed matrix probe	44
18.55 – 19.05 CET	ANNOUNCEMENT OF WINNERS	
19.05 – 19.30 CET	ADJOURN AND CLOSING	

Organised by: Rik Vos, Klazina Kooiman, Annemien van den Bosch, Arend Schinkel, Folkert ten Cate, Nico de Jong.

Scientific board: Mike Averkiou, Mark Borden, Paolo Colonna, Olivier Couture, Beat Kaufmann, Eleanor Stride.

THURSDAY, 14 January 2021

Parallel oral sessions Thursday

The best presentation in each session will be awarded with the ESUCI Research Award supported by Bracco

Organised by: Rik Vos, Klazina Kooiman, Annemien van den Bosch, Arend Schinkel, Folkert ten Cate, Nico de Jong.

Scientific board: Mike Averkiou, Mark Borden, Paolo Colonna, Olivier Couture, Beat Kaufmann, Eleanor Stride.

26th EUROPEAN SYMPOSIUM ON ULTRASOUND CONTRAST IMAGING
14-15 JANUARY 2021, online

FRIDAY, 15 January 2021

Parallel oral sessions Friday

The best presentation in each session will be awarded with the ESUCI Research Award supported by Bracco

Immediate Improvement in Systolic Function Following Sonothrombolysis Applied After Emergent Percutaneous Coronary Intervention in Anterior ST Segment Elevation Myocardial Infarction

Thomas R. Porter, MD

University of Nebraska Medical Center

Introduction

Microvascular obstruction (MVO) and stunning result in significant left ventricular systolic dysfunction following emergent percutaneous coronary intervention (PCI) in left anterior descending (LAD) ST segment elevation myocardial infarction (STEMI).

Although diagnostic ultrasound (DUS) mediated high mechanical index (MI) impulses may reduce MVO during a microbubble infusion, these high MI impulses may have a shear effect on the endothelium that alters coronary flow and could rapid effects on systolic function. We hypothesized that this may have an immediate effect on left ventricular ejection fraction (LVEF) in the immediate post PCI period.

Methods

Twenty six acute anterior STEMI patients who received emergent PCI of the LAD underwent diagnostic real time myocardial contrast echo within one hour of completion of the PCI. All patients had TIMI 2-3 flow in the infarct vessel post PCI. Patients were randomized to low MI (<0.2) imaging only during a 20 minute commercially available enhancing agent infusion (3% Definity), or to low MI imaging with repeated high MI impulses (1.1 MI) in the apical (4, 2, 3) chamber views guided by replenishment. An independent observer analyzed biplane derived contrast enhanced left ventricular ejection fraction (LVEF) on the initial images obtained prior to randomized treatment, and repeated the measurements in the same windows at the end of randomized treatment. Cardiac magnetic resonance imaging (MRI) was performed at three days to assess for microvascular obstruction (MVO).

Results

Immediately after successful PCI, LVEF prior to randomized treatment was not different between groups, 42+7% high MI versus 40+9% low MI only. After randomized treatment, the high MI treated group had a significant increase in LVEF (48+8%; $p<0.0001$) while no change occurred in patients randomized to low MI only (41+1%; $p=0.27$). Extent of MVO (indexed to LV mass) at 3 days by MRI was 1.9+4% in the high MI treated patients compared to 5.2+8% in Low MI only patients ($p=0.12$).

Conclusions

A 20 minute application of sonothrombolysis immediately post PCI in acute LAD STEMI results in an immediate improvement in systolic function that may have an effect on the extent of MVO.

References

[1]. Xie F, Qian L, Goldsweig A, Xu D, Porter TR. Event-free survival following successful percutaneous intervention in acute myocardial infarction depends on microvascular perfusion. Circ Cardiovasc Imaging 2020;13:e010091.doi:10.1161/circimaging.119.010091

Performance of CEUS versus MRI and value of point shear wave elastography for diagnosis hepatocellular adenoma and focal nodular hyperplasia.

P.Taimr[1,4], M.E.E.Broker[2], J.Klompenhouwer[2], R.Dwarkasing[3], J.N.N.IJzermans[2], R.De Knegt[1], R.A.De Man[1]

[1]Department of Gastroenterology and Hepatology, [2]Department of Surgery, [3]Department of Radiology, Erasmus MC, Rotterdam, The Netherlands
[4]Department of Gastroenterology and Hepatology, IKEM, Prague, Czech Republic
Corresponding author: pata@ikem.cz

Introduction

Focal nodular hyperplasia (FNH) and hepatocellular adenoma (HCA) are liver tumors that require different management. There is a need to improve the noninvasive diagnosis in order to avoid overtreatment of FNH and undertreatment of HCA. We compared contrast-enhanced sonography (CEUS) with magnetic resonance imaging (MRI) in the diagnosis of HCA and FNH in a large cohort of consecutive patients. Further, we assessed the potential of point shear wave elastography (pSWE) to differentiate thesetwo tumors and the interobserver and intraobserver reliability of pSWE in the examination of these lesions and of native liver tissue (NLT).

Methods

Patients referred to a tertiary centre for hepatobiliary disease who had suspected HCA or FNH on MRI performed with an extracellular liver specific gadolinium-based contrast agent underwent a prospective workup including CEUS (Hitachi 900, Hitachi Preirus and Philips Epiq) with contrast agent Sonovue. Diagnosis was definite when the findings of CEUS and MRI were concordant; tumor tissue biopsy was performed for cases with discordant findings. Descriptive statistics and the association between categoric variables were presented as numbers and percentages and were assessed using the Fisher exact test. The primary analysis was patient based. Sensitivity, specificity, and AUC and predictive values for the diagnosis of HCA and FNH were calculated separately for CEUS and MRI.

pSWE (Philips, Epiq) was performed by two experienced liver sonographers (O1 and O2) and acquired within the lesion of interest and NLT. Group differences, optimal cutoff for characterization and interobserver reliability was assessed with Mann-Whitney-U, area under the ROC curce (AUROC) and intraclass correlation coefficient (ICC). Intraobserver reliability in NLT was assessed in 20 healthy subjects using ICC.

Results

A total of 181 patients were selected for the first analysis. Findings from CEUS and MRI were concordant for 132 patients (73%) and discordant for 49 (27%). Tumor biopsy was performed for 26 of the 49 patients with discordant findings (53%), with findings indeterminate for two of these patients, the findings of MRI with a liver-specific contrast agent correct for 21 of the remaining 24 patients (87.5%), and the findings of CEUS correct for three of these 24 patients (12.5%) ($p < 0.05$). For further analysis, 156 patients with concordant findings or tumor biopsy-proven cases were included. For CEUS, the sensitivity and specificity for the diagnosis of HCA and FNH were 85% and 87%, respectively; the ROC AUC value was 0.856; and the positive predictive value and negative predictive value were 79% and 90%, respectively. For MRI the sensitivity and specificity were 95% each, the ROC AUC value was 0.949, and the positive predictive value and negative predictive value were 92% and 97%, respectively, for the diagnosis of HCA and FNH.

For the second analysis we included 88 patients (65 FNH, 23 HCA). Median stiffness was significantly higher in FNH than in HCA (7.01 kPa vs 4.98 kPa for O1 ($P< 0.017$) and 7.68 kPa vs 6.00 kPa for O2 ($P < 0.031$)). A cutoff point for differentiation between the two entities could not be determined with an AUROC of 0.67 (O1) and 0.69 (O2). Interobserver reliability was good for lesion- stiffness (ICC< 0.86) and poor for NLT stiffness (ICC < 0.09). In healthy subjects, intraobserver reliability for NLT-stiffness was poor for O1 (ICC < 0.23) and moderate for O2 (ICC < 0.62).

In 15 patients either the CEUS versus MRI or biopsy diagnosis did not match, or distinction between FNH and HCA could not be made based on that CEUS imaging modality. The stiffness values for these lesions ranged from 1.65 to 8.75 kPa for FNHs and from 1.29 to 9.36 kPa for HCAs. The pSWE values ranged from low to high for both lesions and pSWE could not provide a contributory argument in these patients.

Conclusions

The findings of CEUS with pure intravascular contrast agent and MRI with a liver-specific contrast agent showed fair agreement for the diagnosis of HCA and FNH. MRI with a liver-specific contrast agent is diagnostically correct significantly more often than CEUS in cases with discordant findings that are biopsy proven. CEUS is less suitable as a stand-alone imaging modality for final diagnosis of FNH and HCA.

pSWE alone cannot reliably differentiate FNH from HCA and pSWE could not provide a contributory argument in patients in whom there was a discrepancy between CEUS and MRI or biopsy diagnosis. Also, interobserver and intraobserver reliability for pSWE in normal liver tissue were insufficient. Interpretation of results gained with this method should be done with great caution.

Ultrasound velocimetry in the diseased aorto-iliac tract: a clinical feasibility study

***Stefan Engelhard*[1,3,4], *Majorie van Helvert*[1,3,4], *Jason Voorneveld*[2], *Johan Bosch*[2], *Erik Groot Jebbink*[1,4], *Michel Versluis*[3], *Michel Reijnen*[1,4].**

[1] *Department of Vascular Surgery, Rijnstate Hospital, Arnhem, NL*
[2] *Department of Biomedical Engineering, Thorax Center, Erasmus MC, Rotterdam, NL*
[3] *Physics of Fluids group, TechMed centre, University of Twente, Enschede, NL*
[4] *Multi-modality Medical Imaging Group, TechMed centre, University of Twente, Enschede, NL*
Corresponding author: s.a.j.engelhard@utwente.nl

Introduction

Accurate quantification of blood flow in the aorto-iliac arteries is challenging due to complex flow phenomena that occur near the aortic bifurcation and around stenotic lesions. These flow phenomena are clinically relevant as they can contribute to atherosclerotic disease progression and stent failures. While standard duplex ultrasound only represents the blood flow to and from the transducer, high-frame-rate contrast-enhanced ultrasound (HFR-CEUS) in combination with particle image velocimetry (PIV), or echoPIV, can be used for 2-dimensional time-resolved blood flow quantification in deep vessels [1].

A feasibility study in healthy volunteers showed that quantitative visualization of blood flow patterns with echoPIV is promising [2]. However, the clinical applicability of echoPIV remains challenging. The aim of this study is to investigate the feasibility and clinical applicability of echoPIV in the aorto-iliac tract in patients with Peripheral Arterial Disease (PAD)

Methods

35 patients, recently diagnosed with an aortoiliac stenotic lesion, underwent 1 or 2 HFR-CEUS measurements 1 month after starting supervised exercise therapy. 2 measurements were performed if the inflow and outflow tract of the stenosis could not be visualized within 1 image plane. A Verasonics Vantage 256 US machine (Verasonics, Kirkland, WA) and a curved array transducer (GE C1-6D, GE company, boston, MA**)** was used for a spherical wave acquisition scheme with 3 different insonification angles at a pulse repetition frequency of 6 kHz.

PIV analysis was performed via pairwise cross-correlation of all captured ultrasound images. Visual evaluation of the velocity data was performed by 5 observers (qualitative analysis). Contrast-to-Background ratio and average vector correlation was calculated during the systolic and diastolic phase of the cardiac cycle (quantitative analysis). These results were used to evaluate the ability of the echoPIV technique to provide accurate visualization of local blood flow patterns.

Vector complexity [3] and vorticity was calculated in 2 patients where visual evaluation showed disturbed flow. In these patients, 2 separate regions with disturbed and undisturbed flow were compared, to quantify these flow field disturbances with echoPIV.

Results

42 HFR-CEUS measurements were performed. The imaged vessels were located at a depth of 20-70 mm on the HFR-CEUS images. The typical Mechanical Index (MI) at this depth was: 0.04-0.06.

Qualitative analysis showed that partial flow visualisation (i.e. only during systole or in part of the vessel segment) could be achieved in 41/42 measurements. In 16/42 measurements, blood flow could be visualized in the entire imaged vessel segment and during the entire cardiac cycle. In the other 25 measurements, only partial flow visualization was possible, because one or multiple issues occurred, such as: loss of correlation due to high flow velocities or shear during systole (12 cases); short vessel segment in the imaged plane due to complex geometry (7 cases); ultrasound shadow regions in the imaged segment due to calcifications in (8 cases) and loss of contrast during diastole due to contrast destruction (5 cases).

Quantitative analysis showed that the contrast-to-background ratio of the HFR-CEUS images was higher during systole, while the vector correlation was lower during systole. Flow complexity and vorticity was higher in regions with disturbed flow, compared to an undisturbed region in the same vessel (fig. 1).

Conclusions

Partial flow visualisation was possible in all measurements, while complete visualization of blood flow patterns was achieved in 15/42 measurements. In patients with disturbed blood flow, these flow field disturbances could be clearly distinguished from undisturbed flow, by calculating vector complexity and vorticity. Clinical follow-up of the current patient cohort will be performed to investigate how these flow parameters can be used to predict clinical outcome and assist clinical decision support.

References

[1]. Vos HJ, Voorneveld JD, Groot Jebbink E, et al. Contrast-Enhanced High-Frame-Rate Ultrasound Imaging of Flow Patterns in Cardiac Chambers and Deep Vessels. Ultrasound Med Biol. 2020;46(11):2875–90

[2]. Engelhard S, Voorneveld J, Vos HJ, et al. High-frame-rate contrast-enhanced US particle image velocimetry in the abdominal aorta: First human results. Radiology. 2018;289(1):119–25.

[3]. Saris AECM, Hansen HHG, Fekkes S, et al. In Vivo Blood Velocity Vector Imaging Using Adaptive Velocity Compounding in the Carotid Artery Bifurcation. Ultrasound Med Biol. 2019;45(7):1691–707.

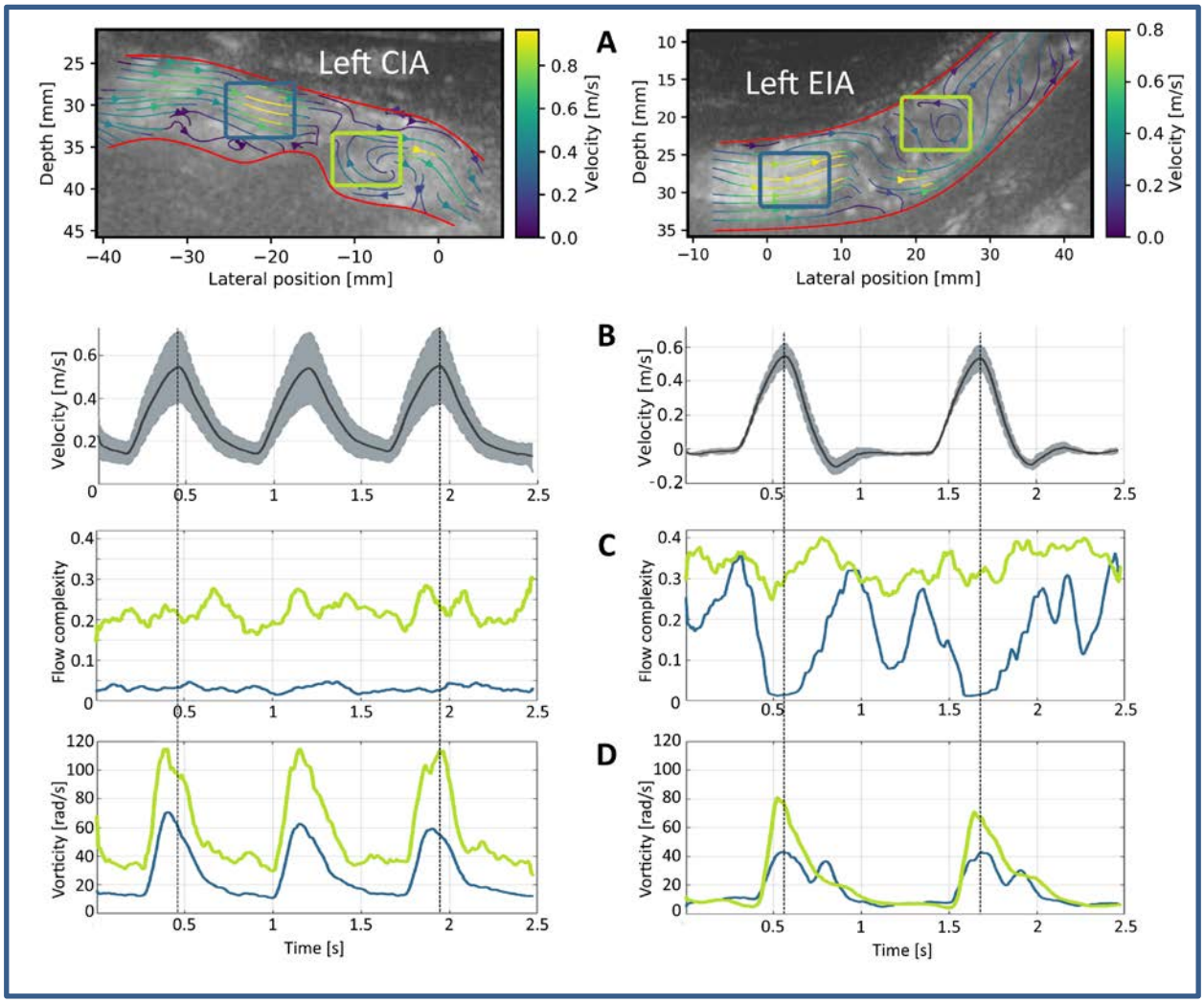

Figure 1. A: Streamline velocity data during systole in 2 patients where visual evaluation showed flow disturbances. Flow parameters were calculated in a region with undisturbed flow (blue box) and disturbed flow (red box). **B:** Temporal velocity profiles, measured in 5 locations along the center of the lumen (Average velocity with variations plotted as shaded bars). **C:** Flow complexity is higher in the regions with disturbed flow, in the right patient this is mostly the case during systole. **D:** Vorticity occurs in both patients in both regions during systole, but is higher in the regions with disturbed flow.

Genetically Encoded Acoustic Biosensors for Ultrasonic Imaging of Intracellular Enzyme

Anupama Lakshmanan [1,#], Zhiyang Jin[1,#], Suchita P. Nety[1], Daniel P. Sawyer[1], Audrey Lee-Gosselin[1], Dina Malounda[1], Margaret Swift[1], David Maresca[1], and Mikhail G. Shapiro[1].

[1]California Institute of Technology, Pasadena, US. [#]Contributed equally.
Corresponding author: mikhail@caltech.edu

Introduction

A major goal of biomolecular ultrasound is to develop contrast agents that can dynamically sense physiologically relevant molecules or their activity within living cells. Gas vesicles (GVs) – genetically encoded gas-filled protein nanostructures – are a promising candidate for the development of such contrast agents due to their ability to be engineered at the genetic level and expressed heterologously as genetic reporters[1-4]. Building on these capabilities, we engineered 'dynamic GVs' (dGVs) that change non-linear ultrasound contrast dynamically in response to the activity of proteases: an important class of enzymes underlying cellular homeostasis and disease processes, and a target of drug discovery. Here we demonstrate the functionality of dGVs inside living cells and *in vivo*.

Methods

We engineered dGVs that produce enhanced non-linear acoustic signals upon sensing the activity of three types of proteases **(Fig. 1A)**. Genetic modification of the GV shell protein 'GvpC', by incorporation of a protease recognition motif or degradation tag, enables its subsequent cleavage or degradation by the protease and this dynamic weakening or removal of GvpC causes the GV shell to become less stiff, undergo non-linear buckling in response to ultrasound, and produce enhanced contrast under amplitude modulation imaging. dGVs were tested in purified form *in vitro*, and expressed in bacteria to demonstrate their intracellular functionality and *in vivo* in the mouse colon **(Fig. 1A-D)**.

Results

GVs showed significant enhancement in non-linear contrast upon sensing protease activity *in vitro* **(Fig. 1E)**. dGV-expressing bacteria also showed stronger non-linear contrast with the target protease inside the cells than with it absent **(Fig. 1F)**. Furthermore, non-linear contrast of the cells could be 'tuned-down' by expression of non-degradable GvpC upon addition of a chemical inducer **(Fig. 1G)**. dGV-expressing bacteria with intracellular protease activity could be acoustically distinguished from those with the absence of active protease inside the colon of live mice **(Fig. 1H)**.

Conclusions

These results show that GVs can be engineered as dynamic biomolecular sensors for ultrasound imaging of intracellular enzyme activity, extending the capabilities of this modality into an important area of biological imaging.

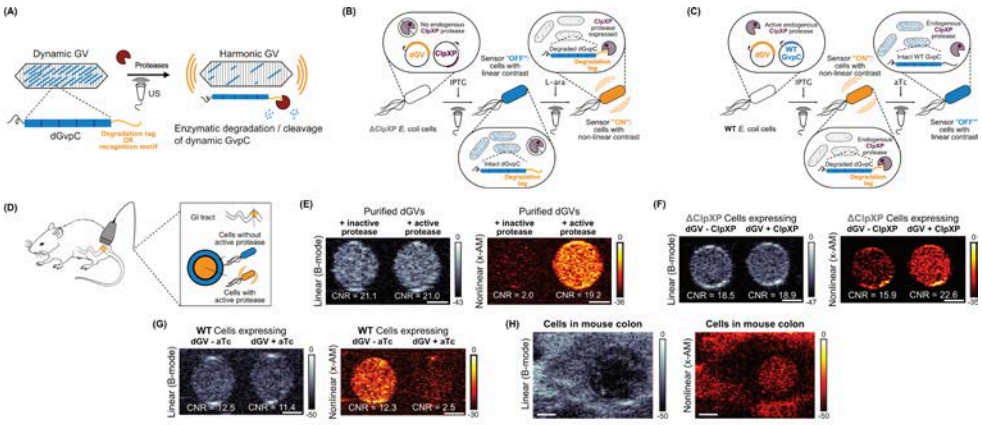

Fig.1 (A) Schematic illustration of dynamic gas vesicles (dGVs) respond to proteases and produce enhanced nonlinear ultrasound signal in reconstituted cell-free systems. (B) Schematic illustration of dGVs expressed in genetically modified probiotics *E. Coli* Nissle (ECN) cells without endogenous ClpXP protease activity (Δ ClpXP), where those cells showed nonlinear contrast with active ClpXP upon addition of L-arabinose (L-ara). (C) Schematic illustration of nonlinear contrast produced by dGV expressing wild-type (WT) ECN cells and eliminated by expression of non-degradable GvpC upon addition of anhydrotetracycline (aTc). (D) Schematic illustration of mouse colon imaging with dGV expressing Δ ClpXP ECN cells with and without intracellular ClpXP protease activity. Ultrasound images of (E) dGVs in reconstituted cell-free system *in vitro*, (F) dGV expressing Δ ClpXP ECN cells without and with intracellular ClpXP protease, (G) dGV expressing WT Nissle cells with and without aTc, (H) dGV expressing Δ ClpXP ECN cells in mouse colon *in vivo*. Ultrasound image acquired at 15.625 MHz using B-mode and a custom cross-amplitude modulation pulse sequence (xAM) for Scale bars: 1 mm.

References

[1]. Shapiro, M.G. et al. Biogenic gas nanostructures as ultrasonic molecular reporters. Nature Nanotechnology 9, 311-316 (2014).

[2]. Lakshmanan, A. et al. Molecular Engineering of Acoustic Protein Nanostructures. ACS Nano 10, 7314-7322 (2016).

[3]. Bourdeau, R.W. et al. Acoustic reporter genes for noninvasive imaging of microorganisms in mammalian hosts. Nature 553, 86-90 (2018).

[4]. Farhadi, A., Ho, G.H., Sawyer, D.P., Bourdeau, R.W. & Shapiro, M.G. Ultrasound imaging of gene expression in mammalian cells. Science 365, 1469 (2019).

Microbubbles-enabled sonobiopsy for noninvasive diagnosis of brain tumors

***Hong Chen*[1], *Christopher Pham Pacia*[1], *Lifei Zhu*[1], *Arash Nazeri*[1], *Yimei Yue*[1], *Jinyun Yuan*[1], *H. Michael Gach*[1], *Michael R. Talcott*[1], *Weijun Liu*[1], *Xiaowei Wang*[2], *Gavin P. Dunn*[1], *Allegra A. Petti*[1], *Eric C. Leuthardt*[1]**

[1]*Washington University in St. Louis, Saint Louis, MO, USA*
[2]*University of Illinois at Chicago, Illinois, USA*
Corresponding author: hongchen@wustl.edu

Introduction

Blood-based liquid biopsy is a promising noninvasive diagnostic technique to acquire a comprehensive molecular tumor profile by detecting cancer-specific biomarkers (e.g., DNA, RNA, and protein) [1]. However, there has been limited progress for brain tumor applications partially because of the blood-brain barrier (BBB), which hinders the release of brain tumor biomarkers [2]. We developed the microbubble-enabled sonobiopsy technique, which uses microbubbles activated by focused ultrasound (FUS) to increase the BBB permeability and thus enhance the release of brain tumor-specific biomarkers into the bloodstream for the noninvasive diagnosis of brain tumors by blood tests.

Methods

Mice with intracranial injection of enhanced green fluorescent protein (eGFP)-transduced glioblastoma cells were sonicated by FUS at various pressure levels in the presence of systemically injected microbubbles at different doses. Contrast-enhanced MR images were acquired before and after the FUS sonication to quantify the BBB permeability changes. The effect of FUS on plasma eGFP mRNA levels was determined using quantitative polymerase chain reaction. The safety of FUS sonication was evaluated by the quantification of microhemorrhages density based on histological staining of *ex vivo* brain slices. The feasibility and safety of sonobiopsy were also evaluated using a porcine model. The plasmas concentrations of two brain-specific protein biomarkers, glial fibrillary acidic protein (GFAP) and myelin basic protein (MBP), before and after FUS sonication were quantified using enzyme-linked immunosorbent assays (ELISA). The safety of sonobiopsy in the porcine model was assessed by combining *in vivo* MR imaging and *ex vivo* histological analysis.

Results

The circulating levels of eGFP mRNA were 1,500–4,800 fold higher in the FUS-treated mice than that of the untreated mice (Fig. 1A, B). Microhemorrhage density associated with FUS at 0.59 MPa was significantly lower than that at higher acoustic pressures (1.296 MPa and 1.58 MPa) and not significantly different from the control group. There were significant increases in plasma eGFP mRNA levels as the ultrasound pressure and microbubble concentration increases. Post-sonication MRI contrast enhancement had a strong linear correlation with the level of FUS-induced biomarker release. Sonobiopsy was also found to be feasible in the porcine model with significant enhancement of blood concentrations of GFAP and MBP detected after FUS sonication as compared with before FUS (Fig. 1C, D). There was no detectable tissue damage as assessed by T_2*-weighted MRI and histological analysis of the porcine brain.

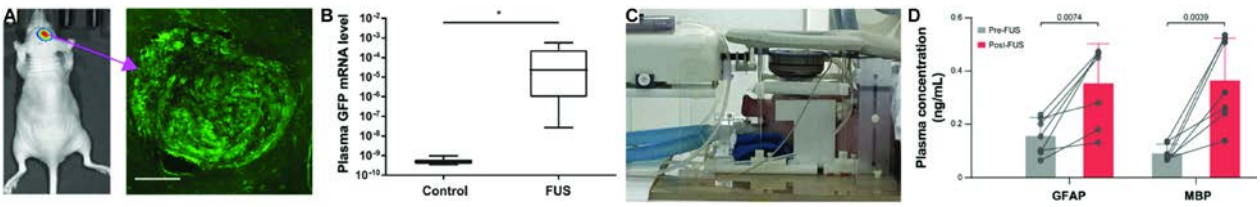

Figure 1. Microbubbles-enabled sonobiopsy in mice (A, B) and pigs (C, D).

Conclusions

Microbubbles-enabled sonobiopsy is feasible and safe in the murine glioma model and porcine model. Sonobiopsy provides a promising technique for noninvasive and localized diagnosis of the molecular profiles of brain diseases with the potential to translate to the clinic.

References

[1]. Cohen JD, *et al.,* Detection and localization of surgically resectable cancers with a multi-analyte blood test. *Science*, *359*(6378): 926–930, 2018

[2]. Bettegowda C, *et al.,* Detection of circulating tumor DNA in early- and late-stage human malignancies. Sci Transl Med 6: 224ra24, 2014

Non-invasive receptor-specific millimeter-precision manipulation of brain circuits

Paul M. Johnson[1,2,†], Mehmet S. Ozdas[1,2,†], Aagam S. Shah[1,2,†], Nisheet Patel[1], Markus Marks[1,2], Tansel Baran Yasar[1,2], Urs Stalder[3], Laurent Bigler[3], Wolfger von der Behrens[1,2], Shashank R. Sirsi[1,4] and Mehmet Fatih Yanik[1,2]

[1]Institute of Neuroinformatics, ETH Zürich, Switzerland
[2]Neuroscience Center, Zurich
[3]Department of Chemistry, University of Zurich, Switzerland
[4]Department of Bioengineering, University of Texas at Dallas, Texas 75080, USA
[†]Equal Contribution
Corresponding author: yanik@ethz.ch, shah@ini.ethz.ch

Introduction

Targeted non-invasive, receptor-specific modulation of brain circuits can lead to breakthroughs in the treatment of brain disorders. To address this, we systemically deliver engineered ultrasound-sensitive drug carriers. We then apply a two-component Aggregation and Uncaging focused ultrasound sequence (AU-FUS) to a brain region. The first sequence concentrates the drug carriers with millimeter precision, then second sequence uncages the carrier's cargo focally to achieve high target specificity and low off-target effects without opening BBB. Upon release from the carriers, the drug locally crosses the intact BBB. We show circuit-specific manipulation of sensory signaling in motor cortex in rats by locally concentrating and releasing a $GABA_A$ receptor agonist (muscimol) from ultrasound-sensitive carriers. Our focal-concentration approach requires use of orders of magnitude less drug, which significantly reduces off-target effects as we show by recordings from neighboring brain areas.

Methods

Female Long Evans (200-300 g, n=43 for all experiments) were anesthetized under isoflurane (1.5-2%). A Neuronexus probe (A2x16-10mm) was inserted in the vibrissae motor cortex (vM1) for electrophysiological recordings. A custom 2.5 MHz FUS transducer (Sonic Concepts) was positioned on the skull such that it targets vibrissae sensory cortex (vS1) with the aid of an ultrasound collimator and sterile gel (Fig. 1). vS1 and vM1 are functionally connected however anatomically distant regions from each other. This electrode configuration was used to avoid confounding effects due to possible mechanical FUS effect on the electrodes and the BBB disruption upon electrode insertion itself. Custom liposomes are loaded with muscimol and conjugated with microbubbles then injected through tail-vein (0.2mL/min,6e8/mL concentration for 20-25 mins). 30s following injection start AU-FUS sequence was repeatedly applied until 2-3 mins after injection end. BBB integrity was verified with Evans Blue, gadolinium and PCD. For evoked local field potential (eLFP) analysis, the raw data was low pass filtered (3^{rd} order Butterworth filter) at 300 Hz. The eLFPs were aligned to the whisker stimulus averaged over 2 mins and then normalized to the average response amplitude of the baseline All data shown is mean ± s.e.m. Extracellular spike detection and sorting was done with Klustakwik. All electrophysiological data analysis was done in custom Python scripts.

Results

We show that evoked extra-cellular multi-unit activity and eLFPs in vM1 can reversibly be inhibited (Fig.1b), and our control experiments shows that inhibition in vM1 occurs only when muscimol loaded particles are sonicated with AU-FUS in vS1 (Fig.1c-d). An equivalent inhibition in vM1 with AU-FUS and ultrasound controlled drug carriers can be achieved with orders of magnitude less drug than systemic muscimol injection (Fig. 2). We show that the drug delivery is limited to a small brain region by recording visually evoked activity from a neighboring circuitry (visual cortex) which is not involved in whisker evoked

sensory information flow (Fig. 1e-f). Our PCD, Evans Blue and MRI contrast agent experiments show that the drug delivery is done without disruption of the BBB (Fig. 3).

Conclusions

We developed a reliable and safe method for targeted, non-invasive, receptor specific neuromodulation of brain circuits. Our *in-vivo* results prove that drugs can be delivered to targeted brain regions with high resolution without BBB opening. Our next plan is to deliver FDA approved neuromodulators to specific brain regions to alter the phenotype of animal models of neuro-psychiatric disorders.

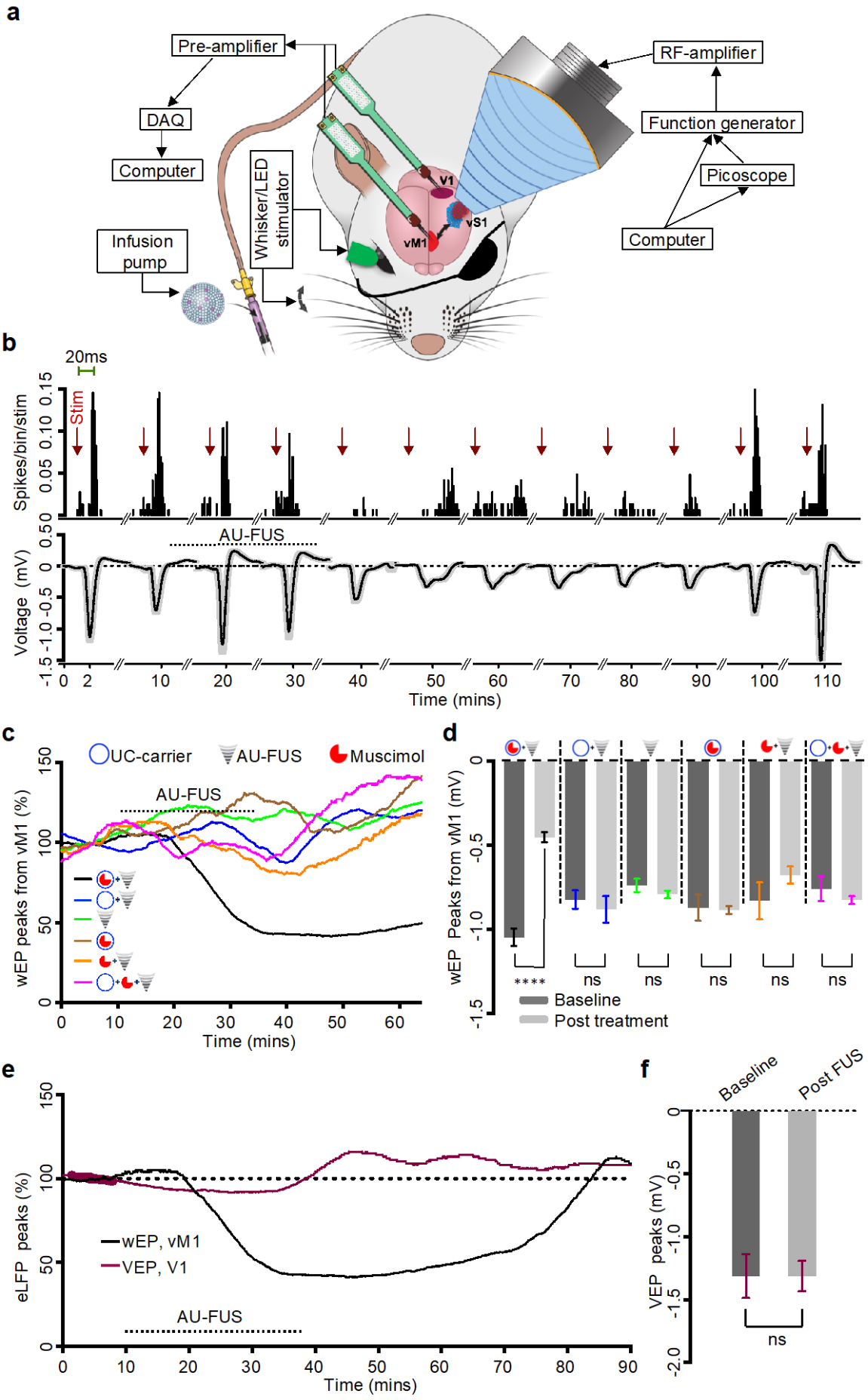
a
Pre-amplifier
DAQ
Computer
Infusion pump
Whisker/LED stimulator
RF-amplifier
Function generator
Picoscope
Computer
V1
vS1
vM1
b
20ms
Stim
Spikes/bin/stim
AU-FUS
Voltage (mV)
Time (mins)
c
UC-carrier
AU-FUS
Muscimol
AU-FUS
wEP peaks from vM1 (%)
Time (mins)
d
wEP Peaks from vM1 (mV)
****
ns
Baseline
Post treatment
e
eLFP peaks (%)
wEP, vM1
VEP, V1
AU-FUS
Time (mins)
f
Baseline
Post FUS
VEP peaks (mV)
ns

Figure 1. **Receptor-specific modulation of a cortical circuit in vivo**

a. Experimental setup for in vivo drug delivery. V1 and vM1 recordings were performed in separate cohorts.

b. Representative peri-stimulus time histograms (PSTHs, top, bin size 2 ms) and wEPs (bottom) upon focal aggregation of drug carriers (muscimol-loaded UC-carriers) and uncaging of muscimol from one experiment.

c-d. Time course of normalized wEPs (negative peak) in vM1. Muscimol-loaded UC-carriers with AU-FUS (black line, n = 6 rats x 4 recording sites), vehicle-loaded UC-carriers with AU-FUS (blue line, n = 6 rats x 4 recording sites), AU-FUS without UC-carrier injection (green line, n = 9 experiments [from 5 rats] x 4 recording sites), muscimol-loaded UC-carrier injection without AU-FUS (brown line, n = 5 rats x 4 recording sites), systemic injection of free muscimol (250 ng) with AU-FUS (orange line, n = 5 rats x 4 recording sites), systemic injection of free muscimol (250 ng) and vehicle-loaded UC-carriers with AU-FUS (pink line, n = 5 rats x 4 recording sites). Evoked responses were averaged with a moving window (Window Size = 180 whisker deflections). All results are mean values.

e-f. Locally uncaged muscimol does not spread to neighboring cortical areas. Time course of the normalized eLFP (negative peak) responses (VEP, purple line, , n = 4 rats x 4 recording sites) in neighboring V1 (without significant connectivity with vS1), as compared to responses (wEP, black line, , n = 4 rats x 4 recording site) in vM1. V1 and vM1 recordings were done on separate cohorts. The same ultrasound parameters were used for both vS1-vM1 and vS1-V1 paradigms.

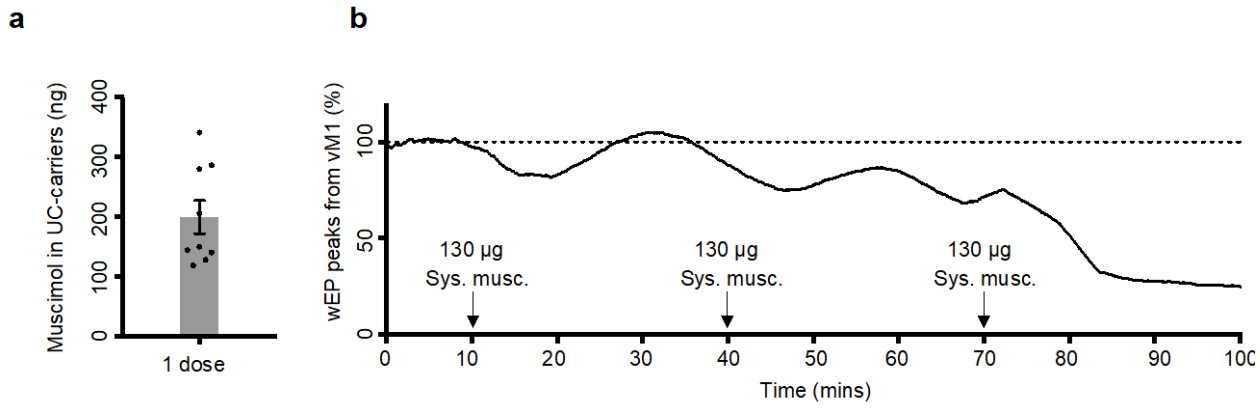

Figure 2. **1300-fold focal enhancement of drug by AU-FUS compared to systemic levels.**

a LC-HR-MS/MS quantification of muscimol loaded in 1 dose of AU-FUS treatment. All data is mean ± s.e.m, showing all points. Average = 199.7 ng, n = 9.

b Time course of wEPs (negative peak) in vM1 during systemic muscimol ("sys. musc.") injection (IV). Following 10 mins of baseline, 130 µg of muscimol (~650 times single muscimol-loaded UC-carrier injection dose) is manually injected over 1 min, every 30 mins (black arrows). Data is plotted as the moving average (window size = 180 whisker deflections). All data is mean ± s.e.m. n = 4 rats x 4 recording sites. Equivalent inhibition by AU-FUS would occur between 260 and 390 µg systemically.

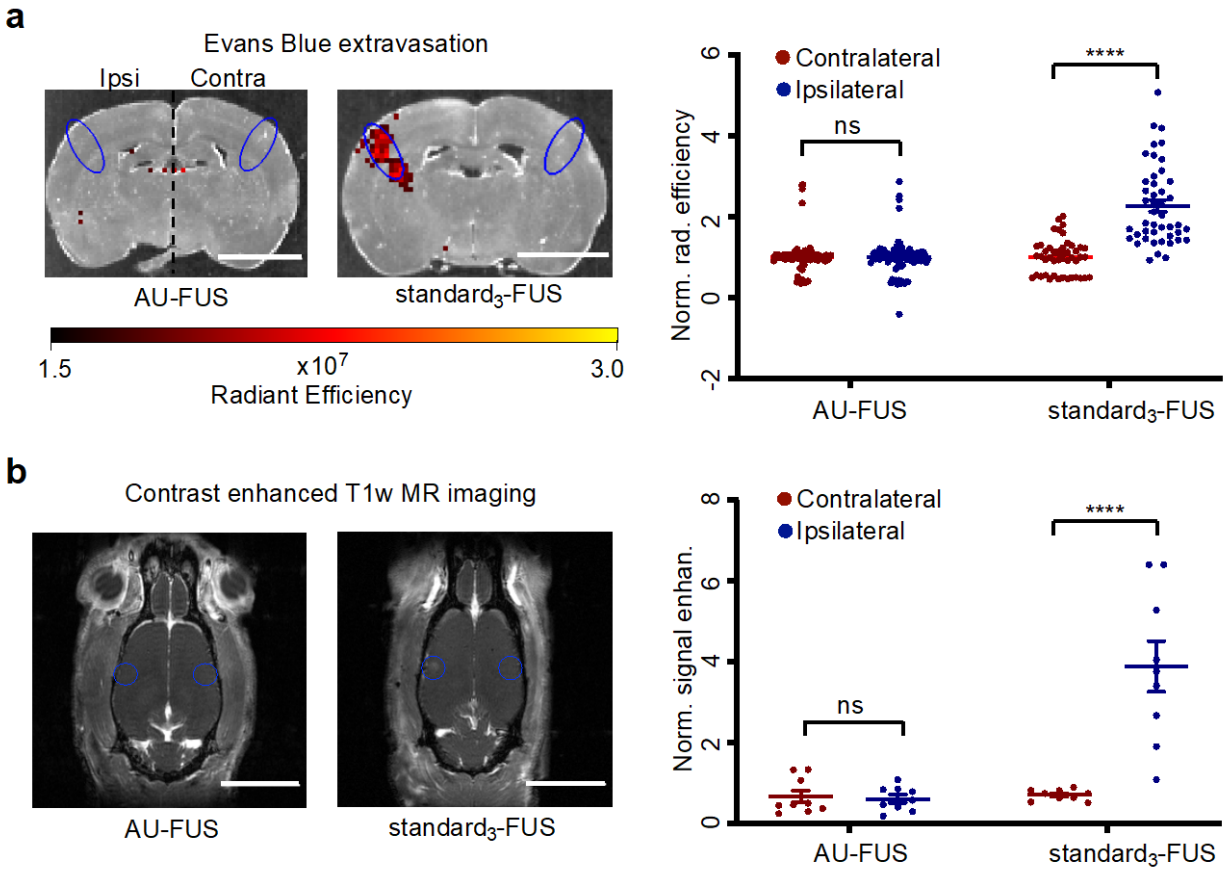

Figure 3. **Preservation of blood-brain barrier integrity following AU-FUS.**

a Evans Blue extravasation. Evans blue was injected post-sonication and allowed to circulate for 30 mins before transcardial perfusion. Representative brain sections, imaged with IVIS spectrum, at the FUS target location of vS1 following AU-FUS (muscimol-loaded UC-carriers with FUS, left image) vs standard$_3$-FUS (right image) for BBB opening. Regions of interest (ROIs) (1.5 mm x 3.5 mm, blue) were measured as radiant efficiency [(photons/sec/cm^2/sr) / (µW/cm^2)] ipsilateral to FUS application and were compared to the contralateral vS1 (scale: 0.5 cm). Radiant efficiency values within ROIs for AU-FUS and standard$_3$-FUS sequences were quantified (n = 6 rats x 15 brain sections each for AU-FUS; same rats as in Fig. 3c; n = 3 rats x 15 brain sections each for standard$_3$-FUS). Pairwise Mann-Whitney rank sum test AU-FUS (ipsilateral vs. contralateral, p = 0.6577), standard$_3$-FUS (ipsilateral vs. contralateral, ****p < 0.0001).

b MRI-contrast agent extravasation. Animals were injected with Omniscan post-sonication and imaged. Representative brain images, imaged with Bruker 7T MR scanner, at the FUS target location of vS1 when AU-FUS (left image) was used for drug delivery as compared to standard$_3$-FUS sequence (right image) for BBB opening. ROIs (1.0 mm x 1.0 mm, blue, approximate ROI location) were measured as signal enhanced T1-weighted MR images, following Gd administration, ipsilateral to FUS application, which were compared to the contralateral vS1 (scale: 10 mm). See Supplementary Fig. 7 for zoomed images. Baseline-subtracted contrast enhanced T1-weighted MR image ROIs using AU-FUS and standard$_3$-FUS sequences were quantified (n = 3 rats x 3 brain sections each for AU-FUS and standard$_3$-FUS). Pairwise Mann-Whitney rank sum test, AU-FUS (ipsilateral vs. contralateral, p = 0.9494), standard$_3$-FUS (ipsilateral vs. contralateral, ****p < 0.0001).

Vancomycin-targeted microbubbles for the treatment of *Staphylococcus aureus* biofilms under flow

Joop J.P. Kouijzer*[1], Kirby R. Lattwein[1], Inés Beekers[1], Simone A.G. Langeveld[1], Mariël Leon-Grooters[1], Nico de Jong[1,2], Antonius F.W. van der Steen[1,2], Alexander L. Klibanov[3], Willem J.B. van Wamel[4], Klazina Kooiman[1]

[1] Department of Biomedical Engineering, Thoraxcenter, Erasmus MC, Rotterdam, the Netherlands
[2]Acoustical Wavefield Imaging, Delft University of Technology, Delft, the Netherlands
[3] Cardiovascular Division, Department of Medicine, University of Virginia, Charlottesville, Virginia, United States of America
[4]Department of Medical Microbiology and Infectious Diseases, Erasmus MC, Rotterdam, the Netherlands
Corresponding author: j.kouijzer@erasmusmc.nl

Introduction

The bacteria *Staphylococcus aureus (S. aureus)* can form difficult to treat biofilms within the human body. These infections are the cause of a multitude of life-threatening and persistent infectious diseases, for example infective endocarditis (IE). IE is a persistent infection of the heart valves, endocardial surface, and/or artificial implants affecting millions of people every year. For patients with IE, it is often crucial to undergo surgery [1, 2]. Such invasive and high-risk operations illustrate the urgency of a new non-invasive treatment [3]. This study aimed to produce vancomycin-targeted microbubbles (vMBs) and to use these vMBs for ultrasound-mediated *S. aureus* biofilm treatment under flow. The antibiotic vancomycin was chosen as the ligand for its 1) high affinity to *S. aureus* bacterial cell walls (Kd ~1 – 4 μM), 2) potential for clinical application, and 3) possibility to covalently couple this compound to the lipid shell of the microbubble without losing its functionality [4].

Methods

To produce vMBs by probe sonication, the antibiotic vancomycin was first covalently coupled to DSPE-PEG(3400)-NHS. DSPC (86.4 mol%), PEG-40 stearate (8.3 mol%;) and the custom-made DSPE-PEG(3400)-vancomycin conjugate (5.3 mol%) were used as the phospholipid components of the microbubble shell with a perfluorobutane (C_4F_{10}) gas core. Vancomycin coupling and distribution on the lipid shell was confirmed with a FITC-labeled anti-vancomycin antibody using high-axial resolution 4Pi confocal microscopy. Control microbubbles (cMBs) did not contain vancomycin. *S. aureus* biofilms from a clinical isolate of IE were grown in plasma-coated IbiTreat μ-slides with a 0.8 mm channel height under continuous laminar flow (5 dyn/cm^2) for 24 h at 37 °C using the Ibidi pump system. Next, fluorescently labeled vMBs and cMBs were added to the biofilm and were allowed to adhere before shear stress was gradually increased every 60 s from 1.5 to 12 dyn/cm^2. The number of microbubbles that remained bound to the biofilm was monitored with confocal time-lapse microscopy. Additionally, biofilms were treated with vMBs in combination with a single ultrasound burst (2 MHz, 250 kPa, 5.000 or 10.000 cycles) under constant flow (5 dyn/cm^2). Live bacteria were stained with SYTO 9 and dead bacteria with propidium iodide (PI). vMB oscillation during ultrasound insonification was recorded with the Brandaris 128 ultra-high-speed camera coupled to a custom-built Nikon A1R+ confocal microscope [4]. The reduction in biofilm area upon ultrasound insonification was quantified using MATLAB.

Results

Before starting flow, the average number of microbubbles in a single field-of-view (210 µm^2) was 51 ± 37 (average ± SD) for vMBs and 61 ± 44 for cMBs (n=8). To distinguish bound from unbound microbubbles, increasing shear stress from 1.5 to 12 dyn/cm^2 revealed that vMBs bound significantly more in comparison to cMBs at all different shear stress values (Fig. 1A). All biofilms grown under flow had an average field-of-view coverage of 89.7% ± 10.7% (n=22 fields of view in 11 different IbiTreat µ-Slides). Comparison between confocal microscopy recordings before (Fig. 1B) and after ultrasound treatment (5.000 cycles) of bound vMB (Fig. 1C) revealed 24.4 % reduction in biofilm area. Bound vMBs in combination with ultrasound reduced the biofilm area significantly more in comparison to control groups (Fig. 1D).

Conclusion

vMBs were successfully developed by chemically coupling vancomycin onto the microbubble shell. The developed vMBs remained bound to *S. aureus* biofilms under increasing laminar flow. After ultrasound treatment at 2 MHz and a low acoustic pressure (250 kPa) for 5.000 or 10.000 cycles biofilm reduction could be observed upon vMB oscillation. This reduction may assist in the treatment of difficult to treat *S. aureus* biofilm-associated diseases.

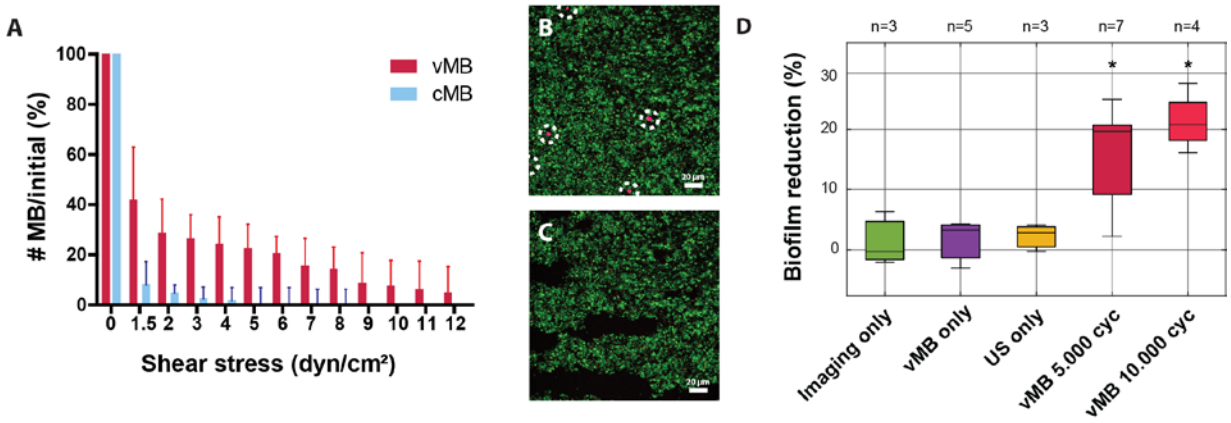

Figure 1. Microbubble binding under increasing shear stress and reduction in biofilm area after vancomycin-targeted microbubbles (vMB) ultrasound insonification. (**A**) Median percentage with interquartile range of vMBs and control microbubbles (cMB) in the field-of-view remaining bound to the *S. aureus* biofilm during increasing shear stress (n = 8). Confocal microscopy image before **(B)** and within 15 s after (**C**) ultrasound treatment at 5 dyn/cm^2. Live bacteria were stained with SYTO 9 (pseudo-colored in green), dead bacteria with PI (pseudo-colored in orange), vMBs with DiD (pseudo-colored in red; are indicated by white dashed circles). A single burst of ultrasound (2 MHz, 250 kPa, 5.000 cycles) was applied. (**D**) Percentage of biofilm area reduction upon US treatment. Boxes show the medians and interquartile ranges, whiskers show the minimum to maximal values. US only was 250 kPa and 10.000 cycles. Statistically significant differences between vMBs in combination with US and the control treatment groups are indicated with * ($p < 0.05$); cyc = cycles, US = ultrasound.

Acknowledgements – This project was funded by the European Research Council (ERC) under the European Union's Horizon 2020 research and innovation programme (grant agreement No 805308).

References

[1]. Athan, E., et al., *Clinical characteristics and outcome of infective endocarditis involving implantable cardiac devices.* JAMA, 2012. **307**(16): p. 1727-35.

[2]. Prendergast, B.D. and P. Tornos, Surgery for infective endocarditis: who and when? Circulation, 2010. **121**(9): p. 1141-52.

[3]. Sandoe, J.A., et al., Guidelines for the diagnosis, prevention and management of implantable cardiac electronic device infection. Report of a joint Working Party project on behalf of the British Society for Antimicrobial Chemotherapy (BSAC, host organization), British Heart Rhythm Society (BHRS), British Cardiovascular Society (BCS), British Heart Valve Society (BHVS) and British Society for Echocardiography (BSE). J Antimicrob Chemother, 2015. **70**(2): p. 325-59.

[4]. McGuinness, W.A., N. Malachowa, and F.R. DeLeo, *Vancomycin Resistance in Staphylococcus aureus.* Yale J Biol Med, 2017. **90**(2): p. 269-281.

[5]. Beekers, I., et al., *Combined Confocal Microscope and Brandaris 128 Ultra-High-Speed Camera*. Ultrasound Med Biol, 2019. **45**(9): p. 2575-2582.

Ultrasound molecular imaging for the guidance of ultrasound triggered release of liposomal doxorubicin and its treatment monitoring in an orthotopic prostatic tumor model in rat.

A. Helbert[1], P. Bussat[1], F. Séchaud[1], M. von Wronski[1], E. Gaud[1], J-L. Mestas[2], S. Cherkaoui[1], J-M. Hyvelin[1], I. Tardy[1], T. Bettinger[1], C. Lafond[2,] F. Padilla[2,3]

[1]Bracco Suisse SA, Bracco Global Research & Development, Plan-Les-Ouates, Geneva, Switzerland.
[2]LabTAU, INSERM, Centre Léon Bérard, Université Lyon 1, Univ Lyon, F-69003, LYON, France.
[3]FUS Foundation, Charlottesville, VA 22903.
Corresponding author: alexandre.helbert@Bracco.com

Introduction

Liposomes encapsulating drugs is a fast-growing field of research in various area including analgesics, photodynamic therapy, fungal diseases, viral vaccines and cancer therapy. In cancer therapy, advantages of liposomes compared to free drugs include an extended circulation time in blood, reduced side effects and intratumoral accumulation by the so-called Enhanced Permeability and Retention (EPR) effect. This effect is effective in pre-clinical models but still debatted in patient. To improve EPR effect, several strategies, such as radiation, hyperthermia, photodynamic therapy or ultrasound are developped. To increase the therapeutic efficacy of encapsulated drugs in liposomes, another approach is to use an external stimilus to locally provoke the release of the drug. Among these external sources, ultrasound can act on specifically designed sono-sensitive liposomes [1,2].

Using sono-sensitive liposomes in this study, we aim 1) to guide ultrasound triggered release of liposomal doxorubicin (L-DXR) by the mean of Ultrasound Molecular Imaging (USMI) with BR55, a targeted ultrasound contrast agent against the vascular growth factor receptor 2 (VEGFR-2), 2) to demonstrate the increased therapeutic efficacy of confocal ultrasound ($US_{confocal}$) combined with L-DXR versus L-DXR alone, and 3) to demonstrate the potential of USMI to monitor the response to the treatment in a orthotopic prostatic G-Dunning rat tumor model.

Methods

Orthotopic tumors in Copenhagen rats were obtained by the injection of G-Dunning R-3327 tumor cells in the left ventral lobe of the prostate. Sonosensitive [1,2-dierucoyl-sn-glycero-3-phosphocholine]-based liposomes encapsulating doxorubicin were produced, their pharmacokinetic was evaluated in blood, and their biodistribution in healthy prostate and tumor in comparison to free doxorubicin (F-DXR). USMI with BR55 was used to guide ultrasound triggered release of doxorubicin from liposomes 48 h after injection. Local release was triggered using a dedicated confocal ultrasound device comprising two focused transducers (frequency 1.1 MHz) which delivers, at focus, peak positive and negative pressures of 20.5 MPa and 13 MPa, respectively. Tumor perfusion and VEGFR-2 expression in response to the treatment were evaluated by USMI with BR55 over a two-week period. Immunohistochemistry of CD31 and VEGFR 2 was performed on tumor cryosections.

Results

Sonosensitive liposomes presented an extended circulation time in blood in comparison to free drug, with 8% of initial dose of L-DXR still in circulation after 72 h versus only ~0.5% after 24 h for the F-DXR. A 9 fold increase of passive doxorubicin accumulation was observed with the L-DXR in the tumor compared to healthy prostate. Over a 7-day period post-treatment, a 2.2-fold and 1.5-fold increase of tumor size was measured in the untreated animals and in the animals treated with confocal ultrasound alone, respectively, while tumor size remained unchanged in animals treated with L-DXR alone. When $US_{confocal}$ was applied 48 h after injection of liposomes, tumor size was decreased by a factor of 3 at day 7 post treatment. Over a two-week period, the tumor size decreased by 20% of its initial value in the L-DXR group, and by 70% in the L-DXR + USconfocal groups ($P < 0.01$). USMI signal intensity and immunohistochemistry staining did not show any substantial variation in perfusion or VEGFR-2 expression over a 14-day follow up period after injection of L-DXR.

Conclusions

Ultrasound molecular imaging can provide precise guidance for ultrasound triggered release of liposomal doxorubicin mediated by a confocal ultrasound device. The combination of L-DXR with cavitational ultrasound treatment increases efficacy of doxorubicin, resulting in a significant reduction in tumor size compared to treatment with L-DXR alone. Treatment response monitoring can be performed by USMI with BR55 and can provide supplemental information to identify areas of the tumor that remained viable. USMI imaging did not reveal variations in terms of perfusion and late phase enhancement but allows accurate delineation of the tumor border. In addition, immunohistochemistry staining confirmed absence of VEGFR-2 expression variation.

References

[1]. T. J. Evjen et al., Lipid membrane composition influences drug release from dioleoylphosphatidylethanolamine-based liposomes on exposure to ultrasound. International journal of pharmaceutics 406, 114-116 (2011).

[2]. J. L. Mestas et al., Therapeutic efficacy of the combination of doxorubicin-loaded liposomes with inertial cavitation generated by confocal ultrasound in AT2 Dunning rat tumour model. Journal of drug targeting (2014).

Which came first, the bubble or the droplet? (and other vaporisation questions)

Q. Wu[1], C. Mannaris[1], L. Bau[1], S. Ferri[2,3], A. Polydorou[2,3], J.P. May[2,3], N.D. Evans[2,3], D. Carugo,[2,4], E. Stride[1]

[1]Department of Engineering Science, University of Oxford, Oxford, UK
[2]MiNaTher, Faculty of Engineering and Physical Sciences, University of Southampton, Southampton, UK
[3]Bone&Joint, Faculty of Medicine, University of Southampton, Southampton, UK
[4]Department of Pharmaceutics, School of Pharmacy, UCL, London, UK
Corresponding author: eleanor.stride@eng.ox.ac.uk

Introduction

Phospholipid-coated perfluorocarbon (PFC) liquid "nano"droplets (NDs) have been explored as a means of addressing the limitations of microbubbles for both diagnostic and therapeutic applications. Due to their smaller diameters (typically <500 nm) and liquid cores, NDs are able to persist in the circulation for longer than microbubbles and also have the potential to extravasate and accumulate at target sites, e.g. within tumours. Upon exposure to ultrasound of sufficient intensity, NDs can be converted into microbubbles. This enables their benefits in terms of echogenicity and ability to promote various therapeutic effects to be realised. Multiple studies, however, have reported that much higher acoustic pressures are typically required for acoustic droplet vaporisation (ADV) than those required for stimulating microbubbles. This can increase the probability of unwanted bio-effects and consequently, a range of different methods has been explored for reducing the pressure threshold for ADV. These include using lower boiling point PFCs, incorporating solid nanoparticles into the NDs to act as nucleation agents and optimisation of the acoustic exposure parameters.

Several studies have shown that the presence of pre-exisiting microbubbles in the suspension can promote ADV, potentially via the local generation of shockwaves when these microbubbles collapse. It is interesting to consider whether this could be one reason for the wide variation in the published values for ADV thresholds in the literature. Microbubbles can be accidentally introduced into ND suspensions during handling or generated as a result of spontaneous vaporisation of a small number of NDs. A related question is whether bubbles formed as a result of ADV will themselves collapse and promote further vaporisation. This talk will review existing data on the relationship between ADV and inertial cavitation (IC) and present new simultaneous high-speed imaging and acoustic emissions data with the aim of further understanding this relationship and addressing the broader question of how ADV and IC thresholds should be defined in the context of diagnostic and therapeutic applications.

Methods

As reported in the presentation by Wu et al, a combination of ultra high-speed imaging and acoustic emissions monitoring was used to study ND vaporisation and the subsequent microbubble dynamics. A schematic of the experimental set up is shown in Figure 1. Phospholipid (DSPC + DSPE-PEG2000) coated perfluorobutane (PFB) NDs were fabricated via sonication and the suspensions washed by centrifugation to remove excess surfactant and any microbubbles. The size and concentration of the NDs were determined by dynamic light scattering and nanoparticle tracking analysis respectively as 237 ± 16 nm (mean ± standard deviation) and $6.6 \pm 0.4 \times 10^{11}$ ND/ml.

NDs were exposed to ultrasound using a spherically focussed single element ultrasound (FUS) transducer (0.5 MHz or 1.0 MHz centre frequency) whilst flowing through a polyethylene tube of 1.2 mm inner diameter and 0.2 mm wall thickness at a constant rate of 0.3 mL/min.

The focus of the FUS transducer was aligned with the tube and also the focus of an objective lens, which was coupled to a high-speed camera capable of running at speeds up to 10 Mfps. A 7.5 MHz spherically focused single element transducer (V320 Panametrics, Olympus, Waltham, USA), also co-focally aligned with the FUS transducer, was used simultaneously to record any acoustic emissions from the tube. A similar set of experiments was performed using an ultrasound imaging system in place of the high-speed camera. Both the spatial and temporal resolution of the ultrasound images were significantly lower than those of the optical images but the field of view was much larger (1.2 x 4 mm compared with <100 x 100 μm).

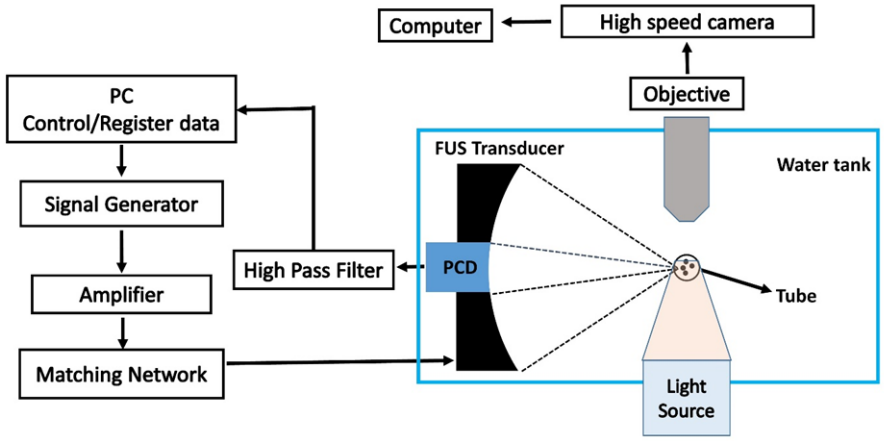

Figure 1. Schematic of the experimental setup for simultaneous ultra high-speed optical imaging and acoustic emissions monitoring of nanodroplet vaporisation.

In the high-speed camera images, ADV was detected by the appearance of an optically resolvable bubble or bubble cluster, manifest initially by a change in grayscale contrast in the optical focal region that was above that due to noise. The number of pixels with a grayscale value of less than 100 (i.e. darker than the mean background level of 174) was counted as an indicator of the volume of bubbles formed. Counts were made from the last 5 frames of the videos for each set of exposure conditions and compared with the count for the first frame i.e., before ultrasound exposure.

From the acoustic measurements, the ADV and inertial cavitation (IC) pressure thresholds of the NDs were defined respectively by calculating the mean relative echo amplitude in a given region of interest (ROI) with B-mode images and probability of inertial cavitation (PIC) from the acoustic emissions recordings. The pressure at which a statistically significant change in optical density (i.e. the number of pixels with a grayscale value <100) was compared with that at which a detectable change in B-mode intensity or the energy of acoustic emissions was seen.

Results

Figure 2 shows a representative set of high-speed camera images and the corresponding acoustic emissions (time and frequency domain) of ND suspensions exposed to increasing peak negative pressures. As expected the quantity of microbubbles observed and the amplitude of the acoustic emissions increased with increasing driving pressure. Broadband noise was detected in all cases when microbubbles were formed, indicating that IC was occuring simultaneously with ADV.

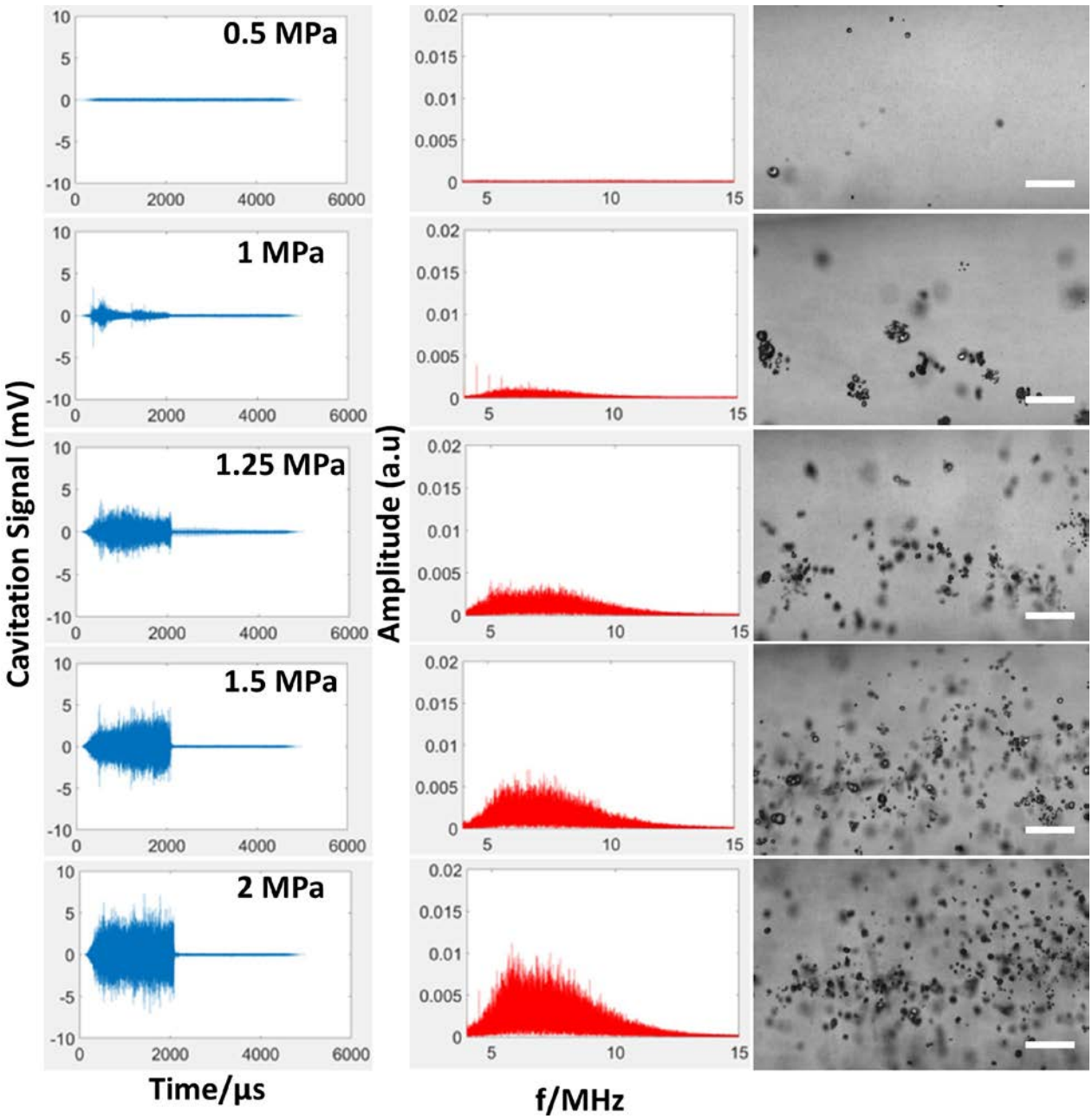

Figure 2. Representative acoustic emissions (first column), their corresponding frequency content (second column) and corresponding optical images (third column) from the high-speed videos for NDs exposed to different peak negative pressures. The frequency, pulse length and PRF were 0.5 MHz, 1000 cycles and 10 Hz respectively. The scale bar is 20 µm.

Figure 3 shows how the optical density in the high speed camera images and the PIC from the acoustic emissions varied with driving pressure. Both curves show a significant increase above the background level at the same peak negative pressure, indicating that the bubbles produced by ADV immediately undergo IC. The curve for the pixel count does not show as pronounced an "S" shape with increasing pressure as does that for the PIC, but it is difficult to make a fair comparison as there is such a large difference in the size of the sampled volume between the optical and acoustical data. In particular, there may have been large numbers of bubbles forming that were not visible to the high-speed camera due to the limited depth of field.

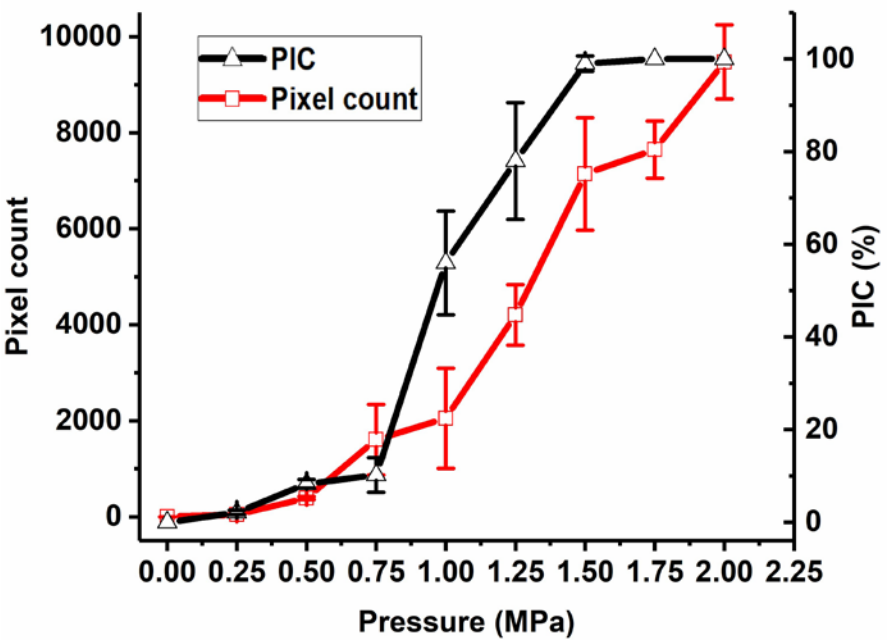

Figure 3. Comparison between the change in optical intensity from the high-speed video images and the PIC determined from the acoustic emissions as a function of peak negative acoustic pressure. The frequency, pulse length and PRF were 0.5 MHz, 1000 cycles and 10 Hz respectively (n=3).

Figure 4 compares the B-mode and acoustic emissions data, showing the normalized REA and PIC of PFB NDs as a function of peak negative acoustic pressure. ADV was detected at lower peak negative driving pressures than IC. This indicates that IC is not required to initiate ADV.

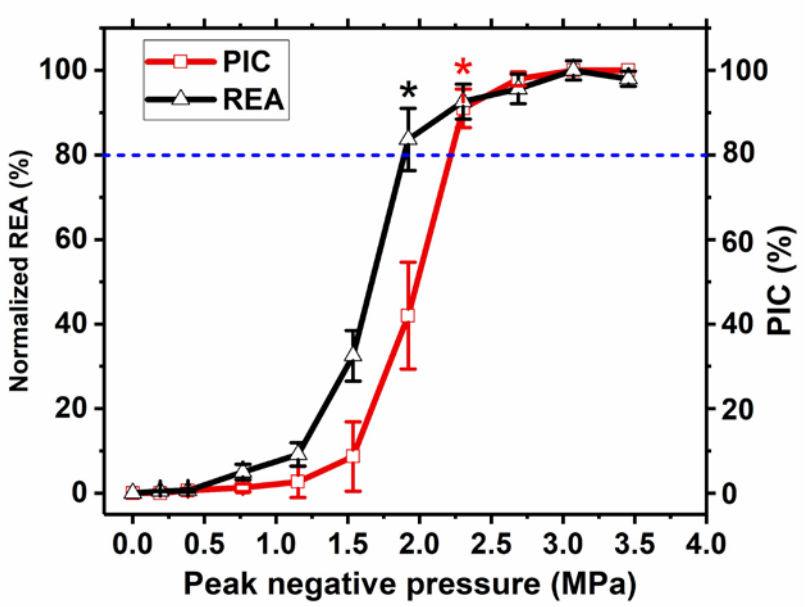

Figure 4. Normalized REA and PIC as a function of peak negative acoustic pressure (1 MHz driving frequency, PRF 10 Hz, pulse length 1000 cycles, n=3). The 80% thresholds for ADV and IC are denoted by the dashed blue line.

The question then arises as to how to define appropriate pressure thresholds for ADV and/or IC. In previous work by the authors, the pressure at which the normalized REA was >80% was defined as the ADV threshold. Similarly the IC threshold was defined as the peak negative pressure corresponding to a PIC > 80%. These levels were selected as enabling consistent physical and/or biological effects to be generated. With these definitions, there was no statistically significant difference between the ADV and IC thresholds at 0.5, 1, or 1.5 MHz. As may be seen in Figure 2, however, at the pressure corresponding to 80% PIC there will already be a signficant number of bubbles formed by ADV. Thus this would likely be an inappropriate threshold definition if safety were the primary concern. Moreover, the high-speed camera footage indicates that there are considerable changes in droplet/bubble response over successive cycles. This indicates that it may not be appropriate to define thresholds in terms of pressure and frequency only, but that pulse length may also be important depending on whether phenomena such as bubble coalescence and fragmentation are desirable or not, e.g. to promote or avoid vascular occlusion or microcapillary disruption.

Conclusions

Simultaneous ultra high-speed optical imaging and acoustic emissions monitoring of PFB NDs indicates that IC is not required for ADV. The results from the high-speed imaging, however, indicate that bubble cloud formation occurs within a few cycles following ADV and this may affect subsequent ND vaporisation and also the likelihood of biological effects being produced. The definition of ADV and/or IC thresholds should therefore be carefully considered depending on the specific therapeutic effect (or avoidance of unwanted bioeffects) required for the application.

Super-localization of superheated nanodroplet vaporization during proton irradiation using high frame-rate differential imaging

Gonzalo Collado[1], Sophie V. Heymans[1,2], Marta Rovituso[3], Bram Carlier[4,5], Yosra Toumia[6], Gaio Paradossi[6], Hendrik J. Vos[1,7], Martin Verweij[1,7], Jan D'hooge[8], Koen Van Den Abeele[2], Nico de Jong[1,7], Verya Daeichin[7]

[1]Department of Biomedical Engineering, Erasmus Medical Center, Rotterdam, The Netherlands
[2]Department of Physics, KU Leuven Campus Kulak, Kortrijk, Belgium [style: _B department]
[3]Holland Proton Therapy Center, Delft, The Netherlands
[4]Molecular Small Animal Imaging Center, KU Leuven, Leuven, Belgium
[5]Department of Oncology, KU Leuven, Leuven, Belgium
[6]Department of Chemical Sciences and Technology, University di Roma Tor Vergata, Rome, Italy
[7]Department of Medical Imaging, TU Delft, Delft, The Netherlands
[8]Department of Cardiovascular Sciences, KU Leuven, Leuven, Belgium
Corresponding author: g.colladolara@erasmusmc.nl

Introduction

Proton therapy may reduce the undesired radiation dose to healthy tissue in comparison to conventional radiotherapy. Since most of the proton energy is deposited in a confined spot (i.e. the Bragg peak), the irradiated volume can be better conformed to the tumor shape. However, when applied *in vivo*, the accuracy of the Bragg peak positioning is compromised due to various uncertainty sources, potentially leading to deviations from the planned dose [1]. A method to locate the Bragg peak position in real time appears crucial, but to date no approach has been adopted in the clinical routine. Superheated nanodroplets have recently been shown to vaporize upon irradiation in a proton beam, turning into microbubbles (MBs) [2]. Localization of individual proton-droplet interactions could be exploited for range verification and dosimetry, but high concentrations eliminate the sparsity condition for localizing individual MBs in post-irradiation ultrasound images. In this study, we investigated high frame rate ultrasound imaging as a method for detecting and localizing single vaporization events in a proton beam in real time.

Methods

Two phantoms were made by dispersing perfluorobutane (boiling temperature -2°C) nanodroplets with a polyvinyl alcohol shell [3] in a carbomer gel [4]. The gel entrapped the nanodroplets while allowing their vaporization and the oscillation of the resulting microbubbles. The phantoms were irradiated using a 154 MeV pencil proton beam at the research beam line of the Holland Proton Therapy Center in Delft (Fig. 1a). One phantom was irradiated at 37°C and the other at 50°C with averaged doses of 3.19 and 1.05 Gy respectively, yet the same nanodroplet concentration was used in both phantoms. A linear probe (ATL L12-5, 38 mm) was used with a Vantage 256 system (Verasonics) to acquire plane-wave images at 1000 frames per second during the irradiation. A peak negative pressure of 370 kPa (11.3 V transmit voltage) was used, well below the acoustic vaporization threshold of these droplets [5]. Differential imaging was performed by subtracting consecutive frames (Fig. 1b), revealing newly formed MBs as sparse bright spots in the resulting differential image (Fig. 1c). Events with an intensity above a threshold (maximum intensity of differential frames without proton irradiation + 5dB) were super-localized using the weighted averaged

centroid of their point spread function. The map of vaporization events was compared to an independent measurement of the dose deposition profile performed with an ionization chamber.

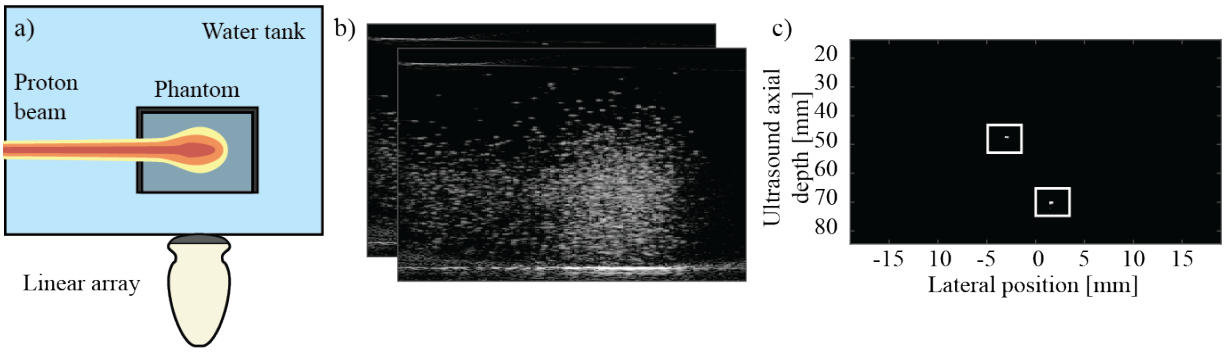

Figure 1. (a) Schematic of the setup used for the phantom imaging during irradiation with a pencil proton beam. Two consecutive frames (b) were subtracted, revealing sparse vaporization events (c). Two events are highlighted.

Results

The events localized from all the acquired frames are displayed in Fig. 2a and 2b (37°C and 50°C, respectively), overlaid on the normalized proton dose distribution. Although a higher dose was delivered at 37°C, the number of events was much lower and occured only in front of the Bragg peak (maximum dose spot). This was expected, as perfluorobutane droplets are not sensitive to primary protons at this temperature, but only to nuclear reaction products, which are relatively rare [2]. At 50°C, however, the droplets were sensitive to primary protons, and about 25x more events were detected. In this case, most of the vaporizations were located near the Bragg peak. In the direction perpendicular to the proton axis, the events followed a gaussian distribution with a standard deviation of 5.33 mm at 37°C and 5.57 mm at 50°C, compared with a beam value of 5.21 mm derived from the ionization chamber measurement. In the direction parallel to the proton axis, the location of the maximum number of events at 50°C was within 3.2 mm of the Bragg peak position, and within 0.7 mm of the proton range.

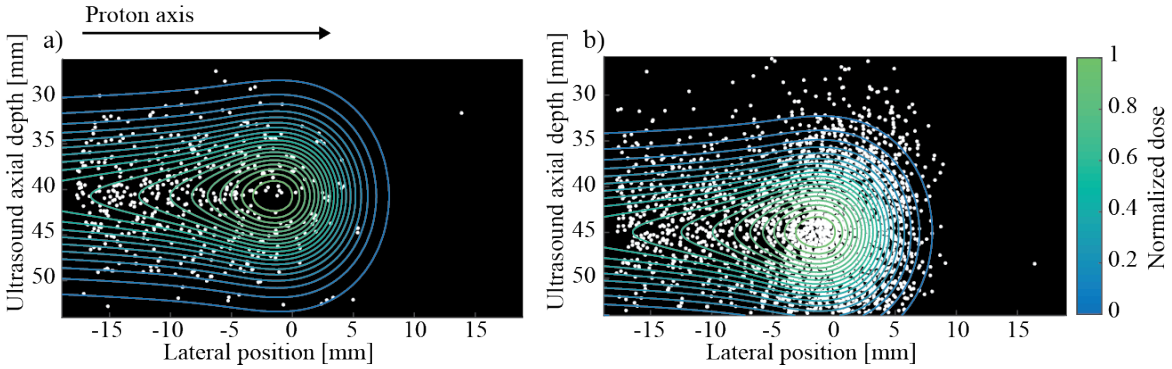

Figure 2. Vaporization event maps at 37°C (a) and 50°C (b) overlaid on the normalized dose distribution.

Conclusions

High frame rate differential imaging was successfully applied for the detection and localization of nanodroplet vaporization events in a proton beam, even at high microbubble concentrations. The spatial distribution of vaporization events showed a good agreement with an independent measurement of the dose distribution profile. Consequently, the proposed method appears promising for radiation mapping in real time during proton therapy.

References

[1]. H. Paganetti, Range uncertainties in proton therapy and the role of Monte Carlo simulations, Phys. Med. Biol., vol. 57, no. 11, 2012.

[2]. B. Carlier et al., Proton range verification with ultrasound imaging using injectable radiation sensitive nanodroplets: A feasibility study, Phys. Med. Biol., vol. 65, no. 6, 2020.

[3]. Y. Toumia et al., Phase Change Ultrasound Contrast Agents with a Photopolymerized Diacetylene Shell, Langmuir, vol. 35, pp. 10116–10127, 2019.

[4]. T. Brunet et al., Sharp acoustic multipolar-resonances in highly monodisperse emulsions, Appl. Phys. Lett., vol. 101, no. 1, p. 011913, Jul. 2012.

[5]. P. S. Sheeran et al., Design of ultrasonically-activatable nanoparticles using low boiling point perfluorocarbons, Biomaterials, vol. 33, no. 11, pp. 3262–3269, 2012.

Dilatational surface tension curves of monodisperse microbubbles with a tuned shell stiffness

Benjamin van Elburg[1], Kim Bruil[1], Guillaume Lajoinie[1], Michel Versluis[1] and Tim Segers[1,2]

[1]Physics of Fluids Group, Technical Medical (TechMed) Center and MESA+ Institute for Nanotechnology, University of Twente, The Netherlands
[2]BIOS Lab-on-a-Chip group, Max-Planck Center Twente for Complex Fluid Dynamics, MESA+ Institute for Nanotechnology, University of Twente, The Netherlands
Corresponding authors: b.vanelburg@utwente.nl, t.j.segers@utwente.nl

Introduction

To date, local blood pressure measurement *in vivo* is only possible through the invasive insertion of a pressure sensitive catheter. Pressure measurement deep in the body, e.g. in arteries or the portal vein, is therefore not only challenging and painful but also risky as it may induce hemorrhage and infection. Phospholipid-coated microbubbles bear potential as a noninvasive alternative for pressure sensing since their nonlinear echo response has been shown to strongly depend on the ambient pressure [1]. The pressure-induced change in subharmonic signal in particular originates from the dependence of interfacial tension on surface dilatation [2] that affects the packing density of the lipid molecules in the shell, and the interfacial tension of the bubble "at rest", around which it oscillates. The subharmonic response is then governed by the change in stiffness around the equillibrium interfacial tension [2]. Accurate knowledge of the dilatational interfacial tension curve is therefore crucial to predict and understand subharmonic generation in Rayleigh-Plesset type models. Furthermore, control over the interfacial tension curve is of great interest as it will allow for designing the optimal non-invasive bubble pressure sensor.

We have previously shown that the interfacial tension curve can be measured acoustically through attenuation measurements at a low driving pressure while changing the ambient pressure. A linear model fit then provides a direct measure of the shell stiffness as a function of bubble surface area which can be integrated to obtain the surface tension curve [3]. Here, we use this technique to measure the interfacial tension curves of bubbles designed to have a shell stiffness of 0.5, 1.5, or 2.5 N/m. The maximum shell stiffness was tuned through the addition of palmitic acid to the phospholipid coating.

Methods

Monodisperse bubble suspensions were produced in a flow-focusing device (Fig. 1A). The C_4F_{10} and CO_2 [4] filled bubbles were formed at a temperature of 60°C to minimize bubble coalescence [5]. The lipid mixtures comprised DSPC and DPPE-PEG5000 mixed at a molar ratio of 9:1 at a total concentration of 12.5 mg/mL. Palmitic acid (PA) was added for up to 50 mol% to tune the shell stiffness. The shell properties were characterized acoustically by narrowband attenuation measurements (Fig. 1B) at transmit frequencies ranging from 0.5 MHz to 5.0 MHz and using an acoustic peak negative pressure amplitude of 5 kPa. During the characterization procedure, the ambient pressure was decreased from atmospheric pressure down to 60 kPa and increased from atmospheric pressure up to 135 kPa. The bubble size distribution was measured using a Coulter counter. The bubble size as a function of the ambient pressure was measured optically in a flow cell and was input to the model. The viscoelastic properties were extracted by fitting a linearized attenuation model [2] to the measured spectra.

Results

Fig. 1C shows a typical attenuation measurements on a monodisperse bubble suspension (60 mol% palmitic acid, R_0=3.6 +/- 0.18 micrometer) at different ambient pressures. At atmospheric pressure (blue curve) the resonance frequency is as high as 4 MHz. Upon applying a small overpressure (black curve), the resonance frequency increases by ~10%. For a higher overpressure of 28 kPa (red curve), the bubbles show a 3-fold decrease in resonance frequency as compared to that measured at atmospheric pressure. The decrease in resonance frequency is caused by the vanishing shell stiffness as the shell buckles. Similarly, for an underpressure of 40 kPa (orange curve), the resonance frequency drops by a factor of 4 as compared

to that measured at atmospheric pressure. Here, the shell dilates, increasing the area per lipid molecule and, as a consequence, the surface tension increases until it reaches that of water. At the same time, a decrease in ambient pressure lowers the resonance frequency through an increase in bubble size, which explains the remaining difference in resonance frequencies at ambient pressures of 60 and 128 kPa. This behavior is captured in Fig. 1D that shows the change in resonance frequency as a function of the ambient pressure.

Fig. 1E shows the full dilatational stiffness curve for the 3 different palmitic acid concentrations. When no PA is present in the shell (red curve) the stiffness quickly plateaus as the bubble area increases, after which is slowly drops to zero. The addition of PA (blue and black curves), however, produces a different dilatational behavior, i.e., the stiffness rapidly increases to a high maximum stiffness value, and subsequently quickly drops to a lower stiffness value where it plateaus before dropping to zero. Interestingly, the three curves plateau at a very similar shell stiffnes of approximately 0.4 – 0.5 N/m.

Fig 1F shows the resulting surface tension curves obtained by integration of the stiffness curves. The zero percent PA case shows a gradual transistion from the zero surface tension state to the elastic state. There, it follows a linear trend until it approaches the surface tension of water. The curves obtained for bubbles with palmitic acid in their shell show a steeper increase of the interfacial tension in the region close to buckling. At higher surface dilatation, the curves abruptly change slope to match that of the case where no PA was added.

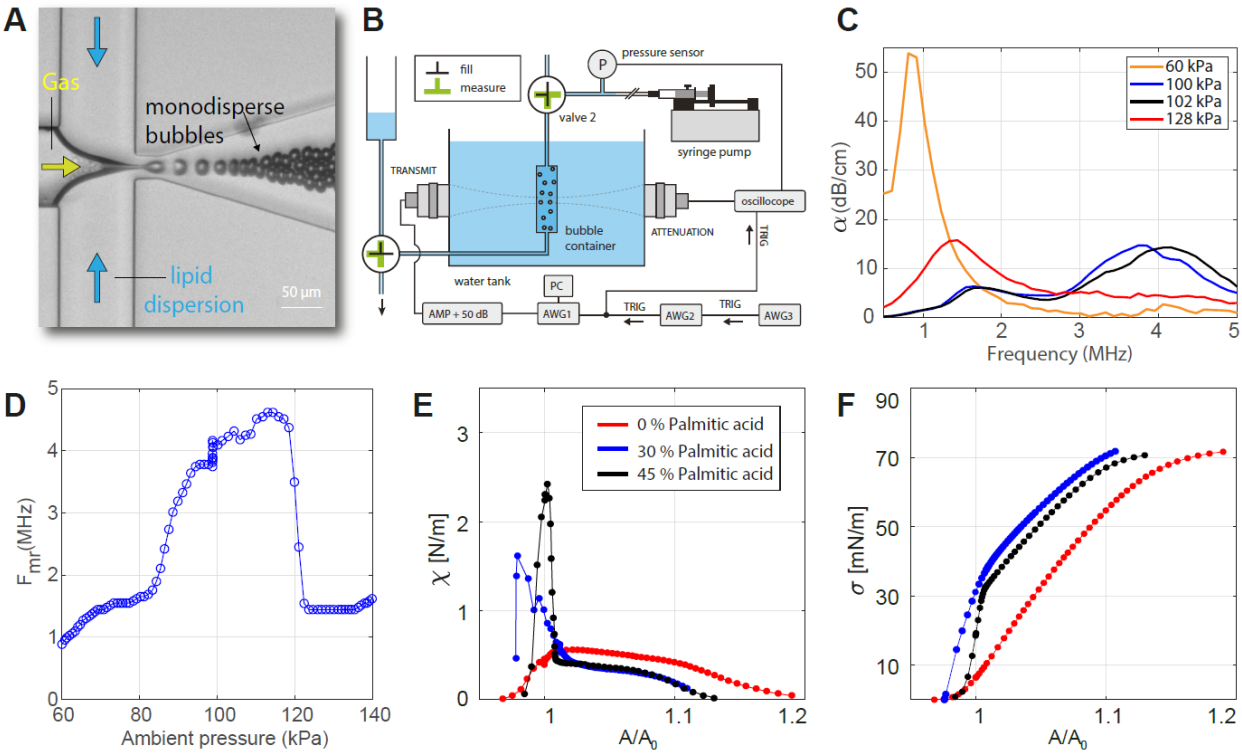

Figure 1. A) The employed microfluidic flow-focusing chip. B) Schematic of the experimental setup. The bubble container could be pressurized such that attenuation spectra could be obtained at different ambient pressures. C) Attenuation spectra at different ambient pressures of 60% Palmitic acid bubbles with R = 3.6 +/- 0.18 micrometer. D) The resonance frequency as function of the ambient pressure E) Shell stiffness as a function of bubble surface normalized by the surface area at atmospheric pressure for different palmitic acid concentrations. F) Surface tension as a function of bubble surface normalized by the surface area at atmospheric pressure for different palmitic acid concentrations.

Conclusions

We measured the full dilatational shell stiffness curves for bubbles with a shell stiffness of 0.5, 1.5, and 2.5 N/m. Interestingly, the shell stiffness curves show similar trends when the shell is dilated. However, upon compression, the shell stiffness for the 1.5 N/m (30% PA) and 2.5 N/m (45% PA) cases rapidly

increase to their maximum value before dropping to zero. For the 0.5 N/m (no PA) case this rapid increase is not observed. The dilatational stiffness curves were integrated to obtain the dilatational surface tension curves. The measured curves provide valuable input to Rayleigh-Plesset type models and will be used in future work to predict and explain the subharmonic response.

References

[1] C. Tremblay-Darveau, R. Williams, and P. N. Burns. Measuring absolute blood pressure using microbubbles. Ultrasound in Medicine & Biology 40(4), 775-787 (2014).

[2] J. Sijl, B. Dollet, M. Overvelde, V. Garbin, R. Rozendal, N. De Jong, D. Lohse, and M. Versluis. Subharmonic behavior of phospholipid-coated ultrasound contrast agent microbubbles. The Journal of the Acoustical Society of America 128(5), 3239-3252 (2010).

[3] T. Segers, E. Gaud, M. Versluis, and P. Frinking. High-precision acoustic measurements of the nonlinear dilatational elasticity of phospholipid coated monodisperse microbubbles. Soft Matter 14(47), 9550-9561 (2018).

[4] T. Segers, E. Gaud, G. Casqueiro, A. Lassus, M. Versluis, and P.Frinking. Foam-free monodisperse lipid-coated ultrasound contrast agent synthesis by flow-focusing through multi-gas-component microbubble stabilization. Applied Physics Letters 116, 173701 (2020).

[5] T. Segers, A. Lassus, P. Bussat, E. Gaud, and P. Frinking. Improved coalescence stability of monodisperse phospholipid-coated microbubbles formed by flow-focusing at elevated temperatures. Lab on a Chip 19(1), 158-167 (2019).

Lipid handling and phase distribution affect the acoustic behavior of DSPC-based microbubbles

Simone A.G. Langeveld[1], Inés Beekers[1], Gonzalo Collado-Lara[1], Antonius F.W. van der Steen[1,2], Nico de Jong[1,2], Klazina Kooiman[1]

[1]Department of Biomedical Engineering, Thoraxcenter, Erasmus University Medical Center, Rotterdam, the Netherlands
[2]Department of Imaging Physics, Delft University of Technology, Delft, the Netherlands.
Corresponding author: s.a.g.langeveld@erasmusmc.nl

Introduction

Phospholipid-coated targeted microbubbles (MBs) unite two remarkable characteristics: they oscillate in response to ultrasound and can be directed to a biomarker of choice with molecular precision [1, 2]. These features make MBs excellent candidates for ultrasound molecular imaging and localized drug delivery. However, the currently available MBs have a heterogeneous response to ultrasound, even when they are of the same size and type [3], thereby reducing the predictability of a theranostic application. It has been suggested previously that microstructures in the coating influence the MBs' acoustic behavior [4]. These microstructures originate from lipid phase separation of the coating components into the liquid condensed (LC) and liquid expanded (LE) phases. To pave the way for the development of a safe and effective MB that responds to ultrasound in a reproducible way, we investigated the effect of lipid phase distribution on the variability in acoustic behavior of DSPC-based phospholipid-coated MBs with or without cholesterol. Cholesterol is known to affect the lateral molecular packing of phospholipids in a monolayer [5] and was used to alter the LC phase area of the MB coating. Given that lipid handling prior to MB production can alter the distribution of coating component DSPE-PEG2000 [6], the effect of lipid handling on the acoustic response of MBs was investigated as well.

Methods

Three types of MBs were produced : DSPC-based made with the direct method (DSPC-D), DSPC-based made with the indirect method (DSPC-I), and DSPC-based made with the indirect method and including different concentrations of cholesterol (DSPC-I-chol). As previously described [6], the direct method means that lipids were dispersed in saline solution (0.9% NaCl) directly, whereas for the indirect method lipids were first dissolved and mixed in chloroform/methanol (9:1), dried to form a lipid film, and then dispersed in saline. All MBs had a C_4F_{10} gas core and were made by probe sonication. The coating components included DSPC (84.8 mol%), PEG40-stearate (8.2 mol%), DSPE-PEG2000 (5.9 mol%), and DSPE-PEG2000-biotin (1.1 mol%). All MBs were fluorescently labeled with Rhodamine-DHPE, an LE phase marker.

The effect of cholesterol on lipid phase (Rhodamine-DHPE) and ligand distribution (fluorescently labeled streptavidin conjugated to the MB coating) was determined using 4Pi confocal microscopy, and quantified using custom-developed MATLAB software as published by Langeveld et al. [6]. MBs were manually scored for the presence of buckles on the outside of the coating.

The acoustic behavior and lipid phase distribution were studied simultaneously using the combined confocal microscope and Brandaris 128 ultra-high-speed camera system [7]. MBs were injected into a CLINIcell (10^5 MBs/mL). Before and after ultrasound insonification, a z-stack was made with the confocal microscope using the 561 nm laser to excite Rhodamine-DHPE. MB spectroscopy was performed as described previously [8]. In short, individual MBs were insonified with 8-cycle Gaussian tapered sine wave bursts from 1 to 4 MHz in steps of 200 kHz, either at 50 kPa, or first at 20 kPa and then at 150 kPa external peak negative pressure (PNP). The MB oscillation behavior was recorded with the Brandaris 128 ultra-high-speed camera at approximately 17 million frames/s. MB oscillations were quantified using custom-

developed MATLAB software, determining the change in radius as a function of time (R-t cuve) [8]. Next, the resonance frequency and shell parameters were determined at 50 kPa using the harmonic oscillator model [9]. The interquartile range (IQR) of the relative oscillation amplitude at 50 kPa was used to quantify the variability in acoustic response. Fast Fourier Transforms (FFTs) of the R-t curves were used to assess the non-linear behavior. The confocal data was scored manually for buckles in the MB coating and LC domain size.

Results

Typical examples of DSPC-I MBs with different concentrations of cholesterol in the coating are presented in Figure 1. MBs with 0 mol% (N = 58) or 12 mol% (N = 61) cholesterol had a homogeneous ligand distribution. MBs with 7 mol% (N = 34), 10 mol% (N = 40), or 14 mol% (N = 45) cholesterol had a significantly more heterogeneous ligand distribution. DSPC-I MBs without cholesterol had the largest mean LC phase area (34% of total surface area), while DSPC-I MBs with 12 mol% cholesterol had the smallest mean LC phase area (9% of total surface area). MBs with increasing concentrations of cholesterol also had increasing numbers of buckles in the coating. Based on these results, DSPC-I-chol MBs with 12 mol% of cholesterol in the coating were chosen for acoustic characterization.

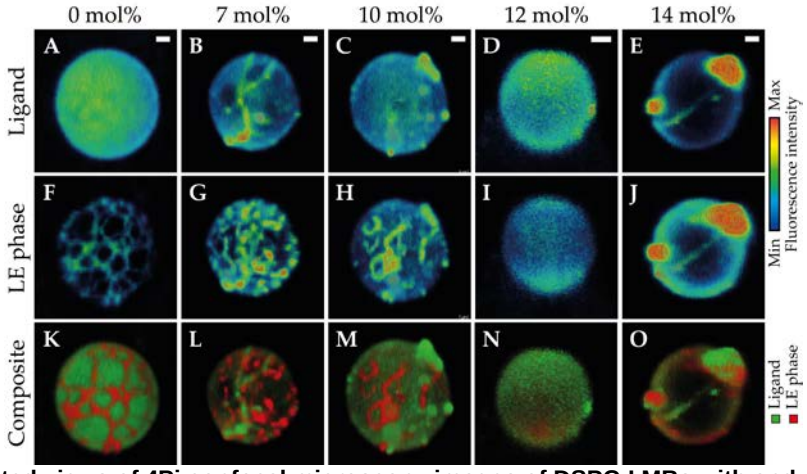

Figure 1. Selected views of 4Pi confocal microscopy images of DSPC-I MBs with and without cholesterol, presenting the ligand (top row) and lipid phase distribution (LE phase, middle row), and a composite of both signals (bottom row). Scale bars represent 1 µm.

The shell elasticity (median (IQR)) was highest for DSPC-D MBs (0.14 (0.12-0.15) N/m), followed by DSPC-I MBs (0.03 (0.01-0.06) N/m), while DSPC-I-chol MBs had the lowest shell elasticity (0.01 (0.01-0.02) N/m), approaching that of an uncoated bubble. The shell viscosity (median (IQR)) was highest for DSPC-I-chol MBs (1.39 (0.97-1.55) $\times 10^{-8}$ kg/s), followed by DSPC-I MBs (0.99 (0.89-1.40) $\times 10^{-8}$ kg/s), while DSPC-D MBs had the lowest shell viscosity (0.43 (0.38-0.61) $\times 10^{-8}$ kg/s).

Figure 2 shows the variability in acoustic response, with DSPC-I-chol MBs having the largest maximum IQR (10.2) and DSPC-D MBs having the highest median IQR (1.5). Acoustic stability was assessed by the relative diameter decrease, with DSPC-D MBs being the least stable and DSPC-I MBs being the most stable. At 50 kPa, DSPC-D MBs had the highest response rate at 2nd harmonic frequencies. At 150 kPa, >80% of MBs had a 2nd harmonic response for all three types of MBs. Finally, DSPC-D MBs had a significantly larger oscillation amplitude than DSPC-I and DSPC-I-chol MBs.

DSPC-I-chol MBs had more buckles than DSPC-I and DSPC-D MBs. No correlation was found between buckles in the coating and the oscillation amplitude. DSPC-I MBs with both large and small LC domains in the coating (N = 11) had a significantly higher oscillation amplitude than those with only large LC domains (N = 11). DSPC-I-chol MBs had no LC domains and for DSPC-D MBs no significant difference was found. Finally, the median oscillation amplitude of MBs that experienced a change in the coating during insonification, by buckling or shedding, was significantly larger than the amplitude of MBs with unchanged coatings.

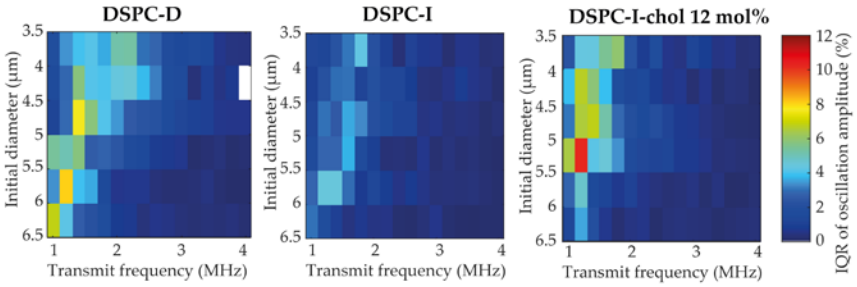

Figure 2. Variability in acoustic response represented as IQR of the oscillation amplitude (%) for different sized MBs (initial diameter in µm) at different frequencies (MHz) at 50 kPa.

Discussion

Lipid phase distribution in the DSPC-based MB coating was altered by the addition of cholesterol. For MBs with 12 mol% cholesterol in the coating all components were miscible and in the same phase, likely because the cholesterol molecules disturb the highly structured LC phase. Reduction of the LC phase area resulted in a reduction of the microbubble coating stability, as indicated by increased buckling due to spontaneous dissolution behavior prior to insonification. These results suggest that diffusion of gas from the microbubble core to the outside medium is increased when the phospholipids in the coating are in a less structured state. DSPC-I-chol MBs with 12 mol% cholesterol had the highest maximum variability in acoustic response, which could not be explained by the presence of buckles prior to insonification, suggesting that factors other than the coating microstructures are causing variability in acoustic response. Lipid handling prior to MB production significantly affected the acoustic behavior of MBs, including the shell parameters, acoustic stability, and non-linear behavior. As DSPC-D and DSPC-I microbubbles have different distributions of DSPE-PEG2000 in their coating [6], this may be the cause of differences in their acoustic response. Based on their stability and uniform response to ultrasound, DSPC-I MBs are the most promising candidates for ultrasound molecular imaging and localized drug delivery.

Acknowledgements – This project was funded by the Phospholipid Research Center in Heidelberg, Germany.

References

[1]. Kosareva A, Abou-Elkacem L, Chowdhury S, Lindner JR, Kaufmann BA. Seeing the Invisible—Ultrasound Molecular Imaging. Ultrasound in Medicine & Biology. 2020;46(3):479-97.

[2]. Kooiman K, Roovers S, Langeveld SAG, Kleven RT, Dewitte H, O'Reilly MA, et al. Ultrasound-Responsive Cavitation Nuclei for Therapy and Drug Delivery. Ultrasound Med Biol. 2020;46(6):1296-325.

[3]. Emmer M, Vos HJ, Versluis M, de Jong N. Radial modulation of single microbubbles. IEEE Trans Ultrason Ferroelectr Freq Control. 2009;56(11):2370-9.

[4]. Helfield BL, Cherin E, Foster FS, Goertz DE. Investigating the subharmonic response of individual phospholipid encapsulated microbubbles at high frequencies: a comparative study of five agents. Ultrasound Med Biol. 2012;38(5):846-63.

[5]. Miyoshi T, Kato S. Detailed Analysis of the Surface Area and Elasticity in the Saturated 1,2-Diacylphosphatidylcholine/Cholesterol Binary Monolayer System. Langmuir. 2015;31(33):9086-96.

[6]. Langeveld SAG, Schwieger C, Beekers I, Blaffert J, van Rooij T, Blume A, et al. Ligand Distribution and Lipid Phase Behavior in Phospholipid-Coated Microbubbles and Monolayers. Langmuir. 2020:3221-33.

[7]. Beekers I, Lattwein KR, Kouijzer JJP, Langeveld SAG, Vegter M, Beurskens R, et al. Combined Confocal Microscope and Brandaris 128 Ultra-High-Speed Camera. Ultrasound Med Biol. 2019;45(9):2575-82.

[8]. van der Meer SM, Dollet B, Voormolen MM, Chin CT, Bouakaz A, de Jong N, et al. Microbubble spectroscopy of ultrasound contrast agents. The Journal of the Acoustical Society of America. 2007;121(1):648-56.

[9]. van Rooij T, Luan Y, Renaud G, van der Steen AF, Versluis M, de Jong N, et al. Non-linear response and viscoelastic properties of lipid-coated microbubbles: DSPC versus DPPC. Ultrasound Med Biol. 2015;41(5):1432-45.

Task-Adaptive Beamforming for Microbubble Localization using Deep Learning

Jihwan Youn[1], Ben Luijten[2], Mikkel Schou[1], Matthias Bo Stuart[1], Yonina C. Eldar[4], Ruud J. G. van Sloun[2,3], Jørgen Arendt Jensen[1]

[1]Dept. of Health Technology, Technical University of Denmark, Lyngby, Denmark
[2]Dept. of Electrical Engineering, Eindhoven University of Technology, Eindhoven, The Netherlands
[3]Philips Research, Eindhoven, The Netherlands
[4]Dept. of Computer Science and Applied Mathematics, Weizmann Institute of Science, Rehovot, Israel
Corresponding author: jihyoun@dtu.dk

Introduction

Ultrasound Localization Microscopy (ULM) can break the resolution limit of conventional ultrasound imaging by localizing individual microbubbles (MBs) and superimposing their positions across many frames. Accurate and robust MB localization is crucial to achieving a high resolution since it directly determines the resolution of ULM images. Overlapping point spread functions (PSFs) of MBs are often inevitable but degrade the ULM image quality because it is challenging to estimate MB positions accurately when the overlaps appear. Recently, several deep learning methods have been introduced to tackle MB localization under overlapping PSFs [1-3]. This work proposes a deep neural network that jointly performs task-adaptive beamforming as well as downstream MB localization. It is trained in an end-to-end fashion to fully tailor the beamforming stage to ULM, thereby further improving deep unfolded ULM [3].

Methods

Data for training were simulated in the Field II pro [4] using synthetic aperture imaging [5]. To simulate radiofrequency (RF) channel data for one image frame, point scatterers were placed randomly in the region of interest, and 12 diverging waves were transmitted using 32 elements among 150 elements. MBs were static during transmissions for one frame in the simulation. The excitation pulse was a two-cycle sinusoid at a frequency of 8MHz. The simulated RF channel data were delayed but not summed on a $\lambda/4$ image grid, resulting in the size of $12 \times N_{bf} \times 150$, where N_{bf} is the number of beamforming points. A total of 2,048 frames were used for training.

The proposed network was constructed by incorporating Adaptive Beamforming by deep LEarning (ABLE) [4] and deep unfolded ULM [3]. The network takes delayed RF channel data as input and returns MB positions on a $\lambda/16$ image grid. The proposed network was trained in an end-to-end fashion even though it can conceptually be divided into two parts. ABLE calculates weights for apodization, learns a weighted summation for compounding, and outputs a beamformed and compounded image. Therefore, ABLE learns the apodization weights that are optimal for the downstream task, i.e., MB localization. The resulting images by ABLE are thus not optimized to be perceptually appealing for humans with low sidelobe levels and high contrast but to ease subsequent MB localization.

Deep unfolded ULM is a model-based neural network that solves MB localization as a sparse coding problem. Proximal gradient methods are commonly used to solve sparse coding problems, but many iterations might be required, and the solution highly depends on hyper-parameters. Deep unfolded ULM uses learned iterative shrinkage-thresholding algorithm (LISTA) [5] to handle such problems. The network is made by unfolding the iteration parts as a *K*-layer neural network. Additionally, the hyper-parameters are embedded in the network so they can be learned from data [8]. Therefore, no time-consuming iterative procedure is required, and more robust localization is available by learning diverse PSF models. It has been

shown that deep unfolded ULM can achieve similar performance to data-driven neural networks with much fewer parameters and, as a result, better generalization [9-10].

Results

The beamformed and compounded image by delay-and-sum (DAS) and ABLE (before downstream MB localization) on simulated test data are shown in Fig. 1. A trade-off between sharpness and noise has been observed. The ABLE image (Fig. 1B) resulted in sharper peaks at MB positions while showing more noise compared with the DAS image (Fig. 1A). Even so, the noise did not affect the localization of the proposed method, as shown in Fig.1C. For closely spaced MBs, the proposed method localized each MB successfully thanks to the sharper peaks, which were not attained by centroid detection on the DAS image due to the overlap.

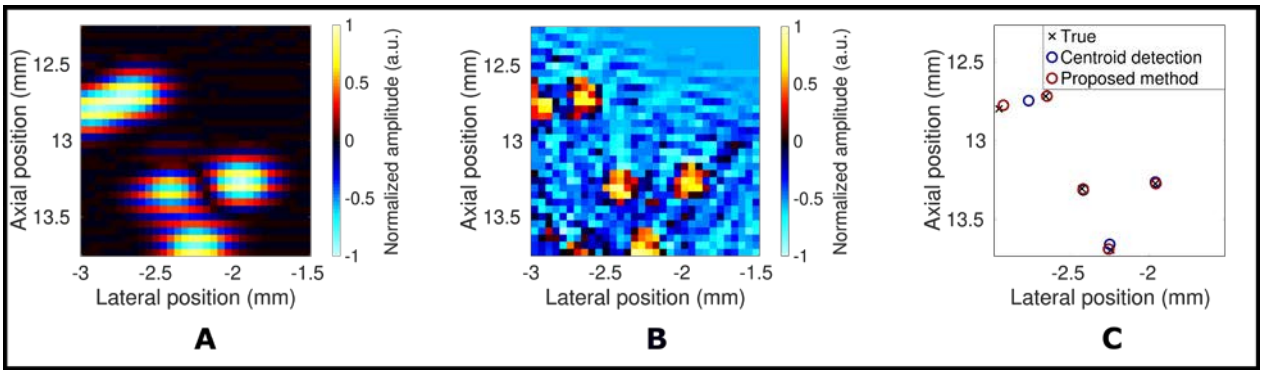

Figure 1. A comparison of beamformed images by (A) delay-and-sum and (B) proposed ABLE on simulated test data. True and estimated microbubble positions by subsequent centroid detection on the DAS image and the proposed method are shown in (C).

Conclusions

A model-based neural network that performs optimal beamforming for the downstream task, i.e. MB localization, is proposed. Interestingly, the task-adaptive beamforming produced sharper peaks than DAS beamforming. That allowed localization of closely spaced MBs, which cannot be achieved by centroid detection. The proposed network can potentially lead to shorter data acquisition time for ultrasound localization microscopy by localizing more MBs accurately on the same image frames. In future work, we envisage extending the current framework to also jointly learn optimal sparse array designs for ULM [11].

References

[1]. R. J. G. van Sloun, O. Solomon, M. Bruce, Z. Z. Khaing, H. Wijkstra, Y. C. Eldar, and M. Mischi, “Super-resolution ultrasound localization microscopy through deep learning,” arXiv:1804.07661v2 [eess.SP], 2018.

[2]. J. Youn, M. L. Ommen, M. B. Stuart, E. V. Thomsen, N. B. Larsen, and J. A. Jensen, “Detection and localization of ultrasound scatterers using convolutional neural networks,” IEEE Trans. Med. Imag., 2020.

[3]. R. J. G. van Sloun, R. Cohen, and Y. C. Eldar, “Deep learning in ultrasound imaging,” IEEE Proc., vol. 108, no. 1, pp. 11–29, 2020.

[4]. J. A. Jensen, “A multi-threaded version of Field II,” in Proc. IEEE Ultrason. Symp. 2014, pp. 2229–2232.

[5]. J. A. Jensen, S. I. Nikolov, K. L. Gammelmark, and M. H. Pedersen, "Synthetic Aperture Ultrasound Imaging," Ultrasonics, vol. 44, pp. e5-e15, 2006.

[6]. B. Luijten, R. Cohen, F. J. De Bruijn, H. A. W. Schmeitz, M. Mischi, Y. C. Eldar, and R. J. G. van Sloun, “Adaptive ultrasound beamforming using deep learning,” IEEE Trans. Med. Imag., 2020.

[7]. K. Gregor and Y. LeCun, “Learning fast approximations of sparse coding,” in Int. Conf. Machine Learning, 2010, pp. 399–406.

[8]. V. Monga, Y. Li, and Y. C. Eldar, “Algorithm unrolling: interpretable, efficient deep learning for signal and image processing,” to appear in IEEE Signal Process. Mag.

[9]. G. Dardikman-Yoffe and Y. C. Eldar, “Learned SPAR-COM: unfolded deep super-resolution microscopy,” Opt. Express, vol. 28, no. 19, pp. 27736–27763, 2020.

[10]. J. Youn, B. Luijten, M. B. Stuart, Y. C. Eldar, R. J. G. van Sloun, J. A. Jensen, “Deep learning models for fast ultrasound localization microscopy,” in Proc. IEEE Ultrason. Symp. 2020.

[11]. I. A. M. Huijben, B. S. Veeling, K. Janse, M. Mischi, and R. J. G. van Sloun, “Learning sub-sampling and signal recovery with applications in ultrasound imaging,” IEEE Trans. Med. Imag., 2020.

Microbubble Localization in High-Clutter Environments using Fullwave Simulations and Model-Based Deep Learning

Thomas M. Kierski[1], Ben Luijten[2], Massimo Mischi[2], Ruud J.G. van Sloun[2], Gianmarco F. Pinton[1], Paul A. Dayton[1]

[1]Joint Dept. of Biomedical Engineering, University of North Carolina, Chapel Hill, NC, USA
[2]Dept. of Electrical Engineering, Eindhoven University of Technology, Eindhoven, The Netherlands
Corresponding author: w.m.b.luijten@tue.nl

Introduction

Image quality for ultrasound localization microscopy (ULM) is driven by the ability to detect and accurately localize individual microbubbles (MBs). This task can be difficult in certain scenarios, such as when the local concentration of MBs is large or when the contrast-to-tissue ratio (CTR) is poor. To improve upon conventional algorithms such as centroid detection and iterative (sparsity based) schemes, there has been a significant interest in deep learning-based approaches [1]. Commonly, such methods rely on encoder-decoder structures borrowed from computer vision. However, a downside of using standard deep learning structures is the requirement for large amounts of training data to guarantee robust inference. In this work, we address these issues as follows:

- First, we will use the Fullwave simulation tool [2] to generate realistic data for training deep neural networks for bubble detection.
- Next, we design our deep learning model with the corresponding measurement model in mind. As such, we employ the deep unfolded ULM model [3], which provides a robust, model-based, structure with a much lower number of trainable parameters by embedding a sparsity prior.

Methods

Plane wave super-resolution imaging is simulated with Fullwave [2] in a transabdominal scenario that was experimentally validated in terms of aberration, reverberation, clutter, and bubble brightness. A total of 1,500 images were generated, of which 1,200 were used training, 200 for validation, and 100 for testing. The 100 test samples will be used to quantitatively compare the performance of the network and conventional localization. All samples were composed of an input x and a label y, where x and y are 2-dimensional arrays with the shape [572, 572]. Input x contains beamformed RF data, and y is the corresponding sparse matrix where ones indicate the ground truth location of each microbubble. Each iteration of y is randomly generated according to the constraint of 4 bubbles/cm^2. Input x is the sum of three components, denoted RF_{noise}, $RF_{clutter}$, and RF_{bubble}. These were generated as follows:

- RF_{noise} : A sample of raw noise from a Verasonics 256 scanner equipped with a P4-1 phased array transducer was used to set the parameters of a random generator in MATLAB (functions *makedist* and *random*). This generator was sampled to generate realistic channel noise.
- $RF_{clutter}$: Random images from the human abdomen were selected from the Visible Human project [4]. Custom MATLAB routines were used to create Fullwave field maps of density, speed of sound, and nonlinearity from these images. No scatterers were added to isolate the effects of reverberation clutter from the laminar structure of the abdomen. It should be noted that abdominal slices were chosen such that the clutter produced by each image is decorrelated from its neighbors to prevent overfitting.
- RF_{bubble}: Ground truth positions from y were used to add microbubbles to otherwise homogeneous Fullwave field maps. The same P4-1 model was used to transmit a plane wave with a random aberrator with RMS width of 100 nsec applied over the transmit aperture.

All components were beamformed using delay-and-sum with $F\#$ = 1.5, and a grid size of 12 points per wavelength (f_0 = 2.5MHz). Finally, we scaled and summed the separate RF contributions as an augmentation step to achieve a final CTR value between -10 and 20 dB. CTR was defined here as the ratio between the

maximum bubble intensity and the mean of the background intensity (noise + clutter) of the envelope-detected image.

In deep unfolded ULM [3], the localization of microbubbles is seen as a sparse recovery task. Conventionally, such a problem can be solved in an iterative fashion (LISTA); however, this may need a large number of iterations to converge. Instead, we unfold such an iterative scheme, yielding a forward network of N-folds, and effectively learning an optimal step size and direction through convolutional layers. In this work, we considered a model with 25 folds and convolutional kernels of size 7x7.

Results

In Figure 1, we show the network predictions for a sample of simulated RF data from the testing set. Panel (a) contains the beamformed RF which is contaminated by a large amount of reverberation clutter, especially in the upper-right quadrant. The resulting network predictions are shown in panel (b) with a 10% confidence threshold applied. Local maxima from this output are considered localizations. In panel (c), we show the ground truth bubble locations (red) along with the network predictions (green) overlaid on the envelope-detected input. In this demonstration, the network is able to "see through" the very bright speckle ringing down from the superficial abdominal layers. It is also able to detect and precisely locate bubbles at depth, even when they are very dim relative to the background.

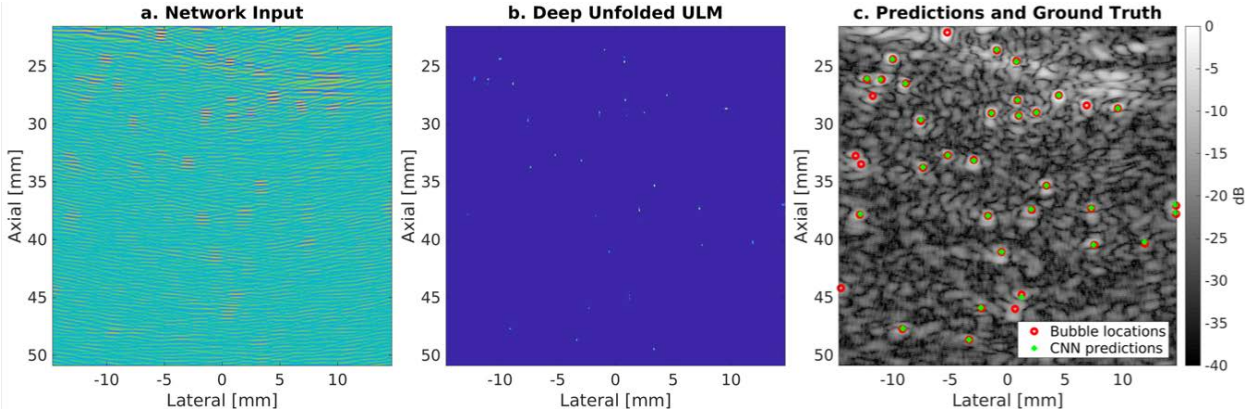

Figure 1. Visualization of a) the RF network input (power-compressed for visualization), b) the network prediction (after thresholding), and c) the true bubble locations and estimations of the proposed method.

Conclusions

We here show that the combination of realistic simulation data, together with a model-based neural network, is capable of accurate and precise predictions in difficult imaging scenarios. We anticipate that this approach will yield higher-fidelity ULM images *in vivo*, where artifacts can corrupt signal quality and cause deviations between the final picture and ground truth microvascular structure. This is an especially important advancement in instances where vessel morphology is used for classification and monitoring of disease. In future work, we will benchmark the performance of this network against conventional ULM methods using *in vitro* and *in vivo* datasets.

References

[1] R. J. G. Van Sloun *et al.*, "Super-resolution ultrasound localization microscopy through deep learning," *IEEE Trans. Med. Imaging*, 2020.

[2] G. F. Pinton, J. Dahl, S. Rosenzweig, and G. E. Trahey, "A heterogeneous nonlinear attenuating full-wave model of ultrasound," *IEEE Trans. Ultrason. Ferroelectr. Freq. Control*, vol. 56, no. 3, pp. 474–488, 2009.

[3] R. J. G. van Sloun, R. Cohen, and Y. C. Eldar, "Deep Learning in Ultrasound Imaging," *Proc. IEEE*, pp. 1–19, 2019.

[4] M. J. Ackerman, "The visible human project," *Proc. IEEE*, vol. 86, no. 3, pp. 504–511, 1998.

Contrast-enhanced single-RF-line simulations and super-resolution microbubble detection using deep learning.

***Nathan Blanken*[1], *Jelmer M. Wolterink*[2], *Hervé Delingette*[3], *Christoph Brune*[2], *Michel Versluis*[1], *Guillaume Lajoinie*[1]**

[1]*Physics of Fluids group, Techmed Centre, University of Twente, Enschede, The Netherlands*
[2]*Department of Applied Mathematics, Techmed Centre, University of Twente, Enschede, The Netherlands*
[3] *EPIONE team, INRIA, Sophia Antipolis, France.*
Corresponding author: n.blanken@utwente.nl

Introduction

The resolution of conventional ultrasound (US) imaging modalities is typically limited to the wavelength of the transmit pulse, which challenges the detection of small lesions. Recently, several super-localization approaches aided by ultrasound contrast agent microbubbles have been reported to circumvent this limitation [1]-[4]. The advantage is twofold: i) theoretically, a resolution is achievable that is on the order of the size of capillary vessels, and ii) short-wavelength high-frequency US, which has a limited penetration depth, is no longer required. Mathematically, super-resolution imaging of a distribution of contrast agent is equivalent to a deconvolution problem, which has been extensively studied in optics. Neural networks have turned out to be successful in solving this problem [5]. In this study, we investigate a deep-learning approach to ultrasound super-resolution. A convolutional neural network estimates the axial coordinates of a monodisperse ensemble of coated microbubbles from a single simulated radiofrequency (RF) line. No filtering or compression is applied: the network uses the full information content of the raw data. Moreover, we demonstrate that our network is capable of multi-task learning: it can simultaneously estimate the acoustic pressure field and the bubble locations.

Methods

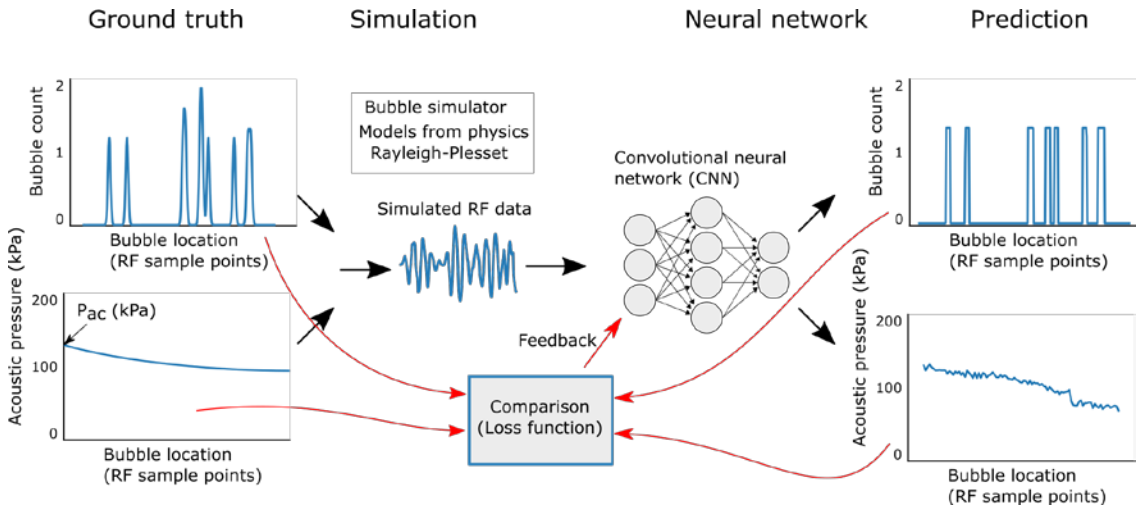

Figure 1. Overview of the training scheme, including generation of the data and training of the convolutional neural network.

Our strategy involves two core components: i) simulation of ultrasound data with a one-dimensional RF-line simulator and ii) training of a neural network to recover information from the simulated data. The approach is summarized in Figure 1. The use of simulated data has three major advantages over experimental data: i) we can rapidly generate a large, diverse dataset, ii) we have direct access to the ground truth that we

want to recover from the ultrasound data, and iii) we can easily modify the system and environmental parameters (e.g. acoustic attenuation) to investigate their effect on the performance of the neural network.

The simulator defines a random spatial distribution of bubbles (monodisperse in size) and simulates its response to an incoming plane wave which has a randomly allocated acoustic pressure. The simulator solves a Rayleigh-Plesset-type equation to find the response of each microbubble and accounts for acoustic attenuation and nonlinear propagation in the medium.

We use a convolution neural network (CNN), as CNNs are effective neural network architectures for the extraction of spatial or temporal features from data [6]. The CNN performs two tasks simultaneously by predicting both the presence of a bubble and the acoustic pressure for each RF sample point. We use a supervised-learning scheme to train the network. Output values predicted by the network are compared to the ground truth, and guided backpropagation is used to update the parameters of the network. In this proof of concept, we trained our network on a dataset in which each RF-line contains a low bubble count: 10 to 100 bubbles. The acoustic pressures in the dataset ranged from 5 to 250 kPa. The network was trained for 1000 epochs (full iterations of the dataset).

Results

The simulator successfully generated 3000 RF lines that were used to train the neural network. The output of the network on the validation dataset (new and unseen data not used for training) after 1000 training epochs is shown in Figure 2. We found that the network accurately detects the microbubbles, with a sensitivity > 95% and a specificity close to 100% for the validation dataset. Bubbles are even detected when they are considerably closer together than a wavelength, demonstrating the potential for super-resolution imaging. The high performance of the network for these locally dense clusters of bubbles is promising for dense bubble populations. The network also accurately predicts the acoustic pressure field, as shown in Figure 2d.

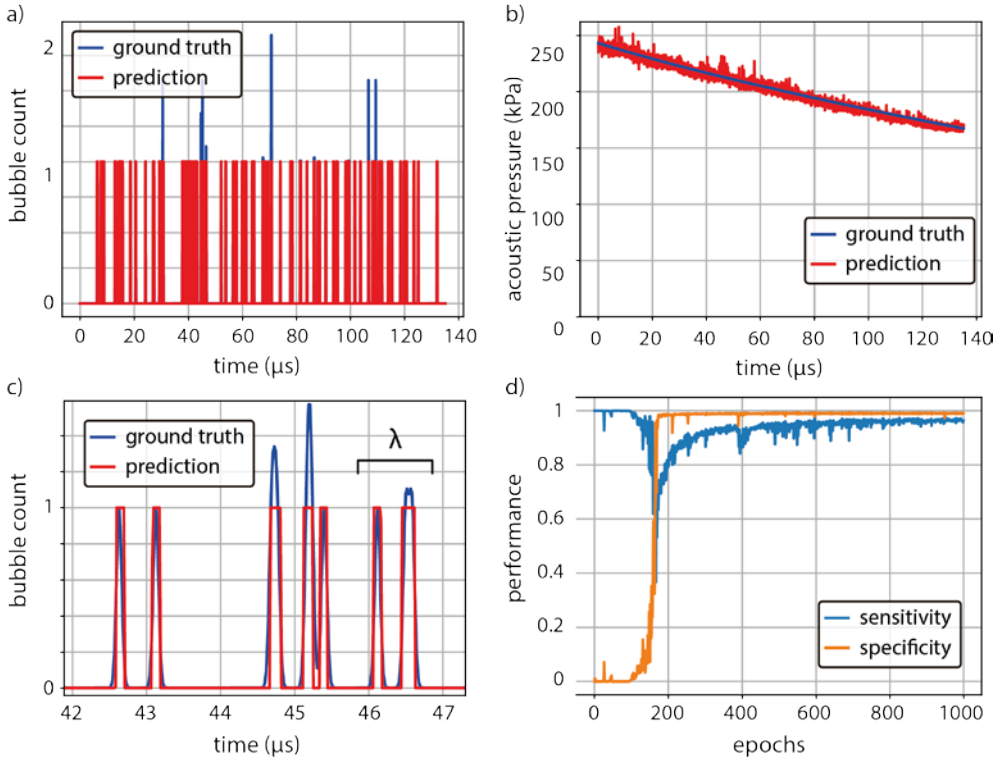

Figure 2. Output of the trained neural network and performance metrics of the network on the unseen validation data set. a) Predicted bubble locations and ground truth. b) Predicted acoustic pressure field and ground truth. c) Zoomed version of a), showing one wavelength separation. d) Performance metrics as a function of training time (epochs) on the validation data set.

Conclusions

We have demonstrated that a neural network can be used to detect microbubbles in a single RF line containing 10 – 100 microbubbles with sub-wavelength accuracy. This makes deep learning a promising strategy for super-resolution ultrasound. We have also shown that the neural network can be trained to estimate the acoustic pressure field simultaneously. The effect of increased bubble density, strong linear scatterers and system noise on the performance of the network will be investigated in the near future. We will also investigate if our method can be extended to polydisperse microbubbles, or if monodispersity is key to its success.

References

[1]. Christensen-Jeffries K, Couture O, Dayton PA, Eldar YC, Hynynen K, Kiessling F, O'Reilly M, Pinton GF, Schmitz G, Tang MX, Tanter M, Super-resolution ultrasound imaging, Ultrasound in Medicine & Biology, 46(4):865-91, 2020.

[2]. Couture O, Hingot V, Heiles B, Muleki-Seya P, Tanter M, Ultrasound localization microscopy and super-resolution: A state of the art, IEEE transactions on ultrasonics, ferroelectrics, and frequency control, 65 (8): 1304-20, 2018

[3]. Errico C, Pierre J, Pezet S, Desailly Y, Lenkei Z, Couture O, Tanter M. Ultrafast ultrasound localization microscopy for deep super-resolution vascular imaging, Nature, 527 (7579): 499-502, 2015

[4]. Van Sloun RJG, Solomon O, Bruce M, Khaing ZZ, Eldar YC, Mischi M, Deep Learning for Super-resolution Vascular Ultrasound Imaging, ICASSP 2019 - 2019 IEEE International Conference on Acoustics, Speech and Signal Processing (ICASSP): 1055-1059, 2019.

[5]. Pu T, Ou JY, Papasimakis N, Zheludev NI, Label-free deeply subwavelength optical microscopy, Applied Physics Letters, 116 (13): 131105, 2020.

[6]. He K, Gkioxari G, Dollár P, Girshick R. Mask R-CNN. Proceedings of the IEEE international conference on computer vision, 2961-2969, 2017.

Challenges and Opportunities in Microbubble Localization for Super-Resolution Microvascular Imaging

Pengfei Song[1]

[1]Department of Electrical and Computer Engineering, University of Illinois at Urbana-Champaign, Urbana, USA
[2]Beckman Institute, University of Illinois at Urbana-Champaign, Urbana, USA
Corresponding author: songp@illinois.edu

Introduction

In the last five years we have witnessed the rapid rise of the field of super-resolution ultrasound microvascular imaging (SR-UMI) [1, 2]. SR-UMI effectively enables the imaging resolution of optics at the imaging penetration of acoustics, which opens new doors for numerous clinical and preclincial applications that involve tissue microvasculature characterization. Among the various SR-UMI techniques, localization-based methods rely on accurate localization of spatially-isolated microbubbles (MB) to break the diffraction limit of ultrasound and realize super-resolution. In practice, localization is often hampered by MB signal overlap that commonly occurs under bolus MB injections as well as within larger vessels with higher blood flow volume. Although reducing the concentration of MB administration effectively alleviates the issue of MB signal overlap, it significantly reduces the probablility of MB localization at the microvascular level, resulting in prolonged data acquisition time that can be prohibitive in practice.

Methods

To study the time and flow kinetics of MB perfusion in tissue microvasculature and its implications on MB localization for SR-UMI, we conducted experiments using confocal imaging and fluorescently labeled MBs on a chorioallantoic membrane (CAM) microvessel model [3]. Ultrasound imaging of the same CAM microvessel bed was also conducted to compare with optical imaging. A discrete-time Markov chain network was used to model the CAM microvessel bed, and a Monte Carlo random-walk simulation was used to estimate perfusion times based on experimental data. To alleviate the issue of MB overlap under high MB concentrations, we present a MB separation technique to separate MBs into sub-populations based on differences in MB flow dynamics such as movement speed, flow direction, and signal decorrelation [4]. We then further explored the use of deep learning-based techniques to localize MB signals under various conditions of MB concentration. Both phantom and *in vivo* studies were conducted on various types of tissues.

Results

The confocal imaging study of fluorescently labeled MBs in capillary vessels provided results that were consistent with a probability-derived explanation for the long data acquisition times required for SR-UMI. The estimated time to fully perfuse the capillary network was 193 s, which is in good agreement with the values reported in literature. We also found that the unbalanced transition probabilities, as a result from heterogeneous MB flow through the capillary bed, can extend the estimate for full perfusion by at least an order of magnitude. We then demonstrated the effectiveness of the proposed MB separation technique in alleviating the issue of MB signal overlap and accelerating the data acquisition speed (by approxiamtely 18-fold at 30% saturation). Finally, we showcase preliminary results of MB localization based on deep learning as well as other experimental results based on optical imaging that are illuminating for future development of MB localization techniques.

Conclusions

While the data acquisition speed of SR-UMI is fundamentally limited by the physiological perfusion rate of blood flow, we are still not at 100% efficiency of MB localization to fully utilize the available MB signals detected by ultrasound. The combination of the rich spatiotemporal MB data acquired from ultrafast

ultrasound and deep learning creates new possibilities for robust MB localization under the conditions of high MB concentration.

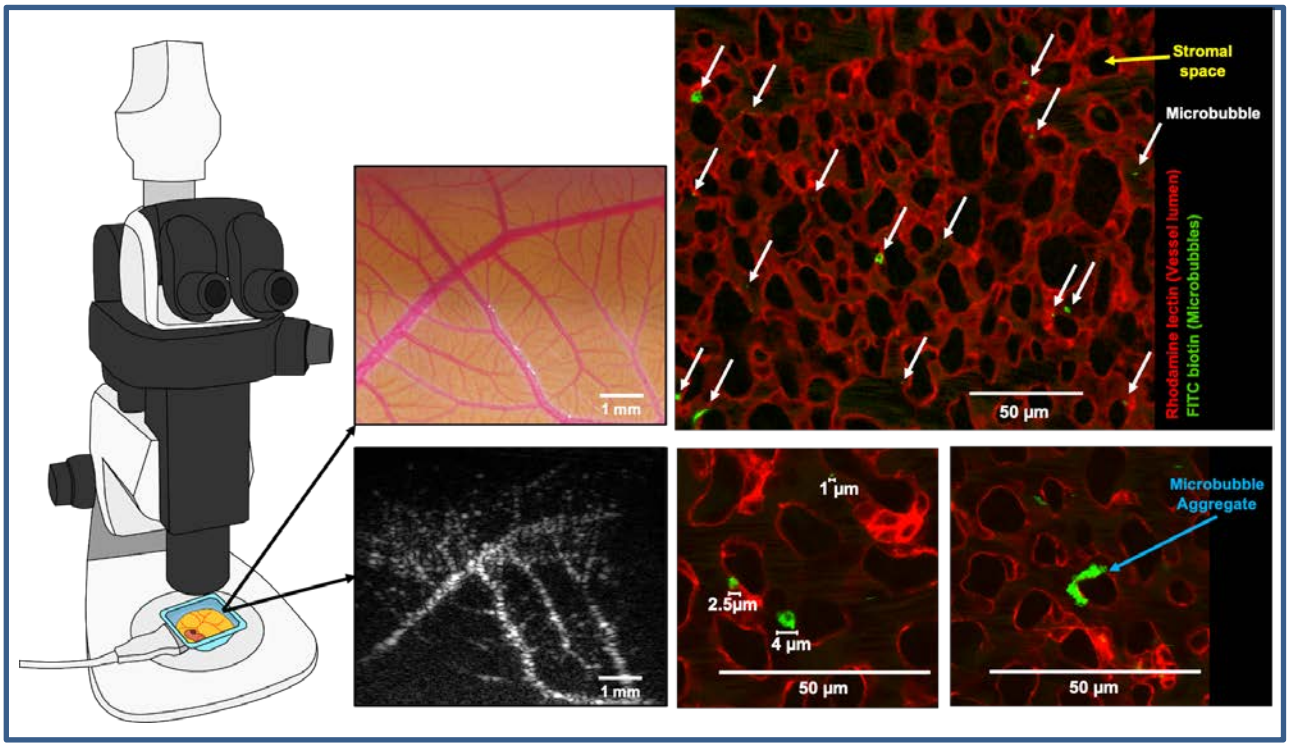

Figure 1. Ultrasound and microscopic imaging of the chicken embryo chorioallantoic membrane (CAM) microvessels.

References

[1] K. Christensen-Jeffries, O. Couture, P. A. Dayton, Y. C. Eldar, K. Hynynen, F. Kiessling, M. O'Reilly, G. F. Pinton, G. Schmitz, M.-X. Tang, M. Tanter, and R. J. G. van Sloun, "Super-resolution Ultrasound Imaging," *Ultrasound in Medicine & Biology*, vol. 46, no. 4, pp. 865-891, 2020/04/01/ 2020, doi: https://doi.org/10.1016/j.ultrasmedbio.2019.11.013.

[2] O. Couture, V. Hingot, B. Heiles, P. Muleki-Seya, and M. Tanter, "Ultrasound Localization Microscopy and Super-Resolution: A State of the Art," *IEEE Transactions on Ultrasonics, Ferroelectrics, and Frequency Control*, vol. 65, no. 8, pp. 1304-1320, 2018, doi: 10.1109/TUFFC.2018.2850811.

[3] M. R. Lowerison, C. Huang, Y. Kim, F. Lucien, S. Chen, and P. Song, "In Vivo Confocal Imaging of Fluorescently Labelled Microbubbles: Implications for Ultrasound Localization Microscopy," *IEEE Transactions on Ultrasonics, Ferroelectrics, and Frequency Control*, pp. 1-1, 2020, doi: 10.1109/TUFFC.2020.2988159.

[4] C. Huang, M. R. Lowerison, J. D. Trzasko, A. Manduca, Y. Bresler, S. Tang, P. Gong, U. W. Lok, P. Song, and S. Chen, "Short Acquisition Time Super-Resolution Ultrasound Microvessel Imaging via Microbubble Separation," *Scientific Reports*, vol. 10, no. 1, p. 6007, 2020/04/07 2020, doi: 10.1038/s41598-020-62898-9.

3D Transcranial Ultrasound Localization Microscopy in rat with a multiplexed matrix probe.

A. Chavignon[1], B. Heiles[2], V. Hingot[1], O. Couture[1]

[1]Sorbonne Université, CNRS, INSERM, Laboratoire d'Imagerie Biomédicale, 15 rue de l'Ecole de Médecine, 75006 Paris, France.
[2]Maresca Lab, TU Delft, Netherlands
Corresponding author: arthur.chavignon@upmc.fr

Introduction

Ultrasound Localization Microscopy (ULM) allows ultrasound imaging to surpass the diffraction-limit and maps microvasculature with quantitative velocimetry at micrometric scales [1-2]. 3D haemodynamic imaging down to the scale of arterioles has recently been demonstrated using 3D Ultrasound Localization Microscopy (ULM) [3] in a craniectomized rat brain. However, the need for complex ultrasound scanners to drive 2D array probes and for invasive craniotomy surgery is a deterrent to the widespread of preclinical studies using that technique. We demonstrate here that transcranial ULM is possible using a conventional 256 channels plane-wave scanner within tens of minutes of acquisition time.

Methods

A 1024 elements multiplexed matrix probe (Vermon, France) was driven at 8MHz with a Vantage 256™ (Verasonics, USA). Boli of Sonovue microbubbles were injected in an anesthetized rat under isoflurane. For each of the 5 emitted tilted plane waves, 10 combinations of synthetic emissions/receptions with different sub-apertures were required to insonify the full volume above the probe. 150,000 volumes were acquired by blocs of 200 volumes at 500 Hz, with pauses for data transfert. Radio frequency data were beamformed, filtered and processed with a 3D ULM algorithm using a radial symmetry based localization algorithm [4]. Microbubbles were localized and tracked to build a set of paths. Density and haemodynamic volumes were built by accumulating microbubbles paths along with 3D velocity vectors.

Results

The custom set of transmits/receives enabled volumetric imaging using a conventional ultrasound scanner and provide a precise detection, localization, and tracking of microbubbles through the intact rat skull. 630k tracks of microbubbles were detected under 10 minutes of acquisition. A vascular (figure 1a) and haemodynamic volume (figure 1b) of a rat brain were reconstructed. The attenuation of the skull bone hinders a correct detection of microbubbles, and shadowed zones, for example in the middle, above the sagittal suture, or under coronal (bregma) and lambdoid (lambda) sutures.

Conclusions

By using a multiplexed probe and a conventional ultrafast ultrasound scanner, we demonstrated the possibility to perform 3D transcranial ULM in rat. This system widens the application of volumetric super-resolution ultrasound imaging to preclinical studies with longitudinal follow-up such as strokes recovering studies.

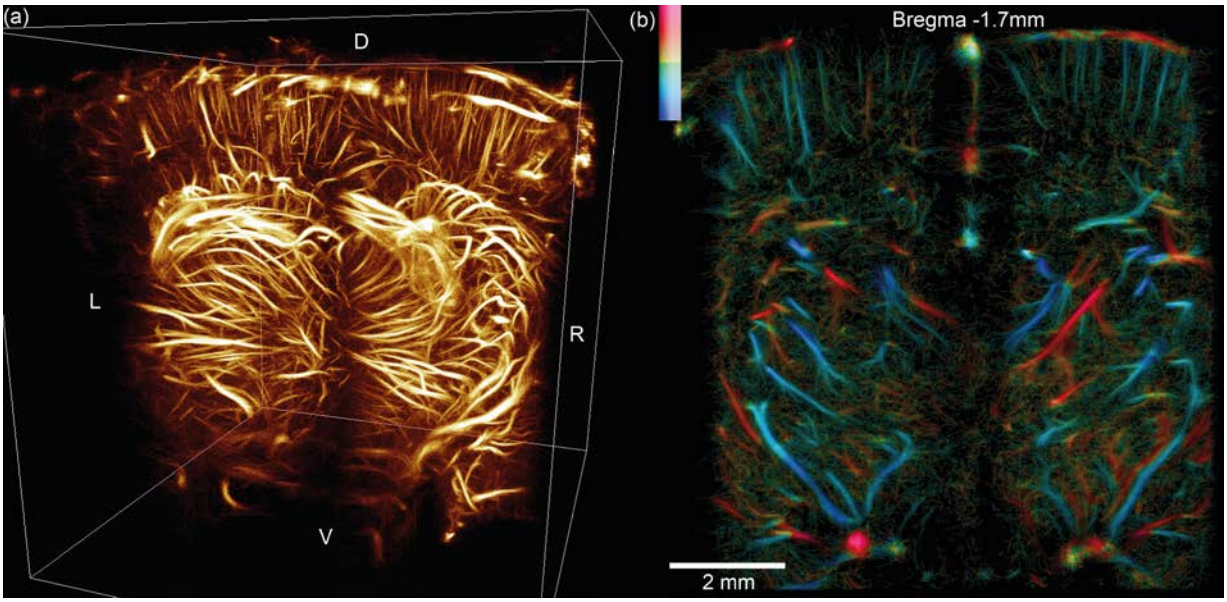

Figure 1. (a) 3D rendering of a vascular density map of a rat brain (isotropic voxel of 10µm) (V: ventral, D: dorsal, R: right, L: left) (b) 400µm slice of the velocimetric map at bregma -1.7mm. Velocities up to 60mm/s are encoded in blue for upward flows, and in red for downward flows.

References

[1]. O. Couture, V. Hingot, B. Heiles, P. Muleki-Seya, and M. Tanter, "Ultrasound localization microscopy and super-resolution: a state-of-the-art," IEEE Transactions on Ultrasonics, Ferroelectrics, and Frequency Control, pp. 1–1, 2018.

[2]. C. Errico et al., "Ultrafast ultrasound localization microscopy for deep super-resolution vascular imaging," Nature, vol. 527, no. 7579, pp. 499–502, Nov. 2015.

[3]. B. Heiles, M. Correia, M. Pernot, J. Provost, M. Tanter, and O. Couture, "Volumetric Ultrafast Ultrasound Localization Microscopy using a 32x32 Matrix Array", IEEE International Ultrasonics Symposium (IUS), 2018.

[4]. B. Heiles, M. Correia, V. Hingot, M. Pernot, J. Provost, and O. Couture, "Ultrafast 3D Ultrasound Localization Microscopy using a 32x32 Matrix Array," IEEE Transactions on Medical Imaging, p. 13, 2019.

Enhanced visualization of ultrasound contrast agents using normalized singular spectrum area and singular value thresholding.

Elizabeth B Herbst[1], F William Mauldin Jr.[1], John A Hossack[1]

[1]Department of Biomedical Engineering, University of Virginia, Charlottesville, VA, USA
Corresponding author: jh7fj@virginia.edu

Introduction

Ultrasound molecular imaging (USMI) is a diagnostic technique which combines ultrasound imaging with molecularly targeted microbubbles (MBs). This method allows for highly sensitive quantification of disease markers presented on the vascular endothelium. Typical contrast-mode imaging techniques rely upon frequency-based filtering to improve the contrast-to-tissue ratio (CTR) of microbubble signals. However, these methods are highly susceptible to tissue leakage artifacts, thus necessitating manual segmentation of microbubble signals. Furthermore, differentiation between adherent and non-adherent MB signals typically requires the use of a technique called differential targeted enhancement (dTE), which destroys MBs in the transducer field of view to quantify adherent MB signals. In this study, normalized singular spectrum area (NSSA), a technique previously validated to differentiate between adherent and non-adherent MBs, was combined with singular value thresholding (SVT) to produce an integrated filtering method which automatically segments and classifies adherent and non-adherent MB signals.

Methods

For *in vivo* experiments, C57BL/6 mice were implanted with subcutaneous MC38 hindlimb tumor cells following an institutionally-approved ACUC protocol. When tumors had grown for approximately 10 days or had reached a maximum diameter of 10 mm, mice were imaged using a Vantage 256 imaging system with an L12-5 Philips transducer programmed with a custom-designed pulse inversion mode sequence. Mice were injected via tail vein catheter with MBs conjugated to VEGFR-2 or isotype control antibodies. Mice were divided into two experimental groups (n = 8). The first group was injected with isotype control MBs and imaged 1 min after injection. The second group was injected with VEGFR-2 MBs and imaged 6 min after injection. For each injection, 100-frame ensembles of in-phase/quadrature (IQ) data were acquired.

Our SVT method was based upon evidence that strongly reflecting static tissue signals are mostly defined along lower-rank principal components, while more spatiotemporally incoherent MB signals have energy that is more evenly distributed among low- and high-rank principal components. Therefore, removal of the first principal component of ultrasound ensemble data would result in higher overall MB CTR. To perform SVT, singular value decomposition was performed on 100-frame ensembles of ultrasound IQ data, and the first singular value component was discarded.

NSSA was used to classify MB signals as adherent or non-adherent, using a previously described NSSA filtering method [1]. NSSA was calculated on smaller ensembles of ultrasound data using a window size of $5 \times 5 \times 50$ samples, or 1.0 mm × 0.5 mm × 2.5 s in the axial, lateral, and temporal dimensions, respectively. The performance of SVT was measured by calculating the CTR of manually segmented MB signals in PI images before and after SVT was applied. The performance of dTE, SVT, NSSA, and SVT+NSSA filtering methods in classifying MB signals from surrounding tissue and noise signals was measured using receiver operating characteristic (ROC) analysis. Differences between ROC area-under-the-curve (AUC) measurements were assessed using a Hanley and McNeil [2] test ($p < 0.0001$) and Bonferroni correction.

Results

Images of the SVT+NSSA signal showed clear delineation of adherent and non-adherent MB signals (Fig. 1). SVT was shown to increase the CTR of MB signals by 9.81±1.04 dB compared to PI signals. SVT+NSSA filtering was shown to significantly improve MB classification performance compared to dTE filtering, as well as SVT or NSSA filtering alone (Fig. 2).

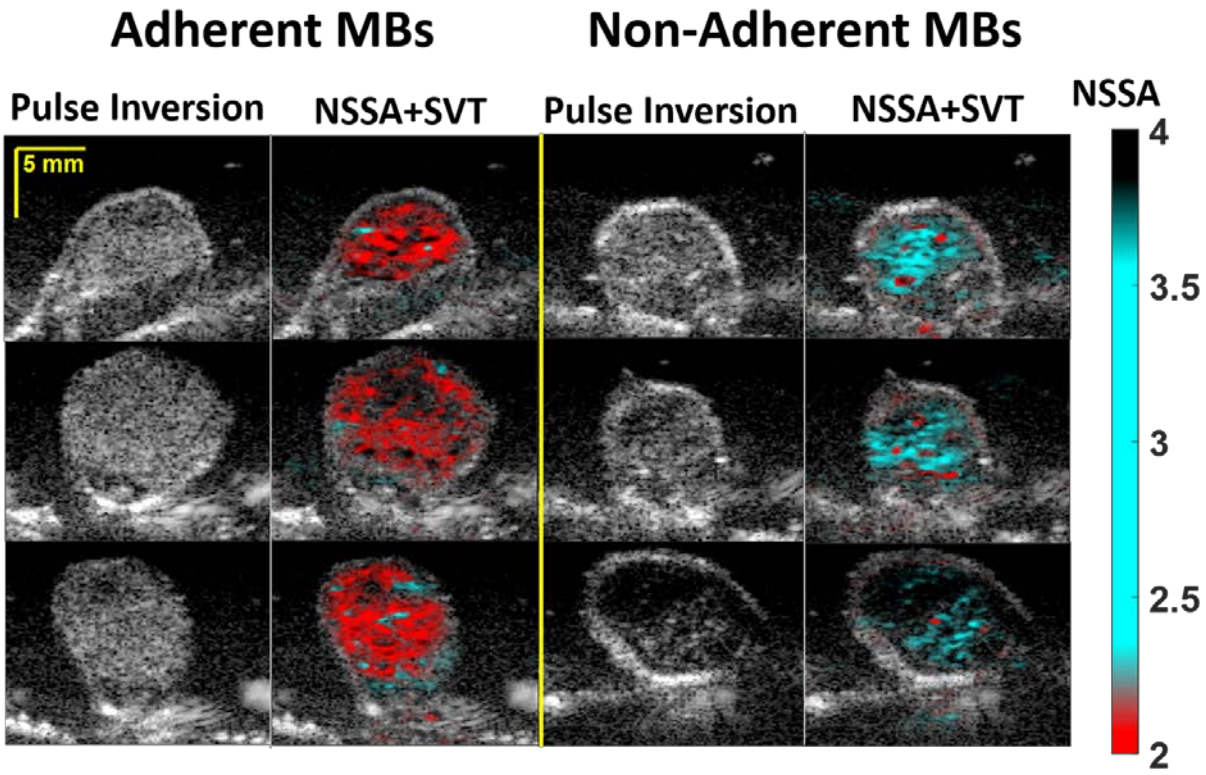

Figure 1. NSSA+SVT filtering allows for enhanced visualization of adherent and non-adherent MB signals. To create filtered images, PI images were first singular value thresholded to remove the first principal component and increase MB CTR. SVT output was then colormapped based on NSSA value. This colormapped image was then overlaid on the original PI tumor images.

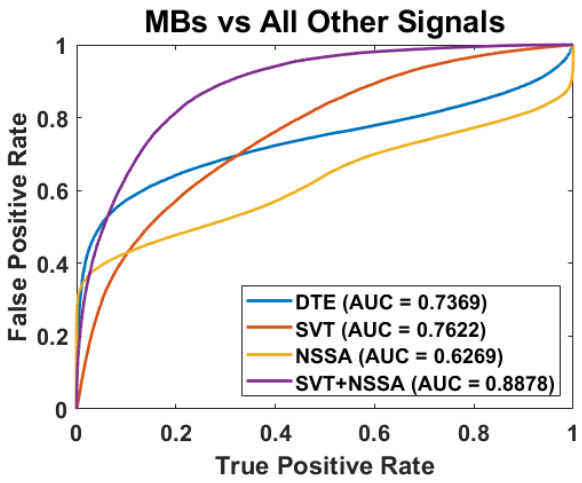

Figure 2. Classification performance of dTE, SVT, NSSA, and SVT+NSSA filtering in segmenting MB signals. ROC analysis revealed that combining SVT with NSSA filtering resulted in higher MB classification performance than all other methods.

Conclusions

The results from this study revealed that SVT+NSSA filtering is an effective tool for automatic segmentation of MB signals from surrounding tissue signals, in addition to automatic classification of MB signals as adherent or non-adherent. The non-destructive nature of SVT+NSSA filtering allows for potential real-time monitoring of MB dynamics in future studies. The enhanced visualization of adherent and non-adherent MB signals using this filtering method could allow for greater clinical uptake of USMI techniques and faster workflow in future diagnostic settings.

References

[1]. Herbst EH, Unnikrishnan S, Klibanov AL, Mauldin Jr. FW, Hossack JA, Validation of normalized singular spectrum area as a classifier for molecularly targeted microbubble adherence. 2019, Ultrasound in Medicine and Biology, 45: 2493-2501.

[2]. Hanley JA, McNeil BJ, A method of comparing the areas under receiver operating characteristic curves derived from the same cases. 1983, Radiology. 148: 839-43.

Improved Acoustic Reporter Genes for Sensitive and Specific Imaging of Gene Expression

***Robert C. Hurt*[1], *Katie Wong*[2], *Daniel Sawyer*[1], *Ramya Deshpande*[2], *David R. Mittelstein*[3], *Mikhail G. Shapiro*[2]**

[1] *Division of Biology and Biological Engineering, California Institute of Technology, Pasadena, CA, USA*
[2] *Division of Chemistry and Chemical Engineering, California Institute of Technology, Pasadena, CA, USA*
[3] *Division of Engineering and Applied Sciences, California Institute of Technology, Pasadena, CA, USA*
Corresponding author: mikhail@caltech.edu

Introduction

A major challenge in the field of biological imaging and synthetic biology is noninvasively visualizing the functions of natural and engineered cells inside opaque samples such as living animals. One promising technology that addresses this limitation is ultrasound, with its penetration depth of several cm and spatial resolution of tens of μm. Recently, the first genetically encoded ultrasound contrast agents—a unique class of air-filled proteins called gas vesicles (GVs)—were developed to link ultrasound to cellular function via heterologous expression in commensal bacteria and mammalian cells. Just as the discovery of fluorescent proteins was followed by the improvement and diversification of their optical properties through directed evolution, here we describe the evolution of GVs as acoustic reporters. To accomplish this task, we introduce a strategy for high-throughput acoustic screening of GVs in bacterial colonies and validate its ability to identify new phenotypes in mutant libraries.

Methods

As a starting point for engineering the nonlinear contrast and collapse pressure of GVs, we chose the two GV gene clusters that have previously been shown to produce the most US contrast when expressed in *E. coli*: the wild type *Bacillus megaterium* ATCC 19213 cluster[1] (lacking GvpA, GvpP, and GvpQ) and a hybrid cluster composed of structural protein genes from *Anabaena flos-aquae* and "assembly factors" from *B. megaterium*[2] (Fig. 1a). The primary GV structural protein--GvpA or its homolog GvpB--creates the cigar-shaped body of the GV, and optionally GvpC may attach to the outside of this structure and reinforce it mechanically (Fig. 1b).

GVs are known to respond to ultrasound in three regimes, depending on the input pressure applied: linear scattering, nonlinear scattering, and collapse[3] (Fig. 1c). Of particular interest for *in vivo* imaging is the nonlinear scattering regime in which GVs produce significantly more contrast than tissue, putatively by "buckling" of their shells.[4] However, this property has only been demonstrated for purified GVs, as GV-expressing *E. coli* cannot currently produce enough nonlinear signal to be discriminated from background tissue signal. Thus, we set out to engineer the following phenotypes in GV-expressing *E. coli*: 1) increase the amount of nonlinear signal (either by increasing GV expression or by increasing the nonlinear scattering content of each GV), 2) alter (widen, contract, or shift) the pressure range over which GVs produce nonlinear signal, and 3) increase or decrease the pressure at which GVs begin to collapse (Fig. 1c).

To engineer nonlinear signal and collapse pressure phenotypes, we developed a method for high-throughput, semi-automated characterization of US contrast and GV collapse pressure in *E. coli* (Fig. 1d). After constructing scanning site saturation libraries of GvpA or GvpB in the starting point clusters (Fig. 1a), we first performed a selection for high levels of GV expression by inducing transformants on dual-layer plates and picking only colonies that appeared white (GV-expressing bacteria appear white because

GVs scatter light, in addition to US). These mutants were then expressed in confluent bacterial patches on new agar plates (Fig. 1e). These plates were imaged using an automated scanning setup in which a Matlab-controlled 3D translating stage (Fig. 1f) raster scans an US transduce above submerged Petri dishes, producing an US image in which bacterial patches with high GV expression appear bright (Fig. 1g). This pipeline (Fig. 1d) allowed us to generate and acoustically screen several mutant libraries, from which we identified mutants with significantly enhanced acoustic phenotypes.

Results

In the first round of evolution for GvpB, we obtained mutants with ~11 dB more nonlinear signal than the WT parent (Fig. 2a), and in the second round, we obtained mutants with ~15 dB more nonlinear signal than the WT parent (Fig. 2b). Similar results were obtained for GvpA mutants. Further characterization of these mutants in terms of their morphologies, collapse pressures, and US pressure response functions are ongoing.

Conclusions

Here, we have developed a method for the directed evolution of acoustic reporter genes, and used it to identify mutants of GvpA and GvpB with ~15 dB more nonlinear signal than their WT parents. In prelimary experiments, these mutants appear to also exhibit differences in their collapse pressures and US pressure response functions. In addition to allowing more sensitive detection, the properties of these mutant GVs which will hopefully enable their use in multiplexed imaging.

These results suggest that directed evolution could play as big a role in the engineering of acoustic biomolecules as it has in the development of their fluorescent counterparts.

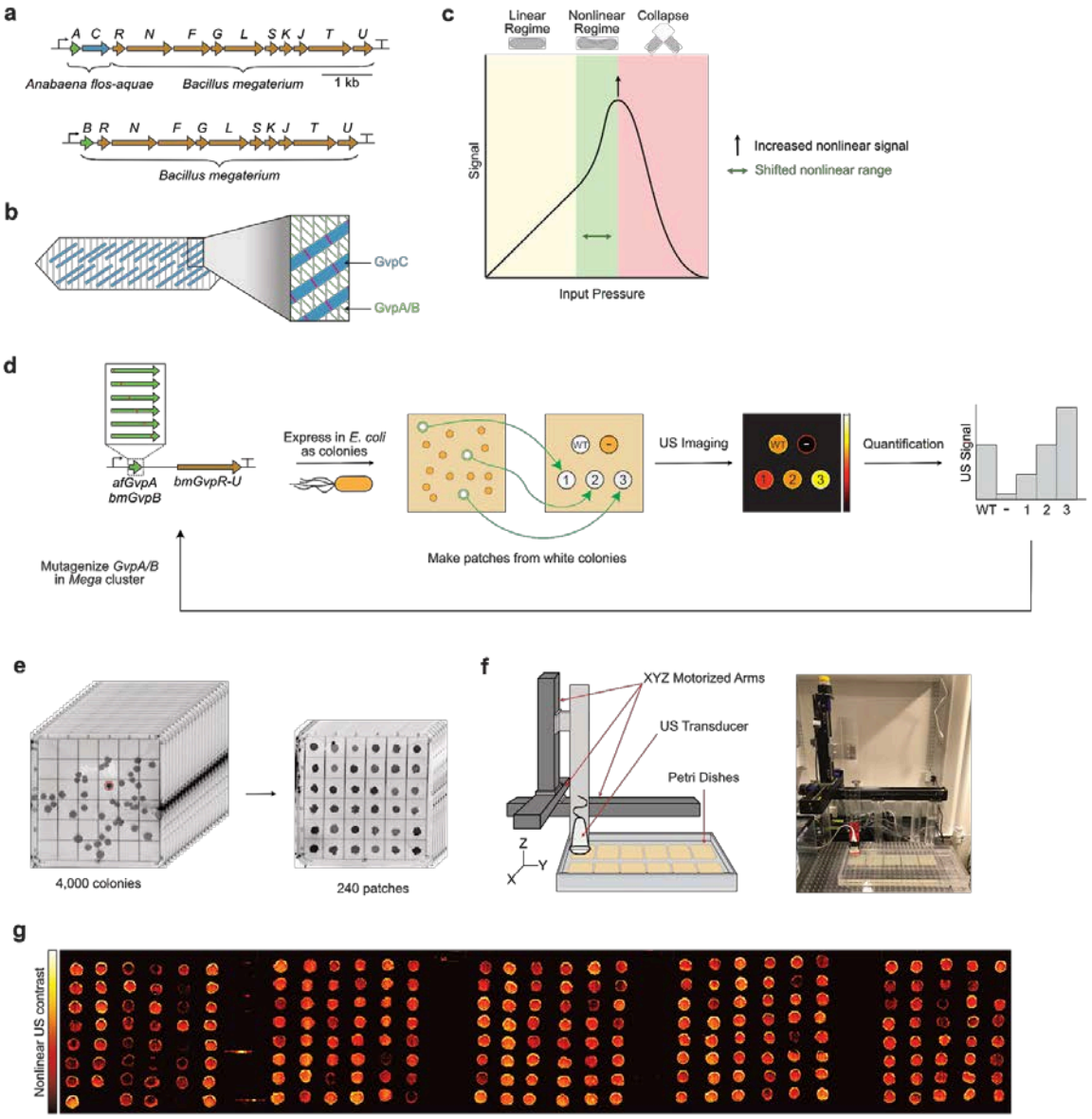

Figure 1. Theoretical basis for evolution of GvpA/B (a-c) and experimental pipeline for evolution (d-g).

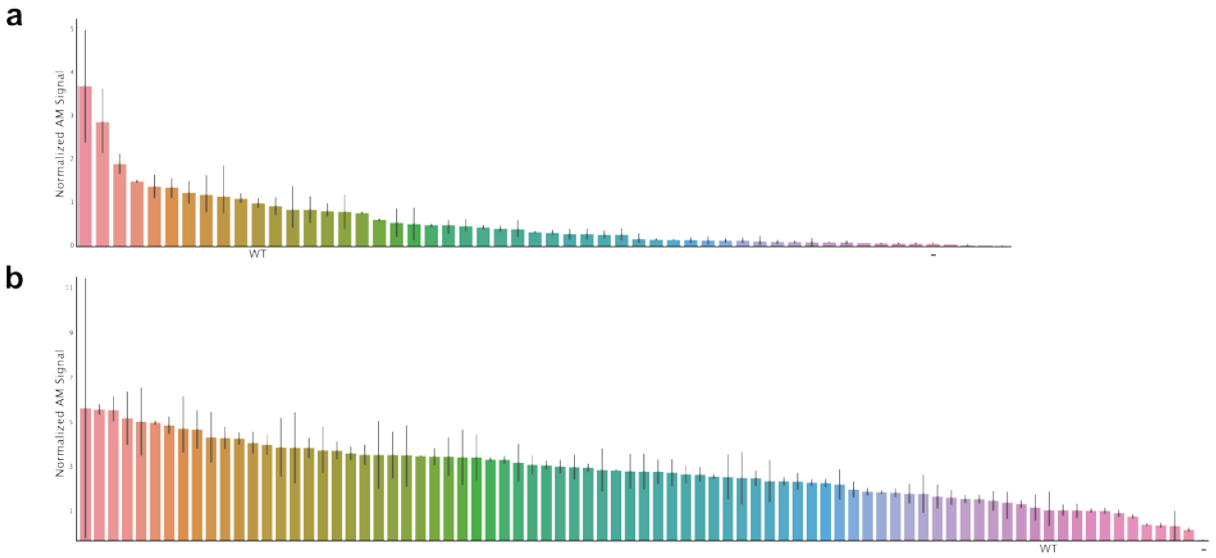

Figure 2. Nonlinear signal quantification for mutants of GvpB from the first (a) and second (b) rounds of evolution. WT and negative control sequences are indicated.

References

[1]. Li, N. & Cannon, M. C. Gas vesicle genes identified in Bacillus megaterium and functional expression in Escherichia coli. *J. Bacteriol.* **180**, 2450–2458 (1998).

[2]. Bourdeau, R. W. *et al.* Acoustic reporter genes for noninvasive imaging of microorganisms in mammalian hosts. *Nature* **553**, 86–90 (2018).

[3]. Maresca, D. *et al.* Nonlinear ultrasound imaging of nanoscale acoustic biomolecules. *Appl. Phys. Lett.* **110**, 073704 (2017).

[4]. Maresca, D., Sawyer, D. P., Renaud, G., Lee-Gosselin, A. & Shapiro, M. G. Nonlinear X-Wave Ultrasound Imaging of Acoustic Biomolecules. *Phys. Rev. X* **8**, 041002 (2018).

Contrast enhanced ultrasound with optimized aperture patterns

Ting-Yu Lai, Michalakis A. Averkiou

Department of Bioengineering, University of Washington, Seattle, USA
Corresponding author: tlai9@uw.edu

Introduction

Contrast-enhanced ultrasound (CEUS) uses microbubbles as a contrast agent and allows visualization of the perfusion of organs and tumors. CEUS is clinically used for liver lesion detection and characterization, and therapy monitoring. In recent years, a new beamforming paradigm has emerged where a single broad beam (typically utilizing the full aperture) is transmitted in the body and multiple receive lines from the same scattered echoes are formed to create images at very high frame rates referred to as ultrafast imaging. When combined with CEUS, ultrafast imaging has enabled recent innovations such as super resolution imaging [1].

Tissue (linear) signal suppression is crucial in CEUS in order to achieve good image contrast and microbubble specificity. However, hardware limitations of the ultrasound system may affect the precision of pulse inversion or amplitude change of the transmitted pulses, resulting in incomplete cancellation of the linear component of the echoes. The result is a "pseudo-enhancement" of tissue that can possibly mask real enhancement caused by microbubbles. Amplitude modulation (AM) with implemented with complimentary apertures improves tissue signal suppression and requires less hardware complexity [2]. The cross talk between transmitting and non-transmitting (on and off) array elements may compromise the degree of tissue signal suppression in AM [3]. The cross talk may be even more severe in ultrafast CEUS compared to conventional focused beamforming since larger apertures are used. The degree of overlap between the two complimentary apertures may also greatly impact the response from microbubbles. In this study, we evaluated the image quality of ultrafast CEUS when using different aperture patterns and compounding angles and suggested an optimal aperture pattern for AM (hereafter referred to as "OAM") that would further increase tissue signal suppression and image contrast for ultrafast CEUS.

Methods

AM consists of transmitting 3 pulses with the following sequence: $\boldsymbol{p_{even}}$, $\boldsymbol{p_{full}}$, and $\boldsymbol{p_{odd}}$. With this technique, the transmit voltage and transmit beamforming delays are never changed among $\boldsymbol{p_{even}}$, $\boldsymbol{p_{full}}$, and $\boldsymbol{p_{odd}}$, yet only even elements are used for transmitting $\boldsymbol{p_{even}}$, only odd elements are used for $\boldsymbol{p_{odd}}$, while all the elements are used for $\boldsymbol{p_{full}}$. We can further generalize AM by transmitting 3 pulses with the following sequence: $\boldsymbol{p_1}$, $\boldsymbol{p_{full}}$, and $\boldsymbol{p_1^*}$. Half of the elements are randomly selected and used for transmitting $\boldsymbol{p_1}$, other half of the elements are used for $\boldsymbol{p_1^*}$, while all the elements are used for $\boldsymbol{p_{full}}$.

Two combinations of aperture patterns used for $\boldsymbol{p_1}$ and $\boldsymbol{p_1^*}$ are shown in Fig. 1, where the elements in blue are used for $\boldsymbol{p_1}$ and the elements in white are used for $\boldsymbol{p_1^*}$. A combination of the aperture patterns can be characterized by two parameters: the degree of overlap of the two complementary aperture patterns [Fig. 1 (a)] and the number of on/off interfaces between elements in the aperture pattern [Fig. 1 (b)]. The acoustic fields of $\boldsymbol{p_1}$ and $\boldsymbol{p_1^*}$ are more uniform across the whole aperture when the complimentary apertures have more overlap with each other. Also, the cross talk increases when there's more on/off interfaces in an aperture pattern.

We first evaluated the changes in contrast to tissue ratio (CTR) when using 26 combinations of random aperture patterns for AM in a flow phantom system. CTR was calculated as the mean intensity difference between contrast region and tissue background in dB. The aperture design that achieved the highest CTR in the flow phantom was called optimized AM (OAM). Next, we compared the CTR of AM with OAM when using 1, 7, and 15 compounding angles. Finally, we compared OAM with AM in images produced by the maximum intensity projection method (MIP) in a perfused pig liver model. This model provides an ideal environment for pre-clinical imaging investigations since it is very similar to an *in vivo* environment. We formed time-intensity curve (TIC) from regions of interest (ROI) in the liver microcirculation.

We implemented the proposed apertures for nonlinear imaging on a L7-4 linear array with a transmit frequency of 3.5 MHz. Sonazoid microbubbles (GE Healthcare, UK) were prepared as described by the manufacturer. They were then drawn from the vial with a 21G aeriated syringe and diluted to a 1/10000 concentration in deionized water.

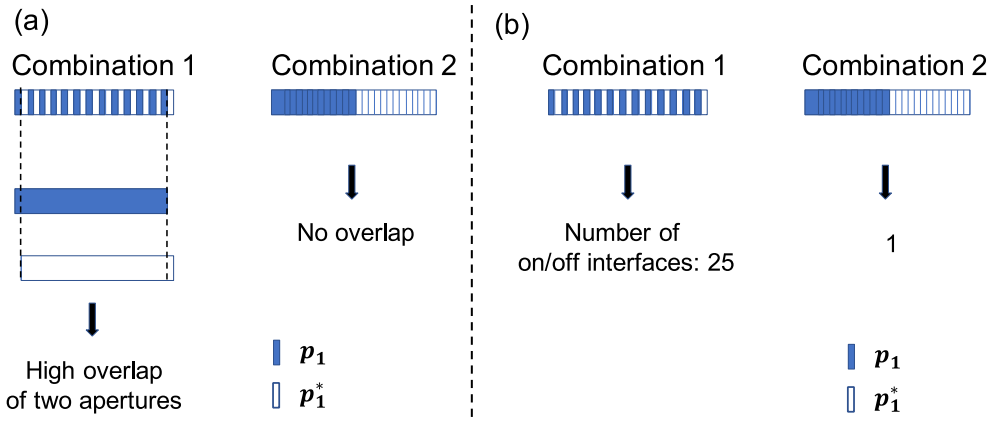

Figure 1: Two of the 26 combinations of aperture patterns. The blue elements are used for p_1 and the white elements are used for p_1^*. (a) Combination 1 has high overlap of its two complementary aperture patterns while combination 2 has no overlap. (b) Combination 1 has more on/off interfaces compared to combination 2.

Results

Field II simulations of the acoustic field produced by 5 (of the 26) combinations of aperture pattern evaluated in this study are shown in Fig. 2 (a-e). We only show the $\boldsymbol{p_1}$ fields in the figure since $\boldsymbol{p_1}$ and $\boldsymbol{p_1^*}$ are complementary. The numbers in parenthesis at the top of the figure represents the number of on/off interfaces and overlap in terms of elements of the complementary apertures, respectively. The acoustic field produced by AM is shown in Fig. 2 (e). We note that the acoustic field is indeed more uniform across the whole aperture when the complimentary apertures have more overlap with each other [(a), (b) vs (c), (d), (e)]. The CEUS image of the flow phantom and the ROIs for calculating CTR of the image are shown in Fig. 2 (f), where the ROIs for contrast signals are shown in red and ROIs for tissue signal are shown in yellow. The CTR of the 26 aperture patterns is shown in Fig. 2 (g). We observe that when the number of on/off interfaces remains the same, the sensitivity of detecting contrast signal increases when the aperture patterns for $\boldsymbol{p_1}$ and $\boldsymbol{p_1^*}$ are more overlapped with each other. Fig. 2 (h) shows that the intensity of the contrast signal improved by ~5 dB as the overlap increased while on/off interfaces remain constant (15 in this example). The OAM aperture pattern that has the highest CTR is the one shown in Fig. 2 (d). Although conventional AM and OAM have similar overlap of complementary apertures (63 and 62, respectively), OAM has half the number of on/off interfaces, which indicates lower cross talk and thus better tissue signal suppression, compared to AM.

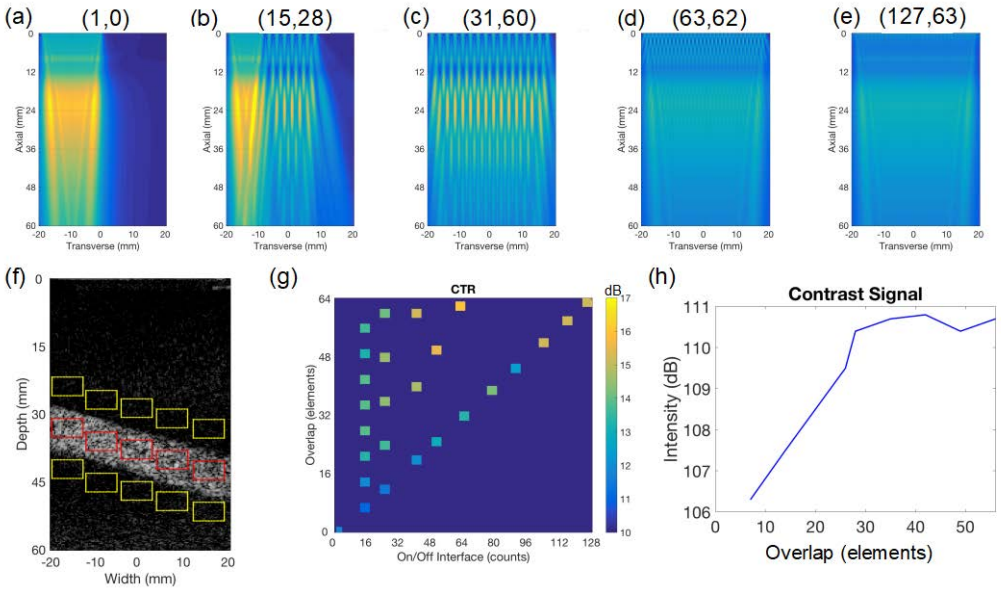

Figure 2: (a-e) The beams produced by 5 (out of the 26) apertures. (f) The CEUS image of the flow phantom and the ROIs for calculating CTR. ROIs for contrast signal are red and tissue signal are yellow. (g) CTR of the 26 apertures evaluated in this study. (h) The intensity of the contrast signal produced by 8 combinations of aperture patterns with different degree of overlap of the aperture patterns but same number of on/off interfaces.

In Fig. 3 we compared the CTR between AM and OAM when multiple compounding angles were used for imaging the flow phantom. Figure 3(a) shows the AM and (b) the OAM image produced with 15 compounded angles. OAM has better tissue signal suppression [Fig. 3 (a-b)] and higher CTR compared to AM [Fig. 3 (c)]. By increasing the number of compound angles the CTR for the OAM image increased more than that with AM.

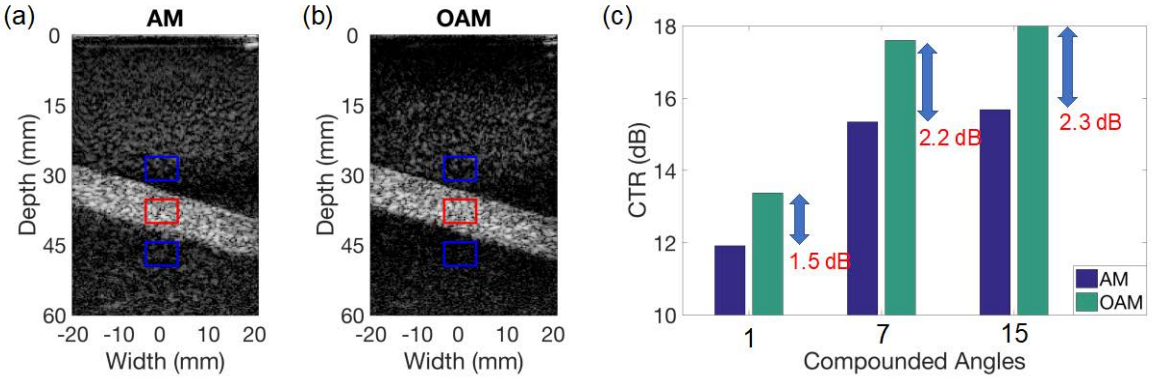

Figure 3: CEUS images produced by (a) AM and (b) OAM with 15 compounded angles. (c) CTR of AM and OAM images when using different compound angles.

MIP Images of a pig liver were produced by (a) AM and (b) OAM with 7 compounded angles are shown in Fig. 4. With the OAM, we observe that fine vasculature structures [pointed by red arrows in Fig. 4 (b)] are better defined than with AM. The TICs in Fig. 4 (c) show that OAM has better tissue signal suppression and thus better image contrast compared to AM.

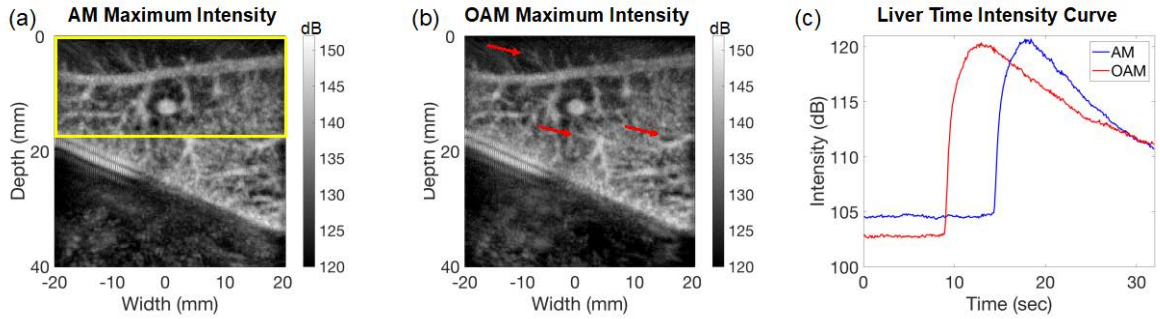

Figure 4: Maximum intensity projection images of a pig liver produced with (a) AM and (b) OAM with 7 compounded angles. The time intensity curves acquired with AM and OAM are shown in (c) and the ROI for tracking the time intensity curve is shown in yellow in (a).

Conclusions

We evaluated the effect of aperture overlap and cross talk produced by the on/off interfaces of complimentary apertures used for AM in order to find an optimal aperture design. We used CTR from flow phantom and machine perfused pig liver images as the evaluation metric. The aperture that uses alternating groups of 2 elements (2 on, 2 off) had the highest CTR.

References

[1] C. Errico *et al.*, "Ultrafast ultrasound localization microscopy for deep super-resolution vascular imaging," *Nature*, vol. 527, no. 7579, pp. 499-502, 2015.

[2] C. Tremblay-Darveau, "Contrast-enhanced Doppler ultrasound imaging using plane waves," 2016.

[3] M. A. Averkiou, M. F. Bruce, J. E. Powers, P. S. Sheeran, and P. N. Burns, "Imaging Methods for Ultrasound Contrast Agents," *Ultrasound in Medicine & Biology*, 2019.

Measuring resolution in Ultrasound Localization Microscopy

Vincent. Hingot[1], Arthur. Chavignon[1], Baptiste. Heiles[2], Olivier. Couture[1]

[1]Laboratoire d'Imagerie Biomédicale, Sorbonne University, Paris, France
[2]Maresca Lab, T.U Delft, Netherlands
Corresponding author: vincent.hingot@upmc.fr

Introduction

The resolution is the ability of an imaging system to distinguish small and close features. Ultrasound Localization Microscopy (ULM) relies on the detection and localization of numerous individual and punctual sources to map the vasculature [1]. Conventional definitions of the resolution based on the point spread function do not apply. Several methods have been proposed to estimate the spatial resolution in ULM but with strong limits. In particular, the localization precision is a good indicator of the maximum resolution that can be achieved with a given imaging system, however it does not acount for acquisition times which has been showed to be equally important [2]. Analysis of individual vessels or feature can be performed directly on in vivo data but are heavily dependant on the operator and on the feature selection step.

In this study, we introduce a practical method for the measure of the resolution based on the Fourier Ring Correlation (FRC) [3]. It computes the correlation between two Fourier transforms of any two sub images made from the original dataset on iso spatial frequency rings. Moreover, we propose a simple model for the spatial and temporal resolution tradeoff based on the Nyquist theorem for sampling [4]. It is based on the localization precision δ_{loc} and on a typical length we call the Nyquist dimension δ_{Nyq}. The resolution is then estimated as the quadratic sum of these two lengths.

Methods

ULM was performed with a 15 MHz probe in five different datasets acquired over different rodents organs and with different imaging conditions detailed in Table 1. MB were separated from tissues using high pass spatio-temporal filters. MB were localized using a radial symmetry based algorithm and images were represented on a 5 µm x 5 µm grid. The FRC was calculated with (1) by randomly separating the original list of detections (Figure 1.a) to form two sub images (Figure 1.b). Then the correlation of the two spatial Fourier transforms F_1 & F_2 was calculated along iso frequency rings r (Figure 1.c) to produce the FRC curve (Figure 1.d). Resolution is estimated using various threshold methods that will be discussed.

$$\mathrm{FRC(r)} = \frac{\sum_{\mathrm{ring}} F_1(r)F_2(r)^*}{\sqrt{\sum_{\mathrm{ring}}|F_1(r)|^2 \sum_{\mathrm{ring}}|F_2(r)|^2}} \qquad (1)$$

The localization precision was estimated on individual tracks as the mean distance between all detected points and a virtual center line. The complete distribution of these distances was computed and the localization precision was definded as the mean of the resulting distribution. The Nyquist dimension was calculated using (2) from the measure of the total number of detected MB which is representative of the density ρ of microbubble (MB) adjusted for the dimension κ. The resolution R can then de estimated in (3) as the quadratic sum of these two lengths.

$$\delta_{\mathrm{Nyq}} = \frac{2}{\rho^{1/\kappa}} \quad (2) \quad \& \quad \mathrm{R} = \sqrt{\delta_{\mathrm{loc}}^2 + \delta_{\mathrm{Nyq}}^2} \quad (3)$$

Results

For all the datasets, the FRC resolution, the Nyquist dimension and the localization precision were all measured and reported in Table 1. Data are considered well sampled when the Nyquist dimension is smaller than the localization precision. In the two rat's brain, data are correctly sampled and the FRC resolution is in good accordance with the localization precision. For the tumor however, the Nyquist dimension is larger, indicating that the data may be undersampled. There, the FRC resolution is higher than the localization precision. For the two kidney datasets, the resolution is significatively higher than both the localization

precision and the Nyquist dimension, showing that motions can also have a large impact on the resolution, independantly of a precise localization and adequate sampling. Still, the FRC does acount for the actual resolution of the image, and is able to detect an improvement in resolution due to motion compensation.

Conclusions

This FRC curve provides a method to measure the resolution directly on the data, and independantly of the imaging systems and operator. In a situation where motions do not impact image reconstruction, the resolution is well acounted for by two characteristic length, the localization precisino and the Nyquist dimension which is representative of the good spatial sampling of the data. This expression synthetises the fundamental tradeoff in ULM between the spatial and temporal resolutions.

Table 1. Resolutions measures for the five tested datasets

Dataset	Injection	Number of Frames	Acquisition Time	Nyquist Dimension	Localization Precision	FRC resolution
Rat BrainInfusion	80 µL/min	192 000	240 s	5 µm	11 µm	11 µm
Rat BrainBolus	200 µL bolus	168 000	210 s	8 µm	13 µm	14 µm
Mouse Tumor	100 µL bolus	30 000	150 s	25 µm	15 µm	32 µm
Rat Kidney	200 µL bolus	192 000	240 s	9 µm	13 µm	36 µm
Rat KidneyMoCo	200 µL bolus	192 000	240 s	9 µm	13 µm	31 µm

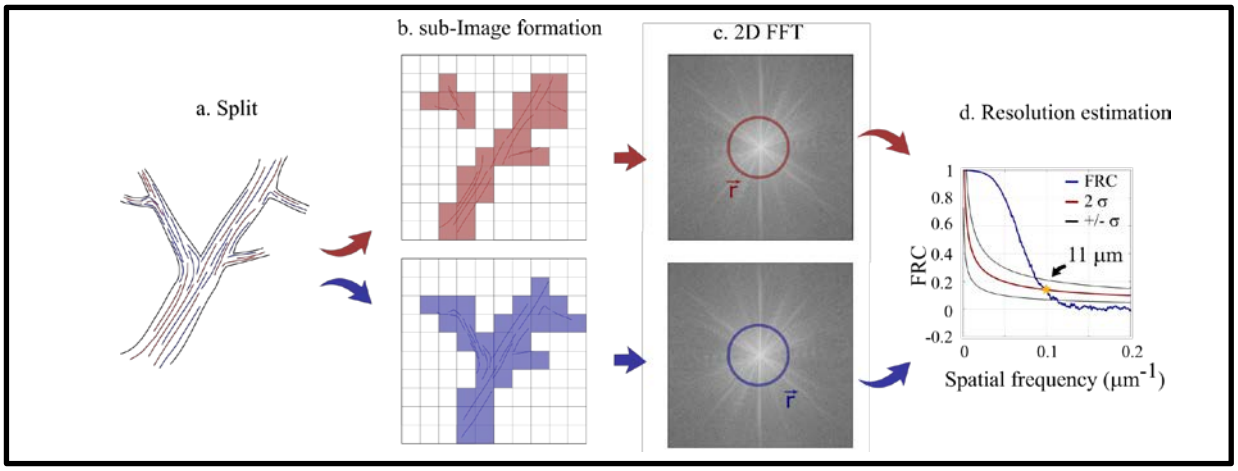

Figure 1. FRC to estimate spatial resolution in ULM. a. The list of detection is split in two by separating odd and even numbered localizations. b. From these two sets of localization are formed two sub images. c. From these two images are calculated the two spatial Fourier transforms. d. Finally, the FRC curve is calculated along iso frequency rings and the resolution is measured.

References

[1]. O. Couture, et al, « Ultrasound Localization Microscopy and Super-Resolution: A State of the Art », *IEEE Trans. Ultrason. Ferroelectr. Freq. Control*, vol. 65, nº 8, p. 1304-1320, août 2018

[2]. V. Hingot et al, « Microvascular flow dictates the compromise between spatial resolution and acquisition time in Ultrasound Localization Microscopy », *Sci. Rep.*, vol. 9, nº 1, p. 2456, déc. 2019

[3]. R. P. J. Nieuwenhuizen *et al.*, « Measuring image resolution in optical nanoscopy », *Nat. Methods*, vol. 10, nº 6, Art. nº 6, juin 2013

[4]. A. Oddone, et al, « Super-resolution imaging with stochastic single-molecule localization: Concepts, technical developments, and biological applications », *Microsc. Res. Tech.*, vol. 77, nº 7, p. 502-509, 2014

In Vivo Volumetric Vasculature Imaging Using a Sparse Spiral Array

Luxi Wei[1], Geraldi Wahyulaksana[1], Bram Meijlink[1], Alessandro Ramalli[2], Emile Noothout[3], Martin Verweij[3], Enrico Boni[2], Klazina Kooiman[1], Antonius F.W. van der Steen[1], Piero Tortoli[2], Nico de Jong[1,3], Hendrik J. Vos[1,3]

[1]Thoraxcenter, Dept Biomedical Engineering, Erasmus University Medical Center Rotterdam, Rotterdam, the Netherlands
[2]MSD Lab, Department of Information Engineering, University of Florence, Florence, Italy
[3]Acoustical Wavefield Imaging, Faculty of Applied Sciences, Delft University of Technology, Delft, the Netherlands
Corresponding author: l.wei@erasmusmc.nl

Introduction

Volumetric ultrasound imaging of microbubbles achieves 3-dimensional (3-D) visualization of the vasculature. We have previously manufactured a prototype piezoelectric sparse array based on a density-tapered spiral layout [1], [2]. This probe has 256 elements that can be individually and simultaneously connected to an open scanner such as the Vantage 256 (Verasonics, Kirkland, WA, USA) or the ULA-OP 256 [3]. This approach enables high flexibility in the design of transmission sequences, making possible different experiments [4]–[6]. Here, we demonstrate that the combination of a 2-dimensional (2-D) high resolution mode for real time guidance with a 3-D high-frame-rate mode for acquisition, together with the use of the spatial coherence (SC) beamformer, allows the 3-D visualization of small structures such as the blood vessels of the chicken embryo chorioallantoic membrane *in vivo*.

Methods

Fertilized chicken eggs were incubated for 5 days, taken out of the shell [7], and placed in a plastic weighboat. The chicken embryo naturally shifts to the top of the yolk in this position. Approximately 4 μL of custom-made microbubbles (F-type, [8]) were injected via a glass syringe [7] into the venous system of the chicken embryo. The weighboat was then placed inside a beaker of 37°C PBS solution. The sparse array (5 MHz center frequency) was placed on top of the beaker at around 3 cm distance from the chicken embryo and in contact with the PBS solution (Fig. 1 a). The array was connected to a Verasonics Vantage 256 system, which was used for data acquisition. During the experiment, 2-D images were acquired, reconstructed, and displayed in real-time to position the probe on top of the chicken embryo. Images were obtained by scanning 100 lines by focused beams (f-number = 3) with 0.3° spacing onto the xz-plane. Image reconstruction was performed using the Verasonics delay-and-sum beamformer. The final frame rate was 10 Hz. After the adjustment of the probe position, a high-frame-rate sequence of volumetric frames were acquired. For each angular compounded frame, 5 steered diverging waves with 30° opening angles were transmitted at 8 kHz pulse repetition, using the central 120 array elements. The steering angles were either 0° or 5° in the azimuth and elevation directions. On reception, all 256 elements were used. This pattern was repeated at 1 kHz frame rate for 3.9 seconds. For the high frame rate acquisitions, radio-frequency (RF) data were saved to be Matlab processed off-line, independently for each angle. The raw RF echo-data were first filtered using singular value decomposition (SVD) and by removing a manually selected number of lower ranks to attenuate stationary signal from the egg yolk surface, blood vessels, and egg white. The filtered data was then beamformed using the SC beamformer. For each voxel location, it calculates the averaged correlation between signal received by all elements. Each volume was reconstructed by calcuating the correlation value for all voxels. This was independently performed for all transmission angles, then averaged to form an angular compounded frame. All frames were averaged to reveal the chorioallantoic membrane of the chicken embryo. The time-averaged SC volume was then normalized by removing all negative correlations, normalizing the maximum to 1, and log compressed for display.

Results

Fig. 1 shows the results from the chicken embryo experiment. In a sample frame obtained during 2-D focused-beam live mode (Fig. 1 b), the chicken embryo (yellow circle) can be seen on top of the egg yolk surface (red dashed line). The egg white is also visible in this example (turquoise dashed line). Focused-beam transmissions yield images with less clutter artefacts and thus are useful for locating the region of interest. However, since the field of view needs to be scanned line by line, focused-beam imaging cannot achieve high volume rates. Fig. 1 c-g are the results of a high-volume-rate experiment. Fig. 1 c and d are photographs taken from the top (c) and the side (d) of the chicken embryo. The chicken embryo and the chorioallantoic membrane blood vessels are distributed on the surface of the yolk, creating a dome-like shape. After averaging all beamformed frames, the chicken embryo heart (white arrow) and the chorioallantoic membrane blood vessels can be seen on the maximum intensity projections from the top (Fig. 1 e) and the sides (Fig. 1 f, g). Some chorioallantoic membrane vessels can be identified by comparing (c) and (e), whose perspectives are the most similar (matching arrowheads). A common vessel (green arrowhead) is selected on both the photographs and the ultrasound image, where the diameter is estimated to be 350 µm from the photograph, indicating the volumetric ultrasound image is able to discern vessels of this size.

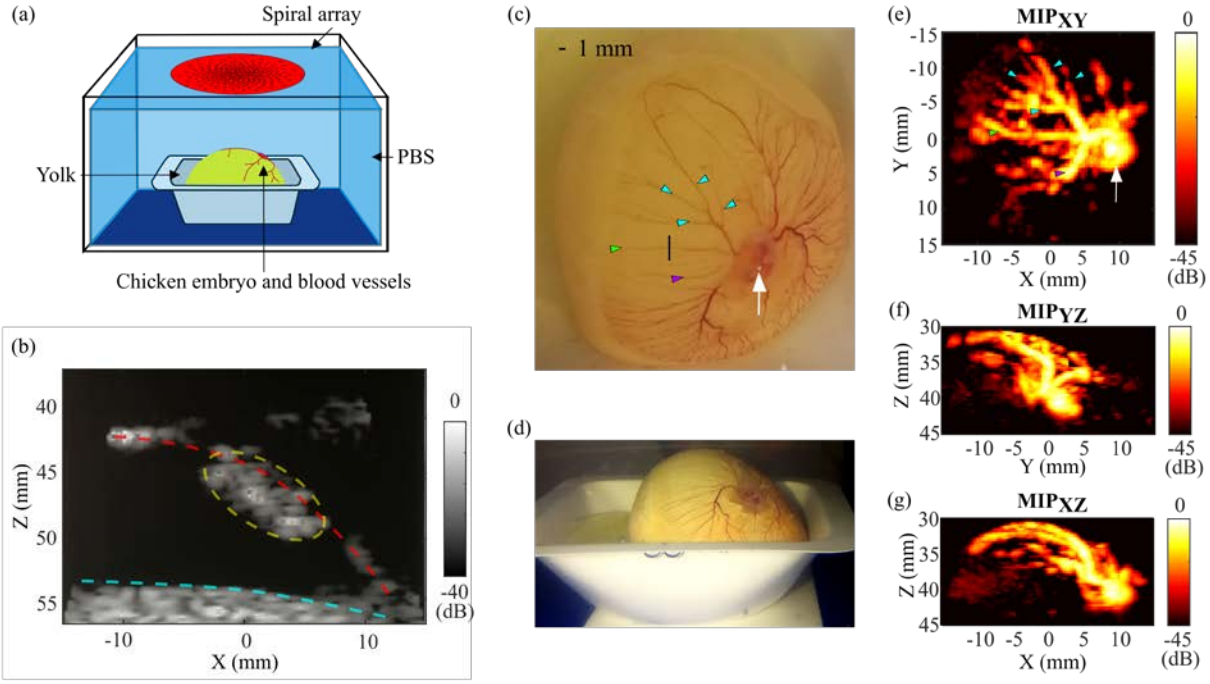

Figure 1. (a) Schematic of the setup. The chicken embryo and egg yolk are submerged in a tank of PBS solution, with the sparse spiral array placed directly on top. (b) Sample still frame obtained during 2-D focused-beam live mode to position the spiral array. The chicken embryo (yellow dashed), the top of the egg yolk (red dashed), and the egg white (turquoise dashed) can be seen in this image. In this example the egg is placed at a deeper depth compared to the high frame rate experiment. (c-d) Photographs of the chicken embryo with the yolk submerged in a PBS solution as seen from (c) the top and (d) the side. The vessel diameter is estimated across the black line. (e-g) Maximum intensity projections (MIP) of the ultrasound volumetric frame, beamformed using the SC beamformer. By comparing (c) the top view of the photograph and (e) the maximum intensity projection of the ultrasound image in depth, the heart (white arrow) and some branches can be identified and matched (arrowheads).

Conclusions

We have demonstrated volumetric imaging of microbubbles in a chicken embryo vascular system using a prototype piezoelectric sparse spiral array. In this study, a focused-beam real-time mode and a divergent-beam high-frame-rate mode were combined to achieve the visualization of the chicken embryo chorioallantoic membrane vasculature *in vivo*. The sparse spiral array offers flexibility in transmission modes, enabling the ability to combine imaging modes for robust experimental design.

Acknowledgments

This work is part of the research programme "Vernieuwingsimpuls – Vidi 2017" with project number QUANTO-16572, which is (partly) financed by the Dutch Research Council (NWO).

References

[1] A. Ramalli, E. Boni, A. S. Savoia, and P. Tortoli, "Density-tapered spiral arrays for ultrasound 3-D imaging," *IEEE Trans. Ultrason. Ferroelectr. Freq. Control*, vol. 62, no. 8, pp. 1580–1588, Aug. 2015.

[2] H. J. Vos *et al.*, "Sparse volumetric PZT array with density tapering," in *2018 IEEE International Ultrasonics Symposium (IUS)*, 2018, pp. 1–4.

[3] E. Boni *et al.*, "ULA-OP 256: a 256-channel open scanner for development and real-time implementation of new ultrasound methods," *IEEE Trans. Ultrason. Ferroelectr. Freq. Control*, vol. 63, no. 10, pp. 1488–1495, Oct. 2016.

[4] A. Ramalli *et al.*, "High-frame-rate tri-plane echocardiography with spiral arrays: From simulation to real-time implementation," *IEEE Trans. Ultrason. Ferroelectr. Freq. Control*, vol. 67, no. 1, pp. 57–69, Jan. 2020.

[5] A. Ramalli *et al.*, "Real-time system for 3D Doppler spectral analysis with sparse arrays," *presented at 2020 IEEE International Ultrasonics Symposium*.

[6] E. Roux, F. Varray, L. Petrusca, C. Cachard, P. Tortoli, and H. Liebgott, "Experimental 3-D ultrasound imaging with 2-D sparse arrays using focused and diverging waves," *Sci. Rep.*, vol. 8, no. 1, p. 9108, Dec. 2018.

[7] T. Faez, I. Skachkov, M. Versluis, K. Kooiman, and N. de Jong, "In vivo characterization of ultrasound contrast agents: microbubble spectroscopy in a chicken embryo," *Ultrasound Med. Biol.*, vol. 38, no. 9, pp. 1608–1617, Sep. 2012.

[8] V. Daeichin *et al.*, "Microbubble composition and preparation for high-frequency contrast-enhanced ultrasound imaging: in vitro and in vivo evaluation," *IEEE Trans. Ultrason. Ferroelectr. Freq. Control*, vol. 64, no. 3, pp. 555–567, Mar. 2017.

[9] N. Bottenus, B. C. Byram, J. J. Dahl, and G. E. Trahey, "Synthetic aperture focusing for short-lag spatial coherence imaging," *IEEE Trans. Ultrason. Ferroelectr. Freq. Control*, vol. 60, no. 9, pp. 1816–1826, Sep. 2013.

Passive detection and super-localization of acoustic signatures from PVA-PFB nanodroplets vaporized by protons

Sophie V. Heymans[1,2], Gonzalo Collado[2], Marta Rovituso[3], Bram Carlier[4,5], Yosra Toumia[6], Gaio Paradossi[6], Hendrik J. Vos[2,7], Martin Verwei[2,7], Nico de Jong[2,7], Jan D'hooge[8], Verya Daeichin[7], Koen Van Den Abeele[1]

[1]Department of Physics, KU Leuven Campus Kulak, Kortrijk, Belgium
[2]Department of Biomedical Engineering, Erasmus Medical Center, Rotterdam, The Netherlands
[3]Holland Proton Therapy Center, Delft, The Netherlands
[4]Molecular Small Animal Imaging Center, KU Leuven, Leuven, Belgium
[5]Department of Oncology, KU Leuven, Leuven, Belgium
[6]Department of Chemical Sciences and Technology, University of Rome Tor Vergata, Rome, Italy
[7]Department of Medical Imaging, TU Delft, Delft, The Netherlands
[8]Department of Cardiovascular Sciences, KU Leuven, Leuven, Belgium
Corresponding author: koen.vandenabeele@kuleuven.be

Introduction

Recently, PVA-shelled nanodroplets with a perfluorobutane core (PVA-PFB) have been introduced as a potential candidate for *in vivo* range verification during proton therapy. While proof-of-concept studies showed radiation-induced nanodroplet vaporization on ultrasound images acquired post-irradiation [1,2], real-time ultrasound imaging would be required to accurately quantify phase changes in physiological conditions, i.e. in the presence of flow. Once vaporized by protons, the resulting microbubbles might persist and circulate in the vasculature, stay fixed in the extravascular space, or dissolve. High frame rate imaging might not allow to distinguish existing microbubbles entering or leaving the ultrasound probe field of view from proton-induced vaporization events, hindering proton range verification and dosimetry. Therefore, taking advantage of the specific acoustic signatures emitted by vaporizing nanodroplets [3], we adapted the time difference of arrival (TDOA) model [4] for use on passively-recorded sparse vaporization events resulting from interactions between single nanodroplets and ionizing radiation. This allowed to specifically localize vaporization events, and unveiled new characteristics of acoustic signatures emitted by polymeric contrast agents vaporized by a radiation source.

Methods

Perfluorobutane nanodroplets encapsulated in polyvinyl alcohol (PVA-PFB) were prepared according to [2] and dispersed in carbomer-based phantoms heated to 37°C or 50°C. The phantoms were fixed in a temperature-controlled water tank and irradiated by a monoenergetic pencil proton beam (154 MeV) at the Holland Proton Therapy Center. An ultrasound probe (P4-2v, -6dB bandwidth: 1.71-3.73 MHz, 64 elements, Verasonics) was fixed on the water tank side facing the phantom, and driven by a Verasonics Vantage system to passively record nanodroplet vaporization signals quasi-continuously (94% of the time) during proton irradiation (Fig. 1a).

In order to localize vaporization signals, the ultrasound radiofrequency data was first filtered to enhance the signal-to-noise ratio. Then, vaporization signals were detected by finding peaks present for at least 50% of the channels. Cross-correlation of all channels allowed to compute the differences in one-way arrival time for each of the 64 elements of the array transducer. Those time differences were fit to a one-way time of flight equation to obtain the axial and lateral coordinates of the vaporization events. Finally, the acoustic signatures of single PVA-PFB nanodroplet vaporization events were obtained by delaying and coherently summing the channel data.

Results

The positions of vaporization events localized from passive ultrasound recordings were found to be in relatively good agreement with the contrast observed on post-irradiation B-mode images (Fig. 1b). For axial distances limited to a few centimeters, the lateral resolution of passive maps is expected to outperform diffraction-limited imaging, potentially improving estimates of the proton range. Due to low signal-to-noise ratio, only 50% of the detected vaporization events could be localized accurately. The vaporization event positions were binned in the axial ultrasound direction and the obtained vaporization profiles were compared to the proton range (Fig. 1c). At 37°C, vaporization counts dropped in front of the Bragg peak, in agreement with previous findings indicating that nanodroplets were only sensitive to secondary reaction products at low degrees of superheat, and at 50°C the vaporization peak was found to coincide with the proton range, as nanodroplets were also vaporized by primary protons [2].

Interestingly, we observed that the individual nanodroplets acoustic signature differed at 37°C and 50°C. As shown in Fig. 1d, the majority of the vaporization events have a center frequency below 0.5 MHz at 50°C, while they are evenly distributed at 37°C. A closer examination of the vaporization signals in the time and frequency domain revealed that at 37°C, the vaporization signals are characterized by an exponentially decaying sinusoid as previously observed in literature for lipidic shells [3]. At 50°C, however, most vaporization signals seem to have two sections: an initial broadband expansion followed by a long-tail oscillation at a lower frequency. We hypothesize that the degree of superheat might play a role in the vaporization dynamics of polymeric-shelled nanodroplets, as higher temperatures may induce more violent vaporization events, potentially leading to shell rupture [5].

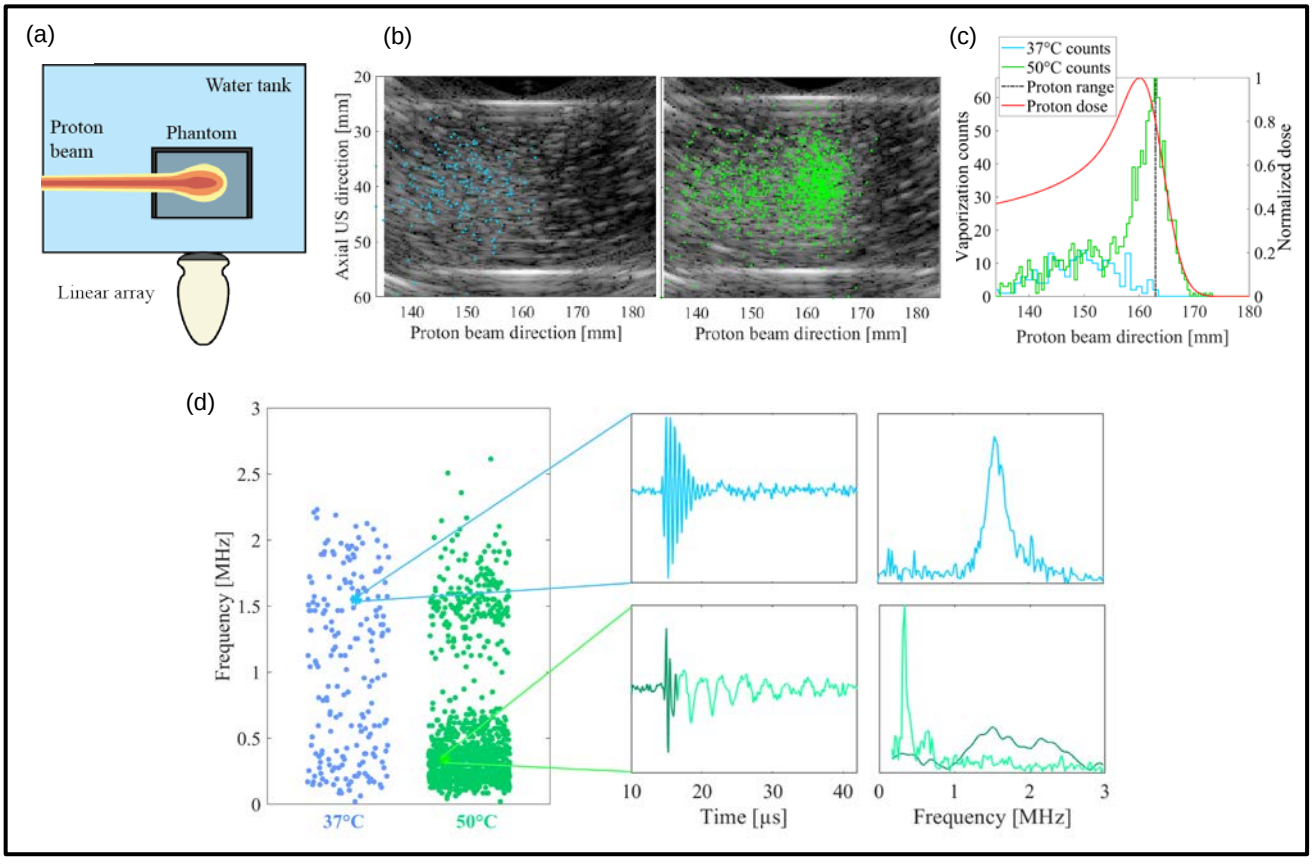

Figure 1. (a) Experimental setup used for passive ultrasound imaging during proton irradiation. (b) Localized vaporization events overlaid on post-irradiation B-mode images for proton irradiations at 37°C (left) and 50°C (right). (c) Corresponding vaporization profiles compared to the proton range and depth-dose deposition profile. (d) Distribution of the center frequency of the detected vaporization events at both temperatures. Time (left) and frequency (right) domain characteristics of typical vaporization signals are shown.

Conclusions

In this study, we implemented a passive recording method to specifically localize interactions between individual PVA-PFB nanodroplets and ionizing radiation with an ultrasound array. While the detection efficiency was significantly impacted by the signal-to-noise ratio, vaporization signals could be localized and related to the proton range with an accuracy superior to B-mode imaging. The temporal and spectral characteristics of individual vaporization signals revealed a temperature dependence, which suggests that the vaporization of polymeric nanodroplets might follow a complex mechanism.

References

[1]. Carlier B, Heymans SV, Nooijens S, et al., Proton range verification with ultrasound imaging using injectable radiation sensitive nanodroplets: a feasibility study, Physics in Medicine and Biology, 65: 065013, 2020.

[2]. Heymans SV, Carlier B, Toumia Y, et al., Modulating ultrasound contrast generation from injectable nanodroplets for proton range verification by varying the degree of superheat, submitted to Medical Physics.

[3]. Sheeran PS, Matsunaga TO, Dayton PA et al., Phase change events of volatile liquid perfluorocarbon contrast agents produce unique acoustic signatures, Physics in Medicine and Biology, 59(2): 379-401, 2014.

[4]. Gyöngy M, Arora M, Noble JA, Coussios CC, Use of passive arrays for characterization and mapping of cavitation activity during HIFU exposure, 2008 IEEE International Ultrasonics Symposium Proceedings, Beijing, 2008.

[5]. Kothapalli SVV, Daeichin V, Mastik F et al., Unique pumping-out fracturing mechanism of a polymer-shelled contrast agent: an acoustic characterization and optical visualization, IEEE Transactions on Ultrasonics, Ferroelectrics, and Frequency Control, 62(3):451-461, 2015.

Motion compensation for high-frame-rate contrast enhanced ultrasound imaging: a simulation study

João M. Ribeiro[1], Matthieu Toulemonde[1], Meng-Xing Tang[1]

[1]Department of Bioengineering, Imperial College London, London, UK
Corresponding authors: joao.ribeiro19@imperial.ac.uk, m.toulemonde@imperial.ac.uk, mengxing.tang@imperial.ac.uk

Introduction

High frame rate (HFR) imaging using unfocused diverging waves transmission and coherent compounding at multiple transmit angles has demonstrated its benefits in many ultrasound imaging fields, such as shear wave elastography [1], echocardiography in both contrast and non-contrast mode [2–5], blood flow dynamics [6, 7], tissue Doppler imaging (TDI) [4, 8] and velocity vector imaging [9]. However, because it relies on coherent summation of transmissions at different angles, it suffers from motion artefacts anytime there is motion between transmissions [4, 10]. If combined with coded transmissions such as Pulse Inversion (PI) or Amplitude Modulation (AM), then incoherence is aggravated, as coherence between pulses is necessary to eliminate linear tissue signal [5, 10]. Several motion compensation schemes have been proposed to eliminate motion artefacts, such as a polar domain Doppler autocorrelator between transmit angles combined with a triangular transmit sequence, named MoCo [4], a two-stage motion estimation using cross-correlation [11], registration-based methods adapted from magnetic resonance imaging [10], a dual aperture motion compensation (DAMoCo) scheme for sidelobe suppression [12], among others.

In this study, we investigate the MoCo approach for contrast-enhanced imaging with coded transmission (both PI and AM) in the Cartesian domain, as well as the effect of the frequency of the transmitted pulse in Doppler aliasing using simulation data. We also propose an adapted MoCo approach, specific for contrast imaging, which accounts for and compensates motion between positive and negative pulses in PI, and between the pulses of different amplitudes in AM.

Methods

A phantom of a rotating disc with anechoic cysts was simulated using MATLAB for posterior use as a sound-speed map in k-Wave ultrasound simulations. A rotating disc phantom was chosen due to having a continuum of axial velocities increasing in the lateral direction. Moreover, rotating disc phantoms have been evaluated in similar motion estimation and compensation studies [4, 9]. k-Wave was the ultrasound simulation software of choice due to its ability to simulate nonlinear propagation and generate harmonic signals [13]. k-Wave simulations were performed on a 2048×2048 2D grid with a simulated P4-1 phased-array transducer transmitting unfocused diverging waves. A nonlinear propagation map coinciding with the disc sound speed map was used to generate harmonics. Several simulations were performed: 12-angle Pulse Inversion and Amplitude Modulation, for both the moving and static disc. Each of the previous simulations was repeated at different frequencies. For AM, the frequencies of 1.25 MHz, 1.75 MHz and 2.5 MHz were used. For PI, only 1.25 MHz and 1.75 MHz were used, since the 2nd harmonic of the 2.5 MHz transmit frequency lies outside the transducer bandwidth. For each tilt angle, two/three consecutive pulses were transmitted to form PI/AM images, respectively. Each dataset was acquired using a triangular angle transmission sequence to suppress sidelobes in accordance with the MoCo approach by Porée et al. [4]. A summary of the phantom parameters and the acquistion parameters are displayed in Tables 1 and 2, respectively.

After simulation, each receive angle for each transmission was beamformed in a Cartesian grid. AM acquisitions were decimated by 2 in fast-time during beamforming since the second harmonic frequencies are not necessary for AM. For PI data, a 5th order Butterworth second-harmonic high-pass filter was applied in case of non-perfect cancellation of linear signal, before IQ demodulation centred at the 2nd harmonic

frequency to acquire complex envelope images. AM beamformed images were IQ demodulated at the fundamental frequency to acquire complex envelope images.

Table 1. Rotating disc phantom parameters.

Parameter	Value	Parameter	Value
Diameter	5 cm	Density	1000 kg m^{-3}
Angular velocity	12 rad s^{-1}	Attenuation coefficient	0.75 dB cm^{-1} MHz^{-2}
Speed of sound	1540 ± 15.4 m s^{-1}	B/A [14]	300

Table 2. Simulation acquisition parameters.

Parameter	Value	Parameter	Value
Medium size	10 cm × 10 cm	Frequency (cycles)	1.25 / 1.75/ 2.5 MHz (4)
Number of angles	12 (×2 PI/ ×3 AM)	Sampling frequency	18.2 MHz
Angle range	30°	PRF	7700 Hz
Angle step	3°	Frame rate	320 / 213 Hz (PI/AM)

For regular MoCo, the positive and negative pulses of the PI acquisition, and the three pulses of the AM acquisition were summed before motion compensation between transmit angles.

For adapted MoCo, motion was compensated first in coded transmission, and only then was motion compensated between transmit angles. Before motion estimation, the PI negative pulses were inverted, and the half-amplitude pulses of AM were doubled for correct estimation. The phase of the lag-one Doppler autocorrelator of the two/three pulses of PI/AM, respectively, was used to compensate motion according to equation 5 in [4]. The pulses whose sign/amplitude were changed before motion estimation were reverted back to their original sign/amplitude. For PI, the two pulses were summed and for AM the first and third pulses were summed while the second was subtracted to eliminate linear tissue signal, generating a motion-compensated IQ sample for each tilt angle. Regular MoCo was then applied between each of the tilt angles afterwards for further correction.

Contrast-to-Noise Ratio (CNR) was measured between the anechoic cysts and the disc as a metric of removal of motion artefacts in motion-degraded images according to equation 1 and figure 1. Each cyst was compared with each region of the disc and the mean of all of them was used for the CNR.

A lateral evaluation of intensity was performed for each acquisition since motion-degraded images in coherent compounding are known to lose intensity in regions where axial velocities are large and axial velocity increases in the lateral directions in a rotating disc. The lateral evaluation consisted in computing the mean across each scan-line, considering only the points of the scan-line that belong to the disc. A plot of mean intensity in function of the lateral direction was obtained for each acquisition with this procedure.

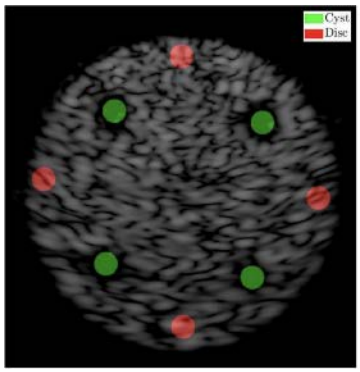

$$CNR\ (dB) = 20\log_{10}\frac{|\mu_{cyst} - \mu_{disc}|}{\sqrt{\sigma_{cyst}^2 + \sigma_{disc}^2}} \qquad (1)$$

Figure 1: The metrics in equation 1 were computed according to the labelled regions in the figure. The green regions correspond to the cysts and the red regions correspond to the disc. In equation 1, μ represents the mean of all pixels in the region and σ^2 represents the variance of all pixels in the same region.

Results

Figure 2 shows the results of motion compensation at 1.25 MHz (rows 1 and 2) and 1.75 MHz (rows 3 and 4), respectively, in both PI and AM acquisitions and at 2.5 MHz for the AM acquisition only (row 5). All rows contain four images. From left to right, these represent: the static phantom; the moving phantom compensated with adapted MoCo; the moving phantom compensated with MoCo; Moving phantom uncorrected. As frequency increases, the more motion artefacts can be observed in figure 2, as highlighted by the white arrows. These artefacts arise from Doppler aliasing since the maximum detectable Doppler velocity is inversely proportional to the transmit frequency according to the classical Doppler velocity equation [8].

Apart from Doppler aliasing artefacts, which are intrinsic to Doppler autocorrelators, the MoCo approach proposed by J. Porée works when applied in the Cartesian domain. Beamforming in the Cartesian domain and applying motion compensation directly is more advantageous than beamforming in the polar domain if the purpose is real-time imaging, as the overhead for polar domain beamforming is higher because extra steps are necessary before reconstruction.

Figure 3 compares CNR measures between both contrast methods, MoCo and Adapted MoCo at all frequencies. As frequency increases, the lower the CNR across all acquisitions. Not only is the CNR of the static acquisitions lower, but the recovered contrast by using MoCo also decreases as the frequency increases, again, due to Doppler aliasing. Intensity recovery using Adapted MoCo is around 0.3-0.4 dB in the first 3 acquisitions but becomes higher as the level of aliasing increases in the latter two. PI acquisitions are more degraded as frequency increases. This can be explained by the frequencies at which the acquisitions are demodulated. Because PI images are 2nd harmonic, these must be demodulated at that frequency before MoCo, while AM are demodulated at the fundamental frequency. The demodulation frequencies are the frequency components that are compensated during MoCo. For each acquisition, PI images are compensated at double the frequency than AM. The maximum detectable Doppler velocity decreases with the demodulation frequency, which explains the faster degradation with frequency of PI, since the frequency jumps are effectively double.

Figure 4 shows the lateral evaluation of all images. We again see the trend of motion compensation becoming more challenging as frequency increases. Lateral degradation from motion, seen by the differences between the static plots and the MoCo plots, can be seen from 1.75 MHz onwards. Adapted MoCo, when compared with regular MoCo, results in improvements of up to 4.7 dB in the regions of higher velocities in PI data. In AM data, the improvements between adapted MoCo and regular MoCo are negligible at 1.25 MHz, but leads to higher intensity recovery as the frequency increases, leading to up to 1.8 dB increases at 1.75 MHz and up to 2.5 dB at 2.5 MHz. One important aspect to consider is the effect of the number of PI/AM pulses in the effective *PRF*, and consequently, the level of Doppler aliasing. The AM acquisition at 2.5 MHz (Figure 4, top right) and the PI acquisition at 1.25 MHz (Figure 4, bottom left) are effectively corrected at the same frequency since the 2nd harmonic of 1.25 MHz is precisely 2.5 MHz. Nonetheless, the level of aliasing (highlighted by the loss of intensity in the lateral directions) is much higher for AM at 2.5 MHz than for PI at 1.25 MHz. For PI, two images are summed before MoCo, so the effective *PRF* is half the original, and for AM, three images are summed before MoCo, so the effective *PRF* is a third the original. This means that whenever *n* pulses are to be summed before MoCo, the maximum detectable velocity becomes:

$$v_{max} = \frac{PRFc}{4n\pi f_{dem}} \tag{2}$$

Where c represents sound velocity, *PRF* the pulse repetition frequency and f_{dem} the demodulation frequency. For PI, $f_{dem} = 2f_0$ and $n = 2$, and for AM $f_{dem} = f_0$ and $n = 3$, thus:

$$v_{max}\,(PI) = \frac{PRFc}{16\pi f_0}, \quad v_{max}\,(AM) = \frac{PRFc}{12\pi f_0} \tag{3}$$

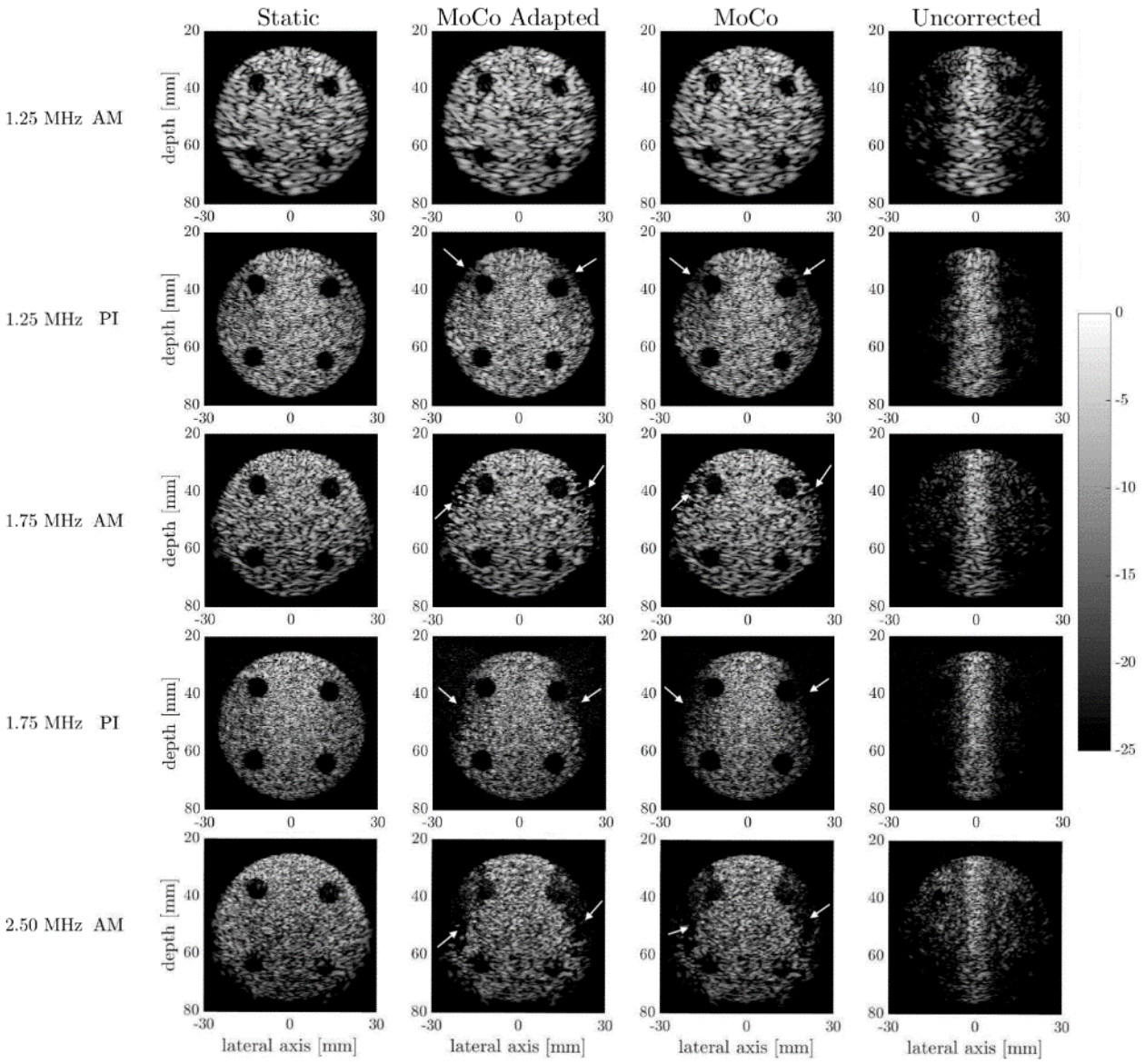

Figure 2. Motion compensation in AM and PI acquisitions at 1.25 MHz (rows 1 and 2), 1.75 MHz (rows 3 and 4) and 2.5 MHz (row 5). Images were depth selected from 20-80 mm and in the lateral direction from -30 to 30 mm for display. Images were normalized according to their own maximum and log-compressed. White arrows point to regions where Doppler aliasing occurred and resulted in loss of intensity. At 1.25 MHz, no aliasing occurs in AM, but a small amount occurs in PI. As the frequency increases, loss of intensity in the edges occurs since the highest velocities occur nearer the edges of the disc.

Conclusions

In this paper, the Doppler-based motion compensation developed for B-Mode images was applied and evaluated in the Cartesian domain for two modalities of HFR contrast imaging – Amplitude Modulation and Pulse Inversion. The frequency dependence of the motion estimator was also evaluated.

The MoCo approach, despite having been developed for application in polar coordinates, also works in the Cartesian domain. We found that PI acquisitions are more susceptible to motion artefacts as transmit frequency increases. We also determined that PI can achieve greater contrast than AM at the lower frequencies evaluated. PI may, thus, be more adequate when lower frequencies are used (~ 1.25 MHz), while AM is a better choice when higher transmit frequencies are necessary (1.75 MHz and higher). To fully support this claim, more evaluations at a wider range of frequencies must be performed.

Additionally, equation 2 is proposed as guidance for Doppler velocity limits in motion compensation for coherent compounding and multi-pulse contrast imaging.

This study was performed uniquely on simulation data. Due to the Covid-19 pandemic, we were not able to perform any other acquisitions. In-vitro studies with tissue-mimicking phantoms must be carried out to complement the results on simulation data, as more factors influence image quality in a real acquisition scenario. In the future, we hope to evaluate the same metrics in in-vitro and in-vivo acquisitions with a wider range of transmit frequencies.

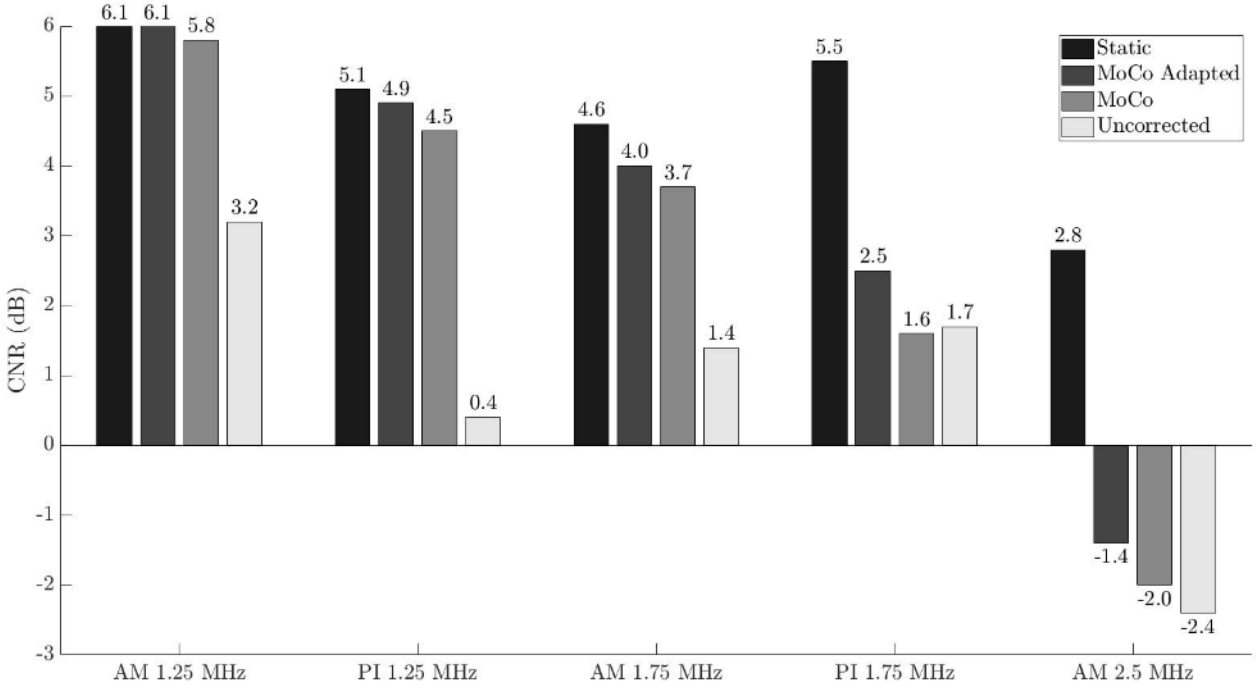

Figure 3. Contrast-to-Noise Ratio (CNR) comparison between all acquisitions, computed according to equation 1 and figure 1.

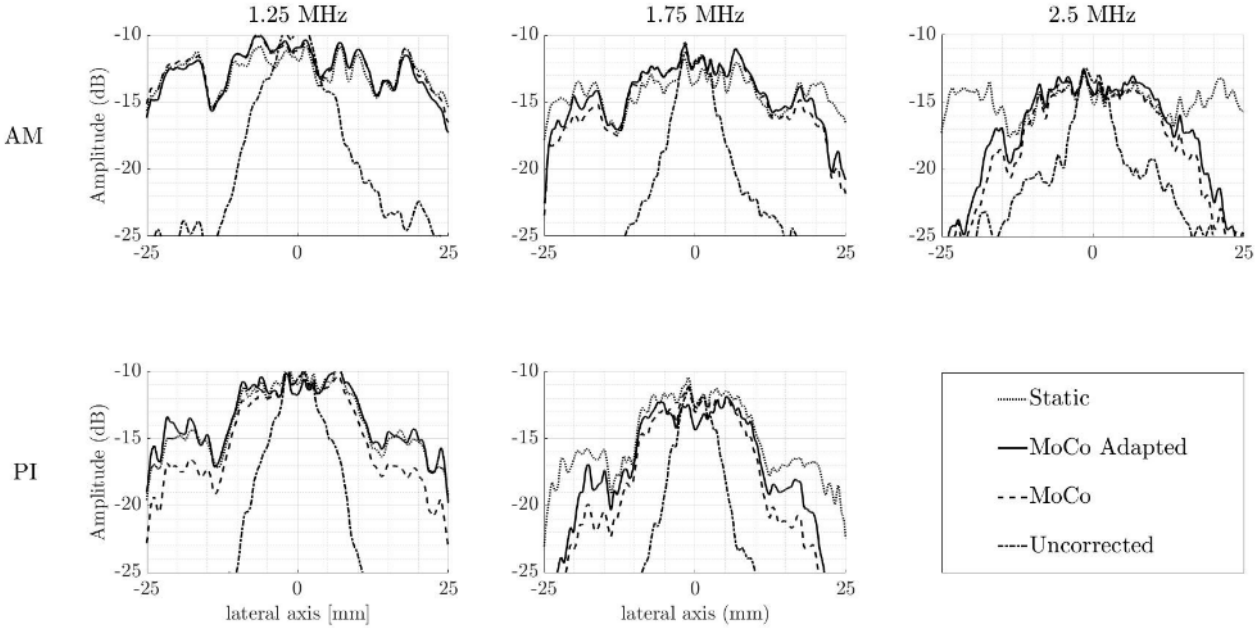

Figure 3. Lateral evaluation of all acquisitions. Each point in each curve is the mean of intensities in the disc across the fast-time samples. Each image was normalized according to their own maximum before mean computation. Each plot was later log-compressed. The lateral axis was cut from -25 to 25 mm because those are the locations in which the disc lies in the lateral axis.

References

[1]. M. Correia et al. “Ultrafast Harmonic Coherent Compound (UHCC) Imaging for High Frame Rate Echocardiography and Shear-Wave Elastography”. In: IEEE Transactions on Ultrasonics, Ferroelectrics, and Frequency Control63.3 (2016), pp. 420–431.

[2]. G. Matrone et al. “High Frame-Rate, High Resolution Ultrasound Imaging With Multi-Line Transmis-sion and Filtered-Delay Multiply And Sum Beamforming”. In: IEEE Transactions on Medical Imaging36.2 (2017), pp. 478–486.

[3]. C. Papadacci et al. “High-contrast ultrafast imaging of the heart”. In: IEEE Transactions on Ultrason-ics, Ferroelectrics, and Frequency Control61.2 (2014), pp. 288–301.

[4]. Jonathan Porée et al. “High-Frame-Rate Echocardiography Using Coherent Compounding With Doppler-Based Motion-Compensation”. In: IEEE Transactions on Medical Imaging35 (Feb. 2016), pp. 1–1.

[5]. Matthieu E.G. Toulemonde et al. “High Frame-Rate Contrast Echocardiography: In-Human Demon-stration”. In: JACC: Cardiovascular Imaging11.6 (2018), pp. 923–924.

[6]. J. Faurie et al. “Intracardiac Vortex Dynamics by High-Frame-Rate Doppler Vortography—In Vivo Comparison With Vector Flow Mapping and 4-D Flow MRI”. In: IEEE Transactions on Ultrasonics, Ferroelectrics, and Frequency Control64.2 (2017), pp. 424–432.

[7]. Solveig Fadnes et al. “In Vivo Intracardiac Vector Flow Imaging Using Phased Array Transducers forPediatric Cardiology”. In: IEEE Transactions on Ultrasonics, Ferroelectrics, and Frequency Control64(Apr. 2017), pp. 1318–1326.

[8]. Birger Brekke et al. “Ultra-high Frame Rate Tissue Doppler Imaging”. In: Ultrasound in Medicine & Biology 40.1 (2014), pp. 222–231.

[9]. P. Joos et al. “High-frame-rate velocity vector imaging echocardiography: an in vitro evaluation”. In:2016 IEEE International Ultrasonics Symposium (IUS). 2016, pp. 1–4.

[10]. A. Stanziola et al. “Motion Artifacts and Correction in Multipulse High-Frame Rate Contrast-Enhanced Ultrasound”. In: IEEE Transactions on Ultrasonics, Ferroelectrics, and Frequency Control66.2 (2019), pp. 417–420.

[11]. L. Nie et al. “High-Frame-Rate Contrast-Enhanced Echocardiography Using Diverging Waves: 2-D Motion Estimation and Compensation”. In: IEEE Transactions on Ultrasonics, Ferroelectrics, and Frequency Control 66.2 (2019), pp. 359–371.

[12]. Iason Apostolakis et al. “Dual Aperture Motion Compensation (DAMoCo)”. In: Oct. 2019, pp. 2015–2018.

[13]. Bradley E. Treeby et al. “Modeling nonlinear ultrasound propagation in heterogeneous media with power law absorption using a k-space pseudospectral method”. In: The Journal of the Acoustical Societyof America 131.6 (2012), pp. 4324–4336.

[14]. J. Wu and J. Tong. “Measurements of the nonlinearity parameter ba of contrast agentes”. Ultrasound in Medicine & Biology, 24(1):153 – 159, 1998.

The influence of motion on contrast detection for ultrafast imaging: quantification and compensation

Geraldi Wahyulaksana[1], Jasper Schoormans[1], Luxi Wei[1], Antonius F.W. van der Steen[1], Nico de Jong[1,2], Hendrik J. Vos[1,2]

[1]Thoraxcenter, Dept Biomedical Engineering, Erasmus University Medical Center Rotterdam, Rotterdam, the Netherlands

[2]Acoustical Wavefield Imaging, Faculty of Applied Sciences, Delft University of Technology, Delft, the Netherlands

Corresponding author: g.wahyulaksana@erasmusmc.nl

Introduction

Clutter signal originating from tissue motion is a major artifact affecting the sensitivity and quality of ultrasound contrast perfusion imaging [1], [2]. Singular value decomposition (SVD) has been used widely to suppress clutter and tissue signal in ultrasound imaging applications as it generally performs better than the conventional frequency filter. However, it has been reported that the effectiveness of the SVD filter to detect slow flow degrades proportionally with tissue motion velocity [3]. This is a critical issue in cardiac perfusion imaging, where high velocity myocardial motions are expected [4]. In this work, we evaluated the effectiveness of three techniques for contrast/flow detection during motion: SVD only, a motion compensation method + SVD, and SVD + independent component analysis (ICA).

Methods

An in-vitro experiment was performed on a tissue-mimicking wall-less flow phantom, consisting of polyvinyl alcohol (PVA) and background scattering particles (Fig 1A). Diluted in-house contrast agent (F-type [5]) was continuously infused through a 1mm diameter channel with a mean flow speed of ~6mm/s. Measurements were performed with an L7-4 probe connected to a Vantage 256 system (Verasonics Inc., Redmond, WA). The transmission sequence consisted of 5 tilted plane waves from -7° to 7° with 3.5° increments with a pulse repetition frequency of 5000Hz. The used scan time was 0.4 seconds. The pulses had a centre frequency of 5.2 MHz (fundamental imaging). The probe was attached to a linear stage and moved during acquisition to emulate rigid tissue motion, for a range of velocities (0 mm/s to 25mm/s with a 5mm/s interval). Probe direction was either axial or lateral in separate experiments.

Delay-and-sum beamforming and angular compounding was performed with the Ultrasound Toolbox [6] in Matlab (2020B, the Mathworks, Natick, 2020) on a 0.5 λ resolution grid. Next, we applied three techniques to compare:

SVD only: Singular value decomposition was performed using an ensemble length of 200 frames and 20% overlap. Microbubble contrast signal was separated by a rank-selection algorithm based on spatial correlation [7].

Motion compensation + SVD: After initial beamforming, the image displacement over the entire sequence was estimated by a cross-correlation algorithm evaluated on the B-mode images. Then, as opposed to conventional motion compensation methods, the beamforming *grid per frame* was warped with the estimated displacement per location per frame. With this warped grid a second round of delay-and-sum was applied, albeit displayed at the original grid. This results in a pseudo-static beamformed image, while maintaining the correct time-of-flight calculations that underlay the delay-and-sum beamforming. On this data, SVD was performed similar to technique 1 above. This technique is in parts similar to that reported in [8].

SVD + ICA: we implemented the SVD filter but applied on every tilt-angle image sequence separately, and then used the ICA algorithm to compound the resulting multi-angle data into single frames[9].

Regions-of-interest (ROI) were drawn inside the channel and in the background (Fig 1B) for all techniques alike. The filter performance was assessed by calculating contrast-to-background ratio (CBR) as $CBR = 20\log_{10}\left(\frac{RMS_{contrast}}{RMS_{background}}\right)$.

Results

Figure 2 shows representative microbubble contrast images. In the static reference, the three filter methods all show good contrast separation. For motion, the SVD performance degrades monotonically with velocity, while both motion compensation and ICA show a cleaner contrast image. Figure 3 shows the results for all velocities. Motion compensation improves the CBR, especially during high velocities (15-25 mm/s); ranging 7 - 14dB for axial and 3 - 6dB for lateral motion. ICA also improves the CBR for higher velocities; 2 - 5dB for axial and 4 - 7dB for lateral motion.

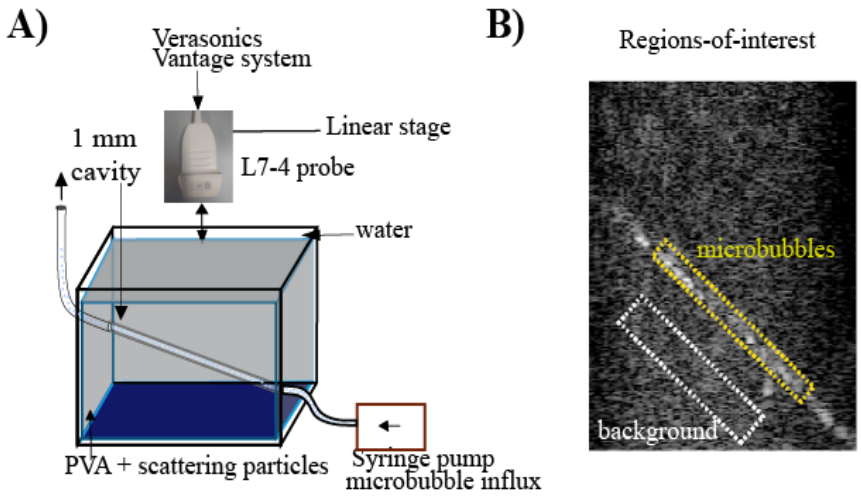

Figure 1. A) Experimental set-up of the flow phantom. B) B-mode image of the flow phantom with regions-of-interest for CBR calculation indicated by the dotted lines (yellow = microbubbles, white = background).

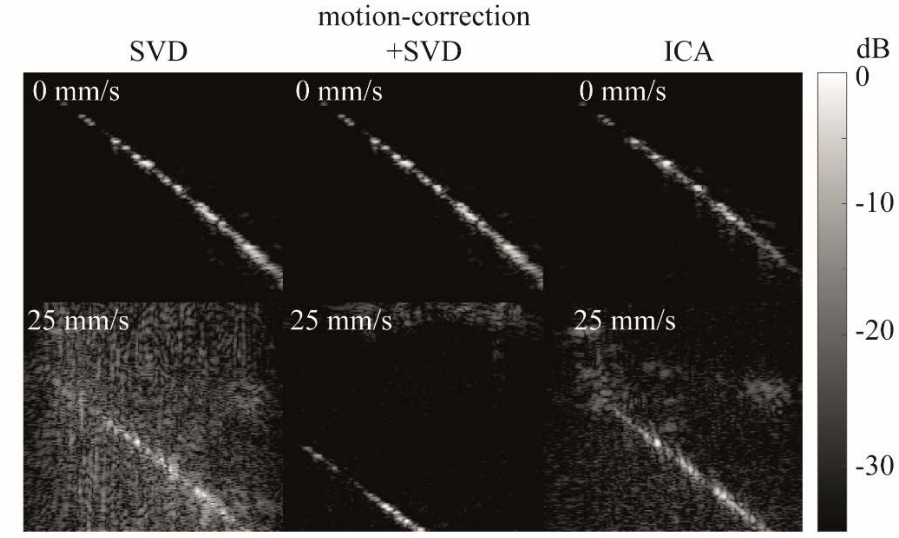

Figure 2. Representative filtered contrast images for the static (0 mm/s) and axial probe motion (25 mm/s) experiments.

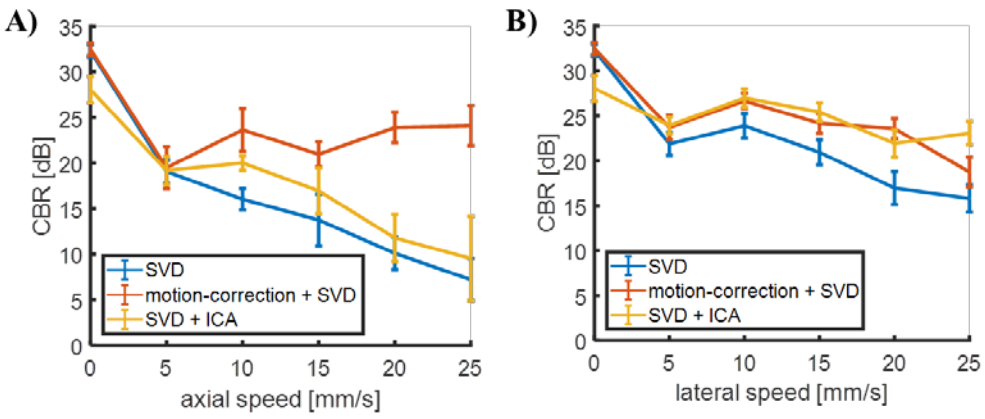

Figure 3. Contrast-to-background values after SVD, for SVD, motion-compensated SVD, and ICA, for a range of velocities. A) Axial probe motion, B) Lateral probe motion

Discussion and Conclusions

SVD performance declined proportionally to tissue velocity. To our knowledge, this has not been systematically evaluated at such high velocity ranges before. It has been reported that longer ensemble lengths correspond to better contrast separation [10], [11], but in an additional analysis (not reported here) we could not observe any improvement of CBR when varying the SVD ensemble length.

The filter performance on motion-corrected images remained fairly constant over the velocity range, around 10 dB lower than the static reference. While ICA performance was slightly lower in the static condition, it outperformed SVD-only over all velocities. It should be noted that all three techniques relied on SVD in some way, and, in our experience, the exact selection of contrast-containing SVD ranks remains difficult, and some further fine-tuning of rank selection is needed.

We demonstrated here that the filter improvements can increase the CBR during axial and lateral motion, in the range of expected myocardial speeds. These improvements could provide a significant addition in the field of cardiac perfusion imaging where fast myocardial motion is expected.

References

[1] A. Heimdal and H. Torp, “Ultrasound Doppler Measurements of Low Velocity Blood Flow: Limitations Due to Clutter Signals from Vibrating Muscles,” *IEEE Trans. Ultrason. Ferroelectr. Freq. Control*, vol. 44, no. 4, p. 873, 1997.

[2] S. Bjaerum, H. Torp, and K. Kristoffersen, “Clutter filter design for ultrasound color flow imaging,” *IEEE Trans. Ultrason. Ferroelectr. Freq. Control*, vol. 49, no. 2, pp. 204–216, Feb. 2002.

[3] C. Demené *et al.*, “Spatiotemporal Clutter Filtering of Ultrafast Ultrasound Data Highly Increases Doppler and fUltrasound Sensitivity,” *IEEE Trans. Med. Imaging*, vol. 34, no. 11, pp. 2271–2285, 2015.

[4] G. Shechter, J. R. Resar, and E. R. McVeigh, “Displacement and velocity of the coronary arteries: Cardiac and respiratory motion,” *IEEE Trans. Med. Imaging*, vol. 25, no. 3, pp. 369–375, Mar. 2006.

[5] V. Daeichin *et al.*, “Microbubble Composition and Preparation for High-Frequency Contrast-Enhanced Ultrasound Imaging: In Vitro and in Vivo Evaluation,” *IEEE Trans. Ultrason. Ferroelectr. Freq. Control*, vol. 64, no. 3, pp. 555–567, Mar. 2017.

[6] A. Rodriguez-Molares *et al.*, “The UltraSound ToolBox,” in *IEEE International Ultrasonics Symposium, IUS*, 2017.

[7] B. Arnal, J. Baranger, C. Demene, M. Tanter, and M. Pernot, “In vivo real-time cavitation imaging in moving organs,” *Phys. Med. Biol*, vol. 62, pp. 843–857, 2017.

[8] P. Cormier, J. Porée, C. Bourquin, and J. Provost, “Dynamic Myocardial Ultrasound Localization Angiography,” *presented at 2020 IEEE International Ultrasonics Symposium.* .

[9] G. Wahyulaksana, L. Wei, J. Voorneveld, N. de Jong, A. F. W. van der Steen, and H. J. Vos, “Plane Wave Compounding with Blind Source Separation Framework for Perfusion Imaging During Tissue Acceleration,” *poster presented at 2020 IEEE International Ultrasonics Symposium.*

[10] J. Voorneveld *et al.*, “High-frame-rate contrast-enhanced ultrasound for velocimetry in the human abdominal aorta,” *IEEE Trans. Ultrason. Ferroelectr. Freq. Control*, vol. 65, no. 12, pp. 2245–2254, 2018.

[11] J. Zhu *et al.*, “High Frame Rate Contrast-Enhanced Ultrasound Imaging for Slow Lymphatic Flow: Influence of Ultrasound Pressure and Flow Rate on Bubble Disruption and Image Persistence,” *Ultrasound Med. Biol.*, vol. 45, no. 9, pp. 2456–2470, 2019.

Ultrasound Frequency-Dependent Targeting: A Step Toward Multi-Color Ultrasound Molecular Imaging

Ilaria Angelini[1,2], Maju Kuriakose[3], Awaneesh Upadhyay[3], Marco A. Inzunza-Ibarra[3], Mark A. Borden[2,3]

[1]Department of Chemistry, University of Rome Tor Vergata, Italy
[2]Biomedical Engineering Program, University of Colorado Boulder, USA
[3]Department of Mechanical Engineering, University of Colorado Boulder, USA
Corresponding author: mark.borden@colorado.edu

Introduction

Targeted ultrasound contrast agents, such as ligand-coated microbubbles, can be employed for molecular imaging by specific interactions with receptors expressed on endothelial cells at sites of angiogenesis, inflammation or thrombus [1]. Previously, it was demonstrated that microbubble targeting can be improved by displacement induced by acoustic radiation forces, significantly increasing bubble/cell contact and ligand/receptor interactions [2]. We hypothesized that size-isolated microbubbles [3] will allow selective targeting using medical ultrasound, which would be a significant step toward multi-color ultrasound molecular imaging. As spatial displacement of maximizes at the resonance frequency, one can selectively displace microbubbles by matching the driving frequency to bubble resonance [4]. In this study, we demonstrate differences in microbubble targeting using two size-isolated samples under distinct ultrasound frequencies at the bandwidth limits of a clinical imaging probe (3 vs. 7 MHz).

Methods

DBPC:DSPE-PEG(2000)-Biotin (90:10 mole percent) microbubbles with a perfluorobutane core and a mean diameter of 0.7 µm or 2.5 µm were size-isolated by differential centrifugation (Fig. 1a, 1b). The 0.7 µm or 2.5 µm diameter microbubbles were marked with DiO or DiI fluorophores, respectively. The microbubbles were mixed and diluted in phosphate buffered saline ($1x10^7$ MBs/mL) and pumped through a 200-µm avidin-coated tube. The tube was insonified with plane-waves from a linear array transducer at 100 kPa and at two acoustic frequencies, 3 MHz or 7 MHz (Fig. 1c). A pulse duration of 6.7 µs was used for both frequencies. A CCD camera connected to an inverted microscope with a 100x objective was used to image the tube section. Ten brighfield and fluorescence images of each tube segment were taken along the z-axis to characterize the number of adherent microbubbles to the tube. For the mixed sample, the tube is insonified by 7 MHz pulses for four minutes, then again with 3 MHz pulses for an additional four minutes.

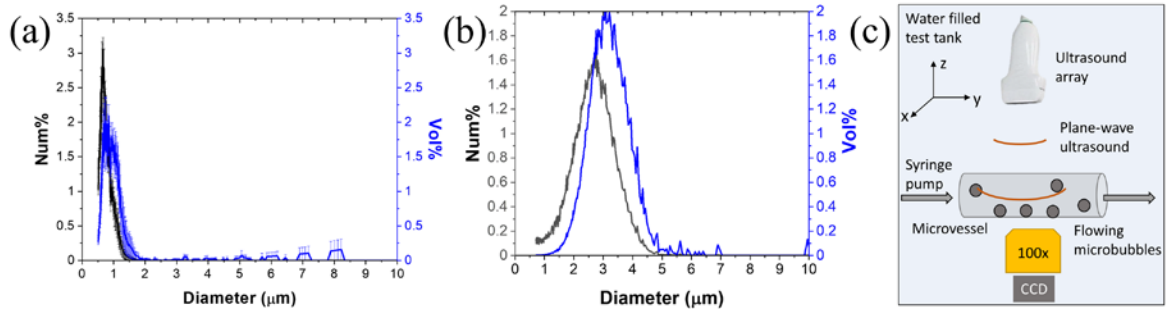

Fig.1 (a) Size-distributions of microbubble with 0.7 µm or (b) 2.5 µm mean diameter. (c) experimental setup.

Results

Our results indicate that the displacement, biotin-avidin binding, and adhesion of microbubbles with different diameters depends on the applied ultrasound frequency. Green and red fluorescence images were used to count the number of adherent microbubbles of each size/frequency combination. The focal planes

of a tube section were processed and displayed in a single image, as shown in Fig. 2, where we see clear differences in the fluoresence associated with microbubble adhesion.

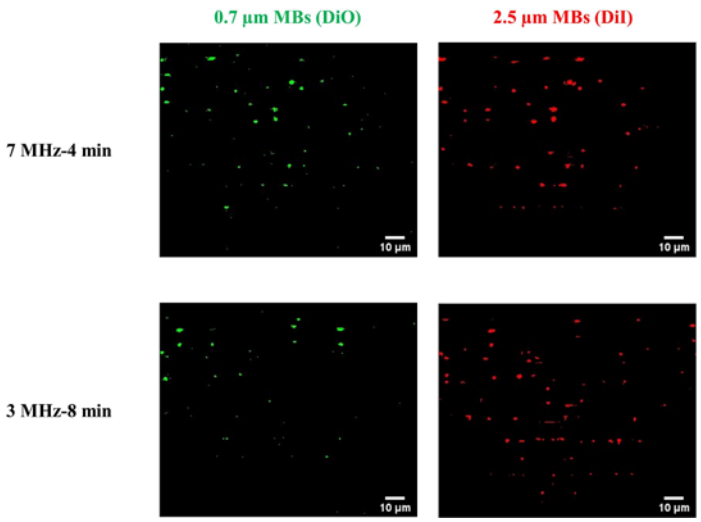

Fig. 2 A section of the tube where we can see attached microbubbles at 7 and 3 MHz. 0.7 µm sized microbubbles are marked with DiO (green bubbles), while 2.5 µm microbubbles with DiI (red bubbles).

In support of our hypothesis, we observed a higher number of adherent microbubbles for 0.7 µm diameter at 7 MHz, which decreased when we changed to 3 MHz. The opposite behavior was observed for 2.5 µm diameter, where a larger number of specifically adhered microbubbles occured at 3 MHz (Table 1).

Table 1 Number of bubbles obtained after irradiation at 7 and 3 MHz, observing three different sections of the tube.

	Number of microbubbles (MBs)	
	0.7 µm MBs (DiO)	**2.5 µm MBs (DiI)**
4 min-7 MHz	163	93
8 min-3 MHz	90	152

Conclusion

In conclusion, we showed that adherence of biotinylated microbubbles to an avidin-coated micro-tube depends on both the size-distribution of the bubbles and the applied ultrasound frequency. Frequency selection of different ligand-bearing microbubble agents may enable multi-color ultrasound molecular imaging.

References

[1]. Sirsi S., Borden M. A., Microbubble compositions, properties and biomedical applications, Bubble Sci. Eng. Technol. 1(**1-2**), 3-17 (2009).

[2]. Zhao S., Borden M. A., Dayton P., Radiation-Force Assisted Targeting Facilitates Ultrasonic Molecular Imaging, Mol. Imaging **3**(3), 135-148 (2004).

[3]. Feshitan J. A., Chen C. C., Kwan J. J., Borden M. A., Microbubble size isolation by differential centrifugation, J. Colloid Interface Sci. 329(**2**), 316–324 (2009).

[4]. Supponen O., Upadhyay A., Lum J., Guidi F., Murray T., Vos H. J., Tortoli P., Borden M. A., The effect of size range on ultrasound-induced translations in microbubble populations, J. Acoust. Soc. Am. **147**, 3236-3247 (2020).

Effects of primary and secondary radiation forces on endoskeletal droplets under standing surface acoustic waves

Gazendra Shakya[1], Tao Yang[1], Apresio K. Fajrial[1], Yu Gao[1], Mark A. Borden[1,2,3], Xiaoyun Ding[1,2]

[1]Department of Mechanical Engineering, University of Colorado at Boulder, CO, USA
[2]Department of Biomedical Engineering, University of Colorado at Boulder, CO, USA
[3]Materials Science and Engineering Program, University of Colorado, Boulder, CO, USA
Corresponding author: xiaoyun.ding@colorado.edu

Introduction

Primary and secondary radiation forces (also known as Bjerknes forces on bubbles) play an important role in the manipulation and interaction of bubbles and particles under acoustic fields. Understanding these hydrodynamic forces is pivotal in understanding particle behavior. A major parameter affecting the interactions is the acoustic contrast factor, which depends on the particle and medium density and compressibilty. Here, we incorporate endoskeletal droplets [1] to integrate both positive and negative contrast factors into one system. This allows us to bring about interesting particle patterning behavior in the liquid droplets as well as the solid disks and study the effect of radiation forces on them.

Methods

We employed microfluidics to generate uniform endoskeletal droplets, which were made with a liquid in solid geometry comprising perfluorododecane as the solid and perfluorohexane as the liquid component. The droplets were stabilized by a lipid surfactant. Standing acoustic waves were generated using surface acoustic wave (SAW) devices which consists of interdigitated transducers patterned on a piezoelectric substrate (Lithium Niobate, $LiNbO_3$). Particle aggregation behavior under standing acoustic waves were observed at 10 and 20 MHz frequency. Comsol simulations were performed for theoretical modeling of the interaction behavior as well as to verify the experimental ovservations.

Results

We show the novel generation of monodisperse endoskeletal droplets using a microfluidics technique. Furthermore we show that, in a standing acoustic field, the endoskeletal droplets are forced to the pressure by the primary radiation force. Whereas the secondary radiation force forms clusters of these droplets because of its negative contrast factor (as opposed to chains for positive contrast factor particles in nodes). Interestingly, we observe that the solid disks, which has a positive contrast factor in reference to the perfluorohexane liquid and are initially randomly oriented, are forced to align perpendicular to the surface under the acoustic field. This phenomenon forms fascinating clusters as seen in figure 1. Moreover, the orientation of the disks can be manipulated on demand by changing the frequency of the acoustic waves as the equillibrium state of the droplets depends on the interplay between the primary radiation force of the traveling wave field in the z-direction (generated from leaky Rayleigh waves) and the secondary radiation force due to the standing wave field in the x-direction. Additionally, we provide simulation results showing the equilibrium position of the droplets and the disks under the standing acoustic field.

Conclusions

Better understanding of the primary and secondary radiation forces is necessary for understanding particle behavior under acoustic waves. In our work, we show the effects of these forces on the clustering and patterning behavior of liquid droplets with a negative acoustic contrast factor as well as solid disks inside the droplets with a positive contrast factor. This peculiar mixture of two contrast factors in one system allowed us to observe fascinating behavior not seen elsewhere.

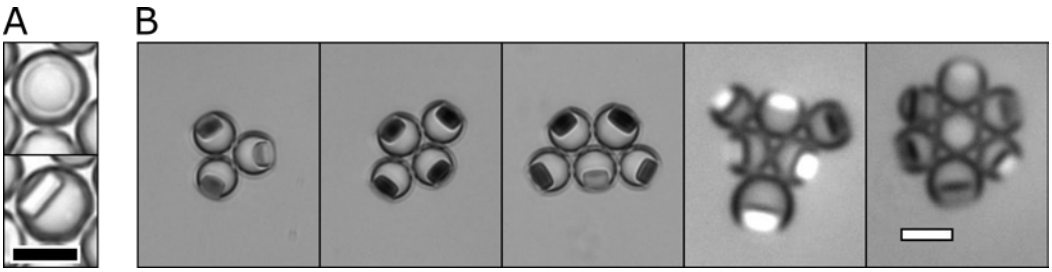

Figure 1. Optical microscopic images of endoskeletal droplets. A. Different orientations of the solid disks seen on the same droplet. Top - parallel to the surface, Bottom - perpendicular to the surface. Scale bar 10 μm. B. Clustering behaviour of the disks and the droplets seen in different sized clusters. SAW waves propagating from +ve and -ve x-direction. Scale bar 15 μm.

References

[1]. Shakya G, Hoff SE, Wang S, Heinz H, Ding X, Borden MA, Vaporizable endoskeletal droplets via tunable interfacial melting transitions. Science Advances, 6, 2020.

Propagation of medical ultrasound through a cluster of nonlinear microbubbles including multiple scattering effects

A. Matalliotakis[1], G. Collado Lara[2], F.R. Deurvorst[1], V. Daeichin[1], H. Vos[1,2], P. L.M.J. van Neer[1], N. de Jong[1,2], M.D. Verweij[1,2]
[1]Medical Imaging, ImPhys, Delft University of Technology, Delft, the Netherlands
[2]Biomedical Engineering, Thorax Center, Erasmus MC, Rotterdam, the Netherlands
Corresponding author: a.matalliotakis@tudelft.nl

Introduction

Gas microbubbles are widely used as ultrasound contrast agents, mainly for medical imaging purposes. Their full potential derives from their ability to reflect sound more efficiently than tissue due to their compressibility, and interact nonlinearly with ultrasound and their surroundings. The dynamics of single bubble oscillations in a pressure field are well understood. However, to fully understand how microbubble clusters behave, their mutual interactions should be taken into account. In combination with the complexity of nonlinear spatiotemporal wave propagation, this imposes a significant challenge both scientifically and computationally. To address this challenge, the Iterative Nonlinear Contrast Source method (INCS) [1] is used for modeling nonlinear medical ultrasound propagation through a microbubble cluster.

Methods

The INCS method is originally developed to compute the nonlinear acoustic pressure field from plane source apertures with a pulsed excitation in a four dimensional spatiotemporal domain. Its core is based on calculating the field of a given source distribution by convolution with the Green's function of the linear and homogeneous background medium. By following this proceedure, first the linear field is calculated. Next, the nonlinearity of the medium is accounted for by using the computed field to derive a distributed nonlinear contrast source, which is again convolved with the Green's function. By repeating this procedure, the field is iteratively corrected, leading to increasingly accurate nonlinear field estimates. Compared with finite difference methods, this procedure has the advantage of coarse discretization and accurate higher harmonic imaging. In this existing framework, the microbubbles were introduced as nonlinear contrast sources, assumed to behave as nonlinear point scatterers. In each iteration, the oscillation of each individual bubble was calculated from an extended version of Rayleigh-Plesset model [2]. The position of the microbubbles was geneterated by a locally random method. The microbubble cluster was assumed to be a cube in space, which was subdivided into a number of smaller cubes equal to the number of the scatterers. Inside each smaller cube, a microbubble was positioned randomly, bounded by the borders of the cube and with a restriction on the minimum mutual distance between the microbubbles in adjacent cubes to avoid overlapping between scatterers. With the applied numerical implementation, the position of the microbubbles is not limited to the location of the gridpoints, rendering the simulation more realistic without losing accuracy. Furthermore, there is an efficiency gain as the number of the gridpoints remains the same by being independent of the cluster concentration. This iterative method takes into consideration the microbubbles' interactions because each iteration introduces an additional order of multiple scattering. The validation of the model was done by using one and two linear and nonlinear scatterers and comparing INCS results to the known analytic solutions.

Results

In Fig. 1, a simulation of a medical ultrasound beam in a spatiotemporal domain is depicted. The simulation took place in a domain with dimensions of X x Y x Z = 22 mm x 10 mm x 50 mm, for a center frequency of 1 MHz and a sampling frequency of 9 MHz. A concentraton of 10^5 monodisperse microbubbles with a radius of 2 μm was used in a volume of 1 ml, indicated in the XZ-plane by the dotted rectangles. The linear field was generated by a phased array transducer of 40 elements transmitting a

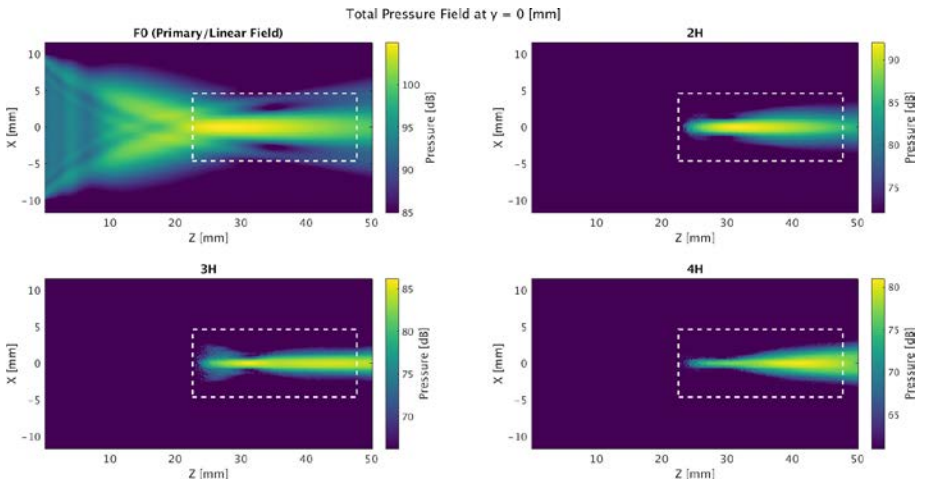

Figure 1. Total pressure field of the fundamental, 2nd, 3rd and 4th harmonic of a cluster of microbubbles (within dotted rectangles) with a concentration of 10^5 ml^{-1}.

gaussian 3-cycle pulse of 50 kPa amplitude. Medium attenuation was not included. At each location, the maximum pressure of the pulse is shown in the figure. In the left top image, the total field is calculated by adding the linear field with the scattered pressure of the microbubbles in the fundamental frequency range. The scattered pressure field is observed in the higher harmonics, as depicted in the remaining three subplots. Since other medium nonlinearities were not added, the higher harmonics are only due to the nonlinear microbubble behavior. Moreover, it is clearly visible that the higher harmonics of the scattered pressure emerge from the area with a peak pressure amplitude of the excitation field. This can be explained by the fact that the microbubbles that are located in this area display a stronger nonlinear behavior in the applied model.

Conclusions

INCS has been succesfully adapted to efficiently simulate the scattered pressure of a microbubble cluster, including the multiple scattering effects. The nonlinear oscillatory behaviour of microbubbles is taken into account and shows up in the higher harmonics that appear at the location of the cluster. This gives the opportunity to extensively study the nonlinear behaviour of entire microbubble clusters, and creates space for other new applications.

References

[1]. J. Huijssen, M. D. Verweij, An iterative method for the computation of nonlinear, wide-angle, pulsed acoustic fields of medical diagnostic transducers, The Journal of the Acoustical Society of America, vol. 127, no. 1, pp. 33-44, Jan. 2010. doi: 10.1121/1.3268599

[2]. Marmottant et al., A model for large amplitude oscillations of coated bubbles accounting for buckling and rupture, The Journal of the Acoustical Society of America, vol. 118, no. 1, pp. 3499 - 3505, Dec. 2005. doi: 10.1121/1.2109427

In-silico simulations of the microbubble flow through porous media mimicking microvascular networks

P. Chen[1], S. Turco[1], R. J.G. van Sloun[1,2], A. M.A.O. Pollet[3], J. M.J. den Toonder[3], H. Wijkstra[1,4], M. Mischi[1]

[1]Department of Electrical Engineering, Eindhoven University of Technology, Eindhoven, Netherlands
[2] Philips Research, Eindhoven, Netherlands
[3] Department of Mechanical Engineering, Eindhoven University of Technology, Eindhoven, Netherlands
[4]Department of Urology, Amsterdam University Medical Centers, Amsterdam, Netherlands
Corresponding author: p.chen1@tue.nl

Introduction

Tumor-driven angiogenic microvasculature is a recognized hallmark of cancer, which is characterized by increased microvascular density (MVD), higher vessel tortuosity, and smaller and irregular vessel diameter. This irregular microvascular network leads to complex blood flow patterns [1, 2, 3]. To assess the blood flow and further analyze the microvascular architecture, dynamic contrast-enhanced ultrasound (DCE-US) provides real-time analysis of the vasculature by imaging the blood flow with the help of intravenously-injected ultrasound contrast agents (UCAs). The temporal evolution of the UCA concentration is reflected in pixel intensity variations over the DCE-US loops. By collecting these variations, time-intensity curves (TICs) can be obtained at each pixel; their analysis enables the assessment of the underlying blood flow patterns and microvascular architecture, aiding with tumor detection. In the past years, extensive work has shown the value of convective-dispersion modeling for the interpretation of the measured TICs, with promising results for the diagnosis of e.g. prostate cancer [4, 5, 6, 7]. According to the results obtained in the prostate, increased velocity and decreased dispersion are observed in tumor tissue. However, a clear link between the estimated parameters and the underlying microvasculature is still lacking.

In previous work, we modeled the microvasculature as a porous medium, and then developed an experimental set-up including dedicated porous phantoms to investigate the relationship between UCA kinetics and the underlying microvascular architecture. These phantoms were realized by packing mono-sized beads in a cylindric tube. The pore size was controlled by tuning the bead diameter, simulating different MVD and vessel diameter [8].

In this work, we developed a simulation framework to further advance our understanding of the UCA dynamics through microvascular networks mimicked by porous media.

Methods

The porous phantoms used in previous in-vitro experiments were built by packing 3% alginate beads in a polyurethane tube. Variable MVD and vessel diameter were realized by packing beads with diameters of 3.1, 2.5, and 1.6 mm, respectively. The in-silico model of these phantoms was realized using a dedicated 3D sphere-packing algorithm. As a first step, we defined a cylinder region representing the polyurethane tube. After that, thousands of mono-sized spheres were uniformly distributed inside this region, allowing overlapping between spheres. Sphere were then seprated iteratively along the connective line between the origins of each pair of spheres until no overlapping occurred anymore. For each 100 iterations, random motion was applied to all the spheres mimicking a shaking process. Finally, a few additional spheres were added to fill those voids that were large enough to contain an individual sphere. This was implemented by a search algorithm that minimized the distance between the newly added spheres and the existing spheres until they touched each other without overlapping. In agreement with our previous experiments, we simulated porous phantoms with sphere diameters of 3.1, 2.5, and 1.6 mm, respectively.

The simulated porous medium phantoms enable us to analyse the architecture of the different porous media. The distribution of the radial porosity within the cylinder was obtained by calculating the void fraction in each concentric layer of 0.04-mm thickness. Moreover, Delaunay triangulation was applied to these phantoms to measure the pore size represented by the size of the inscribed spheres of each connected tetrahedron. Additionaly, the pore density was obtained representing the MVD.

The dynamic simulations of UCA flowing through the porous phantoms were performed in COMSOL. The coordinate of each sphere's origin and the sphere's diameter in the simulated phantoms were first imported into COMSOL, and a solid cylinder was also built representing the cylindric tube. All the spheres were then removed from the solid cylinder. The remaining part is the void space in the phantoms through which the fluid flows, hence defined as the fluid domain. A combination of laminar flow with blood properties (e.g. viscosity and density) and transport of particles was applied to the fluid domain. The time-dependent simulation was then performed.

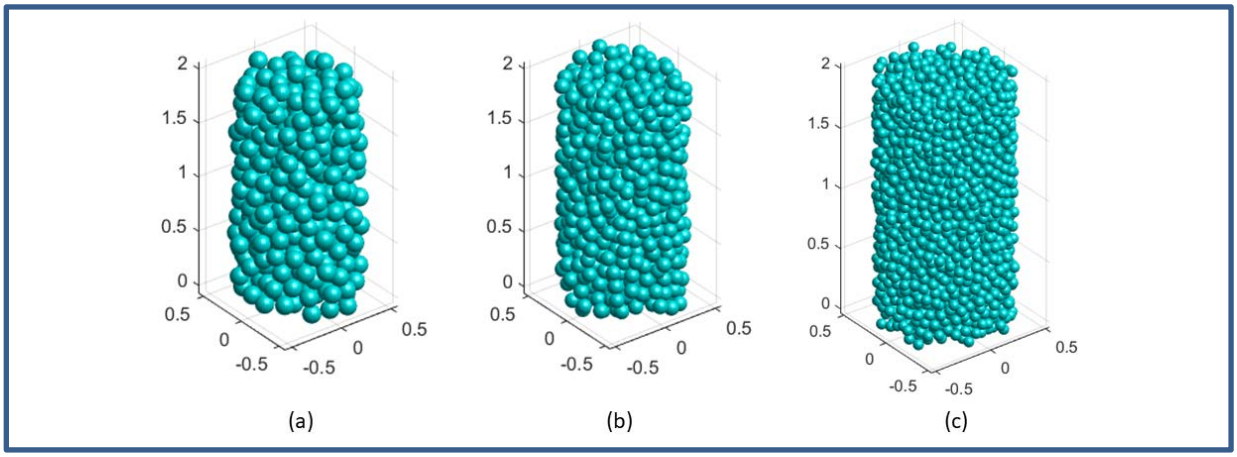

Figure 1. Simulated porous phantoms using a sphere-packing algorithm: the diameters of the spheres are 3.1, 2.5 and 1.6 mm, respectively from (a) to (c). The diameter of the tube is 20 mm and the length of the tube is 40 mm. In this figure, all dimensions are scaled up by a factor of 50.

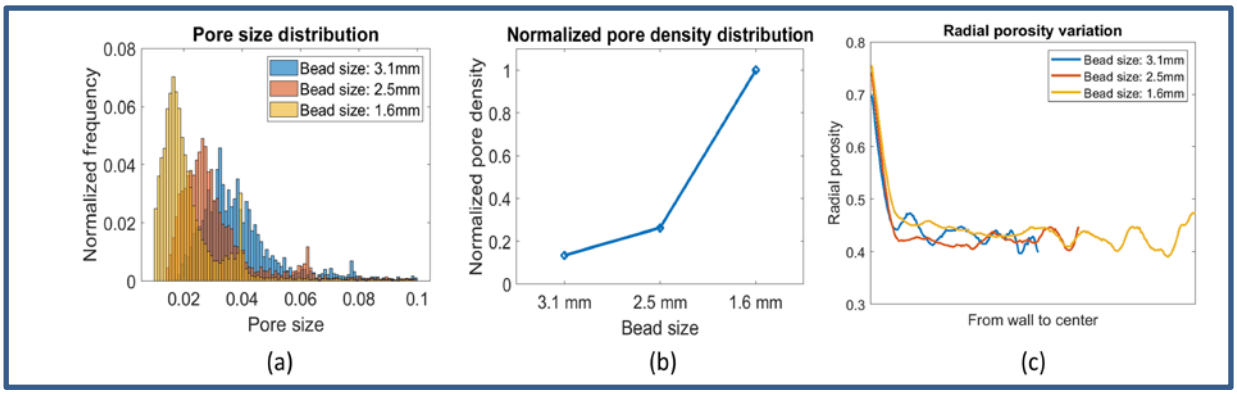

Figure 2. The analysis of the simulated phantoms' architecture: (a) is the pore size distribution; (b) is the normalized pore density; and (c) is the radial porosity variation.

Results

Figure 1 shows the simulated porous phantoms with variable pore size. The results from the analysis of their architecture are depicted in Figure 2. The pore size and density distribution indicate that the pore size decreases while the density increases as the bead size decreases, representing smaller vessel diameter and higher MVD.

Figure 3 presents the structure of the defined fluid domain where fluid flows through and the simulated laminar flow field in this domain. The flow field shows that the flow passes through the void space generated by packed spheres, which is in line with our in-vitro experiments. High velocities are observed in the region near the confining wall. In the inner tube region, the velocity varies only in a small range because the spheres are mono-sized. The velocity in this region is lower than that near the wall.

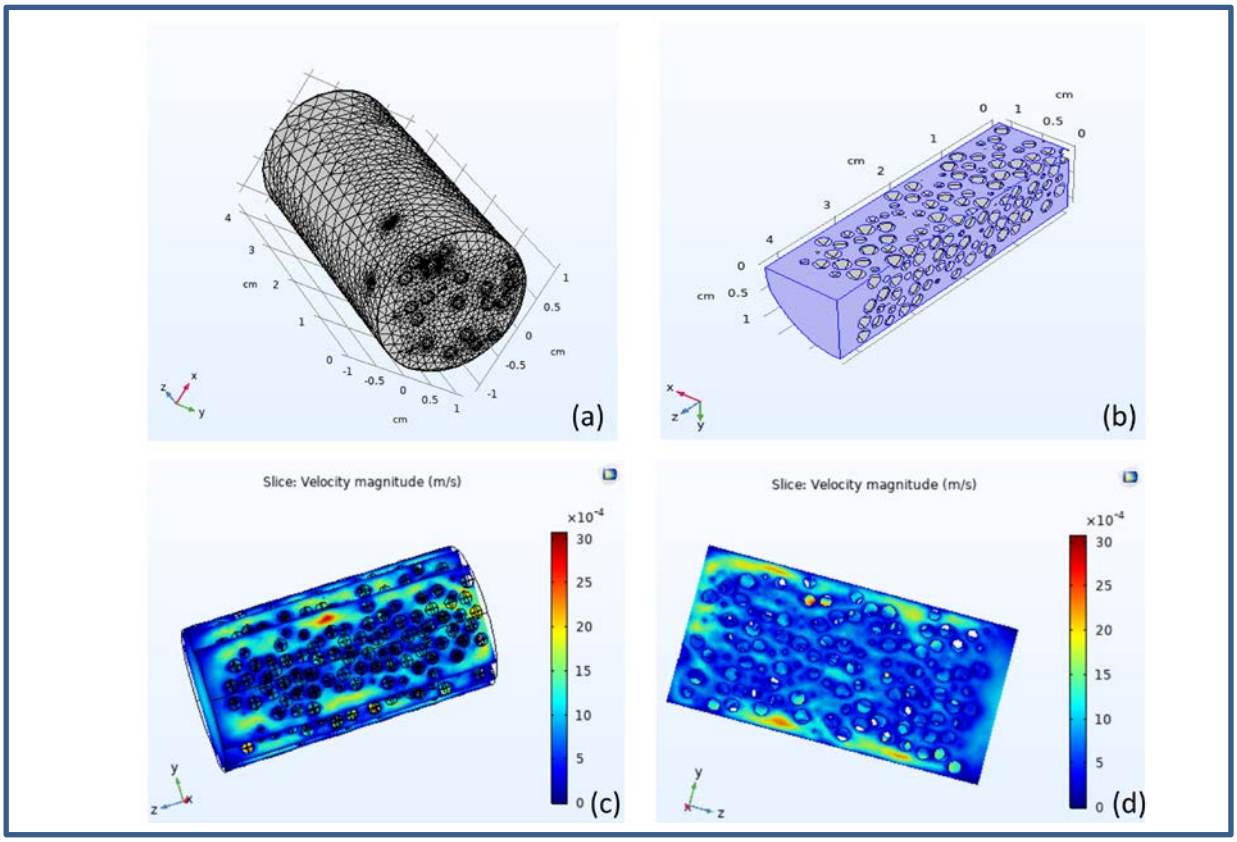

Figure 3. (a) shows the mesh of the defined fluid domain. (b) shows a cropped part of the defined fluid domain, showing that the spheres are removed from the solid cylinder. (c) shows the preliminary results of the simulated flow field through the phantom, and (d) shows one section of the flow field.

Conclusions

In this work, an in-silico simulation framework to study the UCA dynamics through microvascular networks mimicked by porous media was developed. A preliminary result of the flow field in the phantom was obtained. As a next step, the changes of particles' concentration over time, representing the UCA, will be analyzed and further employed for input-ouput analysis, enabling the estimation of velocity and dispersion. Based on that, the relationship between UCA dynamics and microvascular arthitecture will be further investigated, and compared with our in-vitro experimental results.

References

[1]. Folkman J, Role of angiogenesis in tumor growth and metastasis, Seminars in Oncology, 29: 15-18, 2002.

[2]. Weidner N, Carroll PR, Flax J, Blumenfeld W and Folkman J, Tumor angiogenesis correlates with metastasis in invasive prostate carcinoma, The American journal of pathology, 143: 401-409, 1993.

[3]. Russo G, Mischi M, Scheepens W, de la Rosette JJMCH, Wijkstra H, Angiogenesis in prostate cancer: onset, progression and imaging, BJU international, 110: 794-808, 2012.

[4]. Kuenen MPJ, Mischi M and Wijkstra H, Contrast-enhanced diffusion imaging for localization of prostate cancer, IEEE Transactions on Medical Imaging, 30: 1496-1502, 2011.

[5]. van Sloun RJG, Demi L, Postema AW, de la Rosette JJMCH, Wijkstra H and Mischi M, Ultrasound-contrast-agent dispersion and velocity imaging for prostate cancer localization, Medical Image Analysis, 35: 610-619, 2016.

[6]. Kuenen MPJ, Saidov TA, Wijkstra H and Mischi M, Contrast ultrasound dispersion imaging for prostate cancer localization by improved spatiotemporal similarity analysis, Ultrasound Med. & Biol., 39: 1631-1641, 2013.

[7]. Kuenen MPJ, Saidov TA, Wijkstra H, de la Rosette JJMCH and Mischi M, Correspondence-spatiotemporal correlation of ultrasound contrast agent dilution curves for angiogenesis localization by dispersion imaging, IEEE Transactions on Ultrasonics, Ferroelectrics, and Frequency control, 60: 2665-2669, 2013.

[8]. Chen P, Turco S, van Sloun R, Pollet A, den Toonder J, Wijkstra H, and Mischi M, Investigation of the relationship between microvascular architecture and ultrasound-contrast-agent kinetics by controlled porous media, The 25th European symposium on Ultrasound Contrast Imaging, 2020.

Observations of monodisperse microbubble resonance by an 'Acoustical Camera'

S. Spiekhout[1], J.D. Voorneveld[1], B. van Elburg[3], G. Renaud [2], G. Lajoinie[3], T.J. Segers[3], M. Versluis[3], N. de Jong[1,2], J.G. Bosch[1]

[1] Department of Biomedical Engineering, Thorax Center, Erasmus MC University Medical Center, Rotterdam, the Netherlands
[2] Laboratory of Acoustical Wavefield Imaging, Faculty of Applied Sciences, Delft University of Technology, Delft, the Netherlands
[3] Physics of Fluids Group, Technical Medical (TechMed) Center and MESA+ Institute for Nanotechnology, University of Twente, Enschede, the Netherlands
Corresponding author: s.spiekhout@erasmusmc.nl

Introduction

Monodisperse microbubbles (MBs) hold great promise for improved ultrasound applications. With recent developments in microfluidics, reliable production methods for MBs with narrow size distributions at high volume rates have become available [1,2]. However, it cannot be assumed a priori that a monodisperse MB size distribution will automatically result in a uniform acoustic response for each MB. In this work, we focus on assessing the uniformity of the acoustical response of individual monodisperse MBs with the aid of an 'acoustical camera' [3-5], by finding the driving frequency which produces the strongest acoustic amplitude response, and comparing this to a polydisperse bubble population.

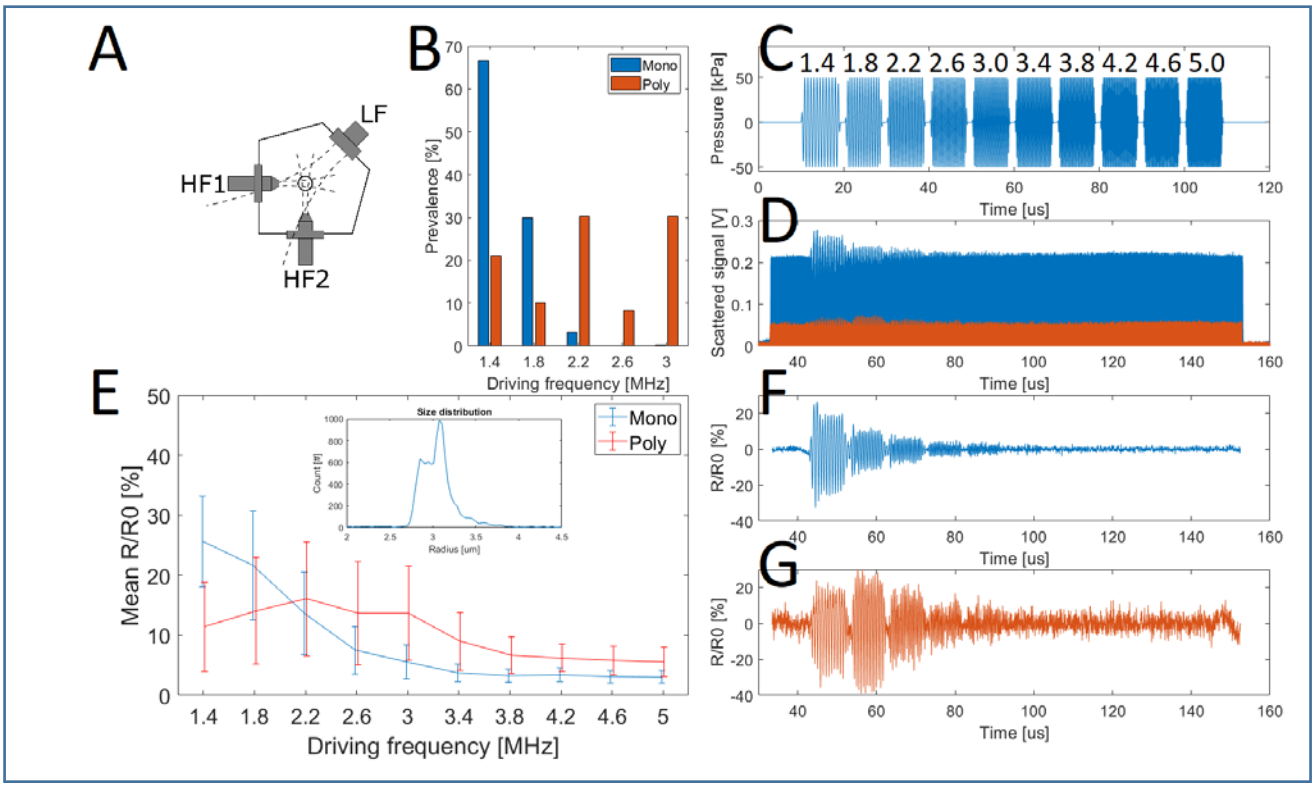

Figure 1.A. Schematic of the acoustical camera setup, three transducers with overlapping foci. B. prevalence of the maximum amplitude response over the different driving frequencies for the polydisperse (n=109) and monodisperse (n=435) bubble populations. C. LF excitation train, with frequencies in MHz. D. Two exemplary raw measurements from the monodisperse population. E mean radial strain as a function of driving frequencies, the error bars display the standard deviation. The inset of 1E shows the size

distribution of the monodisperse MB population, with a mean radius of 3 µm. F and G the radial strain as calculated from the data of 1D for a bubble from the monodisperse and polydisperse populations, respectively.

Methods

The acoustical camera, shown schematically in Fig. 1A, consists of a pentagonal watertank filled with a heavily diluted MB solution, and three transducers with overlapping foci. Pressure variations are induced by a broadband low-frequency (LF) transducer (Precision Acoustics, 1-9 MHz), while a set of high-frequency (HF) transducers (Precision Acoustics, 25 MHz), one transmitting (HF1) and the other receiving (HF2), are used to interrogate periodically the focal zone, which measures about 0.1 mm^3. A bubble in the focus will vibrate due to the LF transducer signal. HF2 receives the signal of HF1 that is scattered by the bubble, which is effectively amplitude modulated by the bubble's changing radius during LF vibrations. The fluid inside the watertank is mildly stirred, such that fresh bubbles enter the interrogation area frequently, while bubble movement is kept to a minimum during the interrogation time of 120 µs. The HF pulse is an untapered 3000-cycle burst of 500 kPa peak pressure. The LF pulse sequence, shown in Fig. 1C, is a series of ten separate pulses, with frequencies ranging from 1.4 MHz to 5 MHz in steps of 400 kHz. Each pulse is 10 µs, Hanning-tapered with 50 kPa peak pressure. The LF sequence is centered inside the 120 µs HF pulse such that a 10 µs non-modulated reference signal before and after the LF sequence is available. The polydisperse MBs were C_4F_{10}-filled phospholipid-shelled bubbles that have been obtained by replacing the headspace from a vial of SonoVue with C_4F_{10} before following the preparation instructions. The monodisperse, phospholipid, C_4F_{10}-filled MBs were produced in a flow-focusing microfluidic device [1,2], and their size distribution – centered around a radius of 3 µm, with the highest peak at 3.1 µm - is shown in Fig. 1E-inset. Bubbles were diluted 250.000 times, resulting in 1600 bubbles/ml. Signals were recorded and stored at 5 Hz using an oscilloscope (Agilent 6000) for 30 minutes resulting in 10k recordings, for each of the two different MB populations. Raw signals, of which two examples are shown in Fig. 1D, were bandpass filtered (15-35 MHz) and demodulated. Next, the radial strain was calculated from the resulting envelope signal by dividing the high-pass filtered envelope signal by the low-pass filtered signal (both separated at 40 kHz). The strains, as calculated from the two examples of Fig. 1D, are shown in Fig. 1F and 1G. Only those results were included that show a clear bubble response, and where the envelope had a signal-to-noise ratio larger than 10 dB compared to the reference sections.

Results

The radial strain was determined as a function of the different driving frequencies for 109 bubbles from the polydisperse MB population, and for 435 bubbles from the monodisperse population. A reason for this difference in samples is the decreased scattering for smaller bubbles from the polydisperse MBs, which was not detected with this setup. The results for maximum amplitude response are given in the barplot shown in Fig. 1B. For the monodisperse population, 67 percent had the strongest amplitude response at 1.4 MHz, 30 percent at 1.8 MHz, and 2 percent at 2.2 MHz. For the polydisperse population, this was more widely spread out over the first of the five driving frequencies: 21, 10, 30, 8 and 30 percent for the 1.4, 1.8, 2.2, 2.6 and 3 MHz driving frequencies respectively. The mean excursion is shown in Fig. 1E. For the 1.4 and 1.8 MHz driving frequencies there was a greater radial excursion for the monodisperse bubbles, for the higher driving frequencies the polydisperse MBs had a greater excursion. The distribution of radial excursion over frequencies was much broader for the polydisperse group, indicated by the lower averages and larger standard deviations per frequency.

Conclusions

Following a simple Minnaert resonance model [6], for a C_4F_{10} gas bubble the resonance frequency $F_r=A/r$, (where A=2.85 Hz.m, r=radius), so strong responses are expected at frequencies ranging from 0.91 to 1.01 MHz (bubble radii of 2.8 to 3.1 µm). Due to the stiffness of the phospholipid coating, the resonance frequency is expected to increase to 1.6-1.8 MHz if a stiffness of 0.5 N/m is assumed [7]. Therefore, it is expected to observe the strongest bubble amplitude response in the lower driving frequencies, as was found

to be the case. In a next step we will measure the monodisperse MBs with smaller intervals around the expected resonance frequency to measure it more accurately. In future work, this setup will be used to study more complex bubble behavior like (sub)harmonic generation with monodisperse MBs. Additionally, a more sophisticated Rayleigh-Plesset-Marmottant type model will be applied to study individual differences in more detail.

References

[1]. T.J. Segers, A. Lassus, P. Bussat, E. Gaud, P. Frinking, Improved coalescence stability of monodisperse phospholipid-coated microbubbles formed by flow-focusing at elevated temperatures, Lab on a Chip 19.1 (2019), pp. 158–167.

[2]. B. v Elburg, G. Collado Lara, G. Bruggert, T.J. Segers, M. Versluis, G. Lajoinie, Feedback control of a microbubble generator producing one million monodisperse bubbles per second. (under review, 2020).

[3]. G. Renaud, J.G. Bosch, A.F.W. van der Steen, N. de Jong, An acoustical camera for in vitro characterization of contrast agent microbubbles, Appl. Phys. Lett. 100, 101911 (2012).

[4]. G. Renaud, J.G. Bosch, A. F. W. van der Steen, N. de Jong, Chirp resonance spectroscopy of single lipid-coated microbubbles using an “acoustical camera”, The Journal of the Acoustical Society of America 132, EL470 (2012).

[5]. G. Renaud, J.G. Bosch, A.F.W. van der Steen, N. de Jong, Low-amplitude non-linear volume vibrations of single microbubbles measured with an ‘acoustical camera’, Ultrasound in Medicine & Biology, Volume 40, Issue 6 (2014), p.p. 1282-1295.

[6]. M. Minnaert. XVI. On musical air-bubbles and the sounds of running water, The London, Edinburgh, and Dublin Philosophical Magazine and Journal of Science, 16:104 (1933), pp. 235-248.

[7]. M. Versluis, E. Stride, G. Lajoinie, B. Dollet, T.J. Segers, Ultrasound Contrast Agent Modeling: A Review, Ultrasound in Medicine & Biology, Volume 46, Issue 9 (2020), p.p. 2117-2144.

Pharmacokinetic maps of PSMA-targeted nanobubbles in subcutaneous mouse tumors

***Chuan Chen*[1], *Simona Turco*[1], *Reshani Perera*[2], *Agata A. Exner*[2], *Massimo Mischi* [1]**

[1]*Eindhoven University of Technology, Eindhoven, the Netherlands*
[2]*Case Western Reserve University, Cleveland, Ohio, United States*
Corresponding author: C.Chen3@tue.nl

Introduction

Nanobubbles (NBs) are new ultrasound contrast agents with a diameter that is 10 times smaller than conventional microbubbles (MBs). Different from MBs, which are intravascular agents, NBs can permeate the vessel wall and target specific receptors overexpressed in cancer cells. This opens new possibilities compared to targeted MBs. MBs targeted to the vascular endothelial growth factor receptor 2 have shown promise for improving the diagnosis of prostate cancer (PCa), but the reported PCa detection rate in humans remains limited to 65% [1]. Besides vascular expressions, the prostate-specific membrane antigen (PSMA) is overexpressed in cancer cells and represents an ideal target for PCa imaging by NBs. PSMA-targeted NBs can bind to the receptors of PCa cells and show selective enhancement of PSMA-positive tumors (PC3-PIP) in mice. Significant differences have been reported in the enhancement of PSMA-positive vs. PSMA-negative tumors (PC3-FLU) in mouse models [2]. In previous work, we have shown the feasibility of quantifying the PSMA-NB binding effect by comparing relative regions-of-interest (ROI) enhancements through pharmacokinetic modeling [3]. Rather than analyzing average NB concentrations over entire ROIs, this work aims at developing pharmacokinetic parametric maps to assess the extravasation and binding effects of plain NBs and PSMA-NBs.

Methods

Four mice were implanted with a PC3-PIP (+PSMA) and a PC3-FLU (-PSMA) subcutaneous tumor in the contralateral flanks. Contrast-enhanced ultrasound (CEUS) loops were acquired using a Toshiba ultrasound scanner (PLT-1204BT probe) at 12 MHz and MI=0.1. After injecting a 200-μL bolus of plain NBs or PSMA-NBs, images were recorded at 1 and 0.2 fps for 5 and 30 min, respectively. Time-intensity-curves (TICs) were obtained at 5x5 pixel resolution and then further processed by singular value decomposition (SVD) filtering to suppress noise and artifacts. We adopted the theoretical model [4]: $C(t) = C_B(t) + C_G(t)$, $C_B(t) = a_B(t - t_0)e^{-\mu_B(t-t_0)}$, $C_G(t) = C_B(t) * (a_G e^{-\mu_G t})$, with t_0 being the injection time, a_B and a_G being the amplitudes of the bolus C_B and the latency C_G, and μ_B and μ_G being their rates, respectively. This model was fitted to TICs by a non-linear least-squares method. Additionally, the residual ratio, which represents the relative contribution of latency, was calculated as $r_{GB} = |C_G(t)|/|C_B(t)|$. The image analysis chain is illustrated in Fig. 1(a).

Results

Figure 1(b) shows parametric maps of r_{GB} (in dBs) displayed in the tumor ROIs for both plain NBs and PSMA-NB. In Fig. 1(c), means and standard deviations of r_{GB} and μ_G within each ROI are presented as error bars for all mice. It is shown that r_{GB} is significantly higher for PSMA-NBs compared to plain NBs in the PC3-PIP ROIs. On average, this residual ratio value is also higher in PC3-PIP ROIs than PC3-FLU ones when using PSMA-NBs.

Conclusions

In this work, pharmacokinetic analysis of plain NBs and PSMA-NBs was performed by estimating parametric maps to assess extravascular binding effects. Our result shows that the residual ratio, which represents the relative contribution of latency, is significantly higher for PSMA-NBs on PC3-PIP tumors. This suggests a longer retention period due to the extravascular binding effect.

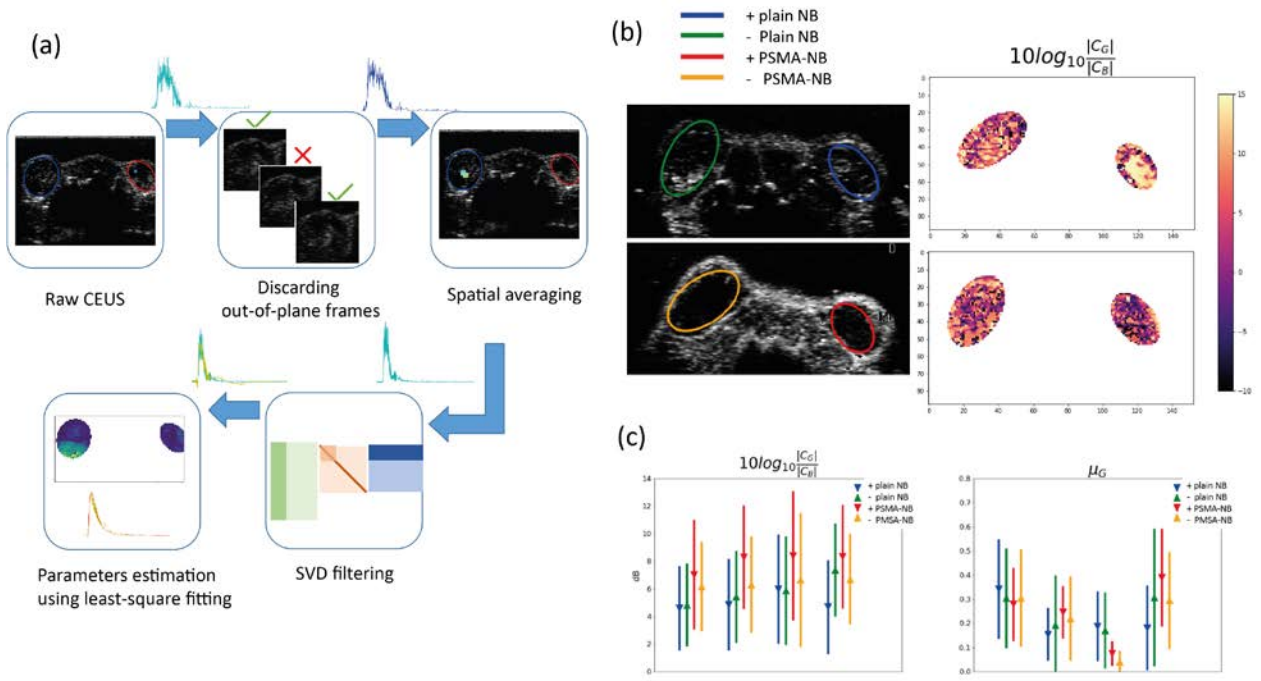

Figure 1. (a) Illustration diagram of CEUS data processing. (b) Four colored tumor ROIs representing CEUS by plain NBs and PSMA-NBs of PC3-PIP (+PSMA) and a PC3-FLU (-PSMA) subcutaneous tumors. The parametric maps of residual ratios in dB scale are shown on the right-hand side. (c) Bar plots (mean and standard deviation) calculated in the four ROIs on the parametric maps. The example in (b) belongs to the second group.

References

[1]. Smeenge, Martijn, et al. "First-in-human ultrasound molecular imaging with a VEGFR2-specific ultrasound molecular contrast agent (BR55) in prostate cancer: a safety and feasibility pilot study." Investigative radiology 52.7 (2017): 419-427.

[2]. Perera, Reshani, et.al. "Real time ultrasound molecular imaging of prostate cancer with psma-targeted nanobubbles." bioRxiv (2019): 634444.

[3]. Turco, Simona, et al. "Quantification of PSMA expression in prostate cancer by pharmacokinetic modeling of targeted ultrasound nanobubbles." 2019 IEEE International Ultrasonics Symposium (IUS). IEEE, 2019.

[4]. Orton, Matthew R., et al. "Computationally efficient vascular input function models for quantitative kinetic modelling using DCE-MRI." Physics in Medicine & Biology 53.5 (2008): 1225.

Ultrasound contrast agents enhance trehalose delivery to erythrocytes *in vitro* for dry storage at ambient temperatures

***Jonathan A. Kopechek*[1], Brett R. Janis[2], Mariah C. Priddy[1], Brian G. Harbrecht[3], Michael A. Menze[2]**

[1]*Department of Bioengineering, University of Louisville, Louisville, Kentucky, USA*
[2]*Department of Biology, University of Louisville, Louisville, Kentucky, USA*
[3]*Department of Surgery, University of Louisville, Louisville, Kentucky, USA*
Corresponding author: jonathan.kopechek@louisville.edu

Introduction

Blood transfusions are critical medical procedures for treatment of trauma and anemia. However, blood shortages often occur due to their limited shelf life of 5-6 weeks when refrigerated, and blood products are generally not available in austere environments where cold storage is not feasible. Therefore, new blood products are needed that can be stored for long periods of time at ambient temperatures. To address this unmet need we are utilizing ultrasound contrast agents *in vitro* to enhance intracellular delivery of trehalose, a naturally occurring cell protectant found in plants and lower animals that enables these organisms to survive water-limited states such as dehydration or freezing [1]. The objective of this study was to characterize ultrasound-enhanced delivery of trehalose into erythrocytes for dry preservation at ambient temperatures.

Methods

Cationic lipid microbubbles were added to erythrocyte solutions with 200 mM trehalose prior to ultrasound treatment in a static chamber or in a flow system [2]. Ultrasound pulses were transmitted into samples in 15-mL centrifuge tubes (static chamber) using a P4-1 probe on a Verasonics Vantage ultrasound imaging system. Acoustofluidic treatment was performed using a PDMS microfluidic device with integrated 5-MHz PZT transducers. Intracellular trehalose was quantified using a trehalose assay kit.

Results

Ultrasound treatment with higher concentrations of ultrasound contrast agents increased intracellular trehalose levels in erythrocytes *in vitro*. As shown in Figure 1, ultrasound treatment in a static chamber with a 10% microbubble concentration increased trehalose delivery in eryothrocytes to 40 mM, compared to 10 mM without ultrasound contrast agents (p<0.05). Acoustofluidic treatment further increased trehalose delivery above 80 mM with 10% microbubble concentration, compared to 55 mM without ultrasound contrast agents (p<0.05).

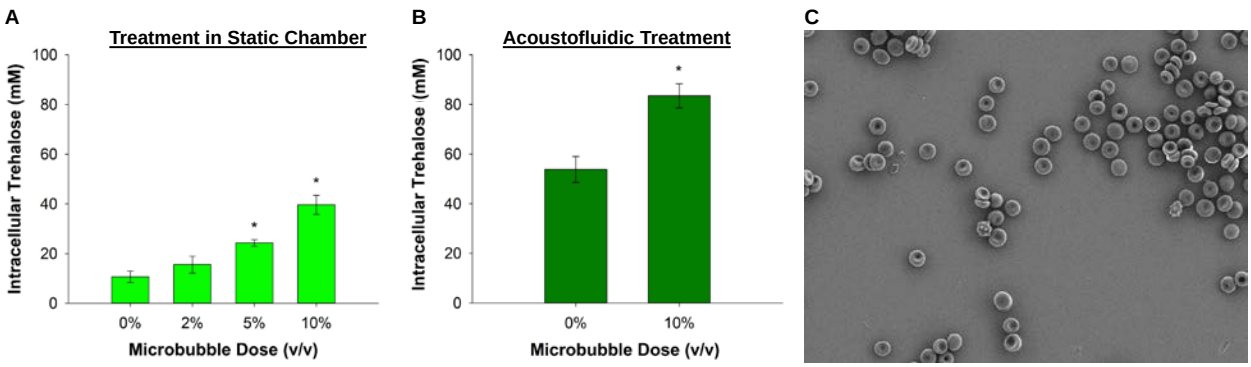

Figure 1: (A) Ultrasound treatment with higher microbubbles doses in a static chamber induced greater amounts of trehalose uptake in erythrocytes *in vitro*. *indicates significant increase above 0% microbubble dose (p<0.05). (B) Acoustofluidic treatment further increased trehalose uptake in erythrocytes. (C) Scanning electron microscopy imaging indicates recovery of intact erythrocytes after dehydration and storage at ambient temperatures for 6 weeks prior to rehydration.

Conclusions

The results of this study demonstrate that ultrasound contrast agents significantly enhance trehalose uptake in erythrocytes. Acoustofluidic treatment further enhanced trehalose delivery compared to bulk treatment of samples in a static chamber. Ultrasound-enhanced delivery of trehalose into erythrocytes conferred increased protection during desiccation and rehydration. These findings suggest that utilizing ultrasound contrast agents for delivery of trehalose into erythrocytes *in vitro* may enable long-term storage of erythrocytes at ambient temperatures to address current challenges with blood storage requirements.

Disclosures

Co-authors JAK, BRJ, and MAM disclose ownership in DesiCorp, Inc., which may financially benefit from products related to this research.

References

1. Hand, S.C. and M.A. Menze, *Molecular approaches for improving desiccation tolerance: insights from the brine shrimp Artemia franciscana.* Planta, 2015. **242**(2): p. 379-88.
2. Centner, C.S., et al., *Ultrasound-induced molecular delivery to erythrocytes using a microfluidic system.* Biomicrofluidics, 2020. **14**(2): p. 024114.

Microbubbles and ultrasound therapy improves antibody distribution in a 4T1 mouse tumor model

Marie Amate[1], Joseph Goldgewicht[1], Balasubramanian Sellamuthu[1], J. Stagg[1], François Yu[1,2]

[1]Centre de recherche du Centre hospitalier de l'Université de Montréal, Montréal, Canada
[2]Département de Radiologie, radio-oncologie et médecine nucléaire, Université de Montréal
[3] Université de Technologie de Compiègne
Corresponding author: francois.yu@umontreal.ca;

Introduction

The dense tumoral extravascular compartment is known to impede the diffusion of molecules, including antibodies (Ab), beyond the vascular space into the tumoral interstitium [1,2]. Microbubble (MB) oscillations in an ultrasound (US) field have been shown to increase vascular permeability and improve the targeted delivery of therapeutic compounds, ranging from small drugs to nanoparticles and even cells, notably to the brain [3-5]. In this study, we hypothesized that MB and US can improve the tumoral distribution and accumulation of intravenously injected Ab in a mouse model of breast cancer.

Methods

Murine mammary carcinoma tumor cells (4T1) were xenografted subcutaneously into female BalbC bilaterally (N=24). When the tumors reached 250 mm^3, an i.v. bolus (100 ug) of fluorescently labeled (AlexaFluor680, Invitrogen) Ab was injected i.v., followed by a slow infusion (4uL/min) of microbubbles (Definity) via the tail vein. Therapeutic US was delivered on the right tumor using a single element transducer (A303S, Olympus) with live guidance using contrast enhanced US imaging (CPS7, Sequoia, Siemens), whereas the left tumor served as a paired control. Therapeutic US consisted of 1 MHz 1.5 MPa 5000 cycle-pulses given every 5 s for 5 minutes, either as a continuous train (5000 cycles) or subdivided into short trains of 10 (500 x 10 cycles) or 40 (125 x 40 cycles) cycles spaced by 100 us (effective duty cycle during the ON phase of respectively 100%, 40% and 10%). Mice were then imaged by NIR optical fluorescence imaging (OptixMX2, GE) at 1h and 4h post therapy. Mice received and injection of vascular stain (Hoescht33342) before sacrifice. Tumors were collected for confocal microscopy imaging.

Results

US treated tumors showed an increase in NIR fluorescence imaging at 0h and 4h time points compared to the control side ($p<0.05$, ANOVA) with all three tested pulses (Figure 1). Since the baseline signal varied between animals, we verified if normalizing all the data by the signal on the untreated side at 0h would affect the observations. The normalized fluorescence signal similarly increased in all groups, with the highest antibody signal at 4h and on the ultrasound treated side ($p<0.05$, ANOVA), confirming that MB+US had an effect on antibody accumulation. These changes at the macroscopic level were corroborated by changes at the microscopic level: using confocal microscopy, Ab could be found penetrating away from the vessels in the treated tumor, whereas they remained restricted to the vascular space in the non-treated tumors (Figure 2).

Discussion and conclusions

Since the Ab accumulation was observed with all therapeutic pulses, with duty cycles ranging from 10% to 100% during the ON phase, it is very likely that the Ab accumulation are caused by cavitation rather than thermal effects. Taken together, these results are suggesting that MB and US can increase the macroscopic accumulation (biofluorescence) of antibodies in solid tumors, and improve the tumoral microscopic tumoral distribution and penetration beyond the vascular space. These findings could lead to improvements in the efficacy of antibody-based treatments against solid tumors.

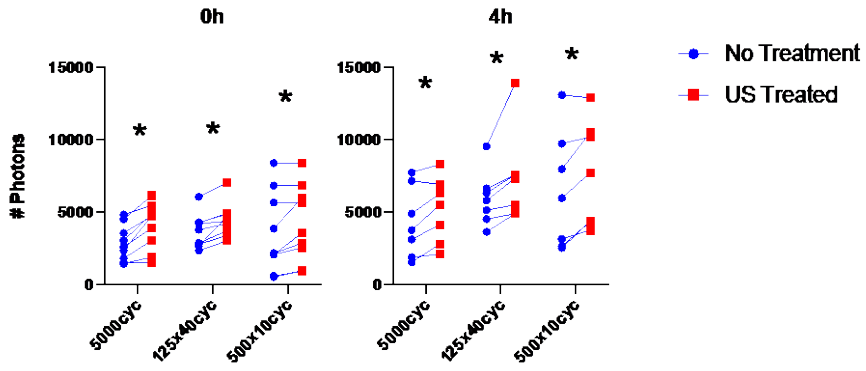

Figure 1. NIR Biofluorescence imaging showed an increase in antibody accumulation on the US treated side will all three US pulses at 0h and 4h post treatment ($p<0.05$, Anova).

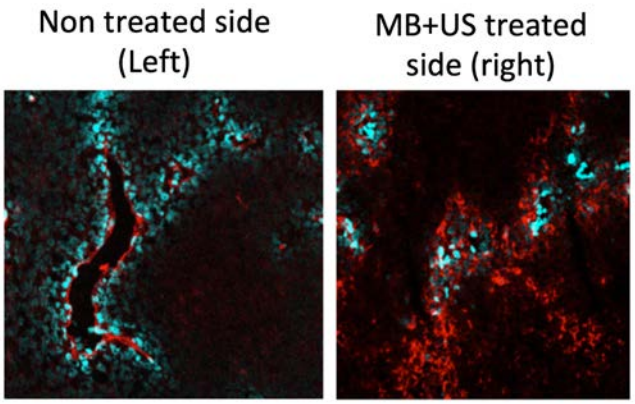

Figure 2. Vessels are stained in blue (perfusion stain injected IV before sacrifice) and antibodies carry a red fluorophore. Notice how the antibodies are located at the vessel border on the control side (left) and have diffused further into the tissue in the after MB+US therapy

[1]. Baker JHE, Kyle AH, Reinsberg SA, Moosvi F, Patrick HM, Cran J, et al. Heterogeneous distribution of trastuzumab in HER2-positive xenografts and metastases: role of the tumor microenvironment. Clin Exp Metastasis. 2018; 35: 691-705.

[2]. Primeau AJ, Rendon A, Hedley D, Lilge L, Tannock IF. The distribution of the anticancer drug Doxorubicin in relation to blood vessels in solid tumors. ClinCancer Res. 2005; 11: 8782-8.

[3]. Tinkov S, Coester C, Serba S, Geis NA, Katus HA, Winter G, et al. New doxorubicin-loaded phospholipid microbubbles for targeted tumor therapy: in-vivo characterization. J Control Release. 2010; 148: 368-72.

[4]. Burke CW, Alexander Et, Timbie K, Kilbanov AL, Price RJ. Ultrasound-activated Agents Comprised of 5FU-bearing Nanoparticles Bonded to Microbubbles Inhibit Solid Tumor Growth and Improve Survival. Mol Ther. 2013.

[5]. Burgess A, Ayala-Grosso CA, Ganguly M, Jordao JF, Aubert I, Hynynen K. Targeted delivery of neural stem cells to the brain using MRI-guided focused ultrasound to disrupt the blood-brain barrier. PLoS One. 2011; 6: e27877.

Ultrasound-Mediated Gemcitabine Delivery Improves Chemoradiation Therapy in Muscle-Invasive Bladder Cancer

***Jia-Ling Ruan*[1], Richard J. Browning[1], Yesna O. Yildiz[1], Luca Bau[2], Sukanta Kamila[3], Michael Gray[2], Christophoros Mannaris[2], James Thompson[1], Amy Elliott[1], Sean C. Smart[1], Lisa Folkes[1], Alix Hampson[1], Anthony P. McHale[3], John F. Callan[3], Borivoj Vojnovic[1], Eleanor Stride[2], Anne E. Kiltie[1]**

[1]Department of Oncology, MRC Oxford Institute for Radiation Oncology and Biology, University of Oxford, Oxford, UK
[2]Institute of Biomedical Engineering, University of Oxford, Oxford, UK
[3]Biomedical Sciences Research Institute, University of Ulster, Coleraine, Northern Ireland, UK
Corresponding author: eleanor.stride@eng.ox.ac.uk

Introduction

Bladder cancer is the ninth most common cancer worldwide with a high incidence rate in the elderly population. Since this population is not always suitable for, nor wishes surgery, chemoradiation therapy has become a widely-used bladder preservation method in managing muscle-invasive bladder cancers. Chemotherapeutic drugs like gemcitabine can enhance the radiosensitisation of tumours, but often cause local and systematic side effects in normal tissues.

Methods

We aimed to improve chemoradiation treatment efficacy by developing several novel gemcitabine delivery systems that can be coupled with ultrasound for controlled drug release. Firstly, we delivered gemcitabine along with microbubbles. Secondly, gemcitabine was coated onto microbubbles by biotin-avidin linkage. Finally, gemcitabine was encapsulated into liposomal nanoparticles and these liposomes were then bio-conjugated to microbubbles by biotin-avidin linkage. The particle size, concentration, and morphology of the gemcitabine delivery systems were characterised and the stability of gemcitabine in all systems assessed by biochemical assays and pharmacokinetics. The ultrasound-mediated delivery efficacy was investigated *in vitro* on RT112 cell lines and *in vivo* using a murine orthotopic muscle-invasive bladder cancer model. The first two microbubble methods were used to study the tumour growth delay and acute normal tissue toxicity in comparison with conventional chemoradiation therapy in the orthotopic model. Tumours in mice were irradiated at 6 Gy using a small animal radiation research platform. The effects of ultrasound and microbubbles alone were also tested. The tumour volumes were measured by 3D ultrasound imaging. Acute normal tissue toxicity was assessed in mice irradiated with 12 Gy to the bowel area. Mice were culled 3.75 days post-treatment and radiation-induced damage was assessed using an intestinal crypt assay.

Results

We showed that attaching drugs onto microbubbles increased the ultrasound mediated drug delivery efficacy *in vitro*. Encapsulation of gemcitabine into liposomes demonstrated prolonged gemcitabine retention both *in vitro* and *in vivo* compared to direct gemcitabine administration. Using gemcitabine decorated microbubbles, ultrasound-mediated gemcitabine delivery showed increase cleaved caspase 3 expression six hours post-treatment. We also observed significant tumour growth delay in the conventional chemoradiation and both microbubble groups A transient weight loss was observed for tumour-bearing mice whose treatment involved ultrasound and microbubble, but this resolved within 10 days post-treatment. A positive correlation was found between the weight loss at Day 3 post treatment and tumour growth delay. The crypt assay demonstrated that the ultrasound-mediated drug delivery methods did not exacerbate acute intestinal toxicity compared to conventional chemoradiation therapy.

Conclusions

We showed that ultrasound-mediated gemcitabine delivery is able to reduce acute intestinal normal tissue toxicity while retaining the same tumour control efficacy as concurrent gemcitabine-based chemoradiation. Our findings indicate that ultrasound-mediated gemcitabine delivery could be a promising new approach for improving chemoradiation therapy in muscle-invasive bladder cancer.

Safety of image-guided ultrasound cavitation treatment for liver cancer in an *in vivo* porcine model

***Sara B. Keller*[1], *Yak-Nam Wang*[2], *Dingjie Suo*[1], *Raymond S. Yeung*[3], *and Michalakis A. Averkiou*[1]**

[1]*Department of Bioengineering, University of Washington, Seattle*
[2]*Applied Physics Laboratory, University of Washington, Seattle*
[3]*Department of Surgery, University of Washington, Seattle*
Corresponding author: maverk@uw.edu

Introduction

Ultrasound-mediated drug delivery with microbubbles has the potential to treat a wide variety of diseases, from cancer [1] to stroke [2]. Since microbubbles are able to be both visualized and activated for therapy, they are ideal conduits for theranostic interventions. Despite promising studies both *in vitro* and *in vivo*, this technique is still not approved for clinical use. We hypothesize that one reason for the bottleneck between preclinical success and clinical adoption may be due to the lack of sufficient safety evaluations in relevant large animal models. The goal of this work was to evaluate the safety of ultrasound cavitation treatment (USCTx) on a healthy porcine model, using conditions previously proven effective at modulating the tumor vasculature and enhancing drug penetration in mice, [4]. We performed a 7-day survival study on 8 female pigs using a Philips EPIQ with S5-1 phased array probe operating in a modified PW Doppler mode as the focused ultrasound source to implement USCTx. We show through quantitative analysis of contrast enhanced ultrasound data, blood and urinalysis, and histology, that this technique is safe and this opens the way to a clincal evaluation.

Methods

Eight 3-5-month-old healthy female pigs weighing between 45 and 55 kg were enrolled in the study. A Philips S5-1 probe with modified research settings was used as the ultrasound source for treatment. The acoustic conditions for USCTx were created in pulsed wave (PW) Doppler mode, which was modified to transmit pulses at 1.6 MHz that were 200 cycles long at pressures of 1-5 MPa with a PRF of 50 Hz for 30 s. The derated pressure at the focus was calculated to be approximately 3 MPa. Sonovue microbubbles were used for both imaging and USCTx.

Pigs were treated with Sonovue and USCTx on Day 1, and overall health (ie, alertness, ability to eat food, etc.) was monitored through daily checkups by attending veterinary staff over the course of one week. Pigs were treated again on Day 7 to evaluate immediate tissue damage. Blood and urine were taken before and after treatment on Day 1 and again on Day 7. Quantitative contrast enhanced ultrasound was performed to evaluate any changes in perfusion as a result of treatment.

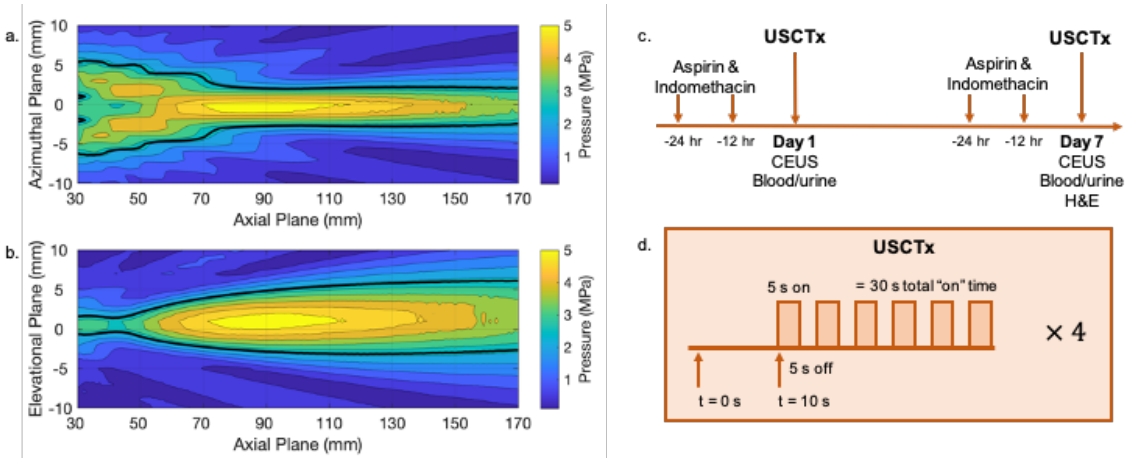

Figure 1. Measured ultrasound field in water from the S5-1 phased array probe used for USCTx (a-b). Overview of experimental study, including timeline (c) and treatment protocol (d).

Results

All animals tolerated USCTx with no adverse clinical signs. Blood liver enzymes were not shown to significantly vary ($p > 0.05$) either immediately after USCTx or seven days after USCTx as compared to the initial baseline sample.

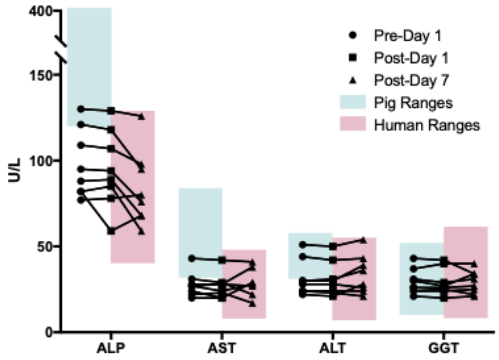

Figure 2: Blood liver enzyme results from before treatment on Day 1, after treatment on Day 1, and 7 days post treatment. No significant differences were observed ($p > 0.05$). The blue squares indicate ranges taken from [5]. The pink squares represent standard human clinical ranges.

Pre- and post-treatment contrast-enhanced ultrasound (CEUS) exams were used to show immediate changes in vascularity following treatment. Contrast agent rise time (RT) was shown to not significantly vary between pre-USCTx and either immediately post- or 7 days post-USCTx. Finally, we saw no signs of damage in H&E stained slides.

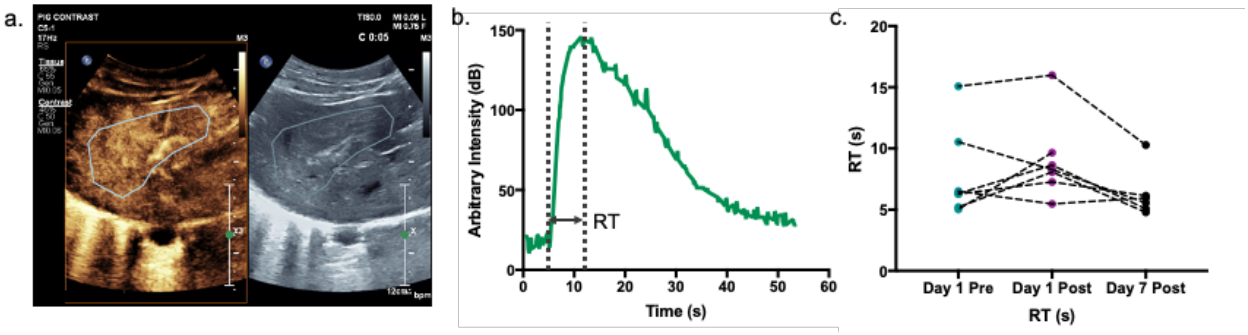

Figure 3: Quantitative CEUS results. (a) shows a representative DICOM image, with ROI outlined in blue. (b) shows a representative TIC, where RT is defined as the time of peak contrast enhancement minus the start time. (c) shows summary data from all animals. There were no significant differences between pre-USCTx and either immediately post-USCTx or 7 days post-USCTx.

In our previous work [4], we observed changes in perfusion in mice with HCC tumors as a result of USCTx using an acoustic amplitude that was approximately half of what was used in the current work. However, in that study, we only observed perfusion changes within the tumor vasculature, and not healthy liver. We hypothesized that the specificity of this effect on tumors was due in part to their unique vascular morphology; where the vasculature of normal liver is well-organized, the vasculature of liver tumors is abnormal and exhibits irregular branching patterns and tortuous geometries. Given that we performed these experiments on healthy pigs, it is reasonable to conclude that we did not see perfusion changes in the liver because healthy blood vessels are less sensitive to cavitation bioeffects. These hypotheses were confirmed in the current study, where even at twice the amplitude, no damage to healthy liver was observed. Finally, although we used a clinical ultrasound probe, the mechanical index (MI) exceeded the FDA limit of 1.9;

however, as a treatment procedure (not an imaging procedure), this would not necessarily be a limitation for clinical adoption of this technique.

Conclusions

The goal of the present work was to establish the safety of ultrasound cavitation treatment (USCTx) in a healthy porcine model. In our previous work [4], we showed that USCTx conditions at half the amplitude of what was used in the current study were sufficient to induce significantly increased drug penetration and vascular disruption. We did not observe any adverse effects from treatment as measured by analysis of blood liver enzyme levels, quantitative CEUS, and H&E staining. We believe that this indicates that the treatment regimen is safe within the timeframe studied, and could be a simple way of enhancing chemotherapy efficacy in the clinic.

References

[1] Goertz DE, Todorova M, Mortazavi O, Agache V, Chen B, Karshafian R, Hynynen K. Antitumor Effects of Combining Docetaxel (Taxotere) with the Antivascular Action of Ultrasound Stimulated Microbubbles. Woloschak GE, ed. PLoS One Public Library of Science, 2012;7:e52307.

[2] Molina CA, Ribo M, Rubiera M, Montaner J, Santamarina E, Delgado-Mederos R, Arenillas JF, Huertas R, Purroy F, Delgado P, Alvarez-Sabín J. Microbubble administration accelerates clot lysis during continuous 2-MHz ultrasound monitoring in stroke patients treated with intravenous tissue plasminogen activator. Stroke Lippincott Williams & Wilkins, 2006;37:425–9.

[3] Ferrara K, Pollard R, Borden M. Ultrasound Microbubble Contrast Agents: Fundamentals and Application to Gene and Drug Delivery. Annu Rev Biomed Eng 2007;9:415–47.

[4] Keller SB, Suo D, Wang Y-N, Kenerson H, Yeung RS, Averkiou MA. Image-Guided Treatment of Primary Liver Cancer in Mice Leads to Vascular Disruption and Increased Drug Penetration. Front Pharmacol Frontiers, 2020;11:1526.

[5] Radostits OM, Gay CC, Blood DC, Hinchcliff KW. Veterinary medicine: a textbook of the diseases of cattle, sheep, pigs, goats, and horses. 9th Editio. W.B. Saunders Company Ltd, 2000.

Nanodroplet triggered drug release for bone fracture healing

Jonathan P. May[1,2], Anastasia Polydorou[1], Qiang Wu[3], Sara Ferri[1,2], Eleanor Stride[3], Dario Carugo[1,2], Nicholas D. Evans[1]

[1] Bone and Joint Research Group, Faculty of Medicine, University of Southampton, Southampton General Hospital, Southampton, UK
[2] Department of Pharmaceutics, School of Pharmacy, University College London (UCL), London, UK
[3] BUBBL Group, Institute of Biomedical Engineering, University of Oxford, Oxford, UK
Corresponding author: j.p.may@soton.ac.uk

Introduction

A significant number of bone fractures (up to 10%) result in costly and debilitating delayed/non-union fractures, affecting patients' quality of life and presenting a significant financial burden for the health service [1]. New treatments are urgently required; however, systemic delivery of bone anabolic molecules is often sub-optimal and can lead to undesirable side effects. This work utilises a stimulated-release nanoparticle drug delivery approach based on nanodroplets (NDs): non-invasive ultrasound (US) responsive nano-sized vehicles [2]. We hypothesized that NDs could be used as stimuli-sensitive delivery vehicles to carry BIO – a GSK-3B inhibitor known to both activate Wnt signaling and promote bone cell differentiation [3] – and to release it under ultrasound stimulation at the site of bone fracture.

Methods

NDs were prepared by sonication of a mixture of DSPC/Chol/DSPE-PEG_{2000} (72:20:8 mol%) and liquid perfluorocarbon (PFB, 100 µL) at -7 to -12°C. For 6-bromoindirubin-3-oxime (BIO)-loaded NDs (BIO-NDs), BIO (8 mol%, drug:lipid 1:9) was added to the lipid mixture before sonication. Size and concentration of NDs was measured by dynamic light scattering (DLS) and nanoparticle tracking analysis (NTA). Ultrasound-mediated vaporisation of NDs was achieved using a 1 MHz focused ultrasound transducer with pressures of 1.1 – 1.98 MPa and a 5% duty cycle. Drug encapsulation efficiency and stability of the ND formulation was measured by HPLC. ND cytotoxicity was assessed in vitro, using primary, patient derived, bone marrow stromal cells (BMSCs), with a cell metabolic activity readout (Alamar Blue®). The activity of ND-encapsulated or released BIO was measured using a 3T3 Wnt-pathway reporter cell line with luciferase readout. Preliminary in vivo studies were performed in WT-MF1 mice (age: 8-12 wks) in a femoral bone hole defect model (~1 mm dia.). Biodistribution of DiR-labelled NDs (100 µL, 10^9 NDs/mL, i.v.) were studied via IVIS imaging at 48 h.

Results

NDs were studied by DLS (Z-average: 235.1 nm; PDI 0.137) and this was in good agreement with NTA (size 205.6 ± 7.4 nm; concentration 5.55 ± 0.22 x10^{11} particles/mL). BIO-NDs were stable on storage in PBS at 4°C (10 days) and retained >90 % of encapsulated BIO in PBS at 37°C (4 h). On US stimulation 98.3 ± 0.7 % of encapsulated BIO was released over a time period of 300 s. Although, BIO-NDs were stable in PBS, on incubation in serum-containing medium 23.8 ± 8.3 % BIO was released over a period of 24 h, as measured by HPLC. This was confirmed in cell activity assays, where 29 ± 1.2 % of encapsulated BIO had become bioavailable after a period of 24 h. BMSC viability was unaffected by unloaded-ND exposure up to 10^9 NDs/mL (24 h), and unloaded-NDs did not directly interfere with Wnt-signalling induced by BIO (5 µM). Preliminary biodistribution of DiR-NDs in a femoral bone hole defect model demonstrated increased localisation at the bone fracture site relative to that found in healthy mice or contralateral femurs (~2-fold).

Conclusions

NDs show considerable potential for US-induced localised release of BIO to promote bone healing. If BIO encapsulation stability can be improved through refinements to the formulation and drug loading, then

the data presented here demonstrates the potential for efficient drug release upon exposure to US. Our data supports the hypothesis that BIO could be delivered in this way to activate the Wnt-signalling pathway, which other reports have shown stimulates bone cell differentiation and potentially bone healing. Furthermore, we have preliminary evidence that the NDs are able to localise in the bone marrow, with double the preference for an injury site.

References

[1]. Einhorn TA, Gerstenfeld LC, Fracture healing: mechanisms and interventions, Nature Reviews Rheumatology, 11: 45-54, 2015.

[2]. Rapoport N, Phase-shift stimuli-responsive perfluorocarbon nanodroplets for drug delivery to cancer, Wiley Interdiscip Rev Nanomed Nanobiotechnol 4: 492-510, 2012.

[3]. Blagodatski A, Targeting the Wnt pathways for therapies, Molecular and Cellular Therapies 2: 28, 2014.

The effects of ultrasound and microbubbles in the paracellular permeability of an *in vitro* blood retinal barrier model

***Charis Rousou*[1,2], *Josanne S. de Maar*[2], *Lea Pirskanen*[3], *Marika Ruponen*[3], *Arto Urtti*[3,4,5], *Enrico Mastrobattista*[1], *Gert Storm*[1,6,7], *Chrit T.W. Moonen*[2], *Roel Deckers*[2]**

[1]*Department of Pharmaceutical Sciences, Utrecht University, the Netherlands*
[2]*Division of Imaging and Oncology, University Medical Center Utrecht, the Netherlands*
[3]*School of Pharmacy, University of Eastern Finland, Finland*
[4]*Faculty of Pharmacy, University of Helsinki, Finland*
[5]*Institute of Chemistry, St. Petersburg State University, Russia*
[6]*Department of Targeted Therapeutics, University of Twente, the Netherlands*
[7]*Department of Surgery, National University of Singapore, Singapore*
Corresponding author: R.Deckers-2@umcutrecht.nl

Introduction

Intravenous retinal drug delivery is limited by the presence of posterior-ocular barriers. These include the outer blood retinal barrier (oBRB) formed by retinal pigment epithelial cells and the inner blood retinal barrier (iBRB) formed by retinal endothelial cells. Like the blood brain barrier, retinal barriers consist of a cell layer that protects the neural retina from harmful substances in the blood circulation and allows only very few molecules to access it.

Ultrasound and microbubbles (USMB) is a proven minimally-invasive method to increase the permeability of retinal barriers in a controlled and reversible manner. Use of USMB can increase the efficacy of retinal drug delivery via the bloodstream [1-2]. In this study, we investigate the effect of ultrasound pressure and permeant physico-chemical properties on the paracellular permeability of an *in vitro* oBRB model.

Methods

Human-derived retinal pigment epithelial cells (LEPI) were cultured for 7 days on transwell membranes (membrane diameter 24 mm, porous size 0.4 μm) into a tight monolayer. Transwells were immersed in a custom-designed bath with PBS with the cell monolayer facing down. SonoVue microbubbles were prepared according to the manufacturer's instructions and 500 μl were injected into the bath using a curved-tip 19 G needle. Microbubbles were allowed to buoy up for 60 s so that direct contact with the cells was assured. Subsequently, ultrasound was applied using an unfocused single-element transducer (frequency = 1.5 MHz, PRF = 1 kHz, duty cycle = 10%, sonication time = 60 s) with acoustic peak negative pressure (P_{neg}) ranging between 0.1-0.6 MPa. A sham sample that was immersed in the PBS bath without USMB was used as a negative control (0 MPa). Cells treated for 10 min with EGTA served as positive control.

Directly after USMB treatment transwell inserts were placed into a 6-well plate on a plate shaker that maintained the samples at 37 ˚C. Various compounds with different physico-chemical characteristics such as molecular weight (M_W) and hydrophilicity (Table 1), were injected into the apical side (1.5 ml). Hydrostatic equilibrium was preserved by adding 2.6 ml of Hank's balanced salt solution (HBSS) into the basolateral side. Permeation of compounds through the cell monolayer was studied by acquiring samples from the basolateral side at 0, 15, 30, 45, 60 and 120 min post-treatment. The apparent permeability coeficcient (P_{app}, cm/s) was calculated using equation 1, where J (ng/s or CPM/s) is the compound flux across the cell monolayer, C_0 (ng/cm^3 or CPM/cm^3) is the initial compound concentration at the apical side and A (cm^2) is the surface area of the cell monolayer.

$$P_{app} = J/(C0 * A) \qquad \text{Equation 1}$$

Table 1. Physico-chemical properties and labelling of the compounds used to study the permeability of the retinal pigment epithelial cell monolayer.

Compound	Hydrophilic/lipophilic (LogD)	Molecular weight (Da)	Labelling
Propranolol	Lipophilic (1.26)	259	Radioactive
Mannitol	Hydrophilic (-4.67)	182	Radioactive
6-carboxufluorescein	Hydrophilic (-3.15)	376	Fluorescent
Dextran	Hydrophilic (not determined)	4,400	Fluorescent
Dextran	Hydrophilic (not determined)	20,000	Fluorescent

Results

As shown in Fig. 1, the P_{app} of the compounds studied decreased with increasing compound size and LogD for both the control and USMB-treated cells.

Treatment of the retinal pigment epithelial cell monolayer with USMB did not have a significant effect on the P_{app} of small molecules (propranolol, mannitol, 6-carboxyfluorescein), despite their differences in hydrophilicity (Fig. 1 A-C). In contrast, for the large hydrophilic dextran with M_w 4, 400 Da, an increase in the P_{app} with increasing ultrasound pressure was observed, which was significant at 0.6 MPa (Fig. 1 D). At this acoustic pressure, the total amount of dextran passed through the cell monolayer 120 min after USMB treatment was 4-fold higher compared to the negative control.

For 20,000 Da dextran the pressure dependent increase of the permeability coefficient was not significant. However, at 0.4 MPa the total amount of dextran permeated was still three times higher than the negative control.

Conclusions

Treatment of a retinal pigment epithelial cell monolayer with USMB did not significantly contribute to increasing the paracellular permeability of small hydrophilic and hydrophobic molecules. However, USMB did increase the paracellular transport of large M_W molecules such as 4,400 Da dextran, although this effect seems limited for very large molecules (i.e. 20,000 Da dextran). To conclude, the added benefit of USMB in the increase of paracellular permeability of drug models depends on the amplitude of acoustic pressure and the physico-chemical properties of the molecule to be delivered.

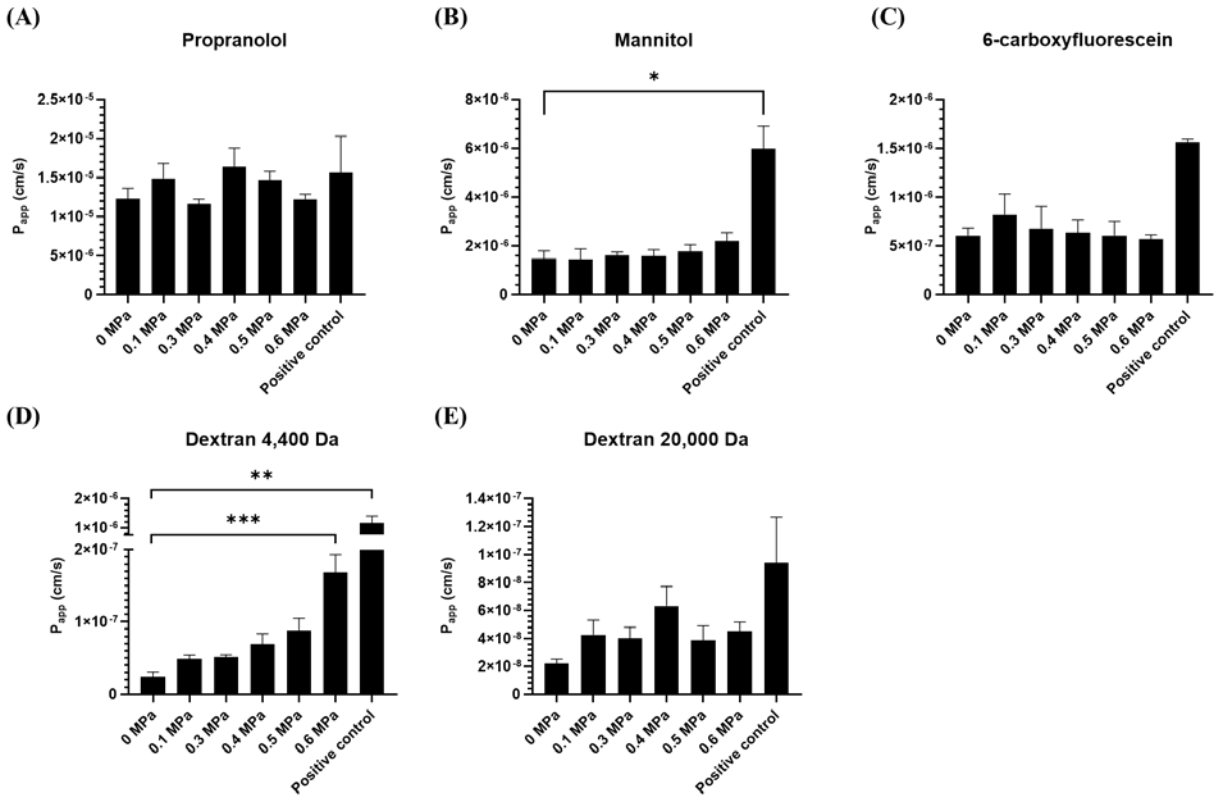

Figure 1. Apparent permeability coefficient (P_{app}, cm/s) of (A) propranolol, (B) mannitol, (C) 6-carboxyfluorescein, (D) 4,400 Da dextran and (E) 20,000 Da dextran after treatment of retinal pigment epithelial cell monolayer with USMB at various acoustic pressures (P_{neg} 0.1-0.6, MPa). In positive control samples, USMB treatment was replaced by a 10 min treatment with EGTA. Statistical analysis was performed using non-parametric one-way ANOVA and Kruskal-Wallis post-hoc test with *p<0.05; **p<0.01; *** p<0.001 as compared to 0 MPa.

References

[1]. Hirokawa T, Karshafian R, Pavlin CJ, Burns PN, Insonation of the eye in the presence of microbubbles, Ultrasound Med, 26:731–738, 2007

[2]. Park J, Zhang Y, Vykhodtseva N, Akula JD, McDannold NJ, Targeted and Reversible Blood-Retinal Barrier Disruption via Focused Ultrasound and Microbubbles, PLOS ONE, 7(8): e42754, 2012

High-throughput Microfluidics for Evaluating Microbubble Enhanced Delivery of Cancer Therapeutics in Spheroid Cultures

Matthew D. Bourn[1,2], Damien V. B. Batchelor[1], Nicole Ingram[2], James McLaughlan[2,3], P. Louise Coletta[2], Stephen D. Evans[1], Sally A. Peyman[1,2]

[1]School of Physics and Astronomy, University of Leeds, UK
[2]School of Medicine, University of Leeds, UK
[3]School of Mechanical Engineering, University of Leeds, UK
Corresponding author: S.peyman@leeds.ac.uk

Introduction

The inability of 2D cell monolayer culture models to accurately predict the *in vivo* efficacy of novel therapeutic treatments has resulted in the development of increasingly complex 3D cell culture models. Whilst 3D spheroid cultures present a step forwards in physiological relevance, the majority of studies are performed under static conditions with systems neglecting to incorporate any fluid flow. This fails to recreate the constant supply and removal of nutrients and waste products experienced *in vivo*, as well as failing to subject cells to appropriate shear stresses. This study reports a new microfluidic device containing an array of spheroid traps, into which multiple pre-grown colorectal cancer spheroids could be loaded and subject to microbubble-enhanced therapeutic treatments under continuous flow. Trap designs were adapted from single cell trapping arrays originally developed by Di Carlo *et al* and further considered by X. Xu *et al* [1,2].

The lack of drug penetration into solid tumours presents a major issue in the effective treatment of cancer. Microbubble (MB)-mediated sonoporation, induced by the application of ultrasound (US), offers a promising solution to this issue and has been studied extensively as a method by which drug uptake in cells can be increased [3 – 6]. The majority of these studies have been conducted on 2D monolayers or on static spheroid cultures, meaning the effectiveness of MB-mediated drug delivery under physiological rates of flow and shear stress is still relatively undocumented [7,8].

Spheroids were loaded on chip and exposed to both free and liposomal doxorubicin (DOX) co-delivered with MBs and US. Drug-loaded MBs (DLMBs) were produced by conjugating DOX-loaded liposomes to the MB surface using biotin-streptavidin binding. Confocal imaging and ATP assay results showed the MBs enhanced accumulation and efficacy in both free and liposomal DOX treatments.

Methods

Figure 1a shows the microfluidic device design consisting of a central trapping chamber alongside inlet and outlet serpentines. Serpentines are used to increase the hydraulic resistance of the channel and reduce the flow rate through the chip to capillary-like velocities (0.3 – 1 mm/s) [9]. Figure 1b shows pre-grown HCT116 – HFFF2 tumour spheroids loaded into the trap array. Figure 1c shows the experimental setup used to expose the spheroid chamber to ultrasound (US) and burst the MBs. Microbubbles were produced

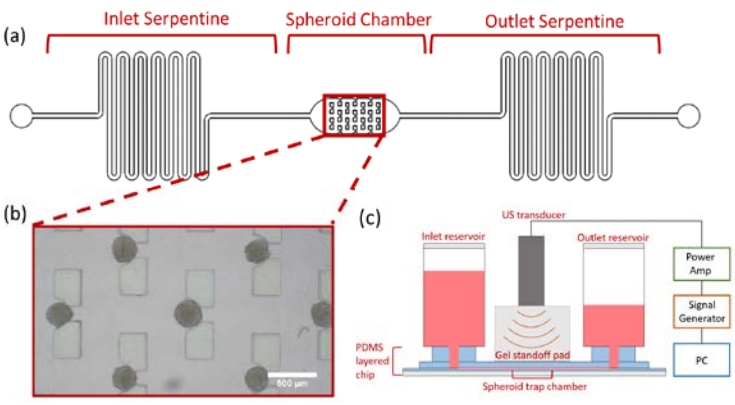

Figure 1: a) Microfluidic spheroid trap design b) Microscopy image of multiple CRC spheroids trapped within the array. c) Schematic of US setup with microfluidic chip and transducer.

using the microfluidic microspray method as described previously [10]. A 2.25MHz US transducer was placed above the chamber with a gel standoff pad used to ensure uniform US waveforms. A 400mV$_{pp}$, 2 second pulse with 1% duty cycle and 1 kHz pulse repetition frequency was applied and found to burst 99.96 % of microbubbles in the spheroid chamber. Spheroids were subject to therapeutic treatment for 8 hours then fresh media added, and spheroids maintained on-chip for a further 48 hours. Confocal fluorescence microscopy was then used to image the spheroids and an ATP viability assay used to determine spheroid viability.

Results

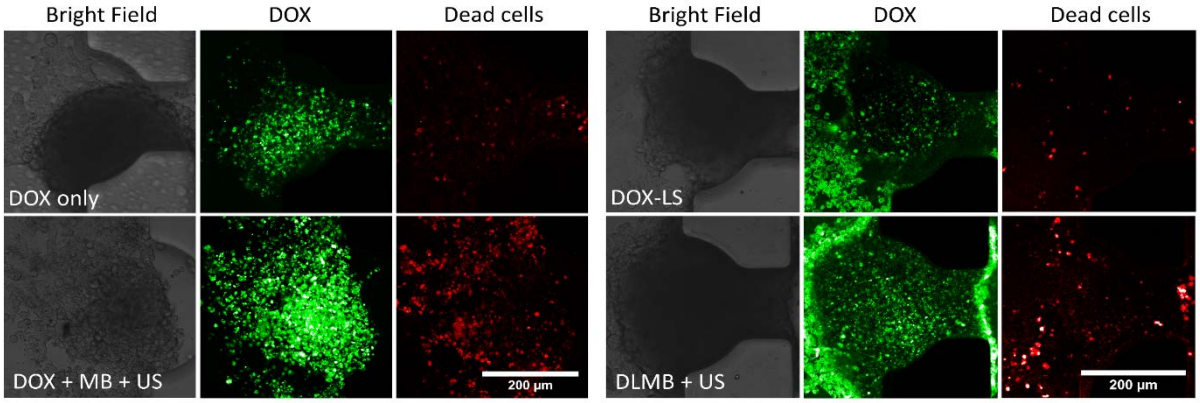

Figure 2: Bright field, DOX and dead cell fluorescent emission from spheroids exposed to DOX only, DOX + MB + US, DOX-LS and DLMB + US.

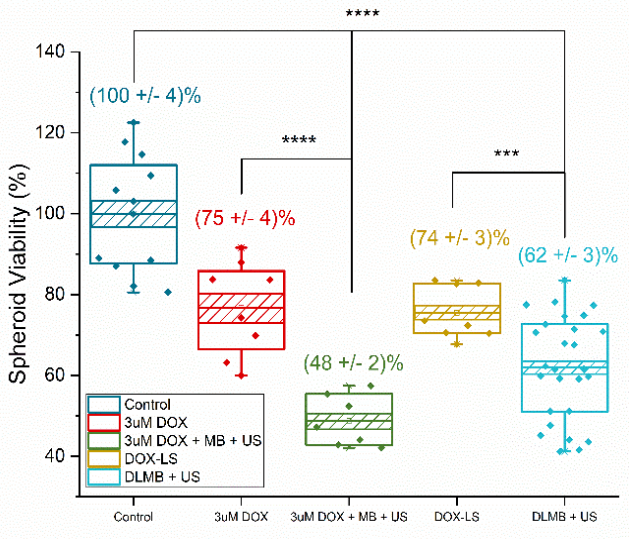

Figure 3: Box plot of spheroid viabilities for various therapeutic exposures. Each data point represents a single chip. Annotated values show Mean ± S.E. Hashed boxes show 95 % confidence interval.

Figure 2 shows fluorescent confocal images of DOX accumulation and dead cells taken 48 hours after spheroids were exposed to various treatments. Increased drug accumulation was observed throughout the spheroids when free DOX was co-delivered with MB + US. This was accompanied by degradation and mass cell death in the spheroid outer layers.

DLMB and US co-delivery was found to result in increased drug accumulation in the outermost layers of the spheroids. This indicates that the bursting of DLMBs does not result in instantaneous release of DOX from the liposomes. It is suggested that liposomes are imprinted onto the spheroid surface where they then release the encapsulated DOX. Figure 3 shows a plot of spheroid viability for each of therapeutic exposures shown in figure 2, showing increased drug efficacy and decreased spheroid viability when MB co-delivery was used.

Conclusions

This study has presented a new microfluidic device allowing for the trapping, culture and therapeutic testing of CRC spheroids under physiological flow conditions. Overall, the co-delivery of MBs + US with DOX has been shown to increase drug efficacy in both free and liposomal formulations.

References

[1] D. Di Carlo, L.Y. Wu, L.P. Lee, Lab Chip 6 (2006) 1445–1449.

[2] X. Xu, P. Sarder, Z. Li, A. Nehorai, Biomicrofluidics 7 (2013) 1–16.

[3] T. Boissenot, A. Bordat, E. Fattal, N. Tsapis, J. Control. Release 241 (2016) 144–163.

[4] M. Wang, Y. Zhang, C. Cai, J. Tu, X. Guo, D. Zhang, Sci. Rep. 8 (2018) 1–12.

[5] I. De Cock, E. Zagato, K. Braeckmans, Y. Luan, N. de Jong, S.C. De Smedt, I. Lentacker, J. Control. Release 197 (2015) 20–28.

[6] H. Lee, J. Han, H. Shin, H. Han, K. Na, H. Kim, J. Control. Release 283 (2018) 190–199.

[7] S. Roovers, J. Deprez, D. Priwitaningrum, G. Lajoinie, N. Rivron, H. Declercq, O. De Wever, E. Stride, S. Le Gac, M. Versluis, J. Prakash, S.C. De Smedt, I. Lentacker, J. Control. Release (2019) 112062.

[8] K. Logan, F. Foglietta, H. Nesbitt, Y. Sheng, T. McKaig, S. Kamila, J. Gao, N. Nomikou, B. Callan, A.P. McHale, J.F. Callan, Eur. J. Pharm. Biopharm. 139 (2019) 224–231.

[9] Elaine N. Marieb, K. H. Human Anatomy & Physiology. (2013).

[10] S.A. Peyman, R.H. Abou-Saleh, J.R. McLaughlan, N. Ingram, B.R.G. Johnson, K. Critchley, S. Freear, J.A. Evans, A.F. Markham, P.L. Coletta, S.D. Evans, Lab Chip 12 (2012) 4544–4552.

Engulfment of targeted microbubbles affects the acoustic response and sonoporation threshold

Inés Beekers[1], Simone A.G. Langeveld[1], Bram Meijlink[1], Antonius F. W. van der Steen[1,2], Nico de Jong[1,2], Martin D. Verweij[1,2], Klazina Kooiman[1]

[1]Department of Biomedical Engineering, Thoraxcenter, Erasmus University Medical Center, Rotterdam, the Netherlands
[2]Department of Imaging Physics, Delft University of Technology, Delft, the Netherlands.
Corresponding author: s.a.g.langeveld@erasmusmc.nl

Introduction

It is widely known that ultrasound-activated microbubbles are potent vascular drug delivery agents [1]. Far less is known about the interaction of a microbubble with a cell prior to the application of ultrasound, even though there have been reports that such an interaction does exist. For example, intact Sonazoid microbubbles can be taken up by Kupffer cells in the liver [2] and similar observations have been made for other macrophage populations and neutrophils outside of the liver [3]. Phagocytosis of microbubbles has been shown to occur within 5 min in Kupffer cells [4] and within 15 min in neutrophils [5, 6]. Although macrophages and neutrophils are the classic examples of phagocytic cells, endothelial cells that line blood vessels can also internalize particles through phagocytosis. Examples are blood clots [7], bacteria [8], micron-sized magnetic beads non-conjugated or conjugated to VEGFR2 antibody [9], and lipid droplets [10]. Recently, Aron et al. [11] showed there is lipid transfer between microbubbles containing the phospholipid lyso-PC and the membrane of A-549 cancer cells. In addition, these ultrasound-activated microbubbles induced a ~5-fold increase in sonoporation compared to microbubbles not containing the lyso-PC. It remains to be investigated if human vascular endothelial cells can phagocytose microbubbles and if so, how that influences sonoporation.

The aim of our study was to investigate the positioning of microbubbles in contact with the endothelial cell membrane using 3D confocal microscopy. The possible engulfment of microbubbles by endothelial cells was evaluated for non-targeted and targeted microbubbles functionalized with antibodies against $\alpha_v\beta_3$, a marker for angiogenesis [12], or CD31, an endothelial cell marker, [13]. For control-targeted microbubbles, the IgG1-κ isotype control antibody was used. Additionally, the oscillatory response and sonoporation potential of these four types of microbubbles was determined by ultra-high-speed Brandaris 128 recordings in combination with confocal microscopy.

Methods

Biotinylated microbubbles with a coating of DSPC (84.8 mol%), PEG40-stearate (8.2 mol%), DSPE-PEG2000 (5.9 mol%), and DSPE-PEG2000-biotin (1.1 mol%) were produced by the indirect method, i.e. using organic solvents, as previously described [14]. The fluorescent dye DiD was incorporated into the microbubble coating for visualization with confocal microscopy. Targeted microbubbles were made by avidin-biotin bridging as previously described [15] using biotinylated antibodies against $\alpha_v\beta_3$, CD31, or IgG1-κ. The microbubbles were added to human umbilical vein endothelial cells (HUVECs) grown to confluency in a CLINIcell such that the microbubbles would float up against the cells. After 5 min, the CLINIcell was mounted in the setup either in this orientation or reversed, the latter resulting in the bound targeted microbubbles being on top of the cells as illustrated in Fig. 1. Between 10 min and up to 2 h after addition of the microbubbles to the HUVEC, microbubble engulfment was studied with 3D confocal

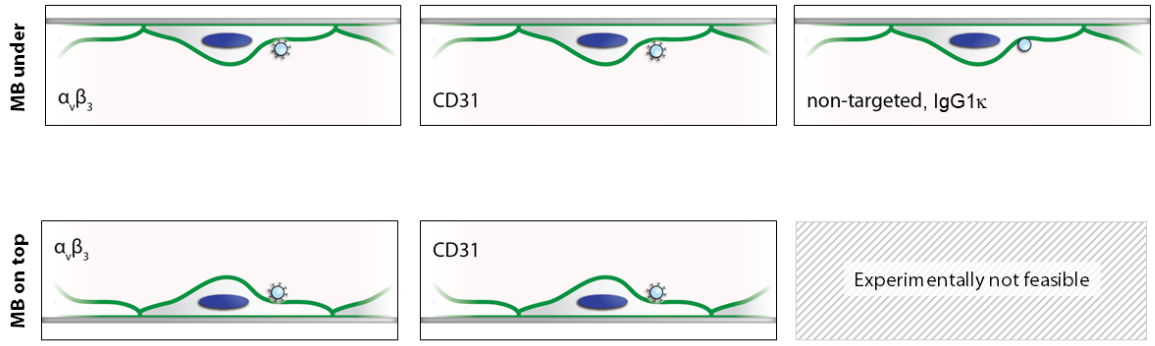

Figure 1. Schematic of setup showing the two different orientations of the cells with respect to the microbubbles: microbubbles (MB) under cells (top row) and microbubbles on top of cells (bottom row). Green: Cell membrane stained with CellMask. Note that due to buoyancy of microbubbles, the configuration with cells below is experimentally not feasible for non-targeted or control-targeted microbubbles with IgG1κ. The microscope objective scanned from above.

microscopy. In addition, the cellular response upon a single oscillating microbubble was imaged with time-lapse confocal microscopy (2.6 fps) up to 10 min after ultrasound (2 MHz, 250 kPa, 10 cycles) using the combined confocal microscope and Brandaris 128 ultra-high-speed camera [16]. Cell membrane integrity was monitored with CellMask Green and intracellular uptake by sonoporation evaluated using Propidium Iodide (PI). The microbubble oscillation was recorded with the Brandaris 128 (17 Mfps). The engulfment, microbubble radius, and PI uptake were quantified for each microbubble type.

Results

Fig. 2 shows typical examples of the four different type of microbubbles in all possible configurations. The gas core of the microbubbles has a different refraction index than the surrounding medium, which impeded visualization of the lower half of the microbubble in all images. Non-targeted (N=63) and IgG1κ-control targeted microbubbles (N=54) were always outside the cells which was also reflected in the engulfment depth of -0.4 µm (-0.9–1.3) (median (IQR)) for non-targeted and 0.2 µm (-1.6–1.1) for IgG1κ-control targeted microbubbles. In contrast, $\alpha_V\beta_3$-targeted microbubbles were always engulfed by the cells; the engulfment depth was 3.7 µm (1.7–6.1) for microbubbles under cells (N=54) and 3.3 µm (2.0–4.9) for microbubbles on top of cells (N= 39). For CD31-targeted microbubbles the engulfment depth was 0.5 µm (-0.5–3.9) for microbubbles under cells (N=50) and 0.2 µm (-0.8–1.5) for microbubbles on top of cells (N=41) thus ranging from partially to fully engulfed in the cell. The orientation of the microbubble with respect to the cell did not cause any significant differences in engulfed depth when comparing the same microbubble type. Engulfment was already observed at the start of the imaging, i.e. within 10 min after microbubble addition, and the amount of engulfment did not correlate with the incubation time of the microbubbles with the cells for the 2 h duration of the study. Phagocytosis of lipid-shelled microbubbles by Kupffer cells or neutrophils is mediated by surface receptors and has been shown to require the C3 component of serum complement [17]. Since culture medium in these *in vitro* studies was supplemented with serum containing complement, the non-targeted microbubbles were likely opsonized by the complement and therefore phagocytosed by the neutrophils or Kupffer cells [4, 6]. Although our cell culture medium also contained serum, the observed engulfment by HUVECs was dependent on the type of receptor the microbubbles were targeted to. Therefore, it is unlikely that opsonization by the C3 component played a role in our study.

All four types of microbubbles oscillated upon insonification. However, the microbubble excursion was smaller for engulfed microbubbles than for non-engulfed microbubbles, as shown in Fig. 3. This is in line with what Dayton et al. [18] reported for microbubbles phagocytosed by neutrophils, and is due to larger viscous damping of the oscillation.

The microbubble's radial excursion amplitude threshold for sonoporation was lower for $\alpha_v\beta_3$-targeted microbubbles (0.72 µm) than for CD31-targeted (0.94 µm), IgG1-κ-control targeted (0.93 µm), or non-targeted microbubbles (0.94 µm).

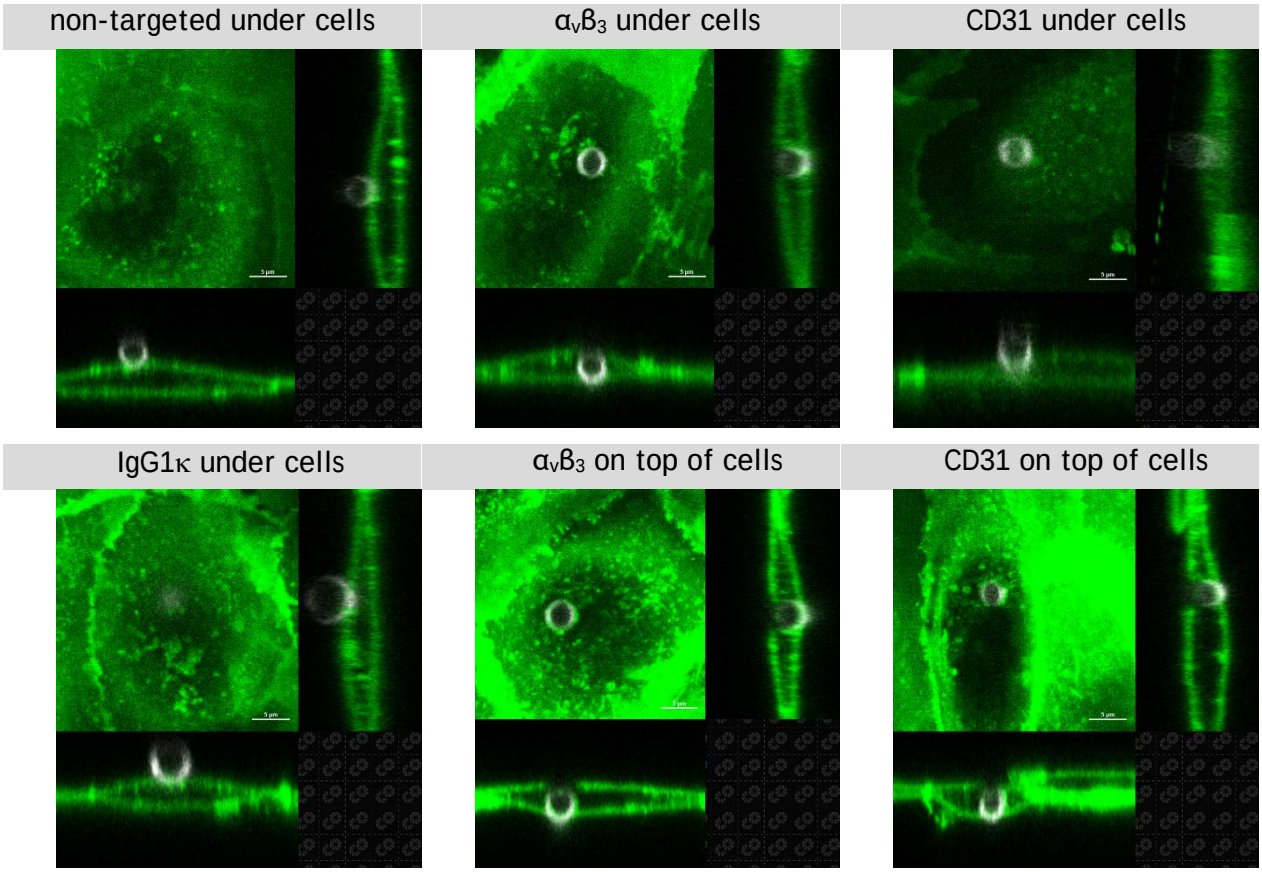

Figure 1. Typical confocal microscopy examples of microbubbles with HUVECs. Each image consists of three planes: the xy-plane (left top), the orthogonal yz-plane (right top), and orthogonal xz-plane (bottom). Note: the images are all presented with the microscope objective scanning from below the xy-plane (from right in the yz-plane). Microbubbles fluorescently labelled with DiD are shown in white; cell membrane stained with CellMask Green is shown in green. Scale bar corresponds to 5 µm and applies to all images.

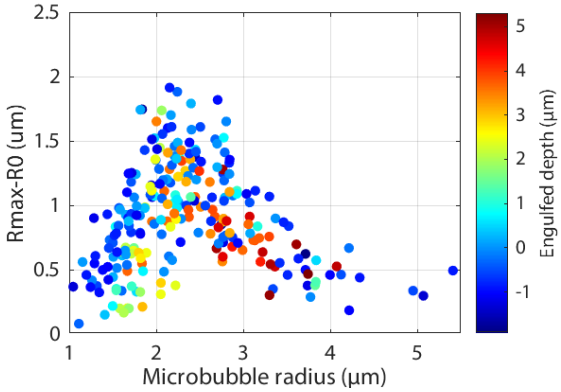

Figure 3. Microbubble excursion amplitude for varying engulfed depths. Rmax = radius at maximal excursion; R0 = radius at rest.

Conclusions

All microbubbles targeted to the angiogenic biomarker $\alpha_v\beta_3$ were fully engulfed by the HUVECs, while those targeted to the endothelial biomarker CD31 varied from partially to fully engulfed. However, non-targeted and IgG1κ control-targeted microbubbles were not engulfed at all and did not alter the cell membrane before insonification. Engulfed microbubbles showed lower excursion amplitudes than non-

engulfed microbubbles. At the same time, the threshold for sonoporation was lower for the engulfed $\alpha_v\beta_3$-targeted microbubbles than for all other microbubble types studied, suggesting they can enhance the susceptibility to sonoporation from within the cell. While in the current paradigm targeted microbubbles are regarded as objects attached to the outside of the cell membrane, the significant difference we found in the microbubble-cell configuration between targeted and non-targeted microbubbles may have substantial consequences for the molecular imaging and therapeutic potential.

References

[1]. K. Kooiman, S. Roovers, S. A. G. Langeveld, R. T. Kleven, H. Dewitte, M. A. O'Reilly, *et al.*, "Ultrasound-Responsive Cavitation Nuclei for Therapy and Drug Delivery," *Ultrasound Med Biol,* vol. 46, pp. 1296-1325, 2020.

[2]. V. Paefgen, D. Doleschel, and F. Kiessling, "Evolution of contrast agents for ultrasound imaging and ultrasound-mediated drug delivery," *Front Pharmacol,* vol. 6, p. 197, 2015.

[3]. G. M. Kindberg, H. Tolleshaug, N. Roos, and T. Skotland, "Hepatic clearance of Sonazoid perfluorobutane microbubbles by Kupffer cells does not reduce the ability of liver to phagocytose or degrade albumin microspheres," *Cell Tissue Res,* vol. 312, pp. 49-54, 2003.

[4]. K. Yanagisawa, F. Moriyasu, T. Miyahara, M. Yuki, and H. Iijima, "Phagocytosis of ultrasound contrast agent microbubbles by Kupffer cells," *Ultrasound Med Biol,* vol. 33, pp. 318-25, 2007.

[5]. J. R. Lindner, P. A. Dayton, M. P. Coggins, K. Ley, J. Song, K. Ferrara, *et al.*, "Noninvasive imaging of inflammation by ultrasound detection of phagocytosed microbubbles," *Circulation,* vol. 102, pp. 531-8, 2000.

[6]. H. Takeuchi, K. Ohmori, I. Kondo, K. Shinomiya, A. Oshita, Y. Takagi, *et al.*, "Interaction with leukocytes: phospholipid-stabilized versus albumin-shell microbubbles," *Radiology,* vol. 230, pp. 735-42, 2004.

[7]. J. Grutzendler, S. Murikinati, B. Hiner, L. Ji, C. K. Lam, T. Yoo, *et al.*, "Angiophagy prevents early embolus washout but recanalizes microvessels through embolus extravasation," *Sci Transl Med,* vol. 6, p. 226ra31, 2014.

[8]. M. Rengarajan, A. Hayer, and J. A. Theriot, "Endothelial Cells Use a Formin-Dependent Phagocytosis-Like Process to Internalize the Bacterium Listeria monocytogenes," *PLoS Pathog,* vol. 12, p. e1005603, 2016.

[9]. J. Thomas, D. Jones, L. Moldovan, M. Anghelina, K. J. Gooch, and N. I. Moldovan, "Labeling of endothelial cells with magnetic microbeads by angiophagy," *Biotechnol Lett,* vol. 40, pp. 1189-1200, 2018.

[10]. J. Aksnes, T. J. Eide, and K. Nordstrand, "Lipid entrapment and cellular changes in the rat myocard, lung and liver after long-term parenteral nutrition with lipid emulsion. A light microscopic and ultrastructural study," *APMIS,* vol. 104, pp. 515-22, 1996.

[11]. M. Aron, O. Vince, M. Gray, C. Mannaris, and E. Stride, "Investigating the Role of Lipid Transfer in Microbubble-Mediated Drug Delivery," *Langmuir,* vol. 35, pp. 13205-13215, 2019.

[12]. P. C. Brooks, R. A. Clark, and D. A. Cheresh, "Requirement of vascular integrin alpha v beta 3 for angiogenesis," *Science,* vol. 264, pp. 569-71, 1994.

[13]. H. M. DeLisser, P. J. Newman, and S. M. Albelda, "Molecular and functional aspects of PECAM-1/CD31," *Immunol Today,* vol. 15, pp. 490-5, 1994.

[14]. S. A. G. Langeveld, C. Schwieger, I. Beekers, J. Blaffert, T. van Rooij, A. Blume, *et al.*, "Ligand Distribution and Lipid Phase Behavior in Phospholipid-Coated Microbubbles and Monolayers," *Langmuir,* vol. 36, pp. 3221-3233, 2020.

[15]. I. Beekers, M. Vegter, K. R. Lattwein, F. Mastik, R. Beurskens, A. F. W. van der Steen, *et al.*, "Opening of endothelial cell-cell contacts due to sonoporation," *J Control Release,* vol. 322, pp. 426-438, 2020.

[16]. I. Beekers, K. R. Lattwein, J. J. P. Kouijzer, S. A. G. Langeveld, M. Vegter, R. Beurskens, *et al.*, "Combined Confocal Microscope and Brandaris 128 Ultra-High-Speed Camera," *Ultrasound Med Biol,* vol. 45, pp. 2575-2582, 2019.

[17]. J. R. Lindner, M. P. Coggins, S. Kaul, A. L. Klibanov, G. H. Brandenburger, and K. Ley, "Microbubble persistence in the microcirculation during ischemia/reperfusion and inflammation is caused by integrin- and complement-mediated adherence to activated leukocytes," *Circulation,* vol. 101, pp. 668-75, 2000.

[18]. P. A. Dayton, J. E. Chomas, A. F. Lum, J. S. Allen, J. R. Lindner, S. I. Simon, *et al.*, "Optical and acoustical dynamics of microbubble contrast agents inside neutrophils," *Biophys J,* vol. 80, pp. 1547-56, 2001.

A transwell-based system to investigate the pathways involved in sonoporation-mediated enhancement of endothelial permeability

Anurag N. Paranjape[1], Thiruganesh Ramasamy[1], Xucai Chen[1], Flordeliza S. Villanueva[1]

[1]Center for Ultrasound Molecular Imaging and Therapeutics, University of Pittsburgh, Pittsburgh, PA, USA; Corresponding author: villanuevafs@upmc.edu

Introduction

Using siRNAs and microRNAs is a novel approach against undruggable targets. However, a major hindrance in using RNA-based therapeutics is the absence of a robust delivery system across the vascular barrier. Ultrasound-targeted microbubble cavitation (UTMC) increases endothelial permeability and enhances RNA delivery, but the underlying mechanisms remain poorly understood. In this study we established an *in vitro* transwell-based system, ideal for studying the effects of UTMC on endothelial barrier permeability and the pathways affected.

Methods

We established an *in vitro* system using human coronary artery endothelial cells (HCAECs) grown to confluence on fibronectin-coated transwells with 0.4 µm pores to study the pathways regulating UTMC-mediated hyperpermeability. A custom-made water tank was used to house the 1-inch immersible ultrasound transducer. Lipid microbubbles (MBs) were made in-house with an average size of 2.8 to 3 µm. Effect of UTMC (f=1 MHz, 10 µs pulse duration, 10 ms pulse intervals for 20 s) on permeability at various acoustic pressures was assessed using transendothelial electrical resistance (TEER) and 4 kDa fluorescent dextran transfer as read-outs. Sonoporation and cell death were quantified using calcein-AM and propidium iodide as markers, while CellMask deep red was used to assess the area of cell coverage.

Results

Various conditions including the transwell pore sizes, insert diameter, number of cells seeded, duration of cell culture, and extra-cellular matrices, were standardized to get a uniform endothelial monolayer with membranous expression of adherens- and tight-junction proteins. We found that 2×10^5 cells seeded on the abluminal side on a fibronectin-coated 10.5 mm transwells with 0.4 µm pores formed a uniform endothelial monolayer after 48 hours, confirmed by lowest dextran permeability and high expression of membranous VE-cadherin, ZO-1, and CD31. Various UTMC parameters such as cell-to-MB ratio, ultrasound pressures, and pulse interval times were tested. With the ratio of 1:5 and 10 ms intervals, we observed pressure-dependent increase in cell death, sonoporation, and loss in area coverage. UTMC treatment resulted in moderate increase in dextran transfer (4 kDa FITC-dextran) at various time points with a concomitant measurable decrease in TEER. In the future, we plan to utilize this system to delineate the pathways involved in regulation of UTMC-induced hyperpermeability.

Conclusions

Our transwell-based system provides a model to study pathways that play a role in regulating UTMC-mediated hyperpermeability, which would be useful to optimize acoustic conditions for effective UTMC-mediated RNA therapeutics.

STAT3 decoy oligonucleotide-carrying microbubbles with pulsed ultrasound for enhanced therapeutic effect in head and neck tumors

***Thiruganesh Ramasamy*[1], *Xucai Chen*[1], *Bin Qin*[1], *Daniel E. Johnson*[2], *Jennifer R. Grandis*[2], *Flordeliza S. Villanueva*[1]**

[1]Center for Ultrasound Molecular Imaging and Therapeutics, University of Pittsburgh, Pittsburgh, PA, USA; [2]Department of Otolaryngology-Head and Neck Surgery, University of California San Francisco, San Francisco, CA, USA.
Corresponding author: villanuevafs@upmc.edu

Introduction

Signal transducer and activator of transcription-3 (STAT3) is an oncogenic transcription factor implicated in carcinogenesis, tumor progression and drug resistance in head and neck squamous cell carcinoma (HNSCC). A decoy oligonucleotide targeting STAT3 offers a promising anti-tumor strategy, but achieving targeted tumor delivery of the decoy with systemic administration poses a significant challenge. We previously showed the potential for STAT3 decoy-microbubbles in conjunction with ultrasound targeted microbubble cavitation (UTMC) to decrease tumor growth in murine squamous cell carcinoma [1,2]. As a next step towards clinical translation, we sought to determine the anti-tumor efficacy of our STAT3 decoy delivery platform against human HNSCC, and the effect of higher STAT3 decoy microbubble loading on tumor cell inhibition.

Methods

Two types of microbubbles were prepared to load STAT3 decoy. The synthesis of STAT3 decoy-loaded cationic lipid microbubbles (STAT3-MB) was reported previously [3]. Cationic liposome containing STAT3 Decoy was prepared by extrusion method first and conjugated to lipid microbubble via biotin-streptavidin interaction to form liposome-microbubble complex (STAT3-LPX). To evaluate *in vitro* anticancer efficacy, CAL33 cells (from human HNSCC) were treated with ultrasound and respective microbubble at a concentration equivalent to 10 microbubbles/cell with microbubble maximally loaded with decoy. UTMC was performed with a single element immersion transducer (1 MHz, 0.50 MPa PNP, 10 µs pulse duration, 1 ms pulse interval) for 10 s. Treatment efficacy was evaluated in terms of viability assay, apoptosis assay, and Hoechst 33342 staining. Anticancer efficacy *in vivo* was performed in a HNSCC-based xenograft model in immunodeficient mice. Therapeutic ultrasound was applied (1 MHz, 0.7 MPa PNP, 100 µs pulse duration repeated 5 times with 1 ms pulse interval every 2 s) during 15 min of STAT3-MB infusion for a total of 3 treatments at 3-day intervals. UTMC with microbubble carrying STAT3 decoy mutant (STAT3-MB-mut) and non-treated groups were used as controls. The tumor was serially imaged using a high-resolution 3-D ultrasound imaging system (Vevo 2100, VisualSonics). Tumor volume was automatically computed from the 3-D reconstructions of the outlines drawn on the cross-sectional images. Survival rate was calculated based on animal sacrifice once the tumor volume reached 1,000 mm^3. The antitumor efficacy was evaluated in terms of tumor volume and survival rate. In a separate group of animals, tumors were extracted 48 h after UTMC and analyzed for gene expression.

Results

UTMC with STAT3-MB *in vitro* caused significantly lower CAL33 cell viability compared to UTMC with STAT3-LPX (56.8±8.4% vs 84.5±8.8%, respectively, $p<0.05$). *In vivo*, UTMC with STAT3-MB had strong anti-tumor effects, with significantly less tumor burden and greater survival compared to that of UTMC with STAT3-MB-mut and untreated control groups ($p<0.05$) (Figure 1).

Conclusions

UTMC with STAT3-MB significantly decreases growth of human HNSSC tumors. These data set the stage for clinical translation of our microbubble platform as an imaged-guided, targeted delivery strategy for STAT3 decoy, or other nucleotide-based therapeutics, in human cancer treatment.

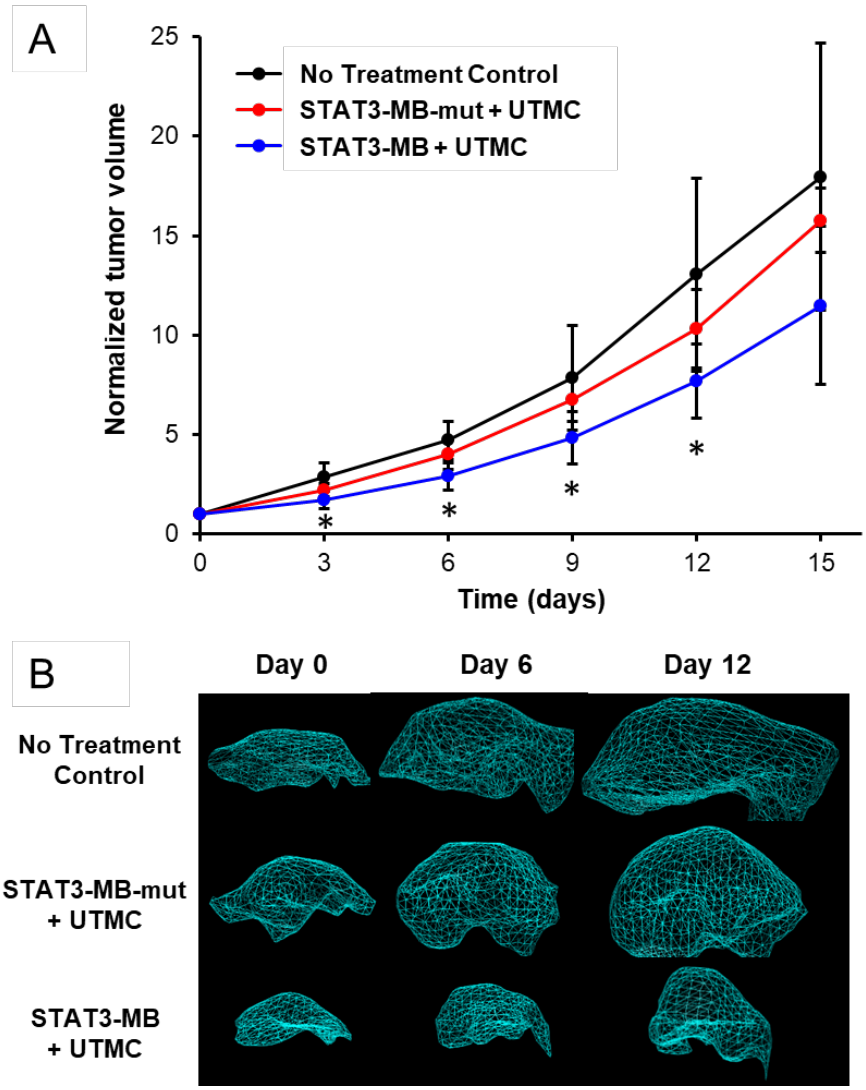

Figure 1. *In vivo* efficacy of UTMC-mediated STAT3 decoy delivery against human HNSCC xenografts. (A) Mean tumor volumes of CAL33 tumor-bearing immunodeficient mice (normalized to initial volume on day 0) for no treatment control (n=8), STAT3-MB-mut + UTMC (n=7), and STAT3-MB + UTMC (n=7). The normalized volumes for STAT3-MB + UTMC group were significantly lower than STAT3-MB-mut + UTMC and no treatment control on days 3, 6, 9, and 12 (*p<0.05). (B) Representative 3-D reconstruction of ultrasound-generated tumor volumes.

References

[1]. Chai EZP, et al, Targeting transcription factor STAT3 for cancer prevention and therapy, Pharmacology & Therapeutics 2016;162:86–97.

[2]. Grandis JR, et al, Constitutive activation of Stat3 signaling abrogates apoptosis in squamous cell carcinogenesis in vivo, Proc Natl Acad Sci USA 2000;97:4227-32.

[3]. Kopechek JA, et al, Ultrasound targeted microbubble destruction-mediated delivery of a transcription factor decoy inhibits STAT3 signaling and tumor growth, Theranostics 2015;5:1378-87.

The effect of the pulse length sonoreperfusion therapy

Francois T.H. Yu, Gary Yu, Xucai Chen and John J. Pacella

Center for Ultrasound and Molecular Imaging and Therapeutics, University of, Pittsburgh, Pennsylvania, USA

Corresponding author: pacellajj@upmc.edu

Introduction

Microembolization during PCI for acute myocardial infarction can cause microvascular obstruction **(MVO)**. MVO severely limits the success of reperfusion therapies, is associated with additional myonecrosis, and is linked to worse prognosis, including death. Long and short pulse ultrasound-targeted microbubble cavitation (UTMC) has been shown to increase perfusion in healthy and ischemic skeletal muscle [1, 2], in pre-clinical animal models of microvascular obstruction [3, 4], and in the myocardium of patients presenting with acute myocardial infarction [5, 6]. There is evidence that the observed microvascular vasodilation is driven by the nitric oxide pathway and purinergic signaling, but the time course of the response and the dependency on ultrasound pulse length is unknown. Therefore, we compared long (5000 cycles) and short pulse (500 × 10 cycles) ultrasound (1.5 MPa, 1 MHz) with an equivalent total number of acoustical cycles hence constant acoustic energy, in a rodent hindlimb model with and without microvascular obstruction (MVO).

Methods

In an intact rat hindlimb, we applied therapeutic ultrasound with a single element transducer (A303S, 0.5 inch, Olympus, Waltham, MA) using long pulses (1 MHz, 1.5 MPa, 5000 cycles, 3 sec pulse interval) or bursts of short pulses (1 MHz, 1.5 MPa, 500 x10 cycles, 100 us pulse interval, repeated every 3s) with the same total number of acoustic cycles, for 2 min, during intra-femoral infusion of lipid encapsulated perfluorobutane filled microbubbles (3.5 ±1.5 μm). Burst-replenishment imaging of the rat hindlimb muscle was performed using a clinical Sequoia ultrasound scanner in contrast mode (CPS, 7 MHz, 0.2 MI) during jugular venous infusion of Definity (2 mL/hr) to monitor the kinetics of perfusion for 30 min following therapeutic ultrasound (3 rats/group). Image intensities of the acquired perfusion cineloops were measured in regions of interest located under the therapeutic ultrasound beam to calculate perfusion (A×B in dB/s) in the microvasculature. Statistical analysis was performed using 2-way ANOVA and Holm-Sidak post-hoc testing (Prism 6, Graphpad software, La Jolla, CA).

Results

We found that (1) both short and long pulses resulted in increased perfusion (AxB), however the temporal responses were distinct (Figure 1A). Initially similar at baseline, perfusion immediately increased post SRP with the short pulse while it decreased with the long pulse. For the short pulse, the increased perfusion peaked between 3 and 15 min and stabilised near baseline values after 60 min. For the long pulse, after an initial spasmic response (5min), perfusion peaked at 15 min and remained high for up to 4h. Because the long pulse caused an initial spasm, we tested if the delayed response could have been caused by reactive hyperemia by inflating an angiocatheter balloon in the decending aorta to cause a 5 min occlusion in the muscle. The response following the balloon release did not ressemble the response of the long pulse (Figure 1B). Finally, we tested the RSP in our model of MVO and compared it with historical data. We found that the RSP was effective in reperfusing MVO in our hindlimb model, but the short pulse required 2 x 10 min treatments to restore blood volume, compared to 1 x 10 min treatment using the long pulse (Figure 1C). Histological analysis of hindlimb muscle post UTMC with either pulse configuration indicates no evidence of tissue damage or hemorrhage.

Conclusions

Our data support that short and long pulses can both cause vasodilation and improve sonoreperfusion therapy, as measured using contrast burst-replenishment imaging. Interestingly the long pulse (but not the short pulse) caused a sustained vasoactive response for up to 4h through a mechanism that remains to be identified. Our results support that the pulse length can be tuned to increase SRP efficacy but the clinical application and safety of the approach remains to be determined.

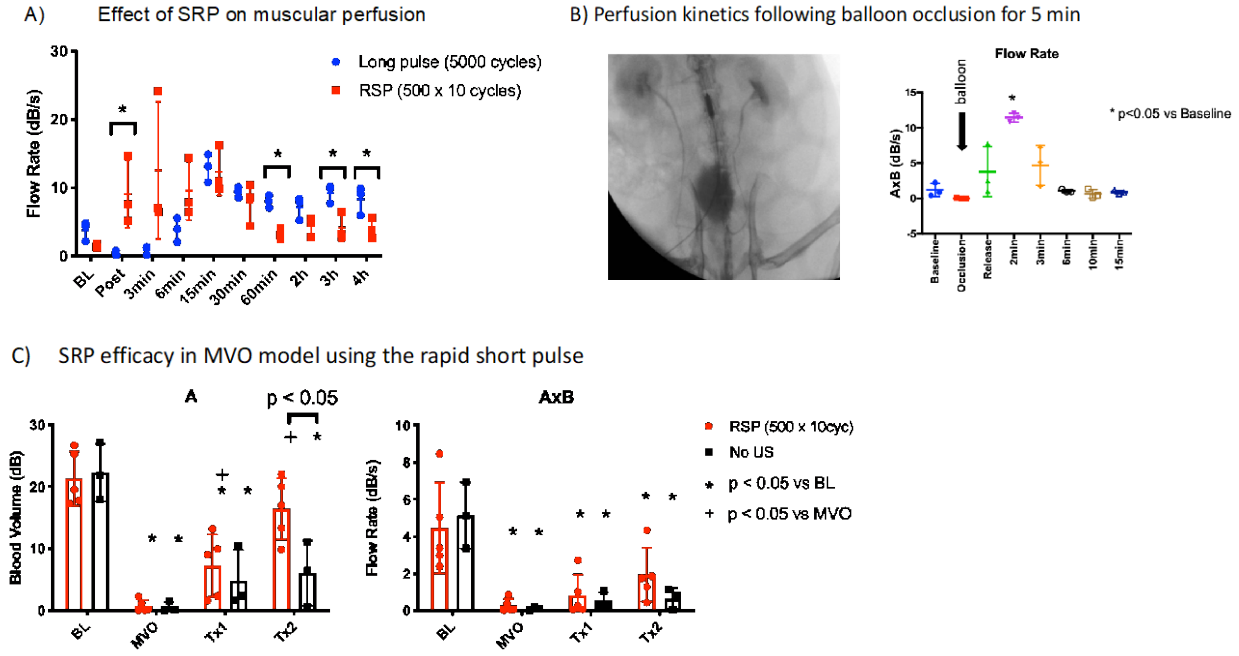

Figure 1 : A) Kinetics of perfusion flow rate (AxB) in a rat hindlimb muscle following 2-min of sonoreperfusion therapy using ultrasound burst replenishment imaging; B) Balloon angiocatheter placed in the rat descending aorta to cause a 5 min occusion and reactive hyperemic response following release of the balloon; C) Blood volume (A) and flow rate (AxB) calculated using contrast enhanced burst replenishment ultrasound imaging at different stages of sonoreperfusion therapy using UTMC with the rapid short pulse (n=5) compared to untreated control groups (n=3) (*p < 0.05 vs baseline; + p < 0.05 vs MVO. A was only different from no treatment after treatment 2.

References

[1] J. T. Belcik *et al.*, "Augmentation of Muscle Blood Flow by Ultrasound Cavitation Is Mediated by ATP and Purinergic Signaling," *Circulation*, vol. 135, no. 13, pp. 1240-1252, Mar 28 2017, doi: 10.1161/CIRCULATIONAHA.116.024826.

[2] J. T. Belcik *et al.*, "Augmentation of limb perfusion and reversal of tissue ischemia produced by ultrasound-mediated microbubble cavitation," *Circ Cardiovasc Imaging*, vol. 8, no. 4, Apr 2015, doi: 10.1161/CIRCIMAGING.114.002979.

[3] J. J. Pacella, J. Brands, F. G. Schnatz, J. J. Black, X. Chen, and F. S. Villanueva, "Treatment of microvascular micro-embolization using microbubbles and long-tone-burst ultrasound: an in vivo study," *Ultrasound Med Biol*, vol. 41, no. 2, pp. 456-64, Feb 2015, doi: 10.1016/j.ultrasmedbio.2014.09.033.

[4] F. T. H. Yu, X. Chen, A. C. Straub, and J. Pacella, "The role of nitric oxide during sonoreperfusion of microvascular obstruction," *Theranostics*, vol. 7, no. 14, pp. 3527-3538, 2017.

[5] W. Mathias, Jr. *et al.*, "Sonothrombolysis in ST-Segment Elevation Myocardial Infarction Treated With Primary Percutaneous Coronary Intervention," *J Am Coll Cardiol*, vol. 73, no. 22, pp. 2832-2842, Jun 11 2019, doi: 10.1016/j.jacc.2019.03.006.

[6] W. Mathias, Jr. *et al.*, "Diagnostic Ultrasound Impulses Improve Microvascular Flow in Patients With STEMI Receiving Intravenous Microbubbles," *J Am Coll Cardiol*, vol. 67, no. 21, pp. 2506-15, May 31 2016, doi: 10.1016/j.jacc.2016.03.542.

Assessment of the Mechanical Properties of Cellulose Nanofiber-Stabilized Droplets Using Acoustophoresis

***Ksenia Loskutova*[1], *Karl Olofsson*[2], *Björn Hammarström*[2], *Anna J. Svagan*[3], *Martin Wiklund*[2], *Dmitry Grishenkov*[1]**

[1]*Department of Biomedical Engineering and Health Systems, KTH Royal Institute of Technology, Stockholm, Sweden*
[2]*Department of Applied Physics, KTH Royal Institute of Technology, Stockholm, Sweden*
[3]*Department of Fibre and Polymer Technology, KTH Royal Institute of Technology, Stockholm, Sweden*
Corresponding author: ksenial@kth.se

Introduction

Acoustic Droplet Vaporization (ADV) is the physical process by which liquid-filled droplets convert into gas-filled bubbles when undergoing acoustic excitation. Recently, ADV has tremendous potential in a wide range of clinical applications such as imaging, localized drug delivery, vascular therapy and histotripsy [1]. Many different types of phase-change contrast agents have been developed throughout the years, with different types of shell and core materials [2]. Previous designs were either limited by low stability or a vaporization pressure threshold above clinically approved levels [3], but recently, a novel type of droplets has been developed by Ghorbani et al. [4]. The droplets were stabilized by a Pickering mechanism, where cellulose nanofibers (CNF) acted as a stabilizing agent at the interface between hydrophobic perfluoropentane (PFC5) and water. These droplets have been shown to vaporize at 200 kPa at room temperature, while also having a long shelf life. This makes them an interesting candidate for ultrasound-mediated clinical applications.

Acoustophoresis utilizes ultrasonic standing waves (USW) to manipulate particles in a gentle non-contact and label-free manner [5]. It has been extensively used in biomedical research for applications such as sorting [6], enrichment [7], and iso-acoustic focusing [8]. It works by applying an acoustic radiation force to particles in a suspension liquid, therefore relocating them to either pressure nodes or anti-nodes [5]. The final position of the relocation and the speed of the relocation depends, among other parameters, on the acoustic contrast factor, which in turn depends on the differences in density and compressibility between the suspension liquid and the particles. Therefore, it is possible to use acoustophoresis to determine the mechanical properties of new materials [9]. The droplets investigated by Ghorbani et al. [4] relocated to pressure anti-nodes, which is more consistent with the behaviour of gas-filled microbubbles [10]. Understanding the mechanical properties of CNF-shelled droplets enable their application in further biomedical research.

In this work, the compressibility of Pickering-stabilized perfluoropentane droplets was determined by using acoustophoresis. Polyamide beads with known density, size and compressibility were used to calculate the pressure amplitude inside the microchannel.

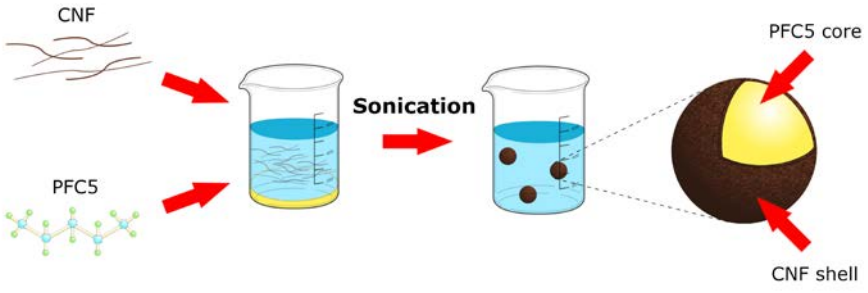

Figure 1. Schematic illustration of the droplet preparation.

Methods

Materials and droplet preparation

PFC5 was purchased from Apollo Scientific (Stockport, UK). Bleached sulfate-pulp (Nordic Paper Seffle AB, Sweden) was used in the production of CNF. A suspension of 0.303 wt% CNF was prepared by diluting the stock CNF with MilliQ water. The CNF-shelled droplets were prepared by mixing a 0.303 wt% cationic CNF suspension with perfluoropentane (Apollo Scientific, Stockport, UK) using a sonicator (VibraCell 750 W, Sonics, USA). A schematic illustration of the droplet preparation is illustrated in Figure 1. Optical microscopy and dynamic light scattering were used to determine the size distribution of the capsules. The mean diameter of the generated droplets from the two techniques was 0.96±0.63 µm and 1.30±0.11 µm, respectively.

Table 1. Density, sound velocity and compressibility of water, polyamide, perfluoropentane at 25°C.

Material	ρ [kg/m^3]	c [m/s]	κ (1/ρc^2) [Pa^{-1}]
Water	1000	1500	$4.4 \cdot 10^{-10}$
Polyamide	1030	2660	$1.4 \cdot 10^{-10}$
Perfluoropentane (PFC5)	1630	477	$2.7 \cdot 10^{-9}$

Acoustic tests

A glass-silicon-glass microfluidic device with a microchannel of 620 µm width was used for acoustophoresis measurements. The structure of the microfluidic device is illustrated in Figure 2. The ultrasound source consisted of a PZT transducer connected to a function generator (DS345, Stanford Research Systems, USA) and an RF amplifier (75A250, Amplifier Research, USA). The frequency was set to 2.40 MHz to match the wavelength criterion for an USW. The device was placed in an optical microscope (Axiovert 40 CFL, Zeiss, Germany) coupled with a monochrome camera (BFS-U3-51S5M-C, FLIR, USA) during the measurements.

Polyamide beads with a diameter of 5 µm were used for pressure calibration. The solution was injected into the microchannel, stabilized until no flow was present and then exposed to USW. Three measurements were performed at three different acoustic pressures, and the movement of the particles was filmed for 30 seconds at 20 FPS. TrackMate, an open-source Fiji plugin [11], and a Matlab script were used to calculate particle velocities and from that determine the acoustic pressure [5]. For the amplifications of 40 dB, 42 dB and 43 dB, the corresponding pressures were calculated to 120 kPa, 153 kPa and 175 kPa, respectively. The mechanical properties of the different materials used in this work are shown in Table 1.

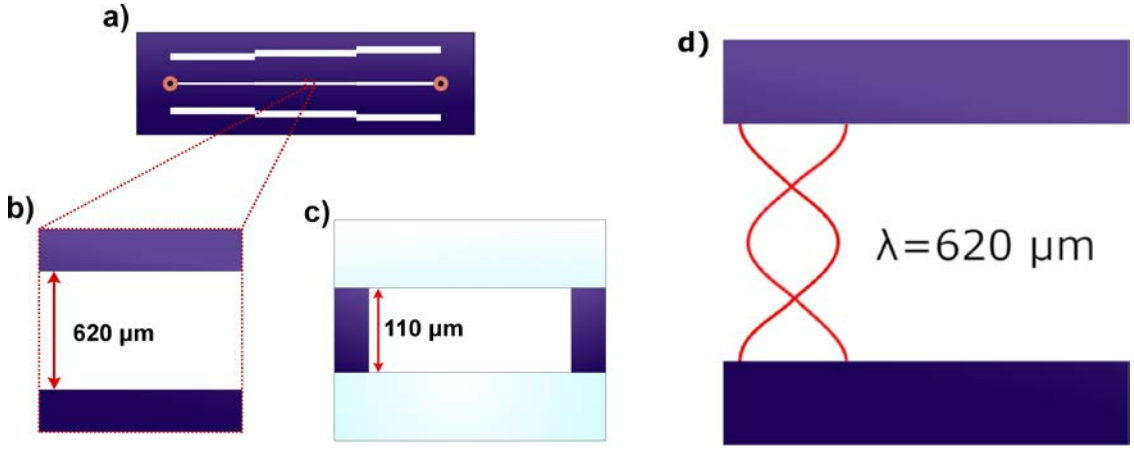

Figure 2. The microfluidic device used in acoustic tests, as seen a) from the top, full view; b) from the top, zoomed in; c) from the cross-section; d) the pressure field inside the microchannel – the full wavelength corresponds to the width of the microchannel.

After the pressure calibration, the same procedure was utilized with the droplets as for polyamide beads. The concentration used was $24.6 \cdot 10^6$ droplets/mL. The density of the droplets was assumed to be the same as for pure PFC5. TrackMate and a modified Matlab script were then used to estimate the compressibility of the droplets.

Results

At 120, 153 and 175 kPa the compressibility of the droplets were measured to be $6.6 \cdot 10^{-10}$, $8.2 \cdot 10^{-10}$ and $8.8 \cdot 10^{-10}$ Pa^{-1}, respectively. The low value for compressibility at 120 kPa is due to the very low velocity of the particles (<1 µm/s). However, even then the calculated compressibility is higher for droplets than for the surrounding water, whose compressibility is shown in Table 1.

As can be seen in Figure 3, the droplets relocate to pressure anti-nodes when exposed to the acoustic radiation force, whilst polyamide beads relocate to pressure nodes in the same setting. This indicates that the acoustic contrast factor was negative for droplets. The density of the droplets are higher than for water, as with time they sediment on the bottom of the microchannel. Therefore, the compressibility of the droplets is higher for droplets than for the suspension liquid.

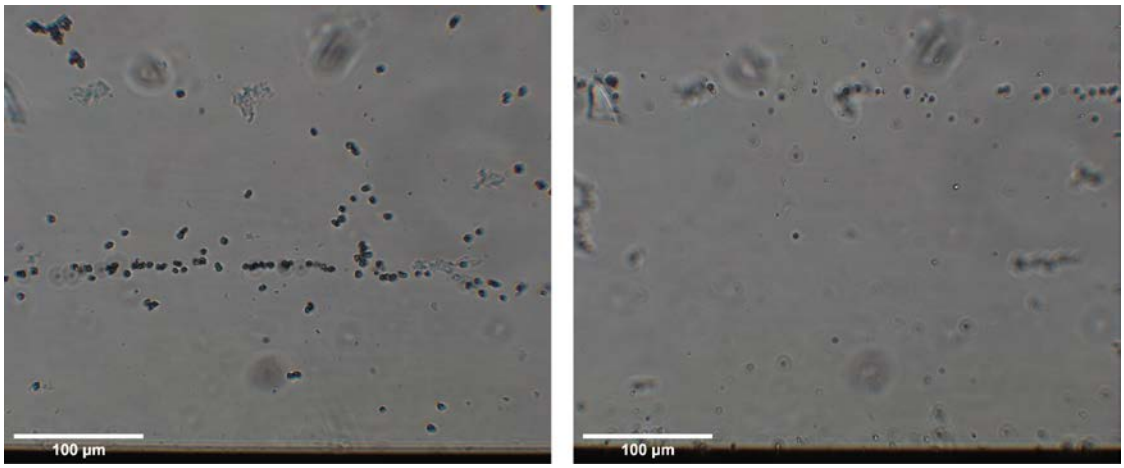

Figure 3. a) Polyamide beads at the pressure node, and b) CNF-stabilized droplets at pressure anti-nodes after 30 seconds of USW actuation, half of the microchannel width is visible.

Conclusions

The results show that the compressibility of CNF-stabilized droplets is significantly higher than for water, but lower than for pure PFC5. This shows promising potential for these droplets to be used in ultrasound-mediated clinical applications. It has also been shown that acoustophoresis can successfully measure the compressibility of pressure-sensitive particles for small USW pressure amplitudes. As the droplets relocate to pressure anti-nodes just as gas-filled microbubbles, it would be possible to study cell-droplet and cell-gasbubble in the same setup.

References

[1]. Loskutova, Ksenia, Dmitry Grishenkov, and Morteza Ghorbani. "Review on acoustic droplet vaporization in ultrasound diagnostics and therapeutics." BioMed Research International 2019 (2019)

[2]. Lea-Banks, H., M. A. O'Reilly, and K. Hynynen. "Ultrasound-responsive droplets for therapy: A review." Journal of Controlled Release 293 (2019): 144-154.

[3]. Sheeran, Paul S., et al. "Methods of generating submicrometer phase-shift perfluorocarbon droplets for applications in medical ultrasonography." IEEE transactions on ultrasonics, ferroelectrics, and frequency control 64.1 (2016): 252-263.

[4]. Ghorbani, Morteza, et al. "Unravelling the Acoustic and Thermal Responses of Perfluorocarbon Liquid Droplets Stabilized with Cellulose Nanofibers." Langmuir 35.40 (2019): 13090-13099.

[5]. Bruus, Henrik. "Acoustofluidics 7: The acoustic radiation force on small particles." Lab on a Chip 12.6 (2012): 1014-1021.

[6]. Burguillos, Miguel A., et al. "Microchannel acoustophoresis does not impact survival or function of microglia, leukocytes or tumor cells." PLoS One 8.5 (2013): e64233.

[7]. Augustsson, Per, et al. "Microfluidic, label-free enrichment of prostate cancer cells in blood based on acoustophoresis." Analytical chemistry 84.18 (2012): 7954-7962.

[8]. Augustsson, Per, et al. "Iso-acoustic focusing of cells for size-insensitive acousto-mechanical phenotyping." Nature communications 7.1 (2016): 1-9.

[9]. Hartono, Deny, et al. "On-chip measurements of cell compressibility via acoustic radiation." Lab on a Chip 11.23 (2011): 4072-4080.

[10]. Kothapalli, Satya VVN, et al. "Investigation of polymer-shelled microbubble motions in acoustophoresis." Ultrasonics 70 (2016): 275-283.

[11]. Tinevez, Jean-Yves, et al. "TrackMate: An open and extensible platform for single-particle tracking." Methods 115 (2017): 80-90.

Ultrafast nonlinear imaging of biomolecular acoustic reporters and simultaneous Doppler measurements

***Claire Rabut*[1], *Bill Ling*[1], *Zhiyang Jin*[2], *Mikhail G. Shapiro*[1]**

[1]*Division of Chemistry and Chemical Engineering, California Institute of Technology, Pasadena, California 91125, USA*
[2]*Division of Engineering and Applied Sciences, California Institute of Technology, Pasadena, California 91125, USA*
Corresponding author: crabut@caltech.edu

Introduction

Ultrafast imaging [1] and biomolecular contrast agents based on gas vesicles (GVs) [2] represent two emerging frontiers of ultrasound imaging. Combining these technologies would enable the simultaneous observation of physiology and cellular function on millisecond time scales. However, existing pulse sequences are not able to capture both hemodynamic and biomolecular contrast, the latter of which is based on GVs' pressure-dependent nonlinear response to ultrasound. Here we present a new imaging modality that enables non-linear amplitude modulation (AM) imaging of GVs at ultrafast framerate, allowing the simultaneous recording of fast events and the Doppler signal.

Methods

To enable a fast, large and uniform coverage of the media, we developed a multi-plane wave imaging paradigm based on the coherent summation of ultrasound images obtained from transmission of successive tilted AM plane-waves. Ultrafast AM (uAM) imaging alleviates nonlinear artifacts with the summing of ultrasound images obtained by transmission of noncollinear tilted plane waves and exhibits improved sensitivity in depth compared to the existing parabolic-AM [3] and cross-AM [4] modalities thanks to the emission of successive waves at each burst (**Fig.1.a**). The multiplane wave paradigm, originally developped to increase signal-to-noise ratio in ultrafast ultrasound imaging [5] without increasing the imaging voltage, enables enhanced GV imaging with pressures below their collapse threshold. The ultrafast imaging framerate can at the same time be leveraged to monitor transient dynamics in the imaging plane, as for Doppler imaging.

Ultrasound sequences were implemented on a research ultrasound scanner (Verasonics) using a probe of 128 linear elements emitting at 15.625 MHz (pitch = 0.1 mm). The transmission scripts, as well as the post-processing codes, were written in Matlab.

Results

In vitro

We showed that the coherent summation of ultrasound images obtained after emission of noncolinear tilted plane waves produces strong nonlinear contrast in GV samples while reducing nonlinear artifacts. In particular, the summation of 8 tilted noncolinear plane waves cancels the spurious dephased nonlinear signals appearing in individual angle images due to the propagation of transmitted waves through the GVs inclusion (**Fig.1.b**).

In vivo

We validated the capacity of uAM to simultaneously measure Doppler signal and visualize acoustic contrast agents by injecting intravenously (IV) 100µl of GVs in an anesthetized mouse and imaging the liver. GVs are quickly taken up by the liver after IV injection. Using uAM, we could image the vascularization of the liver and the enhancement of Doppler signal by circulating GVs and at the same time monitor GV accumulation in the liver tissue (**Fig.1.c**).

Conclusions

These results demonstrate the ability of ultrafast AM to provide simultaneous information about blood flow and non-linear biomolecular contrast. This technique will be useful in future studies combining acoustic reporter genes and biosensors based on GVs with hemodynamic measurements, for example related to the reticuloendothelial system [6] or brain function.

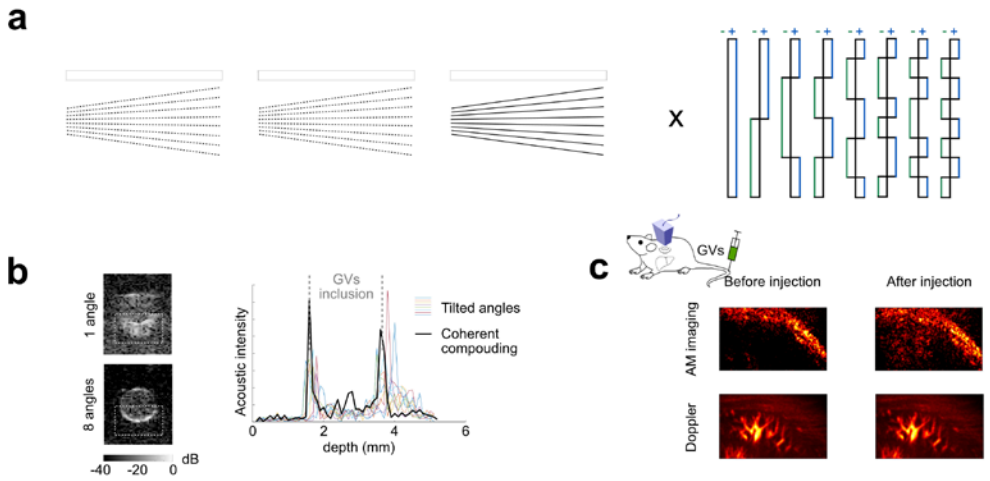

Figure 1. **a.** Schematic of the AM multiplane wave paradigm: three consecutive burst of 8 tilted plane waves of relative amplitudes 1⁄2 , 1⁄2 and 1 are transmitted. This sequence is then repeated eight times, in which the successive plane waves adopt different polarized amplitudes +/- 1. The coding of these amplitudes follow the coefficient of an hadamard matrix of order 8. Each amplitude modulated sequence is then reconstructed as described in [5]. **b.** Nonlinear artifact reduction by the coherent summing of tilted plane waves. **c.** Monitoring of GVs absorption by the liver in a mouse over time. After IV injection of gas vesicles, the nonlinear signal from the liver increases and the blood volume signal is monitored simultaneously.

References

[1]. Mickael Tanter and Mathias Fink, Ultrafast Imaging in Biomedical Ultrasound, IEEE Transactions on Ultrasonics, Ferroelectrics, and Frequency Control, vol. 61, no. 1, January 2014

[2]. Shapiro et al., Biogenic gas nanostructures as ultrasonic molecular reporters, Nature Nanotechnology, vol.9, March 2014

[3]. Maresca et al., Nonlinear ultrasound imaging of nanoscale acoustic biomolecules, Applied Physics Letters, vol 110, February 2017

[4]. Maresca et al., Nonlinear X-Wave Ultrasound Imaging of Acoustic Biomolecules, Physical Review X, vol.8, October 2018

[5]. Tiran et al., Multiplane wave imaging increases signal-to-noise ratio in ultrafast ultrasound imaging, Physics in Medicine & Biology, vol 60, October 2015

[6]. Ling et al., Biomolecular ultrasound imaging phagolysosomal function, vol 14, ACS Nano, September 2020

Endoskeletal Drops for Photoacoustics

Anish Silwal[1], Marco A. Inzunza-Ibarra[1], Gazendra Shakya[1], Mark A. Borden[1,2]

[1]Department of Mechanical Engineering, University of Colorado, Boulder, CO 80309, USA
[2]Biomedical Engineering Program, University of Colorado, Boulder, CO 80309, USA
Corresponding author: mark.borden@colorado.edu

Introduction

Vaporizable endoskeletal droplets were developed by inspiration from work by Caggioni et al. [1], who first described viscoelastic droplets that can stably retain non-spherical shapes by balancing the Laplace pressure of the liquid-liquid interface with the elasticity of an internal crystalline network, which they termed "endoskeletal" drops. We designed and synthesized vaporizable endoskeletal droplets comprising a liquid fluorocarbon (FC) phase and a solid hydrocarbon (HC) endoskeleton with a Zinc chelated naphthalocyanine dye mixed into the HC phase. FC/HC endoskeletal droplets were previously synthesized by Shakya et al. [2] to study how endoskeletal melting aids in the vaporization of the FC phase. Multiple studies have demonstrated droplets to be effective photoacoustic contrast agents as either biotinylated plasmonic particles [3] or dye-loaded particles [4] that absorb pulsed optical electromagentic radiation. During our photoacoustic test, the FC/HC endoskeletal droplets are irradiated with a 760-nm pulse laser. The dye absorbs these near-infrared photons, heats up the HC phase and subsequently melts it. Intefacial melting of the HC endoskeleton and subsequent mixing with the liquid FC reduces the cohesion in the FC phase and depresses its spinodal point [2]. The FC phase spontaneously vaporizes giving off a strong acoustic response.

Methods

The general scheme for sythesizing FC/HC endoskeletal droplets is shown in Fig. 1a. The solid HC and dye were weighed in a glass vial and then heated in a water bath at 75^0C to melt and mix together. Lipid solution (10 mg/mL containing DBPC and PEG5K in 9:1 molar fraction) was added as a surfactant and the mixture was chilled in ice water before adding the liquid FC phase. The vial was then sealed, heated and sonicated in water bath for a minute, and the mixture was emulsified in an amalgamator. The resulting emulsion was quenched in ice water to form the final dye-loaded FC/HC endosleletal droplets.

The schematic for the photoacoustic setup is shown in Fig. 1b. The photoacoustic experiment was carried out inside a water tank with the droplets flowed through a vertical tube using a syringe pump. The droplets inside the tube were illuminated with a 760-nm pulsed laser, and a 20-MHz ultrasound transducer was used to record the acoustic response.

Results

The peak-to-peak voltage amplitude received by the ultrasound transducer is plotted against the laser fluence in Fig. 1c. The figure shows the acoustic response from two kinds of droplets: sample droplets with dye and control droplets without dye. The plot indicates a very strong nonlinear photoacoustic response from the sample with dye compared to the sample without dye. In addition. the plot also demonstrates the acoustic response fom an ink flowed through the same setup. The non-linear response received from the dye-loaded sample suggests that the droplets are vaporizing, which was confirmed with contrast-enhanced ultrasound imaging.

Conclusions

These novel dye-loaded FC/HC endoskeletal droplets have the potential to work as photoacoustic contrast agents given their highly nonlinear response at low fluences. Also, given their low phase-transition temperature, these droplets can be tuned to vaporize at physiologically releveant temperatures, which can make them applicable for contrast-enhanced ultrasound (CEUS) applications.

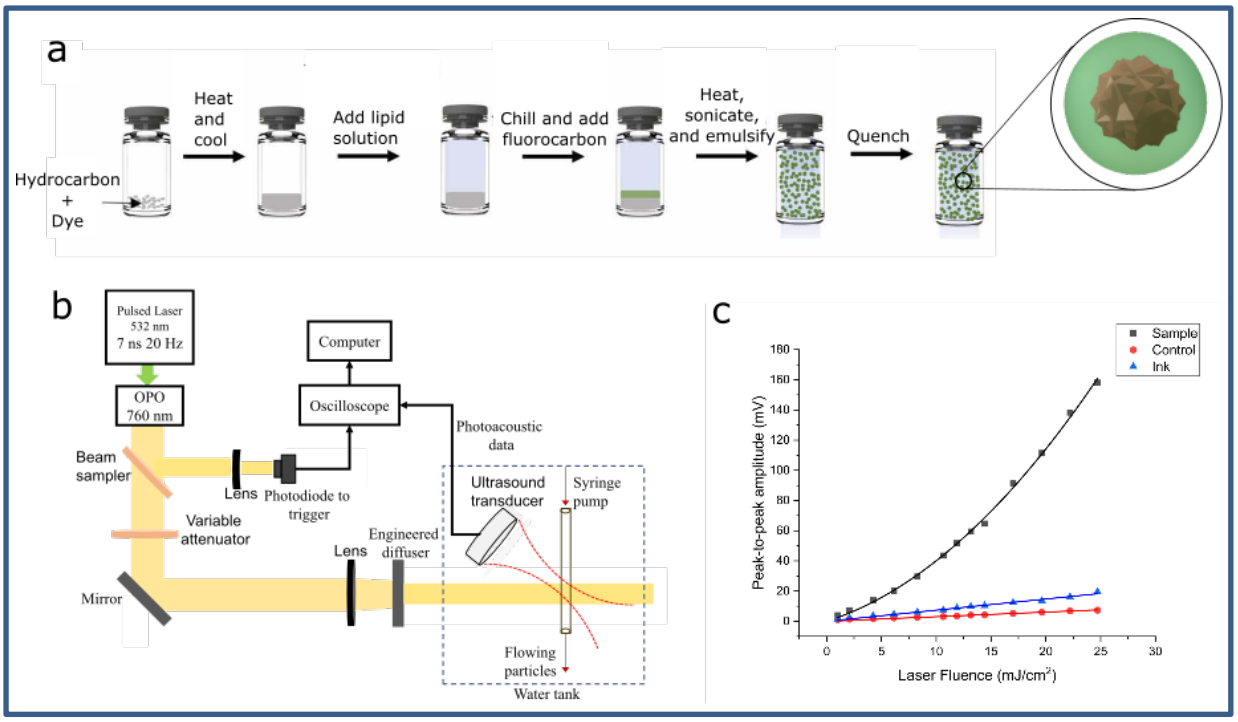

Figure 1 (a) General scheme for FC/HC endoskeletal droplets. (b) The photoacoustic experimental setup (c) Photoacoustic response from the sample droplets with dye, control droplets without dye and ink.

References

[1]. Caggioni M, Bayles AV, Lenis J, Furst EM, Spicer PT, Interfacial stability and shape change of anisotropic endoskeletal droplets, Soft Matter, 10: 7647-7652, 2014.

[2]. Shakya G, Hoff SE, Wang S, Heinz H, Ding X, Borden MA, Vaporizable endoskeletal droplets via tunable interfacial melting, Science Advances, 6(14): eaaz7118, 2020.

[3]. Dove JD, Mountford PA, Murray TW, Borden MA, Engineering optically triggered droplets for photoacoustic imaging and therapy. Biomed. Opt. Express, 5: 4417-4427, 2014.

[4]. Zhang P, Li L, Lin L, Shi J, and Wang LV, “In vivo superresolution photoacoustic computed tomography by localization of single dyed droptlets”, Light Sci. Appl. **8,** (2019).

Therapeutic magnetic microbubbles for the treatment of pseudoaneurysms

***Alec Thomas*[1], Bernard Shieh[1], Luca Bao[1], Lester Barnsley[2], Regent Lee[3], Ashok Handa[3], Eleanor Stride[1]**

[1]*Institute of Biomedical Engineering, University of Oxford, Oxford, UK*
[2]*Jülich Centre for Neutron Sceince at Hienz Maier-Leibnitz Zentrum, Forschungszentrum Jülich GmbH, Garching, Germany*
[3]*Nuffield Department of Surgical Sciences, Oxford, UK*
Corresponding author: alec.thomas@eng.ox.ac.uk

Introduction

The drive towards minimally invasive surgery has increased the frequency of femoral artery puncture to access the vasculature. While these procedures have led to shorter post-operative hospital stays, the presentation of a pseudoaneurysms (PSA) occurs in as high as 8% of these patients [1]. The current standard of care is ultrasound-guided thrombin injection to the perfused sac of the PSA [2]. The injection initiates blood coagulation that arrests the perfusion in the blood cavity and ultimately seals the ruptured vessel. However, a PSA must have an architecture such that the possibility of the injected thrombin to enter the arterial system is sufficiently low to avoid the risk of downstream intra-arterial thrombosis; otherwise, the treatment option is open surgery. Consequently, only a relatively small number of patients are eligible for thrombin injection.

We aim to develop a delivery system for thrombin injections to PSAs that integrates magnetic microbubbles (MM), thrombin and a magnetic-acoustic probe. MMs serve a dual role: first, to provide contrast for ultrasound imaging and second, to enable targeted delivery of the therapeutic. By designing a thrombin conjugated MM (TcMM), the coagulation of blood can be spatially controlled and easily imaged. The device will be a low-profile 64-element Capacitive Micromachined Ultrasonic Transducer (CMUT) integrated above the magnetic stack that provides simultaneous ultrasound monitoring (Fig. 1A).

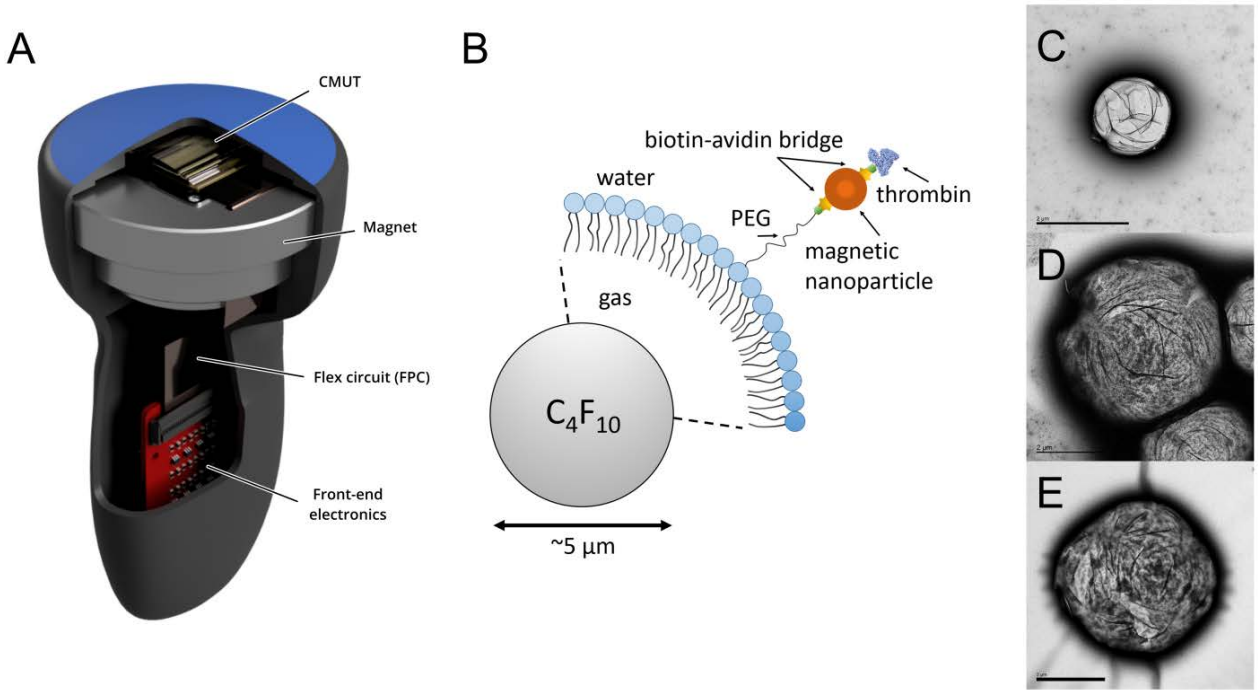

Figure 1 (A) Illustration of the magnetic-acoustic device and (B) the microbubble architecture. (C) TEM images of (C) a nanoparticle-free microbubble, (D) magnetic microbubble and (E) thrombin conjugated magnetic microbubble.

Methods

TcMMs were produced by combining DBPC and DSPE-PEG2000-Biotin to a 9:1 molar ratio and dispersing the lipid in phosphate buffered saline with 15% propylene glycol. Microbubbles were made by tip sonication and washed three times by centrifugation. Separately, super paramagnetic iron oxide nanoparticles (SPION) were biotinylated and then slowly mixed (10 µL/min.) with an avidin (NeutrAvidin) solution (5 mg/mL) to saturate the nanoparticle surface with avidin. Next, the SPIONs coated with avidin were mixed with the freshly prepared microbubble suspension and then washed to remove any unbound SPIONs. Finally, thrombin was biotinylated to facilitate attachment to the MMs by targeting the surface exposed primary amines. This reaction was optimised to ensure maxium activity of the protein was retained. Modified thrombin was then mixed with the MMs and washed once to remove unbound thrombin. The microbubble design is illustrated in Fig 1B with corresponding TEM images of a bubble free of SPIONs, a MM and a TcMM (Fig. 1C-E, respectively).

Magnetic rentention experiments were performed in an agar channel under flow and exposed to a magnetic field. A custom built magnet consisting of 5 concentrically stacked permanent magnetic disks of decreasing diameter housed in an aluminum bracket was positioned 3 or 5 cm below the center of the agar channel. Microbubbles were visualized using a Philips iU22 clinical scanner operating at an MI of 0.04. Image analysis was performed over 25 frames by calclulating the average pixel intensity within the region of interest (ROI) with and without the magnet and compared against the background measurement, as described by Beguin et al. [3]

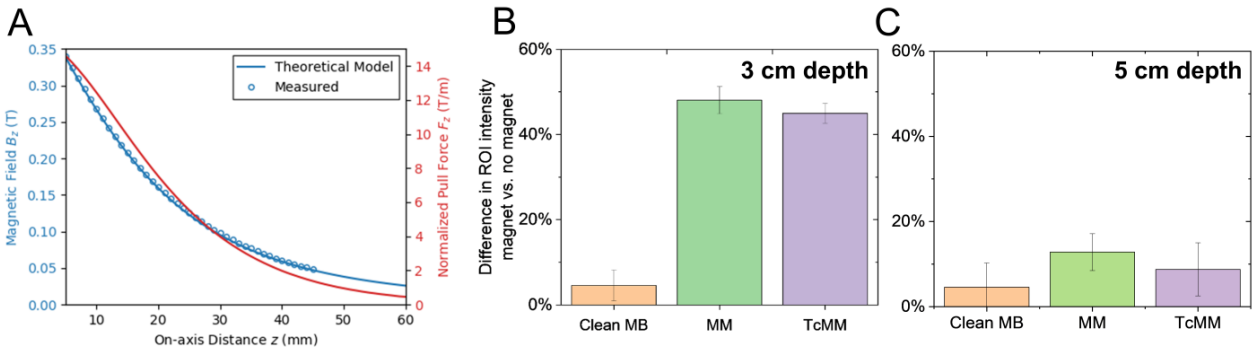

Figure 2 (A) The magnitude of the measured magnetic field strength (left vertical axis) and normalized pull force (right vertical axis) as a function of the axial distance away from the midpoint of the magnet. Magnetic retention experiments performed at two distances away from the magnet, (B) 3 cm and (C) 5 cm.

Results

There was only limited loss of protein activity after biotinylation indicating a strong therapeutic capacity of the bubble to coagulate blood. The magnetic field and force profile produced by our custom assembled magnet is shown in Figure 2A. The retention of microbubbles at a distance of 3 cm between the center of the agar channel and the face of the magnet is nearly 50% greater for both MM and TcMM. This capture effiency corresponds to a normalized pull force of ~5 T/m. At the greater distance of 5 cm, the retention reduces nearly three-fold compared to the shallower depth indicating that a pull force of ~1 T/m is not strong enough to capture a significant portion of bubbles flowing over the magnet.

Conclusions

The TcMM showed it retained significant protein acitivity to induce blood coagulation. The purpose built magnet displayed strong microbubble capture at an intermediate distance of 3 cm. The reduced microbubble rentention efficiency at the 5 cm distance from the magnet face is concerning for clinical translation of this platform. However, the flow rate used in this experiment is higher than the expected flow rates within the PSA, according to flow simulations, and therefore we expect to have acceptable retention at this distance. Experiments are ongoing to show TcMM are retained in tissue phatoms that mimic the PSA artchitecture and flow conditions.

References

[1]. Tisi PV, Callam MJ, Treatment for femoral pseudoaneurysms. Cochrane Database Syst Rev, CD0004981, 2013.

[2]. Kurzawski J, Sadowski M, Janion-Sadowska A, Complication of percutaneous thrombin injection in patients with postcatherization femoral pseudoaneurysm, Journal of Clinical Ultrasound, 188-195, 2015.

[3]. Beguin E, Bau L, Shrivastava S, Stride E, Comparing strategies for magnetic functionalization of microbubbles, Applied Materials and Interfaces, 11, 1829-1840, 2019

Towards high-production rate synthesis of monodisperse ultrasound contrast agents: understanding the local flow field

***Sarah Cleve*[1], *Guillaume Lajoinie*[1], *Tim Segers*[1,2], *Michel Versluis*[1]**

[1] *Physics of Fluids group, MESA+ Institute for Nanotechnology and Technical Medical (TechMed) Center, University of Twente, P.O. Box 217, 7500 AE, Enschede, The Netherlands*
[2] *BIOS Lab-on-a-Chip group, Max-Planck Center Twente for Complex Fluid Dynamics, MESA+ Institute for Nanotechnology, University of Twente*
Corresponding author: s.cleve@utwente.nl

Introduction

Ultrasound contrast agents are nowadays investigated for a broad variety of imaging and therapeutic applications, including non-invasive pressure sensing, sonoporation, blood-brain barrier opening and sono-thrombolysis [1]. All these applications rely on the mechanical response of microbubbles to ultrasound and the scattered nonlinear echo. The bubble response involves volumetric oscillations, which are maximized when the bubble is driven at resonance. Therefore, in a perfect scenario, the clinician uses monosized microbubbles whose size is perfectly tuned to the driving ultrasound frequency. Indeed, a sensistivity increase of up to 2 orders of magnitude has been observed for resonantly driven monodisperse bubbles as compared to commercially available polydisperse bubble agents, both *in vitro* and *in vivo* [2]0.

To produce monodisperse bubbles, flow-focusing devices have shown promising results on laboratory scale [4]. However, upscaling the manufacturing towards industrial quantities remains a major challenge. Even though the parallelization of up to 400 single flow focusing unit has been achieved [5], the regimes for monodisperse bubble production were obtained empiricaly and no reliable predictions or designing tools for desired bubble sizes exist so far. A main challenge of parallelization is the interaction between the different flow focusing units, in particular flow resistances [5] and cross-talk [6], the latter being linked to flow and pressure fluctuations in the device. A first step towards a robust parallelization of multiple flow focusing nozzles is the characterization of flow oscillations in a single unit as these oscillations may result in unstable bubble production.

Methods

Experiments were conducted in a flow-focusing device fabricated in glass as described before [7]. The device has a main channel width of 20.5 µm and height of 16 µm (see Fig. 1(a,b)). Bubbles with radii between 3 and 7 µm were produced at rates exceeding 1 million bubbles per second. The gas used in the present study was compressed air, the liquid was water to which 2% Tween 80 was added to limit coalescence and ensure a stable bubble production. Furthermore, 0.52 µm-diameter tracer particles (red fluorescent microspheres, Thermo Scientific) were added as flow tracers. The liquid flow was controlled via a syringe pump while the air flow was pressure-controlled. Images were captured at a magnification of 120× using an ultra high-speed camera (Shimadzu HPV-X2) operated at a frame rate of 10 million frames per second. The flow field is extracted from the displacement of the tracer particles by particle tracking velocimetry (PTV).

Results

The local flow field in the nozzle of the device can be described by a mean flow (Fig. 1(c)) with superimposed oscillations. A first evidence of oscillatory behavior can be seen when comparing different particle trajectories. Typical particle trajectories are plotted in Fig. 1(d). Note that the particle trajectories at the bottom of the figure intersect in space, which indicates that the flow field is changing over time. The flow oscillations become apparent when plotting the velocity vectors magnitude and direction in time, a typical example for a fixed position is shown in Fig. 1(e). Velocity oscillations have an amplitude of up to 10% of the mean velocity.

Conclusions

We have experimentally investigated the velocity field inside a flow-focusing device and shown that velocity fluctuations are an important component of the total flow field. This is a first important step towards understanding cross-talk in coupled flow-focusing devices for industrial upscaling of the production of monodisperse contrast agents.

Acknoledgements

This work is part of monoRAILS, a project financed by the Connecting Industries program funded by the Netherlands Top Sector High Tech Systems and Materials. Financial support from Bracco Suisse S.A. is kindly acknowledged.

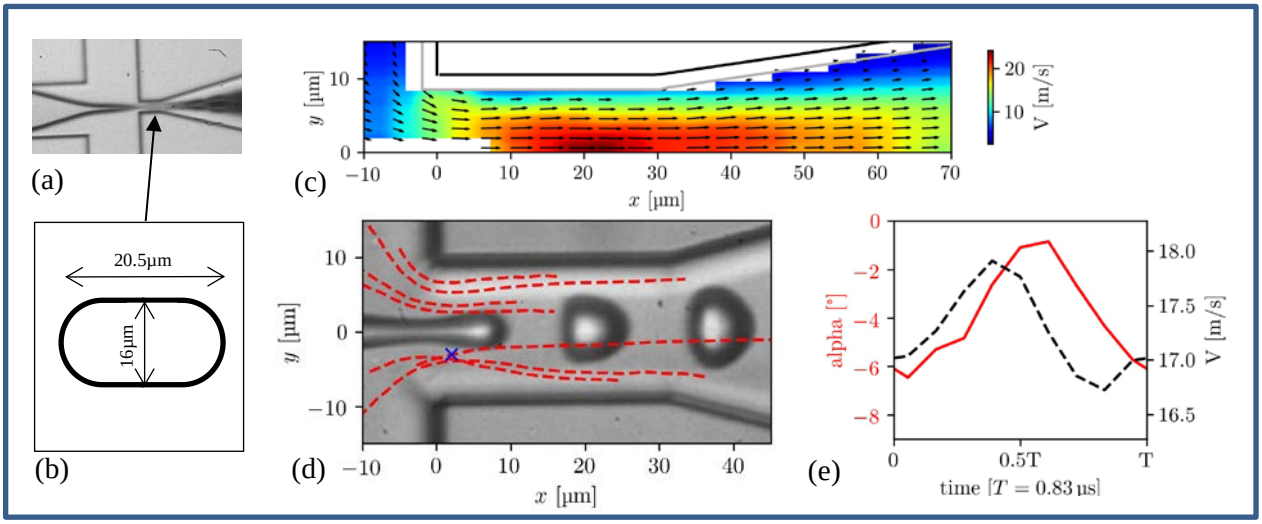

Figure 1. (a) Top view on the flow-focusing channel and (b) geometry of the main channel cross section. (c) Flow field map of the mean velocity (liquid flow rate). (d) Typical particle trajectories superimposed on a bubble production snapshot. (e) Velocity oscillations for the position x = 2.0 µm and y = 3.0 µm (position marked with × in (d)): both the velocity magnitude (dashed line) and the direction (angle alpha with respect to the horizontal axis; red bold line) are varying in time (T=1/f, where f is the production frequency).

References

[1]. Unger EC, Porter T, Culp W, Labell R, Matsunga T, Zutshi R, Therapeutic applications of lipid-coated bubbles, Advanced Drug Delivery Reviews, 56.9, 2004.

[2]. Segers T, Kruizinga P, Kok MP, Lajoinie G, de Jong N, Versluis M, Monodisperse versus polydisperse ultrasound contrast agents: non-linear response, sensitivity, and deep tissue imaging potential, Ultrasound in Medicine & Biology, 44.7, 2018.

[3]. Helbert A, Gaud E, Segers T, Botteron C, Frinking P, Jeannot V, Monodisperse versus Polydisperse Ultrasound Contrast Agents: In Vivo Sensitivity and safety in Rat and Pig, Ultrasound in Medicine & Biology, 46.12, 2020

[4]. Rodríguez-Rodríguez J, Sevilla A, Martínez-Bazán C, Gordillo JM, Generation of microbubbles with application to industry and medicine, Annual Review of Fluid Mechanics, 47, 2015

[5]. Jeong HH, Yadavali S, Issadore D, Lee D, Liter-scale production of uniform gas bubbles via parallelization of flow-focusing generators, Lab on a Chip, 17, 2017

[6]. Hashimoto M, Shevkoplyas SS, Zasońska B, Szymborski T, Garstecki P, Whitesides GM, Formation of bubbles and droplets in parallel, coupled flow-focusing geometries, Small, 4, 2008

[7]. Segers T, Gaud E, Versluis M, Frinking P, High-precision acoustic measurements of the nonlinear dilatational elasticity of phospholipid coated monodisperse microbubbles, Soft Matter, 14.47, 2018

Comparison of nonlinear pulsing schemes for contrast plane wave imaging using monodisperse microbubbles

Rick van Beek[1], Charlotte Nawijn[1], Guillaume Lajoinie[1], Michel Versluis[1] and Tim Segers[1,2]

[1]Physics of Fluids Group, Technical Medical (TechMed) Center and MESA+ Institute for Nanotechnology, University of Twente, The Netherlands
[2]BIOS Lab-on-a-Chip group, Max-Planck Center Twente for Complex Fluid Dynamics, MESA+ Institute for Nanotechnology, University of Twente, The Netherlands
Corresponding authors: t.j.segers@utwente.nl

Introduction

Traditionally, contrast-enhanced ultrasound (CEUS) imaging is performed through line-by-line scanning of the imaging volume with focused ultrasound waves. The 3 most frequently used pulsing schemes for CEUS imaging are pulse inversion (PI), power modulation (PM), and a combination of the two (PMPI) [1]. The maximum frame rate that can be achieved using classical line-by-line CEUS imaging is typically of the order of 50 frames/s which limits its use for the quantification of fast blood flows through [2]. The recent development of high frame rate plane wave imaging overcomes this limitation. The nonlinear pulsing schemes for classic CEUS imaging can be translated to plane wave imaging. However, questions remain as to the optimal pulsing scheme to be used for a maximized signal-to-noise ratio, to the optimal driving conditions for the bubbles in terms of acoustic pressure and resonance behavior, and to the mechanism by which the contrast signal is generated. Three phenomena are known to contribute to the generation of the contrast signal, i.e. the generation of harmonic signal, a power-dependent phase delay between echoes received from pulses transmitted at different power, and a nonlinear dependence of the fundamental echo on the transmit acoustic pressure [3]. In this work, we compare systematically the pulsing schemes PI, PM, and PMPI for contrast-enhanced plane wave imaging at a transmit frequency of 2 MHz. We vary the bubble concentration over 4 orders of magnitude, the acoustic pressure amplitude from 50 to 150 kPa in steps of 25 kPa, and the bandwidth of the transmit pulse by employing 2.5 and 8-cycle pulses. Furthermore, the physical parameter of the bubble size is kept constant by using monodisperse bubble suspensions such that the importance of resonance behavior can be studied. Finally, we study phase delay and the potential nonlinear fundamental response to explain differences in the generated contrast signal.

Methods

Monodisperse microbubble suspensions with mean radii of 1.5, 1.8, 2.1, and 2.8 µm were produced in a flow-focusing device as before (DSPC/DPPE-PEG5000, 9:1 molar ratio) [4]. The bubble suspensions were diluted to final concentrations of 10^2, 10^3, 10^4, and 10^5 bubbles/mL. The diluted suspensions were characterized in a 250 mL sample holder with acoustically transparent walls and with a length of 10 cm. At a distance of 3 cm from the sample holder, a phased array probe (P4-1) was mounted. The probe was connected to a Verasonics system (Vantage 256) that was programmed to transmit 2 MHz pulse trains containing 5 subsequent pulses, i.e. a half-aperture pulse driving the odd elements, a half-aperture pulse driving the even elements, a full-aperture pulse, a phase-inverted half-aperture pulse, and a phase-inverted full-aperture pulse. The time between the transmit pulses was 200 µs and in total 100 frames were transmitted for each experiment consisting of the 5 ultrasound pulses at an interframe time of 1 ms. Measurements were performed at peak-negative acoustic pressures of 50 to 150 kPa in steps of 25 kPa for both 2.5-cycle and for 8-cycle ultrasound pulses. After each measurement of 100 frames, a fresh bubble suspension was loaded into the bubble container. The pulse-echo data were analyzed offline in Matlab. First, the RF-lines were analyzed to obtain the scattered power at the fundamental and at the second harmonic. Numerical modeling of the acoustic response of the different bubble populations was performed by solving a Rayleigh-Plesset type model. The aim of the modeling effort was to compare the measured fundamental- and second harmonic response to that derived from the model. Second, the RF data was processed following

the different pulsing schemes and beamformed. The contrast images were then averaged laterally over a 2 cm area around the centerline of the transducer to obtain axial contrast profiles. From these profiles, the signal-to-noise ratio (SNR) was obtained by dividing the contrast signal averaged over the first 2 cm of the sample holder over that of pure water. Finally, to explain the origin of the measured contrast signal, we quantify the nonlinear fundamental response and the phase delay between transmitted pulses. The nonlinear fundamental is quantified as the root-mean-square (RMS) of the echo amplitude of the full amplitude pulse normalized to that of the summed echo amplitudes of the half-aperture odd and even pulses, both averaged over the first 2 cm of the sample holder to exclude attenuation effects. The phase delay was quantified by cross correlating the sum of the odd and even aperture echoes with the full-amplitude echo. The resulting phase delay versus depth curves were then averaged over an axial distance of again 2 cm around the center of the transducer to obtain at a single phase delay value per measurement.

Results

Figure 1A shows the received echo power at the fundamental (2 MHz) scaled by the acoustic pressure amplitude squared as measured for the four different bubble suspensions (symbols). The dotted red curve shows the modeled fundamental response for a bubble suspension with a single bubble size. The solid blue curve shows the modeled fundamental response when accounting for the full bubble size distribution. Figure 1B is similar to Fig. 1A however, it now shows the received echo power at the second harmonic. Note that for both the fundamental and second harmonic the measured echo response is as expected from the model. Also note the distinct resonance behavior, most pronounced for the second harmonic, with a maximized response for the resonant bubble radius of approx. 2 µm.

Figure 1C shows the measured SNR for the three different pulsing schemes as a function of the acoustic pressure amplitude for a bubble concentration of 10^3 and 10^4 bubbles/mL and for a bubble radius of 1.8 µm. Note that only the power modulation (PM) resulted in a high SNR at a bubble concentration of 10^4 bubbles/mL. The PMPI scheme resulted in contrast signals exceeding the noise floor only for acoustic pressure amplitudes of 100 kPa and higher. Remarkedly, the pulse inversion (PI) scheme resulted in no significant contrast enhancement with a signal below the noise floor for all conditions. Thus, PM outperforms PI and in fact, PI does not generate any contrast at all for the present setup.

The SNR for the power modulation scheme is plotted in Fig. 1D as a function of the bubble radius for the 8-cycle transmit pulses and at an acoustic pressure amplitude of 100 kPa. A distinct resonance behavior is observed with a maximum SNR at a bubble radius of 2.1 µm, equal to the resonant bubble size found in Fig. 1A and B.

Figures 1E and F show the nonlinear fundamental and phase delay for the PM pulsing scheme and Figs. 1G and H those for the PI pulsing scheme. Significant nonlinear behavior of the fundamental echo response is only observed for the transmit pulses of the PM pulsing scheme. Furthermore, the strong phase delay for the PM scheme is entirely absent for the PI scheme. From these results, it can be concluded that PM outperforms PI due to the contrast signal that is generated at the fundamental as a result of contributions from nonlinear fundamental behavior and from a phase delay between the echoes received at the full and half-aperture pulses. From a simulation, we can furthermore show that it is mainly the phase delay that is responsible for the generation of the contrast signal.

Conclusions

Size-dependent resonance behavior was observed as expected from numerical modeling. The power modulation pulsing scheme was found to outperform the pulse inversion pulsing scheme. We showed that PM results in a high SNR whereas PI barely exceeds the noise level at all driving conditions and bubble sizes. PM outperforms PI due to the phase delay between the received echoes at the full and half-aperture pulses and due to the fundamental signal not being equal for both driving amplitudes. Since for PI two pulses of equal power are transmitted for the pulse inversion scheme, no contrast signal is generated at the fundamental but only at the second harmonic. This severely limits the SNR of PI as compared to that of PM.

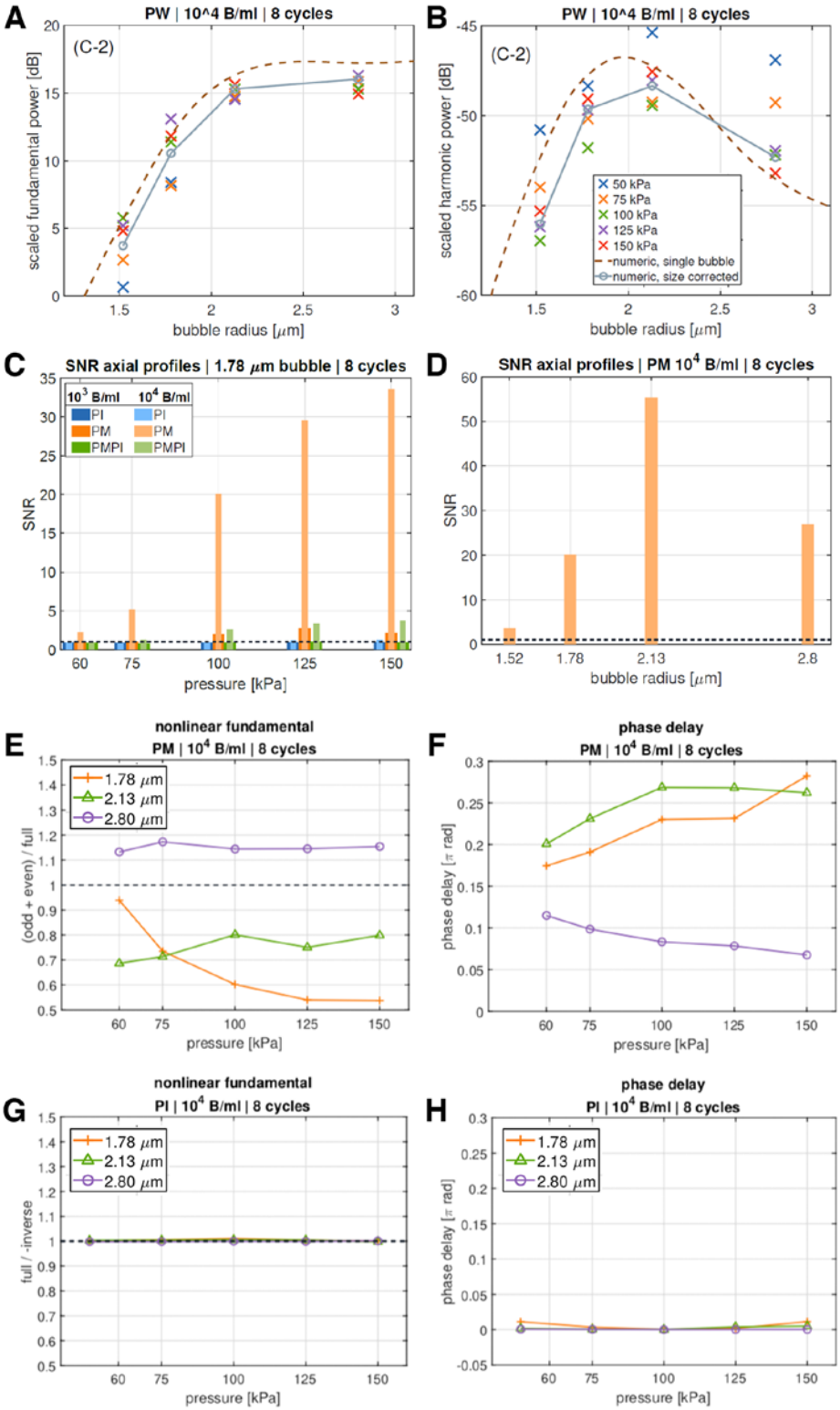

Figure 1. (A) Echo power at the fundamental (2 MHz) scaled by the acoustic pressure squared as a function of bubble radius. The dashed and solid line represent the modeled normalized scattered power. (B) Echo power at the second harmonic scaled by the acoustic pressure amplitude to the fourth power showing resonance behavior. (C) Signal-to-noise ratio (SNR) for the different pulsing schemes as a function of acoustic pressure amplitude and for a bubble concentration of 10^3 and 10^4 bubbles/mL. (D) SNR obtained using the power modulation (PM) pulsing scheme and at a bubble concentration of 10^4 bubbles/mL, as a function of the bubble size. Again resonance behavior is observed. (E) and (F) nonlinear fundamental and phase delay for the PM pulsing scheme, respectively. (G) and (H) nonlinear fundamental and phase delay for the pulse inversion (PI) pulsing scheme. Figures (E)-(H) show that PM performs better over PI due to the strong phase delay and nonlinear fundamental that are absent for PI.

References

[1] M. A. Averkiou, M.F. Bruce, J.E. Powers, P.S Sheeran, and P.N. Burns. Imaging Methods for Ultrasound Contrast Agents. Ultrasound in Medicine & Biology 46(3), 498-517 (2020).

[2] S. Engelhard, J. Voorneveld, H.J. Vos, J.J. Westenberg, F.J. Gijsen, P. Taimr, M. Versluis, N. de Jong, J.B. Bosch, M.M. Reijnen, E. Groot Jebbink. High-frame-rate contrast-enhanced US particle image velocimetry in the abdominal aorta: first human results. Radiology. 289(1), 119-25 (2018).

[3] C. Tremblay-Darveau, P. S. Sheeran, C. K. Vu, R. Williams, Z. Zhang, M. Bruce, and P. N. Burns. The role of microbubble echo phase lag in multipulse contrast-enhanced ultrasound imaging. IEEE transactions on ultrasonics, ferroelectrics, and frequency control (65), 1389–1401 (2018).

[4] T. Segers, E. Gaud, M. Versluis, and P. Frinking. High-precision acoustic measurements of the nonlinear dilatational elasticity of phospholipid coated monodisperse microbubbles. Soft Matter 14(47), 9550-9561 (2018).

Investigation of the acoustic vaporization threshold of lipid-coated perfluorocarbon nanodroplets using simultaneous high-speed optical imaging and acoustic methods

Q. Wu[1], S. Ferri[2,3], A. Polydorou[2,3], J.P. May[2,3], N.D. Evans[2,3], D. Carugo[4], E. Stride[1]

[1]Department of Engineering Science, University of Oxford, Oxford, UK
[2]Faculty of Engineering and Physical Sciences, University of Southampton, Southampton, UK
[3]Bone&Joint, Faculty of Medicine, University of Southampton, Southampton, UK
[4]Department of Pharmaceutics, UCL School of Pharmacy, University College London, London, UK

Corresponding authors: Qiang.Wu@eng.ox.ac.uk; S.Ferri@soton.ac.uk;

Introduction

Impaired fracture healing is a major financial burden for healthcare services; 5-10% of bone fractures result in costly and debilitating conditions such as delayed or non-union, where the bone fails to heal properly. Common treatments are invasive and rely on the immobilisation of the fracture site, with a significant impact on a patient's quality of life. Currently, there is no clinically approved systemic therapy for the treatment of bone fractures. We aim to overcome this limitation by using acoustically-stimulated nanodroplets (NDs) as non-invasive ultrasound (US) responsive vehicles for the targeted delivery of osteogenic compounds. In previous work, we have demonstrated the feasibility of generating drug loaded phospholipid-coated perfluorocarbon NDs and that these can be used for drug delivery *in vitro* at moderate ultrasound intensities. Given the potentially high attenuation of ultrasound at a fracture site, however, it is important to minimise the acoustic pressures and/or pulse lengths required for delivery. The aim of this study was therefore to determine the acoustic exposure parameters required to achieve ND vaporisation and how these are affected by both droplet parameters (droplet composition, size and concentration) and environmental conditions (temperature, geometry, mechanical stiffness).

Methods

A combination of ultra high-speed optical imaging (5 x 10^6 frames/s), B-mode ultrasound imaging and acoustic emissions monitoring was used to study the vaporization process and determine both the acoustic droplet vaporization (ADV) and inertial cavitation (IC) thresholds of phospholipid-coated perfluorobutane nanodroplets (PFB-NDs). Schematics of the experimental set ups for high speed optical and ultrasound imaging are shown in Figure 1.

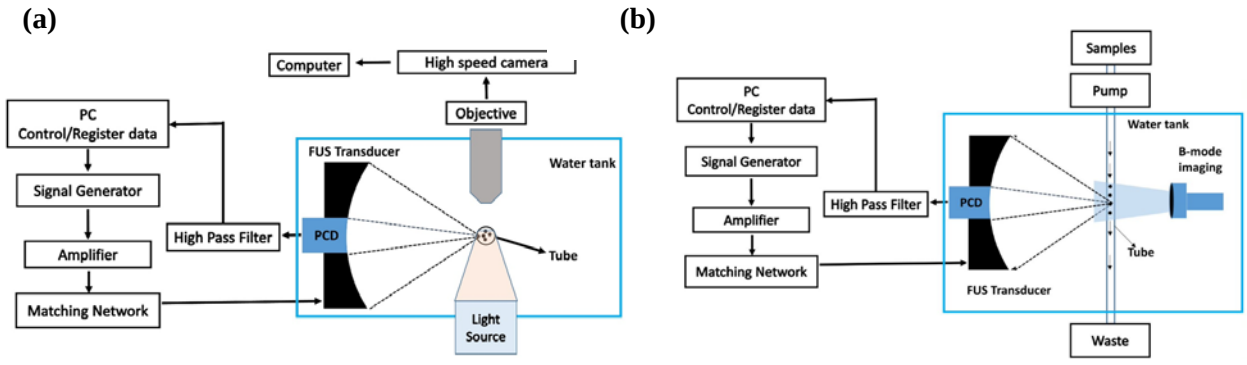

Figure 1. Schematic diagram of the experimental setup employed for a. high-speed microscopy, containing the focused ultrasound transducer, signal generator, amplifier, microscope and high-speed camera; b. for passive ADV and IC threshold measurement, containing the focused ultrasound transducer, signal generator, amplifier, PCD transducer and diagnostic ultrasound imaging probe.

In both experiments, a spherically single element focused ultrasound (FUS) transducer (0.5 MHz or 1.0 MHz centre frequency, H107/H102, Sonic Concepts, USA) was used to excite the NDs which were pumped through a polyethylene tube of 1.2 mm inner diameter and 0.2 mm wall thickness (Advanced Polymers, Salem NH, USA) at a constant flow rate of 0.3 mL/min. For optical imaging, the mid-plane of the tube was optically focused by an objective lens with a numerical aperture of 1.0 on a Nikon Inverted Research Microscope (Eclipse Ti; Nikon Inc, Melville, NY, USA), which was coupled to a high speed camera (HPV-X2, Shimadzu, Japan). For ultrasound imaging, a diagnostic ultrasound imaging probe (L12-5 linear array, operated at 7 MHz using an iU22 imaging system, Philips, Bothell, WA, USA) was used to record B-mode images. In both set ups a 7.5 MHz spherically focused single element transducer (V320 Panametrics, Olympus, Waltham, USA) was used simultaneously to record any acoustic emissions from the focal region of the FUS transducer.

The ADV and inertial cavitation (IC) pressure thresholds of PFB NDs were determined respectively by calculating the mean relative echo amplitude in a given region of interest (ROI) from the B-mode images and probability of inertial cavitation (PIC) from the acoustic emissions recordings. The ADV threshold was defined as the peak negative pressure producing a change of >80% in the B-mode image intensity compared with the pre-exposure level. The IC threshold was similarly defined as the peak negative pressure for which the PIC exceded 80%. IC was deemed to have occurred when the broadband component of the acoustic emissions was higher than the background noise level by a factor of e^3. The effects of ND size, concentration, core material, pulse centre frequency, pulse repetition frequency (PRF), pulse duration and temperature upon the thresholds were investigated. To investigate ND vaporisation in a more physiologically realistic environment, NDs were embedded in a 2% low melting point agarose gel, which was injected into a bone fracture phantom (Sawbones, Washington, USA). The NDs were exposed to US for 30 s at 1 MHz with a duty cycle of 5% and acoustic pressures from 0.04-0.95 MPa.

Results

An example of a series of high-speed images of droplet vaporization and subsequent bubble dynamics is shown in Figure 2. In the first cycle, an initially undetectable ND, or group of NDs, begins to vaporize near the trough of the first rarefactional half-cycle, resulting in a bubble being produced and reaching its maximum size at ~1.0 μs.

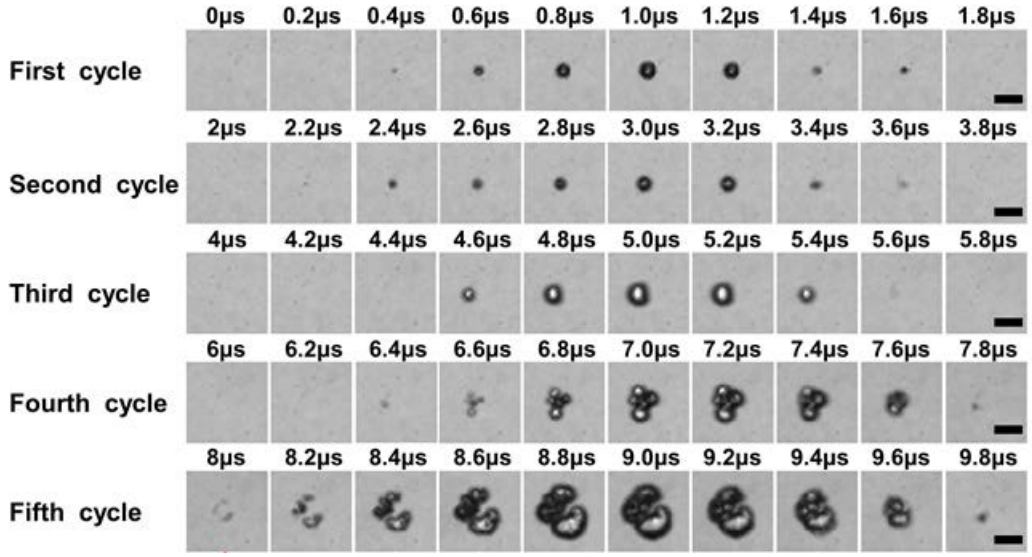

Figure 2. Example of a series of high-speed images of droplet vaporization captured over the first 5 cycles of a 100-cycle ultrasound pulse at 0.5 MHz and peak negative pressure of 1.5 MPa; scale bar is 5 μm. Images were taken at 5 million frames per second with an exposure of 200 ns per frame.

Over the compressional half-cycle, the bubble begins to visibly compress and disappears from view completely by the peak of the compression, most likely due to the optical resolution limit (~500 nm). The bubble then oscillates volumetrically, remaining approximately spherical over the next two cycles, but the size of the bubble increases. In the rarefactional phase of the fourth cycle, several bubbles appear in a cluster, either due to fragmentation of the original bubble or nucleation of additional droplets, and expand and contract. In the fifth cycle, bubbles appear that are highly non-spherical. They grow and then coalesce, appearing to form a single bubble, although this cannot be conclusively stated due to optical resolution limits once again.

The effects of PRF and pulse duration on the ADV and IC thresholds are shown in Figure 3(a) and (b), respectively. In most instances, the ADV threshold was lower than the IC threshold, but no statistically significant differences were observed. Both the ADV and IC thresholds decreased with the PRF and pulse duration. Figure 3(c) shows the IC threshold at all three frequencies with varying pulse length. The threshold was found to increase substantially with increasing frequency. Figure 4(d) shows that the ADV threshold decreased with increasing environmental temperature.

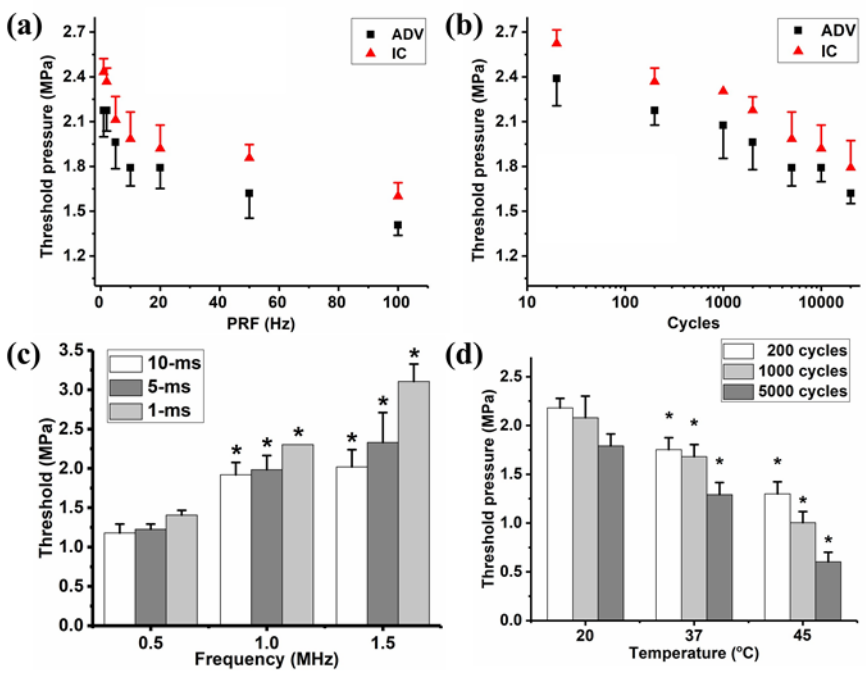

Figure 3. (a) The effect of varying PRF (pulse length 5000 cycles) on ADV and IC thresholds for PFB NDs at 1 MHz driving frequency. (b) The effect of varying pulse length (PRF = 10Hz) on ADV and IC thresholds for PFB NDs at 1 MHz driving frequency. (c) The effect of ultrasound frequency on the IC threshold. Mean IC thresholds of PFB NDs at frequencies of 0.5, 1 and 1.5 MHz with 1-ms, 5-ms and 10-ms pulse length respectively (* means $p < 0.05$ compared to the results of 0.5 MHz). (d) The effect of temperature on the ADV threshold pressure of PFB NDs at different pulse lengths (1 MHz driving frequency, PRF 10 Hz)(* means $p < 0.05$ compared to the results of 20 °C). The droplet size was 237±16nm and the concentration was ~10^9 ND/ml. Error bars indicate the standard deviation, n=3.

Figure 4 shows the effect of size, core material and concentration upon the ADV threshold. As expected PFB NDs were found to have a lower threshold than perfluorpentane (PFP) NDs but a change in diameter of ~2 did not have statistically significant effect. Increasing ND concentration led to a reduction in the ADV threshold. Numerical simulations of the US field within the fracture phantom showed that a standing wave would be expected and correspondingly 'hotspots' of higher acoustic pressure (Figure 5a). Experiments were also performed to investigate PFP ND vaporisation in the phantom. Acoustic emissions indicative of vaporisation were detected when a driving pressure of 0.5 MPa (as measured in water) was exceded at 1 MHz. Comparing with Figure 3, this indicates that there was amplification of the acoustic pressure within the fracture.

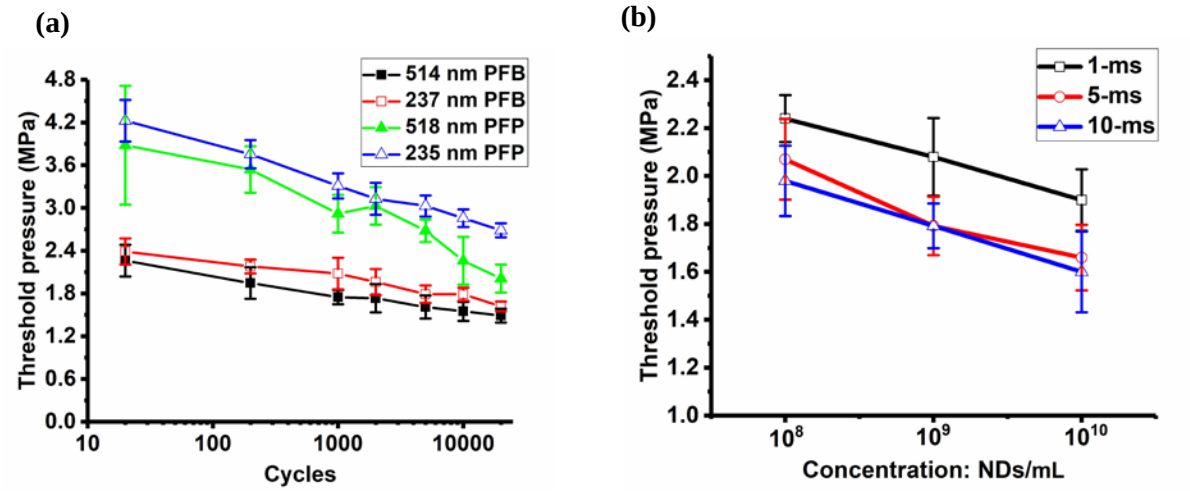

Figure 4. The effect of varying (a) ND size and core material and (b) ND concentration on the ADV threshold (driving frequency 1 MHz, PRF 10 Hz). Error bars indicate the standard deviation, n=3.

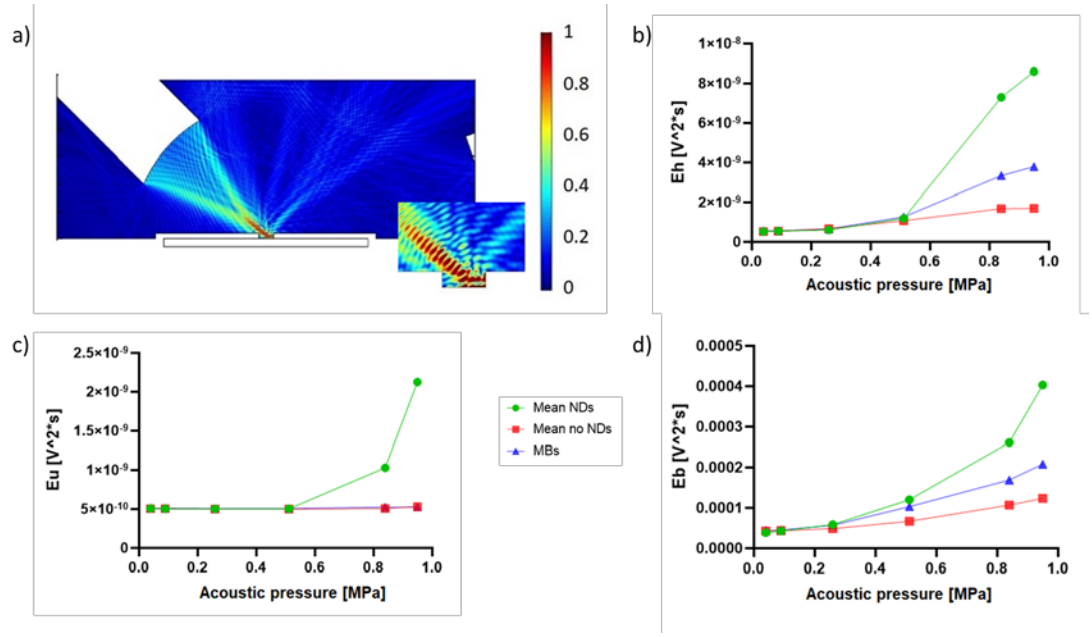

Figure 5. (a) Numerical simulations showing the acoustic pressure field developed in the fracture phantom (pressures are normalised to the maximum). Acoustic emissions measured from the fracture phantom with increasing driving pressure (as measured in water) at 1 MHz, with water, NDs or microbubbles injected into the cavity, (b) harmonic content, (c) ultraharmonic content, (d) broadband content.

Conclusion

We investigated the vaporization of PFC-NDs using both optical and acoustic methods over a range of therapeutically relevant exposure conditions. Consistent with previous studies, both the ADV and IC pressure thresholds were found to decrease with increasing PRF (1-100 Hz), pulse length (20-20000 cycles) and temperature (20-45 ^{o}C). The thresholds were found to increase with increasing driving frequency (0.5-1.5 MHz). ADV thresholds were found to be lower than IC thresholds, but there was no statistically significant difference between them for any of the parameter combinations tested. Overall the results indicate that PFB-ND vaporization can be achieved with exposure conditions that are not substantially higher than those used for therapeutic applications of microbubbles. Testing the NDs in a bone fracture phantom indicated that the creation of standing waves within the cavity and an amplitification in pressure reduced the apparent pressure required for vaporisation. This is encouraging for the potential use of NDs as therapeutic agents in bone healing. Future work will investigate further the observed changes in bubble dynamics over successive cycles following vaporization; confirm ND stability in vivo prior to ultrasound exposure and establish circulation times and clearance mechanisms.

A novel model for lipid-encapsulated microbubbles using transient network theory

Bashir M. Alnajar[1], Shankar L. Sridhar[2], Mark A. Borden[2,3], Franck J. Vernerey[2,3], Michael L. Calvisi[1]

[1]Department of Mechanical and Aerospace Engineering, University of Colorado, Colorado Springs, CO 80918, USA
[2]Department of Mechanical Engineering, University of Colorado, Boulder, CO 80309, USA
[3]Materials Science and Engineering Program, University of Colorado, Boulder, CO 80309, USA
Corresponding author: mcalvisi@uccs.edu

Introduction

Encapsulated microbubbles (EMBs) consist of a gas core surrounded by a stabilizing shell made of lipid, protein, or polymer and are on the order of 1-10 micrometers in diameter. The coating stabilizes EMBs and increases their residence time in the circulatory system, thereby making them effective for diagnostic or therapeutic purposes. The coating also greatly modifies the mechanical properties of microbubbles and affects their response to ultrasound [1,2]. In this study, we develop a novel constitutive model for lipid-coated EMBs that utilizes a statistically-based continuum theory known as transient network theory (TNT). This model accounts for the viscoelastic properties of lipid monolayers and replicates nonlinear effects reported in experiments, such as "compression-dominated" and "shear-thinning" behavior. Furthermore, unlike present models for spherical EMBs, the TNT-based model can be readily extended to modeling nonspherical deformations, which are important in diagnostic and therapeutic applications.

Methods

We consider a spherical, encapsulated gas bubble of instantaneous radius, R, which is suspended in an incompressible, viscous, Newtonian liquid. Due to the encapsulation, we neglect the presence of vapor in the interior and treat it as adiabatic. We assume spherical symmetry and use spherical polar coordinates (r, θ, ϕ) to denote position. If we further assume the shell thickness, h, is small compared to the radius (i.e., $h \ll R$), then in-plane stresses will dominate over bending. Therefore, the governing equations we derive are integrated through the membrane thickness, which is assumed constant due to the invariant length of the lipid molecules comprising the monolayer. Thus, we define a surface stress tensor $\boldsymbol{\sigma}$ (force/length) as the average of the Cauchy stress tensor, $\boldsymbol{\tau}$, across the shell thickness. If we assume the gas density is negligible, and that the shell density and liquid density are comparable, then conservation of momentum in the radial direction yields

$$R\ddot{R} + \frac{3}{2}\dot{R}^2 = \frac{1}{\rho_l}\left[p_{G0}\left(\frac{R_0}{R}\right)^{3\kappa} - p_0 - p_{ac}(t) - 4\mu_l\frac{\dot{R}}{R} + \frac{2\sigma}{R}\right], \tag{1}$$

where ρ_l is the liquid density, μ_l is the liquid viscosity, κ is the ratio of specific heats, R_0 is the initial radius, $\dot{R}$ is the radial velocity, $\ddot{R}$ is the radial acceleration, t is time, p_0 is the hydrostatic pressure of the surrounding liquid, $p_{ac}(t)$ is the applied acoustic pressure, and p_{G0} is the intial gas pressure. Here, σ is not the surface tension – which is assumed zero due to the shell presence – but the tangential component of the surface stress tensor due to the shell, which is equal in the azimuthal and polar directions by spherical symmetry.

To determine σ, we adopt the transient network theory (TNT) of Vernerey *et al.* [3] to a lipid encapsulation. The TNT is a statistically-based continuum theory based on transient networks that provides a general framework for modeling viscoelastic materials, including purely elastic solids or viscous fluids. This approach permits macroscopic continuum quantities − such as stress, elastic energy, and entropy − to be calculated locally based on the network configuration. For the present case, the TNT considers the bubble

encapsulation as an active network of interconnected lipids that dynamically attach to and detach from the network at specified rates.

A lipid membrane differs from a rigid shell, such as a polymer or protein, in that it behaves like a compressible material because the lipid monolayer maintains a constant thickness under deformation equal to the length of a lipid molecule. We begin by considering the arrangement of lipids on the surface of a microbubble that form a hexagonally-packed network in its equilibrium state, as shown in Fig. 1. The total concentration, c_{tot}, is defined as the total number of lipid bonds (attached and detached) per unit surface area of the bubble. When the bubble is deformed rapidly by dilatation, the average distance between the lipid molecules increases due to an increase in surface area. This increases intermolecular forces and thereby increases the surface stress in the tangential direction. The network therefore rearranges to dissipate the increased potential energy, resulting in a phase separation of clustered lipids and liquid medium (Fig. 1).

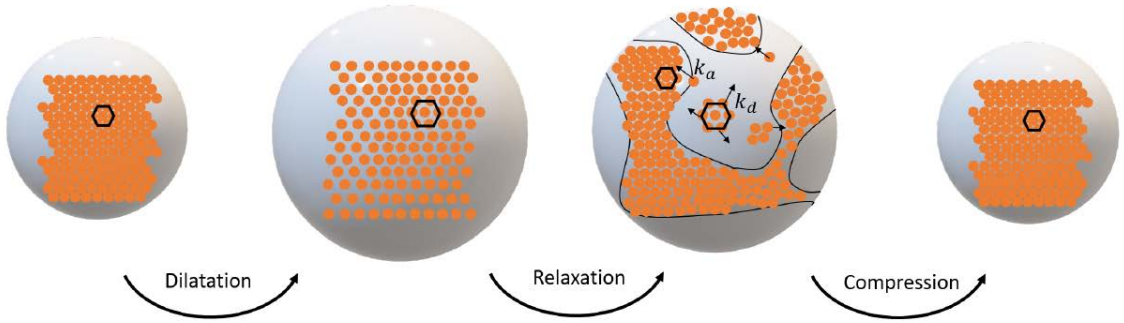

Figure 1. Schematic of the mechanisms of deformation and energy dissipation in a lipid monolayer.

We characterize the time scales of the dissipation mechanism through the rates k_d and k_a, which represent the breaking of lipid bonds in their stretched state and the reformation of new bonds at lower potential energy, respectively. This results in the relaxation of stresses on the surface of the microbubble, thereby making the shell a viscoelastic material. In addition, we also define the concentration, c, which represents the average number of attached (unbroken) bonds per unit area. When the bubble is compressed again, the separated phases merge to form the hexagonal close-packed structure of the initial rest state. The time scales of bubble deformation and lipid network arrangement compete when the bubble is subjected to acoustic vibrations to produce distinct viscoelastic behavior.

The TNT model provides evolution equations for the concentration, c, total concentration, c_{tot}, and the shell stress, σ, which are coupled to the radius, R. When solved simultaneously along with (1), subject to a given acoustic forcing, the radius is determined as a function of time. This model requires five independent parameters to be specified. In addition to the rate coefficients k_d and k_a, the model requires the equilibrium area of a lipid molecule, A_{eq}, the maximum number of bonds per lipid, N_{max}, and the radius at which the shell buckles, $R_{buckling}$. For $R < R_{buckling}$, the packing density of lipids is a maximum and the shell can not sustain further compression, therefore, it buckles. In the buckling regime, the shell stress is assumed to be zero.

Results

First, we use the TNT model to replicate a specific experimental curve of radius vs. time from van der Meer et al. [4], as shown in Tu et al. [5] for a lipid-shelled microbubble with an equilibrium radius of 1.7 μm (BR14, Bracco Diagnostics). The driving acoustic pressure used in the experiment is an 8-cycle Gaussian-tapered pulse with an amplitude of 40 kPa and a frequency of 2.5 MHz. Through trial and error, the TNT model parameters that provide the best fit to the experimental data of van der Meer et al. (2007) are determined to be A_{eq} = 0.43 nm^2, $\boldsymbol{N_{max}}$ = 40 bond/lipid, $R_{buckling} = R_0/\left(2^{1/6}\right)$, $k_d = 8.5 \times 10^6$ s^{-1}, and K_r = 0.77, where $K_r \equiv k_a/(k_a + k_d)$. The minimum standard deviation (STD) between the simulated

and experimental responses is 0.0027 for the TNT model. This result is compared with other models [6-8] in Table 1 in terms of the minimum STD, and it is shown that the present model provides better matching.

Table 1. Minimum STD resulting from different models for replicating the experimental radius vs. time measurements of van der Meer et al. [4].

Model	Minimum STD
Hoff [8]	0.059
Sarkar [7]	0.054
Marmottant [6]	0.054
TNT	0.0027

Second, the TNT model provides an analytical expression for the natural frequency of the bubble by linearizing the radial evolution equation for the case of small amplitude oscillations. The result is the linearized eigenfrequency, f_0 , given by

$$f_0 \approx \frac{1}{2\pi R_0}\left(\frac{3\kappa p_{G0}}{\rho_l} + \frac{4c_{ss}k_B T}{\rho_l R_0}\right)^{1/2}, \tag{2}$$

where c_{ss} is the steady state concentration of the active lipid-lipid bonds, given by

$$c_{ss} = \frac{N_{max}}{A_{eq}}\frac{k_a}{k_a + k_d}. \tag{3}$$

For small bubble size, this formula shows that resonance frequency strongly depends on the lipid packing density on the bubble surface and also on the rates of attachment and detachment. This result is validated against experimental data reported in Doinikov *et al*. [9] for two different ultrasound contrast agents (see Fig. 2). The two data sets are fitted with two different steady-state concentrations, which indicates that the optimum area of Definity® is greater than that of BR-14 at the same temperature.

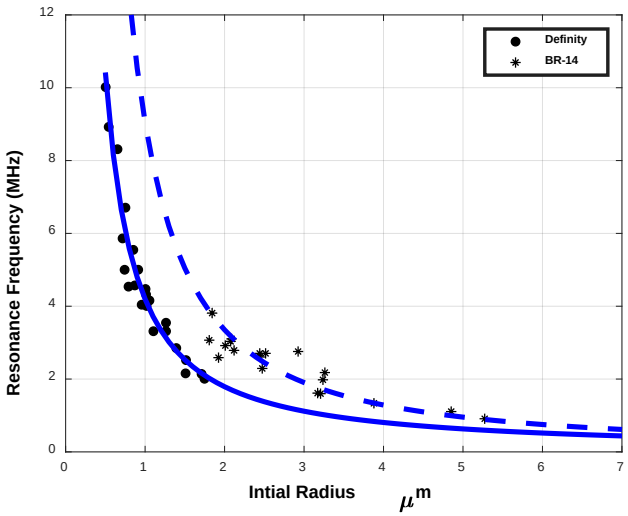

Figure 2. Resonance frequency vs. initial bubble radius for experimental measurements of two ultrasound contrast agents, Definity® and BR-14. The individual points represent experimental meausurements as reported in Doinikov *et al.* [9]. The solid and dashed lines show the linear resonance frequency using equation (2) with $c_{ss} = 2.3 \times 10^{19}$ bonds/ m^2 for Definity® and $c_{ss} = 1.8 \times 10^{20}$ bonds/ m^2 for BR-14.

Finally, experimental investigations of van der Meer *et al*. [4] and Supponen *et al*. [10] have shown a reduction in viscosity of a phospholipid monolayer shell as oscillation frequency increases, which is often referred to as a "strain-softening" or "shear-thinning" effect. Currently, the mechanism for this rheological thinning effect is not understood and, to our knowledge, has not been replicated by existing EMB models [10]. However, the present TNT EMB model demonstrates this strain-softening or shear-thinning effect and suggests an underlying mechanism for this behavior.

In this study, we conduct simulations to replicate the experimental results shown in Fig. 5 of Supponen *et al*. [10] in which a phospholipid-coated microbubble was driven by a small-amplitude sinusoidal acoustic pressure at its corresponding natural frequency over a range of initial radii from 1-5 microns. The shell parameters are fixed here in the TNT model. Note that the natural frequency is inversely proportional to radius, i.e., the natural frequency decreases as initial radius increases. The average dissociation rate of the lipid bonds, $k_d = 5.2 \times 10^6$ s^{-1}, which is assumed constant, is compared to the maximum dilatation rate of each bubble ($\dot{R}/R$). The ratio of these two quantities is plotted against the initial bubble radius in Fig. 3. This figure shows that, as the natural (driving) frequency decreases with increasing initial radius, the dilatation rate decreases relative to the rate of bond dissociation. This implies that the shell becomes more viscous (dissipative) and less elastic as the natural frequency decreases, or, conversely, the shell behaves more elastically as natural frequency is increased. In other words, at larger initial radii (and smaller natural frequency), more bonds are dissociated over a given period of oscillation, resulting in more energy dissipation and more viscous (and less elastic) behavior. This results in less viscous, i.e., shear-thinning, behavior at higher frequency, as borne out by the experiments of Supponen et al. [10].

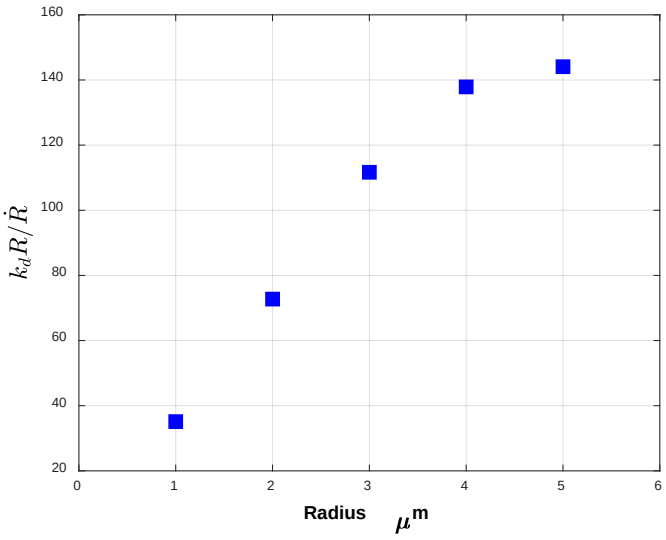

Figure 3. The ratio of the average lipid bond dissociation rate, $k_d = 5.2 \times 10^6$ s^{-1}, to the maximum dilatation rate ($\dot{R}/R$) for different initial radii.

Conclusions

A novel model for lipid-encapsulated microbubbles has been developed based on a statistically-based continuum theory known as transient network theory (TNT). This model replicates experimentally-observed radial responses including nonlinear behaviors, such as compression-dominated or expansion-dominated behavior (not shown here). Similar to previous EMB models [6-8], the TNT model provides evolution equations that describe the radial oscillation of EMBs subject to acoustic forcing. However, the TNT model offers several advantages. First, the model is based on parameters that, in principle, can be independently measured or calculated, rather than determined solely through fitting to experimental data. This offers the possibility of predicting a given EMB response subject to acoustic forcing based on knowledge of the lipid

shell formulation. Second, the model appears to both replicate as well as explain the experimentally-observed strain-softening or shear-thinning behavior of lipid-coated EMBs. Third, unlike other EMB models, the TNT model directly incorporates the physics of the lipid microstructure into the governing equations. Lastly, the model relates stresses and strains based on local deformations and, therefore, can be adopted into nonspherical models of EMBs in which the curvature and local strain vary across the bubble surface.

References

[1]. Frinking PJA, Bounakaz A, Kirhhorn J, Ten Cate FJ J, de Jong N, Ultrasound contrast imaging: current and new potential methods, Ultrasound in Medicine and Biology, 26: 965-975, 2000.

[2]. Ferrara K, Pollard R, Borden M, Ultrasound microbubble contrast agents: Fundamentals and application to gene and drug delivery, Annual Review of Biomedical Engineering, 9: 415-447, 2007.

[3]. Vernerey FJ, Long R, Brighenti R, A statistically-based continuum theory for polymers with transient networks, Journal of the Mechanics and Physics of Solids, 107: 1-20, 2017.

[4]. van der Meer SM, Dollet B, Voormolen MM, Chin CT, Bouakaz A, de Jong N, Versluis M, Lohse D, Microbubble spectroscopy of ultrasound contrast agents, Journal of the Acoustical Society of America, 121: 648-656, 2007.

[5]. Tu J, Guan J, Qiu Y, Matula TJ, Estimating the shell parameters of SonoVue microbubbles using light scattering, Journal of the Acoustical Society of America, 126: 2954-2962, 2009.

[6]. Marmottant P, van der Meer S, Emmer M, Versluis M, de Jong N, Hilgenfeldt S, Lohse D, A model for large amplitude oscillations of coated bubbles accounting for buckling and rupture, Journal of the Acoustical Society of America, 118: 3499-3505, 2005.

[7]. Chatterjee D, Sarkar K, A Newtonian rheological model for the interface of microbubble contrast agents, Ultrasound in Medicine and Biology, 29: 1749-1757, 2003.

[8]. Hoff L, Acoustic Characterization of Contrast Agents for Medical Ultrasound Imaging, (Kluwer, Dordrecht), 2001.

[9]. Doinikov AA, Haac JF, Dayton PA, Resonance frequencies of lipid-shelled microbubbles in the regime of nonlinear oscillations, Ultrasonics, 49: 263-268, 2009.

[10]. Supponen O, Upadhyay A, Lum J, Guidi F , Murray T, Vos HJ, Tortoli P, Borden MA, The effect of size range on ultrasound-induced translations in microbubble populations, Journal of the Acoustical Society of America, 147: 3236-3247, 2020.

Design and testing of a novel nitro-fatty acid microbubble for the treatment of ischemia-reperfusion injury using ultrasound-targeted microbubble cavitation

Gary Yu[1], Thiruganesh Ramasamy[1], Marco Fazzari[2], Xucai Chen[1], Bruce Freeman[2], John Pacella[1]

[1] Center for Ultrasound Molecular Imaging and Therapeutics, Department of Medicine, University of Pittsburgh, Pittsburgh, PA, USA
[2]Department of Pharmacology and Chemical Biology, University of Pittsburgh, Pittsburgh, PA, USA
Corresponding author: pacellajj@upmc.edu

Introduction:

Treatment of microvascular obstruction using ultrasound-targeted microbubble cavitation therapy mechanically relieves the physical obstruction in the microcirculation but does not specifically target the associated inflammatory milieu; nitro-fatty acids, owing to their pleiotropic anti-inflammatory effects, offer strong therapeutic potential but lack a means of rapid targeted delivery. The goal of this study was to develop a novel nitro-fatty acid microbubble, which not only retains the mechanical efficacy of standard MBs, but also provides for rapid targeted delivery of a therapeutic lipid payload to reduce inflammation during ischemia-reperfusion.

Methods:

A novel nitro-fatty acid microbubble (NFAB) was developed and characterized for stability using liquid chromatography/mass spectrometry techniques and for acoustic behavior using ultra-high-speed microscopy. NFAB were then used during ultrasound-targeted microbubble cavitation (UTMC) in both healthy and ischemia-reperfusion injury rat hindlimb models.

Results:

UTMC with NFABs resulted in significantly enhanced tissue delivery of the nitro-fatty acid. In addition, contrast-enhanced ultrasound perfusion imaging of the healthy hindlimb model showed that NFABs with UTMC resulted in significantly enhanced microvascular perfusion compared to free nitro-fatty acid alone or free nitro-fatty acid with UTMC using control microbubbles. In the ischemia-reperfusion injury model, UTMC with NFABs again significantly enhanced microvascular perfusion but importantly, also decreased expression of numerous inflammatory mediators. Tissue analysis of lipid peroxidation showed that UTMC with NFABs also offered significant protection against oxidative stress after ischemia-reperfusion injury compared to both free nitro-fatty acid alone and free nitro-fatty acid with control UTMC therapy.

Conclusions:

Our novel NFABs retain similar dynamic oscillatory properties as MBs that were successful in mechanically relieving MVO. In addition, they offer a rapid, targeted method of therapeutic lipid delivery, and that their application with UTMC represents a novel, targeted anti-inflammatory therapy for the treatment of ischemia-reperfusion injury.

Bracco Suisse SA
Marco Graf, Senior
Communication Events Manager
Cadempino, Switzerland

Mindray Medical Germany GmbH
Hongbo Zhu
Marketing Ultrasound Europe
Darmstadt, Germany

Erasmus University MC - Thorax Center
Prof.dr. Felix Zijlstra,
Head of the department
Rotterdam
The Netherlands

Siemens Healthineers
Helen Cleminson
SHS US IN ADGI
United Kingdom

GE Healthcare
Christopher (Scott) Lee
Product Leader – Optison
Missouri USA

Samsung Medison
Luc van Dalen, account manager HME of the Samsung Electronics Benelux

Philips Healthcare
Radjen Ganpat
Senior Field Marketing
General Imaging Ultrasound
Eindhoven, The Netherlands

Verasonics, Inc
Sara Shager
Marketing and Sales Associate
Kirkland, WA

Oldelft Ultrasound
Stefan Roggeveen
Commercial Manager
Delft, the Netherlands

Fujifilm VisualSonics
Adrie Gubbels, Sales Manager
Visualsonics
Amsterdam, the Netherlands

Solstice Pharmaceutic Managing directorals
Wim van Hoeve, Sales Manager
Enschede, the Netherlands

FIRST ANNOUNCEMENT 2022

27th EUROPEAN SYMPOSIUM ON ULTRASOUND CONTRAST IMAGING

20-21 JANUARY 2022

ROTTERDAM, THE NETHERLANDS

Information on the 27th **EUROPEAN SYMPOSIUM ON ULTRASOUND CONTRAST IMAGING: Sharon Sewell, s.sewell-albert@erasmusmc.nl**

sponsors:

Golden sponsor

Erasmus MC
Erasmus
THORAX CENTRUM

BRACCO
LIFE FROM INSIDE

Silver sponsor

FUJIFILM
VISUALSONICS

SIEMENS
Healthineers

Bronze sponsor

mindray
healthcare within reach

SAMSUNG

Solstice
pharmaceuticals

GE Healthcare

Oldelft
Ultrasound

PHILIPS

The 26th European Symposium on Ultrasound Contrast Imaging, Rotterdam is sponsored by: